



Journal of Engineering

ISSN 1726-4073



A Scientific Refereed Journal
Published by College of
Engineering University of
Baghdad

March
٢٠١٤

Number 3
Volume 20

ISSN 1726-4073

مجلة الهندسة



مجلة علمية محكمة تصدرها
كلية الهندسة - جامعة بغداد

أذار

٢٠١٤

العدد ٣

المجلد ٢٠

List of Contents

English Section:	Page
Development of Pavement Maintenance Management System for Baghdad Urban Roadway Network <i>Prof. Saad Issa Sarsam</i> <i>Asst. Lect. Amina Talal Abdulhameed</i>	1-14
Spatial Prediction of Monthly Precipitation in Sulaimani Governorate using Artificial Neural Network Models <i>Prof. Dr. Rafa H. AL-Suhaili</i> <i>Rizgar A. Karim</i>	15 -27
Competitive Stripping of Multi-Organic Pollutants from Contaminated Water in Bubble Column Semi-Batch <i>Waleed M. Salih</i> <i>Ahmed A. Mohammed</i> <i>Yaseen R. Hasan</i>	28 -40
Evaluating the Crop Coefficient for Cherries Plants in Michigan State <i>Sabah Anwer Dawood Almaraf</i>	41 – 50
Experimental and Modeling Study of Abrasive Wear of Tungsten Carbide Drilling Bit in Wet and Dry Conditions <i>Asst. Prof. Dr. Fathi Al-Shammaa</i> <i>Dr. Amar Hussein Al-Allaq</i> <i>Mohaimen Habeeb Makki</i>	51 - 61
Improving Fatigue Life of Bolt Adapter of Prosthetic SACH Foot <i>Prof. Muhsin J. Jweeg</i> <i>Asst. Prof. Kadhim K. Resan</i> <i>Ali Abdulameer Najim</i>	62 – 71
Numerical Simulation of 3D- Flow Structure and Heat Transfer for Longitudinal Riblet Upstream of Leading Edge Endwall Junction of Nozzle Guide Vane <i>Prof. Dr. Najdat Nashat. Abdulla</i> <i>Asst. Prof. Dr. Ikhlas Mohammed Fayed</i> <i>Asst. Lecturer Kareem Khalf Ali</i>	72- 86
Experimental Study for Materials Prosthetic above Knee Socket under Tensile or Fatigue Stress with Varying Temperatures Effect <i>Asst. Prof. Dr. Hatem Rahim Wasmi</i> <i>Asst. Prof. Dr. Jumaa Salman Chiad</i> <i>M. Sc. Student: Adawiya Ali Hamzah</i>	87 -95
An Experimental Study of the Effects of Coolant Fluid on Surface Roughness in Turning Operation for Brass Alloy <i>Asst. Lect. Suhair Ghazi Hussein</i>	96 - 104

**A Modified Strength Pareto Evolutionary Algorithm 2 based Environmental
/Economic Power Dispatch**

105 - 123

*Asst. Prof. Dr. Hassan Abdullah Kubba
Saif Sabah Sami*

**Estimation of Some Mechanical Soil Properties from Static and Dynamic Plate Load
Tests**

124 - 133

Hayder Alwan Mahdi Al-Zayadi



Development of Pavement Maintenance Management System for Baghdad Urban Roadway Network

Prof. Saad Issa Sarsam

Department of Civil Engineering

College of Engineering

University of Baghdad

Email: saadisarsam3@hotmail.com

Asst. Lect. Amina Talal Abdulhameed

Department of Civil Engineering

College of Engineering

University of Baghdad

Email: eng_aminaa@yahoo.com

ABSTRACT

The road transportation system is considered as major component of the infrastructure in any country, it affects the developments in economy and social activities. The Asphalt Concrete which is considered as the major pavement material for the road transportation system in Baghdad is subjected to continuous deterioration with time due to traffic loading and environmental conditions, it was felt that implementing a comprehensive pavement maintenance management system (PMMS), which should be capable for preserving the functional and structural conditions of pavement layers, is essential.

This work presents the development of PMMS with Visual inspection technique for evaluating the Asphalt Concrete pavement surface condition; common types of Asphalt Concrete distress including (bleeding of Asphalt, patching, block cracking, edge cracking, longitudinal and transverse cracking, rutting, pot holes, longitudinal and transverse deformation) with their various severity and intensity conditions have been included in the system as data base. The surface of the pavement was divided into sections, and the pavement condition is visually evaluated by the raters using specially designed forms, each type of defect was measured, classified, and rated according to type, severity, and extent. Data will be fed to the system using the computer, various types of intensity and severity of distress were analyzed by the system, the present condition rating (PCR) of the pavement section is determined, and the system suggests the required maintenance action. The developed system which is assigned (PMMS-09) was verified in evaluating the pavement surface condition at AL-Jaderiah campus roadway network. The results indicated that the system is sound in evaluation of the pavement condition and in suggestion of the proper maintenance to reserve the pavement condition.

Keywords: asphalt concrete, condition, maintenance, pavement.

استنباط نظام ادارة صيانة الرصف لشبكة الطرق الحضرية في بغداد

م.م آمنة طلال عبد الحميد

قسم الهندسة المدنية

كلية الهندسة / جامعة بغداد

أ. سعد عيسى سرسم

قسم الهندسة المدنية

كلية الهندسة / جامعة بغداد

المستخلص:-

يعتبر نظام النقل بشبكة الطرق من المكونات الرئيسية في البنية التحتية لأي بلد، حيث يكون مؤثراً على تطوير الاقتصاد والفعاليات الاجتماعية. تتعرض الخرسانة الإسفلتية التي تكون المادة الرئيسية في رصف شبكة الطرق في بغداد للخراب المستمر

مع تقدم الزمن نتيجة التعرض لأحمال المرور والظروف المناخية، وهذا يتطلب وجود (نظام إدارة صيانة الرصفة) يكون قادرا على المحافظة على الوضع الخدمي والإنشائي لطبقات الرصفة المختلفة وذلك بالسيطرة على العيوب التي تتعرض لها. تم في الدراسة استنباط (نظام ادارة صيانة الرصف لشبكة الطرق الحضرية في بغداد) باستخدام الحاسوب مع تقنية الفحص البصري لتقييم حالة سطح رصفة الخرسانة الاسفلتية. تمت الاحاطة بكافة انواع عيوب الرصفة المعروفة والتي تشمل (نزف الاسفلت، الترفيع، الشقوق الكنائية، شقوق حافة الرصفة، الشقوق الطولية والمستعرضة، الحفر، والتخدد الطولي والمستعرض) مع درجة الشدة ومدى الانتشار لكل نوع من هذه العيوب وجدولتها في قاعدة بيانات داخل النظام. يتم تقييم سطح الرصفة بصريا باستخدام استمارات صممت لهذا الغرض بعد تقسيم السطح الى مقاطع، ثم ادخال المعلومات الى النظام بالحاسوب حيث يتم تحليل انواع شدة العيوب ومدى انتشارها، ويعطي النظام تقييما لحالة سطح الرصفة (PCR) لكل مقطع مع مقترح لنوع وطريقة الصيانة المناسبة وتكلفة المقترح. تم اختبار هذا النظام والذي تمت تسميته **PMMS-09** بتقييم حالة سطح الرصفة لشبكة طرق جامعة بغداد في مجمع الجادرية وتشير النتائج بان هذا النظام يعتبر سليما لتقييم حالة سطح رصفة الخرسانة الاسفلتية واقتراح طرق الصيانة المناسبة للمحافظة على حالة الرصفة.

الكلمات الرئيسية: خرسانة اسفلتية، حالة، صيانة، رصف

1. INTRODUCTION

Pavement maintenance management systems are designed to manage maintenance and rehabilitation activities to optimize pavement condition with available funds. The use of (PMMS) is becoming increasingly more prevalent due to benefits achieved. It considers current and future pavement condition, priorities, funding, and can reduce pavement deterioration, this helps maintain pavement structural capacity, and may extend pavement life by slowing or limiting future pavement degradation. Pavement condition can be quantified by the pavement condition rating (PCR) which rates the pavement according to the extent and severity of distress types present (cracking, raveling, bleeding, shoving ...etc). (PCR) ranges from 100 to zero (best to worst). A major goal of (PMMS) is to keep pavement condition in the upper (PCR) range of (60-90) by limiting surface structural degradation to keep down rehabilitation cost.

1.1 The Study Area

The road network at AL-Jaderiah campus was constructed and opened to traffic at 1980. It consists of 25cm of compacted sub grade with CBR value $\geq 5\%$, 40 cm of sub base type B with CBR value $\geq 35\%$, 10cm of Asphalt stabilized base course, 7cm of binder course and 6cm of

surface course. The network was subjected to resurfacing with 6cm resurfacing course during the year 2000. **Fig. 1** shows the roadway sections at Al-Jaderiah campus, Sarsam (2008).

2. SECTION LENGTH AND AREA CALCULATION

The actual length of each test section in meters (ACT Length) is calculated by the system using the following equation:

$$\text{ACT Length} = \text{End station} - \text{Beginning station.} \quad (1)$$

Next, three areas are calculated, the pavement section area (PAV), the wheel path area (WP), and the non-wheel path area (NWP) using the formula below:

$$\text{PAV area} = \text{ACT Length} * \text{lane width (3.5m)} \quad (2)$$

$$\text{WP area} = \text{ACT Length} * 50\% \text{ of lane width (1.75m)} \quad (3)$$

$$\text{NWP area} = \text{PAV area} - \text{W Parea} \quad (4)$$

Plate 1 shows the roadway identification and the section information.



3. ASSESSING PAVEMENT SURFACE CONDITION

The first step in the procedure starts when the whole Pavement surface was divided into sections of 100 meter length, then it involves identification of both type and severity of the pavement distresses present in the study area of the road sections by establishing the existing pavement condition using the visual walk through survey. Graphic plots of various types of pavement surface distress of each pavement section were obtained from Sarsam, 2008 and shown in **Plate 2**. This procedure was performed with the use of the South Dakota DOT Manual, 1997, Miller & Bellinger Manual, 2003, WSDOT Manual, 2007, and McGhee, 2002, Sarsam and Talal, 2009 which contains definitions and information concerning pavement distresses.

Table 1 illustrates various types of distress fed to the data base of the software, and the distress types identified at AL-Jaderiah campus.

In the second step, each of the various types of Pavement distresses was identified and measured (i.e. units of linear meter or square meters). In addition, for each distress, a level of severity was determined [low (L), Medium (M), High (H)]. The distresses data were to the Inspection Sheet shown in **Plate 3**, of the system. Once the visual assessment of the road area was complete, calculations were performed by the system using the data collected in the field, through these calculations, a pavement condition rating (PCR) for the road network was determined.

3.1 Assessment Calculations:

Using the data obtained through the assessment procedure shown in Plate 1, the following calculations were performed by the system to determine the pavement condition rating (PCR) for the road network. For each of the different types and severity of distresses, a distress density (extent) was calculated by the system. The following are the formulas Eqs. 5 through 7 that were fed and used to calculate the distress densities:

$$\text{Density} = (\text{Distress amount in square meters} / \text{Unit area in square meters}) \times 100\% \quad (5)$$

$$\text{Density} = (\text{Distress amount in linear meter} / \text{Unit length in linear meter}) \times 100\% \quad (6)$$

$$\text{Density} = (\text{Number of potholes, patches} / \text{Unit area in square meters}) \times 100\% \quad (7)$$

3.2 Distress Severity Assessment

The most common form used for the knowledge representation of the system is (IF-THEN) rule; such forms are fed to the system as described below.

3.3 Block Cracking

IF crack mean width \leq 6mm,
THEN severity is low.

IF crack mean width $>$ 6mm and \leq 19mm,
THEN severity is moderate.

IF crack mean width $>$ 19mm,
THEN severity is high.

Record square meters of affected area at each severity level.

3.4 Longitudinal, Reflection, and Transverse Cracking

IF crack mean width \leq 6mm,
THEN severity is low.

IF crack mean width $>$ 6mm and \leq 19mm,
THEN severity is moderate.

IF crack mean width $>$ 19mm,
THEN severity is high.

Record the length in meter at each severity level for longitudinal cracks, and the length and number of reflection or transverse cracks at each severity level.

3.5 Potholes

IF pothole depth $<$ 25mm,
THEN severity is low.

IF pothole depth > 25mm and < 50mm,
THEN severity is moderate.

IF pothole depth > 50mm,
THEN severity is high.

Record number of potholes and square meters of affected area at each severity level.

3.6 Rutting, Bleeding, Raveling, Polished Aggregate and Shoving

Record maximum rut depth in millimeters, and number of occurrences and square meters of affected area, severity level is not applicable.

3.7 Fatigue Cracking (in the wheel path)

IF an area of cracks with few fine parallel cracks connected, **THEN** severity is low.

IF interconnected cracks forming alligator pattern, **THEN** severity is moderate

IF interconnected cracks forming alligator pattern with sapling and distortion, **THEN** severity is high

Record square meters of affected area at each severity level.

3.8 Patching

IF patch shows no visual distress, **THEN** severity is low.

IF patch shows medium distress with notable roughness, **THEN** severity is moderate.

IF patch shows high distress with distinct roughness, **THEN** severity is high.

Record number of patches and square meters of affected area at each severity level.

3.9 Edge Cracking (area within 0.6m of the pavement edge)

IF cracks are light with no breakup or loss of material, **THEN** severity is low.

IF cracks are well defined with some breakup and loss of material, **THEN** severity is moderate.

IF cracks are well developed with significant breakup and loss of material, **THEN** severity is high.

3.10 Distress Extent Assessment

3.11 Transverse Cracking

IF crack spacing > 15 m, **THEN** extent is low.

IF crack spacing > 7.5 m and < 15 m, **THEN** extent is moderate.

IF crack spacing < 7.5 m, **THEN** extent is high.

3.12 Fatigue Cracking

IF crack is 1% to 9% of wheel path, **THEN** extent is low.

IF crack is 10% to 24% of wheel path, **THEN** extent is moderate.

IF crack is 25% to 49% of wheel path, **THEN** extent is high.

3.13 Patching

IF patching is 1% to 9% of section, **THEN** extent is low.

IF patching is 10% to 24% of section, **THEN** extent is moderate.

IF patching is 25% to 49% of section, **THEN** extent is high.

3.14 Block Cracking

IF cracking is 1% to 9% of section, **THEN** extent is low.

IF cracking is 10% to 49% of section, **THEN** extent is moderate.

IF cracking is > 49% of section, **THEN** extent is high.

The values for the densities (extent) were recorded. Next, using the calculated densities and the severity (i.e. L, M, or H) a deduct value for each distress type was determined. The deduct values were determined through the use of the "Deduct Value Curves" for each of the various distress types identified. The curves are part of the U.S. Army Corps of Engineers Technical Report TR97/104. The mathematical models for each



distress type curve were fed to the system. The deduct values for all the distresses were then summed to produce a "Deduct Total" using the mathematical equation below.

$$\text{Deduct total DT} = \sum_{D=1}^{16} \text{Deduct (patching)} + \text{Deduct (cracking)} + \text{Deduct (bleeding)} \quad (8)$$

Given the "Deduct Total" and a value for the number of deducts greater than 5 points. Equation 8 will be used by the system to determine a "Corrected Deduct Value" or (CDV). Finally, the pavement condition rating (PCR) was calculated using the following equation:

$$\text{PCR} = 100 - \text{CDV} \quad (9)$$

Plate 4 illustrates the final calculations for the physical condition of the pavement by the software.

3.15 Pavement Surface Condition Rating

Given the value of the PCR for the road section, a pavement condition rating was determined using the most common form used for the knowledge representation of the system (IF-THEN) rule, and the information and limitations illustrated in the distress identification manuals previously referred to as below:

IF PCR >0 and ≤ 40, **THEN** PCR= Very poor
IF PCR >40 and ≤ 55, **THEN** PCR= Poor
IF PCR >55 and ≤ 65, **THEN** PCR= Fair to poor
IF PCR >65 and ≤ 75, **THEN** PCR= Fair
IF PCR >75 and ≤ 90, **THEN** PCR= Good
IF PCR >90 and ≤ 100, **THEN** PCR= Very good

4.PAVEMENT MAINTENANCE TREATMENTS DECISION

The selection of the right maintenance strategy at the right time will be influenced by the type, severity, and extent of the pavement surface distresses and the structural and roughness condition of the pavement. Choosing the right treatment also depends on the extent or frequency

that the distress occurs. Some of the treatments may be most applicable when very little distress is present. For each distress, a number of possible maintenance treatments exist. The maintenance treatment strategies were obtained from Pavement maintenance manuals (NDOT-2004; OhioDOT-1999; SHRP-1993), and fed to the system.

4.1 System Logic

Based on the work done by Misra and Rohanirad, 2003, Fred, 1997, Sarsam, 2008, The system describes what to do in particular distress circumstances. There are six major treatments decisions which should be taken into consideration as illustrated below:

1. Do Nothing
2. Crack filling and sealing
3. Patching
4. Milling
5. Thin hot mix overlay application
6. Shoulder maintenance

Each type of pavement distress will lead the system to consider more than one treatment alternatives depending on distress severity, extent and the required extension in Pavement life as follows:

IF Alligator cracking exists, **THEN** select 1, 3, 5
IF Distortion exists, **THEN** select 1, 2, 3, 5
IF Edge cracking exists, **THEN** select 1, 2, 6
IF Rutting exists, **THEN** select 1, 4, 5
IF Longitudinal cracking, **THEN** select 1, 2, 3
IF Bleeding exists, **THEN** select 1, 4, 5
IF Block cracking exists, **THEN** select 1, 2, 5
IF Raveling or weathering exists **THEN** select 1, 5
IF Transverse cracking, **THEN** select 1, 2, 3, 4
IF Coarse texture **THEN** select 1, 4, 5

It must be emphasized that such treatments could be applied and may be effective in treating the distress, and increasing the expected life of the pavement. The Do Nothing strategy may be the most appropriate under certain circumstances.

Plate 2 illustrates typical output of the system.

Plate 5 demonstrates the software output, the software decided the maintenance alternative, and calculate the cost of maintenance of the section by

multiplying the unite cost of the selected alternative by the area of the defected section. The unite cost data must be upgraded periodically.

4.2 Software Environments

Microsoft ACCESS 2003 (which was selected for the development of PMMS for Baghdad urban roadway network) employs three programming languages to enable user to add fine – tuning to an application. The Structured Query Language (SQL) is the language access used behind the scenes in queries that can extract, manipulate and relate data from one or more tables. Macros consist of list of actions that execute in response to an event such a button click or data in a form changes. The developed system processes in four steps, the first step involves field data collection and tabulation while the second step involves creating the table definitions and key field requirements, and data validation rule, define tables linked to look up. Finally data were added to tables to be able to test application thoroughly. The third step is the data entry form, the fields in the form carefully arranged in logical order and with meaning full label to help prevent entry errors. The fourth step considers macros and event procedure , function were added to the form design that it would be perform appropriately to user action as shown in **plate 6**.

5. ANALYSIS AND DISCUSSION OF VISUAL ASSESSMENT OF PAVEMENT SURFACE CONDITION

The original raw data that was collected in the field and the results of the calculation described in the previous section are included in **Plates 2 and 5** which is a summary of the data and results. As shown, there were different types of distresses identified during the inspection of the representative area. The levels of severity for the distresses identified ranged from low severity (L) to high severity (H). The total amount of “deduct” and the corrected deduct value “CDV” was calculated by the system and illustrated in **Plate 4**. The pavement condition rating (PCR) was determined to be in the range of (99-45) % which

results in a rating of "poor to very good" for the road sections based on the rating index provided.

6. CONCLUSIONS AND RECOMMENDATIONS

This paper has produced a methodology that can use the visual data obtained in the field and perform analysis of distress using an expert system. The developed system was tested in a small project that include most of distress types, it could provide a better environment to assess and analyze data about the condition and maintenance of Asphalt concrete pavement, it combines detailed inventory and evaluation procedures with analytical software routines. It is simple to perform, use less expensive techniques and individuals to subjectively rate Asphalt pavement sections based on observed distress, provides job opportunities for Engineers and technicians.

Based on the information obtained during this evaluation, it is recommended to consider using the software, and it should be tested in bigger project to evaluate whether it will be labor intensive.

7. REFERENCES

- Fred F, 1997, *Pavement Management System-Past, Present, And Future* National Workshop on pavement management in New Orleans-L .A. July 20.
- Johanns M. & Craig J, 2004, *Pavement Maintenance Manual* Nebraska DOT.
- Mcghee K.H, 2002, *Development and Implementation of Pavement Condition Indices* Virginia DOT., September.
- Miller J.S. & Bellinger W.Y, 2003, *Distress Identification Manual for the Long Term Pavement Performance Program* FHWA-RD-03-031, US Department of transport, June.
- Misra A. & Rohanirad A, 2003. *Guidelines for Roadway Management System for Local Governments* MTC Project A-01, October.



Ohio DOT, 1999. *Pavement Design and Rehabilitation Manual* January.

Sarsam S., 2008, *Development of Pavement Maintenance Management System using Visual Evaluation of Asphalt Concrete Surface Condition and Expert System*, 2008. Proceeding, 7th International Conference on managing Pavement Assets (ICMPA 7), Calgary, Alberta, Canada, 25-27 June-.

Saad Sarsam and Amna Talal, 2009, *Development of Pavement Maintenance Management System for Baghdad Urban Roadway Network* Proceedings, 1st scientific conference of Civil Engineering College – AL

Baath University, Industry of Engineering Constructions 11-13 May, Humus – Syria.

SHRP, 1993, *Distress Identification Manual for the Long-Term Pavement Performance Project* National research council, SHRP-P 338, Washington DC.

South Dakota DOT, 1997, *Enhanced Pavement Management System- Visual Survey Manual 2001*.

US Army Corps of Engineers, Technical report TR97/104 "Paver asphalt distress manual".

WSDOT, 2007, *Pavement Surface Condition Field Rating Manual for Asphalt Pavement* Northwest Pavement management association, January.

Section Identification : نموذج

PMMS IQ-Baghdad

Province: Baghdad City: AL Jaderiah Zone: AL Rusafa

Section ID: Sec. ٦١٠ - St. ١٧ - Section No. ٢٤ Work Staff: Eng. Ahmed & group

Roadway Rank: Six Lane- Arterial Surface Type: HMA

St. From: ++٢٠٠ To: ++٤٠٠ Lane width m: ٢,٤٥

Sec. Length: 100 m Date: 12/5/2009

Paved Area (PAV)= 240 sqm

Non Wheel Path Area (NWP) 100 sq m

Wheel path Area (WP) 240 sq m

Finish

NUM طريقة عرض النموذج

start 3:43 PM

Plate 1. Roadway identification and section information.

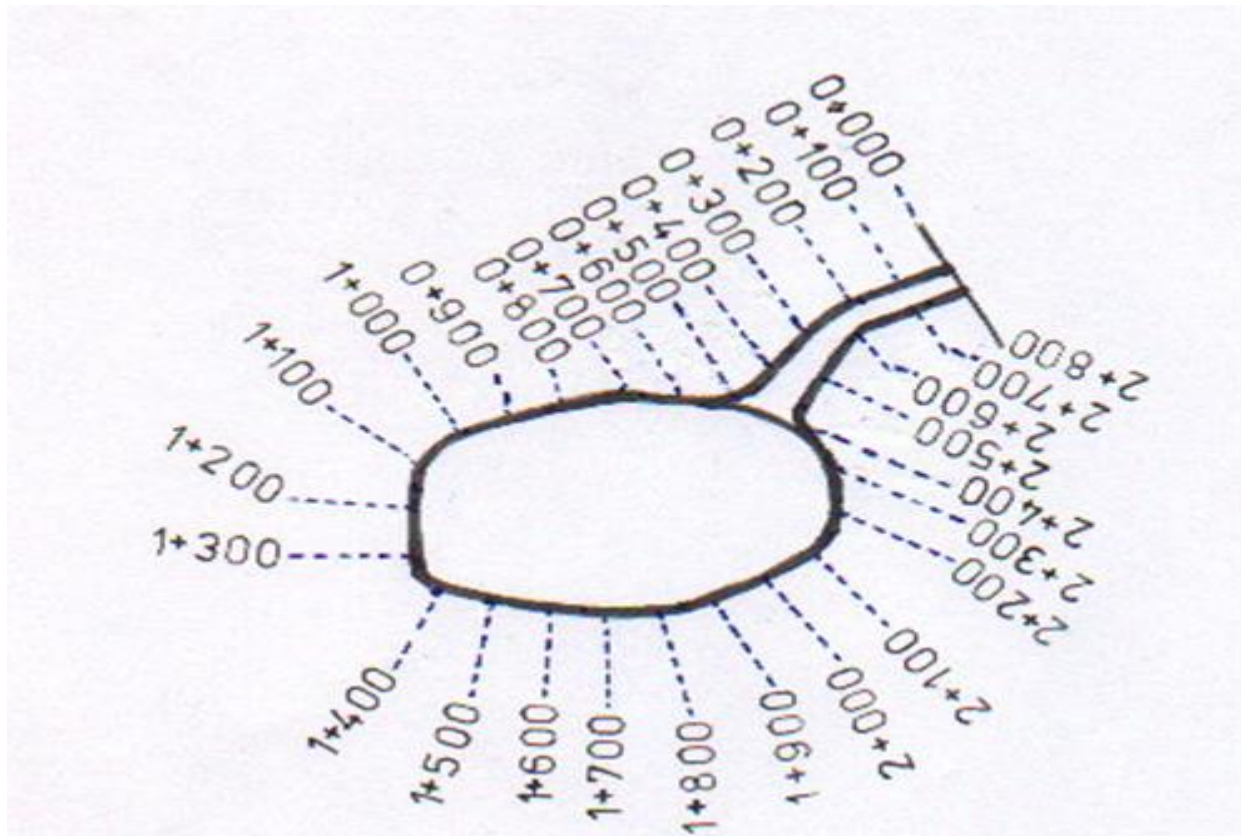
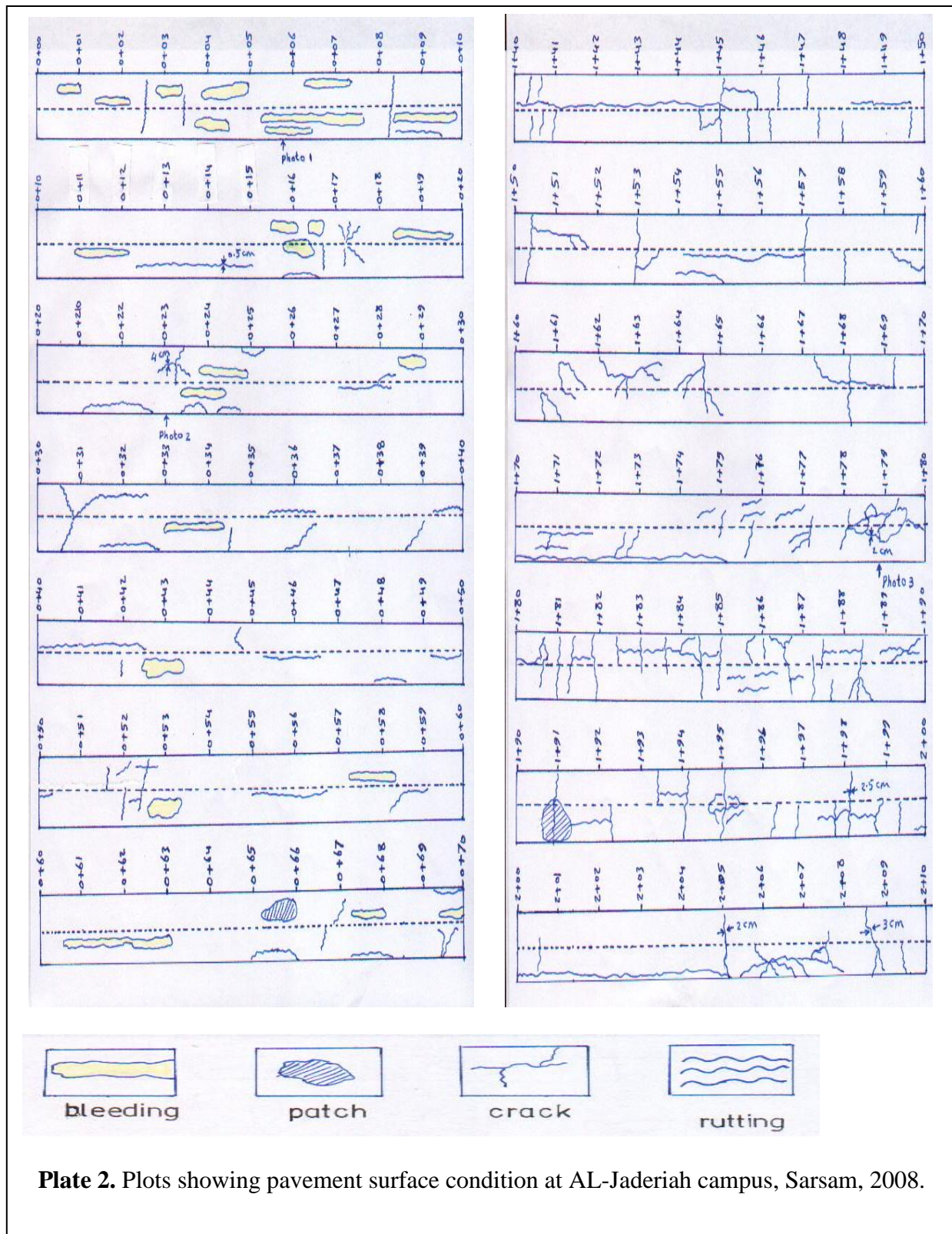


Figure 1. Sections of road network at AL-Jaderiah campus, Sarsam, 2008.

Table 1. Distress types included in the software,Sarsam and Talal, 2009.

Distress types included	Distress types observed at AL Jaderiah campus road network
1- Cracking Fatigue cracking Block cracking Pavement edge cracking Transverse cracking Reflection cracking Longitudinal wheel path cracking Longitudinal non-wheel path cracking	Block cracking Pavement edge cracking Transverse cracking Longitudinal wheel path cracking Longitudinal non-wheel path cracking
2- Surface deformation, Rutting, Shoving	Rutting
3- Patching and potholes	Patch, Pothole
4- Surface defect Bleeding, Lane to shoulder drop off, Polished aggregate, Raveling and Coarse Macro-texture	Bleeding Coarse Macro-texture



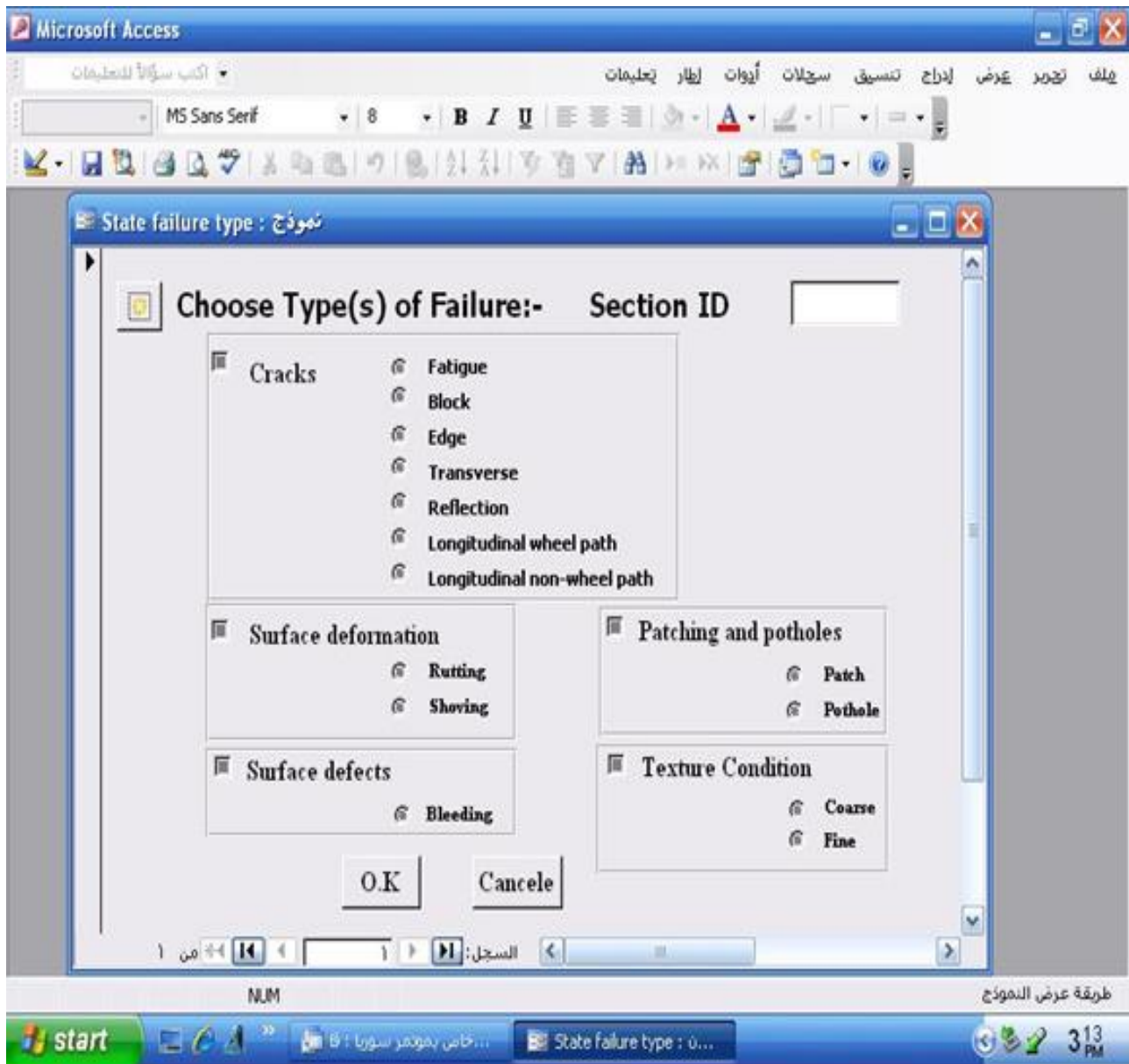


Plate 3. Type of pavement distress.

Microsoft Access

أكتب سؤالاً للتعليمات

ملف تحرير عرض إدراج تنسيق سجلات أيقونات إظهار تعليمات

Tahoma 8 B I U

نموذج : Physical Characteristics

Transvers Cracks

Crack mean width (mm) Severity

crack spacing (mm) Density

Crack Length (m) Extent

no. of cracks

Bleeding

Input Square Meters of Affected Area Density

No. of Occurences Extent

Patching

Select

☒ No Visual Distress

☐ Medium Distress with Notable Roughness

☐ High Distress with DistineRoughness

Severity

Density

Extent

Input No of Patching

Input % of Affected Area

Section Summary Condition Rating

Total Deduct

Corrected Deduct

PCR%

O.K Cancele

NUM OVR

طريقة عرض النموذج

start

فأني بموقع سوريا : ب

Physical Charactersti...

5:43 PM

Plate 4 . Physical characteristics of the pavement.

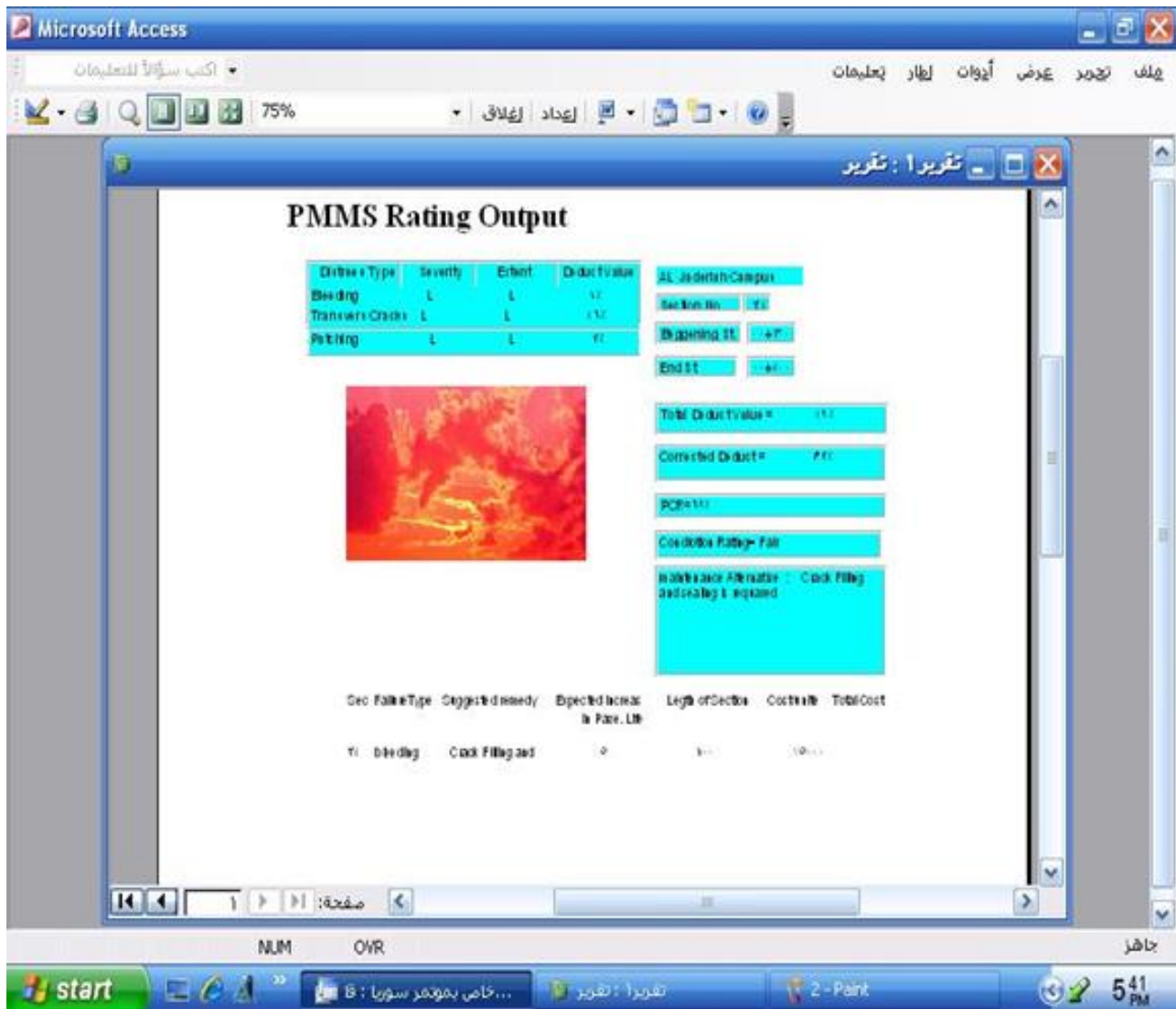


Plate 5. PMMS system output.

The image shows a software window titled "Streets". Inside the window, there is a data entry form. The form consists of several text input fields arranged vertically on the left side, each with a label: "StreetName", "ConstructionDate", "Location", "Province", "City", "Zone", "Type", "TotalLength", "NoOfSections", and "MaintenanceDate". To the right of these fields is a larger text area labeled "notes". Further to the right, there is a dropdown menu and three buttons: "Add Section", "Edit Section Info.", and "Remove Section". At the bottom of the window, there is a navigation bar with Arabic text "السجل:" and "من 5", along with several small icons for navigating between records.

Plate 6. Sample of data entry form.

Spatial Prediction of Monthly Precipitation in Sulaimani Governorate using Artificial Neural Network Models

Prof. Dr. Rafa H. AL-Suhaili

Prof., Civil Eng. Dept., College of Eng., University of
Baghdad, Iraq
Email:rafaalsuhili@yahoo.com

Rizgar A. Karim

Asst. Lec., Dam and W. R. Eng. Dept., Faculty of Eng.,
University of Sulaimani, Iraq
Rizgar_Karim@yahoo.com

ABSTRACT:

ANN modeling is used here to predict missing monthly precipitation data in one station of the eight weather stations network in Sulaimani Governorate. Eight models were developed, one for each station as for prediction. The accuracy of prediction obtain is excellent with correlation coefficients between the predicted and the measured values of monthly precipitation ranged from (90% to 97.2%). The eight ANN models are found after many trials for each station and those with the highest correlation coefficient were selected. All the ANN models are found to have a hyperbolic tangent and identity activation functions for the hidden and output layers respectively, with learning rate of (0.4) and momentum term of (0.9), but with different data set sub-division into training, testing and holdout data sub-sets, and different number of hidden nodes in the hidden layer. It is found that it is not necessary that the nearest station to the station under prediction has the highest effect; this may be attributed to the high differences in elevation between the stations. It can also found that the variance is not necessary has effect on the correlation coefficient obtained.

Keywords: ANN models, monthly precipitation data, weather station networks, prediction, spatial distribution of precipitation.

رزگار أحمد كريم

مدرس مساعد، قسم هندسة السدود والموارد المائية
كلية الهندسة، جامعة السليمانية

الاستاذ الدكتور رافع هاشم السهيلي

أستاذ، قسم الهندسة المدنية، كلية الهندسة
جامعة بغداد

الخلاصة:

تم استخدام تقنية نمذجة الشبكات العصبية الصناعية لتخمين بيانات الأمطار الشهرية في إحدى المحطات الهيدرولوجية المناخية من واقع ثمان محطات في شبكة المحطات المناخية في محافظة السليمانية. تم بناء ثمان نماذج من الشبكات العصبية لكل محطة نموذج. ثم للحصول على نماذج ذات دقة عالية لتخمين الأمطار الشهرية حيث تراوح معامل الارتباط بين الأمطار الشهرية المخمنة و تلك المقاسة من (90% - 97,2%). كل نموذج تم ايجاده بعد محاولات عديدة لكل محطة و تم اختيار النموذج الذي يعطي أعلى معامل ارتباط. جميع النماذج للشبكات العصبية الصناعية وجدت ذات دالة تفعيل نوع (hyperbolic tangent) و (identity) للطبقة المخفية و طبقة المخرجات على التوالي، و بمعدل تعلم للشبكة (0,4) و معامل زخم (0,9) و لكن بمختلف أنواع تقسيم البيانات الى بيانات التدريب، الاختبار و التخمين و مختلف الأعداد للعقد في الطبقة المخفية. كما وجد في تحليل التأثير القياسي بأنه ليس من الضروري أن تكون المحطة ذات المسافة الأقرب من المحطة تحت التخمين ذات أعلى تأثير على الأمطار الشهرية لتلك المحطة وذلك بسبب الفروقات العالية بين منسوب المحطات. كما وجد بأنه ليس من الضروري أن تكون المحطات ذات البيانات التي أعطت أعلى تباين أن تكون ذات أقل معامل الارتباط للقيم المخمنة مع تلك المقاسة.

1. INTRODUCTION:

Prediction of precipitation is essential in most of the hydrological studies and water resources systems design, construction and operation. Weather stations that cover a relatively large area are distributed spatially to reflect the aerial distribution of hydrological variables such as precipitation. When the number of weather stations is large; sometimes measurements in one or more of the stations are not available and need to be accurately predicted. Prediction of those missing values could be done by one of the available approximate method in hydrological science, such as arithmetic mean method, isohyetal method and Thiessen method. However all of these methods are approximate. For more accurate prediction of the missing values in one or more locations of the weather station network, the ANN modeling is expected to produce these more accurate precipitation values.

Belayneh and Adamoski, 2012, had modeled the standard precipitation index in Awash River basin of Ethiopia using three data driven models. Their study compares the effectiveness of these three data driven models, artificial neural networks (ANNs), support vector regression (SVR), and wavelet neural network (WN). These models were compared using Root Mean Square Error RMSE, Mean Absolute Error MAE and Determination Coefficient R^2 . The results indicate that the coupled wavelet neural network (WN) model had produced the best results; however the ANN model had also performed well.

Luk et al., 2000, had used ANN modeling to model rainfall temporal and spatial distribution. Different lags and different numbers of spatial inputs were used to produce different ANNs models. These models were developed for the upper Parramatta River catchment located in western suburbs of Sydney, Australia. The normalized mean square error (NMSE) was chosen as the performance indicator. One important conclusion

Obtained from this study is that the best performed network was lag-1 network with input from the eight nearest neighboring gauge stations.

Bustami et al., 2007, had used ANN models to predict missing readings of precipitation and water levels in the Bedup river catchment in the state of Sarawak, Malaysia. Back propagation ANN model was used for this purpose. The obtained accuracy of prediction of precipitation and water level in this basin are 96.4% and 85.3% respectively. Those results show that ANN is an effective tool in prediction of missing precipitation readings and water levels data.

El-Shafie et al., 2011, had developed a two rainfall prediction models for rainfall in Alexandria, Egypt. These models are ANN model and Multiple Linear Regression MLR model. The rainfall prediction was developed for annual and monthly basis. Comparison of results obtained by the two models was conducted using Root Mean Square Error RMSE, Mean Absolute Error MAE, Coefficient of Correlation R and BIAS. The Feed Forward Neural Network FFNN model has shown better results than the Multiple Linear Regression MLR model. The non-linear ANN mapping tool was found more suitable for rain prediction than the linear nature of MLR model. They concluded that more detailed studies are necessary due to uncertainties inherent in weather forecasting and efforts should be addressed to the problem of quantifying them in the ANN models.

Luk et al., 1999, had applied the ANN models to forecast spatial distribution of rainfall for urban catchment area. Three alternative types of ANN models were used with different multilayer feed forward neural networks. These models were found to provide reasonable prediction of spatial rainfall. They found also that all of the three types of networks had comparable performance.

Dozier, 2012, had investigated the influence of spatial variation in precipitation on artificial neural network rainfall – runoff modeling. An Elman-type recurrent ANN was trained to simulate observed

stream flow for Fountain Creek at Pueblo, CO, using varying amount of spatial precipitation information. They found that spatial variability in precipitation data allows the ANN to achieve better performance.

There have been a number of reported studies that have used ANN to solve problems in hydrology. For example, **French et al., 1992**, used an ANN model to forecast rainfall for a catchment with artificial rainfall inputs, while **Hsu et al., 1995** applied an ANN to model the rainfall-runoff process. ANNs have found increasing use in diverse disciplines ranging over perhaps all branches of engineering and science **ASCE 2000a, b; Maria et al., 2005, cited in Hsu et al., 1995**. Such methods motivate the researchers to utilize in ANN modeling several applications. For example, **El-Shafie et al. 2010**,a reported an application of utilizing Adaptive Neuro-Fuzzy Inference System ANFIS for under water tracking Global Positioning System (GPS) sonobouy. In addition **El-Shafie et al., 2010b**, introduced the Radial Basis Function Neural Network (RBF-NN). ANN has also been used in water resources engineering over the last decade. These include flood forecasting **Garcia 2002**, Wright and **Dastorani, 2001**, rainfall-runoff modeling ,**Tokar and Johnson, 1999**, **Sobri Harun et al., 2002**, **Thurumalaiah and Deo, 2000**, streamflow prediction ,**Dolling and Varas 2001**, **Dastorani and Wright 2002**, **Wright et al., 2002**, water level prediction **Patrick and Collins, 2002**, **Huang et al., 2003**.**Ibrahim, 2012**, had used ANN models coupled with wavelet model to forecast the monthly municipal water consumption of Kirkuk city, Iraq and Madison city, USA, he observed that the use of such model had increased the correlation coefficient from that obtained using SARIMA model. **Saoud, 2009**, had used ANN model to model spatial water quality parameters in AL-Hammar marsh, Iraq. **Al-Suhaili and Ghafour, 2012**, had used ANN model to predict sodium adsorption ratio for Tigris river in Amara city.

In this research an attempt is made for using the ANN modeling to predict the monthly precipitation in one or more weather stations from the real measurements at the other stations. The case study

adopted here is the monthly precipitation values in Sulaimani Governorate weather stations network. This network has eight weather stations distributed over an approximate area of (17023 km² or 6572.96 mil²). **Table 1** shows the names, Latitude, Longitude and elevation of these stations. Figure 1 shows a Google map of the locations of these stations. **Table 2** shows the approximate distances between those stations. The available records of the monthly precipitation in these stations are for eight years 2004-2011, moderate of Agro-meteorological Center - General Directorate of Agricultural, Ministry of Agriculture, KRG. **Table 3** shows the descriptive statistics of these records.

2. ANN MODEL DEVELOPMENT

As mentioned above the ANN modeling is used to predict the monthly precipitation in any of the eight stations in Sulaimani Governorate as output variable using the monthly precipitations at the other stations for the same month as input variables.

ANN modeling techniques are well known by now and proved its capability to model different engineering problems. This modeling technique can represent the non-liner relationship among the input and output variables. It consists of a grouped neurons or nodes in layers. The input layer neuron represents the input variables, while the output layer nodes represent the output variables. In between these two layers there exist hidden layers with a certain number of hidden nodes. The nodes between the layers were interconnected by weights. The input layer nodes receives the input values and transmit it's liner weighted combination with a bias term to the hidden nodes, where it is processed with a suitable activation function to produce an output from each node in the hidden layer. These outputs will combine using weights between the hidden layer and the output layer which is received by the output layer nodes, and processed by an activation function to produce outputs. The process explained above is called feed-foreword.

In ANN modeling the set of data require is of the input variables and corresponding output variables. In order to find weights of the model the network

should be trained using a partial set of the data, hence the original data set is to be divided to training, testing and hold out sub-sets. The training process is performed by using the training sub-set and assuming weights. The input data is subject to a feed-forward process to produce output data using the assumed initial weights. These output are compared with the real output and errors are estimated. These errors are used to adjust weights using certain algorithm such as back propagation (BP). **Fig. 2** shows three-layer ANN architecture.

The ANN modeling is applied for each of the eight weather station monthly precipitation prediction in Sulaimani Governorate, using SPSS (version 19) software. For each model many trials are adopted for the division of the data set into training, testing and holdout data subset. Also many trials are adopted for the selection of the number of the hidden nodes in the hidden layer. The trial that exhibits the highest correlation coefficient between the predicted and the measured monthly precipitation is selected. Table 4 shows the final results of the selected ANN models for the eight weather stations at Sulaimani Governorate. For all these ANN models the selected activation functions for the hidden and the output layers are hyperbolic tangent and the identity functions respectively with a learning rate of 0.4 and a momentum factor of 0.9.

The selected models shown in table 4 above are used to predict the monthly prediction values and compare them with the real measured values. **Fig. 3** shows these comparisons which indicate the capability of the models to predict the monthly precipitation values with excellent accuracy, the correlation coefficients shown in **Table 4** indicates this high accuracy of prediction ranging from (90% to 97.2%).

Fig.4 shows the normalized importance analysis of each variable (input variables) on the output variable. Comparing **Fig. 4** results with the distances between the weather stations shown in **Table 2** indicates that it is not necessary that the nearest station has the highest effect on the station under prediction. This may be attributed to the fact that the difference in elevation between these

stations is high as shown in **Table 1**. **Table 5** shows the normalized importance analysis in descending order with the distance and elevation of each related stations.

3. CONCLUSIONS:

The following conclusions could be deduced from this research.

- The ANN model can provide a good prediction models for predicting the monthly precipitation values for eight weather stations in the Sulaimani Governorate with correlation coefficient ranged (0.9 to 0.972).
- Comparing **Tables 3** and **4**, it is found that it is not necessary that the data set of the highest variance produce the lowest prediction correlation coefficient.
- The network can utilized the hyperbolic tangent and identity activation functions for the hidden and output layers respectively, with learning rate of 0.4 and momentum term 0.9, to produce good prediction results but with different data sub-set division, and different number of hidden nodes in the hidden layer.
- The normalized importance analysis indicates that it is not necessary that the nearest station has the highest importance on the value of precipitation of the station under prediction. This may be attributed to the effect of the high different in elevations of the stations.
- The equations developed can be used to predict any missing precipitation value in any of the eight stations with good accuracy.

4. REFERENCES:

- Al-Suhaili R. H. and Ghafour Z. J., 2012, *Artificial Neural Network Model to Predict Sodium Adsorption Ratio for Tigirs River in Amara*, Accepted for publishing, Journal of Engineering, Collage of Engineering, University of Baghdad.
- Belayneh A. M., Adamowski J. F., 2012, *Standard Precipitation Index Drought Forecasting using Neural Networks, Wavelet Neural Networks and Support Vector Regression* Hindawi Publishing Corporation, Journal of Applied Computational Intelligence and Soft Computing.
- Bustami, R., Bessaih, N., Bong, C., Suhaili, S., 2006, *Artificial Neural Network for Precipitation and Water Level Predictions of Bedup River* IAENG International /journal of Computer Science, 34:2, IJCS_34_2_10.
- Dastorani, M. T., and Wright, N. G., 2002, *Artificial Neural Network Based Real-Time River Flow Prediction*, in the Proceedings of Hydroinformatics.
- Dolling, O. R., and Varas, E. A., 2002, *Artificial Neural Networks for Streamflow Prediction*, Journal of Hydraulic Research. 40(5), pp. 547-554.
- Dozier, A., 2012, *Influence of Spatial Variation In Precipitation on Artificial Neural Network Rainfall-Runoff Model*.
- El-Shafie A, Abdalla O., Noureldin A., Aini H. 2010 a. *Performance Evaluation of a Nonlinear Error Model for Underwater Range Computation Utilizing GPS Sonobuoys*, Neural Computer Application, 19(5): 272-283.
- El-Shafie A, Abdelazim T, Noureldin A., 2010b, *Neural Network Modeling of Time-Dependent Creep Deformations In Masonry Structures*, Neural Computer Application, 19(4): 583-594.
- El-Shafie, A. H., El-Shafie, A., El Mazoghi, H. G., Shehata, A., Taha, M. R., (2011), *Artificial Neural Network Technique for Rainfall Forecasting Applied To Alexandria, Egypt*, International Journal of the Physical Sciences Vol. 6(6), 1306-1316.
- French, M., Krajewski, W., and Cuykendall, R. R., 1992, *Rainfall Forecasting in Space and Time Using a Neural Network*, Journal of Hydrology, 137, p1-31.
- Hsu, K. L., Gupta, V. and Soroshian, S., 1995, *Artificial Neural Network Modeling of the Rainfall-Runoff process*, Water Resources Research, Vol.31, No. 10, p 2517-2530.
- Huang, W., Murray, C., Kraus, N., and Rosati, J., 2003, *Development of A Regional Artificial Neural Network Prediction for Coastal Water Level Prediction*, Ocean Engineering vol. 30, pp. 2275-2295.
- Ibrahim H. M., 2012, *Forecasting Models for Municipal Water Demand*, Ph.D. Dissertation, Collage of Engineering, University of Sulaimani.
- Luk, K. C., Ball, J. E., Sharma, A., 2000, *A Study of Optimal Model Lag and Spatial Inputs to Artificial Neural Network for Rainfall Forecasting*, Journal of hydrology 227: 56-65.
- Luk, K. C., Ball, J. E., Sharma, A., 2001, *An Application of Artificial Neural Networks for Rainfall Forecasting*, Mathematical and Computer Modeling 33(2001) 683-693.
- Patrick, A. R., Collins, W.G., Tissot, P.E., Drikitis A., Stearns, J., Michaud, P.R., and Cox, D.T., (2002), *use of the NCEP Mesoeta Data in a Water Level Predicting Artificial Neural Network*, in the Proceedings of 19th Conf. on weather Analysis and Forecasting/15th Conf. on Numerical Weather Prediction.
- Saoud A. A., 2009, *Water Quality Simulation by Artificial Neural Network Technique for South Al-Hammar Marsh, Iraq*, M. Sc. Theses
- Sobri, H., Hashim, M. K., and Irwan, A. N., 2002, *Rainfall-Runoff Modeling using Artificial neural Network*, Proceedings of 2nd World Engineering Congress. Kuching.

Thirumalaiah, K., and Deo, M. C., 2000, *Hydrological Forecasting using Artificial Neural*

Network, *Journal of Hydrologic Engineering*, 5(2), pp. 180-189.

Tokar, A.S., and Johnson, P.A., 1999, *Rainfall-Runoff Modeling using Artificial Neural Networks*, *Journal of Hydrologic Engineering*, 4(3), pp. 223-239.

prediction, Proceedings of the International Symposium on Environmental Hydraulics, Phoenix.

Wright, N. G., and Dastorani, M. T., 2001, *Effects o River Basin Classification on Artificial Neural Networks Based Ungauged Catchment Flood*

Sulaimani Governorate Weather Station Records ,2004–2011. *Agro-Metrological Center – General Directorate of Agricultural, Ministry of Agriculture, KRG; Iraq.*

Table 1. Names, latitude, longitude and elevation of selected weather stations.

SN	Name of weather station	Latitude	Longitude	Elevation (amsl)
1	Sulaimani	35° 33' 20.56" N	45° 27' 11.61" E	879.65 m
2	Dukan	35° 57' 07.15 " N	44° 57' 29.48" E	514.5 m
3	Darbandikhan	35° 06' 27.75" N	45° 41' 03.10" E	512 m
4	Penjwin	35° 37' 03.71" N	45° 57' 13.12" E	1282.60 m
5	Chwarta	35° 43' 00.89" N	45° 34' 12.35" E	1153 m
6	Halabjah	35° 10' 57.95" N	45° 58' 48.25" E	686.4 m
7	Bazian	35° 36' 00.03" N	45° 08' 13.13" E	819.3 m
8	Chamchamal	35° 31' 58.88" N	44° 50' 02.66" E	708.96 m

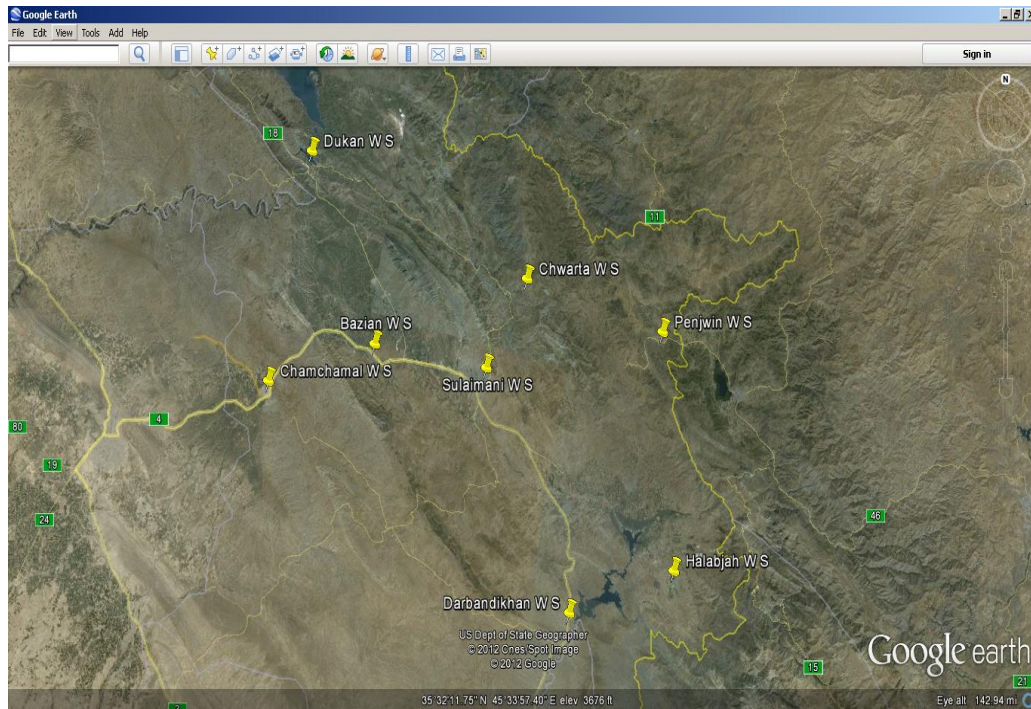


Figure 1. Google map of the locations of the selected weather stations at Sulaimani governorate.

Table 2. Approximate distances between selected weather stations of Sulaimani governorate in (km)

Name of Weather Station	Sulaimani	Dukan	Darbandikhan	Penjwin	Chwarta	Halabjah	Bazian	Chamchamal
Sulaimani	0	62.76	54.00	45.88	20.85	63.36	29.17	56.10
Dukan	62.76	0	114.73	97.10	61.20	125.85	42.00	47.90
Darbandikhan	54.00	114.73	0	61.40	68.68	28.36	73.98	90.57
Penjwin	45.88	97.10	61.40	0	36.53	48.22	74.15	102.12
Chwarta	20.85	61.20	68.68	36.53	0	69.73	41.30	69.90
Halabjah	63.36	125.85	28.36	48.22	69.73	0	89.50	111.05
Bazian	29.17	42.00	73.98	74.15	41.30	89.50	0	28.41
Chamchamal	56.10	47.90	90.57	102.12	69.90	111.05	28.41	0

Table 3. Descriptive statistics of the available monthly precipitation records of the weather stations network in Sulaimani governorate, 2004-2011.

Name of Weather Station	Mean	Standard Deviation	Skewness	Kurtosis	Maximum	Minimum
Sulaimani	76	60.212	1.256	2.161	276	0
Dukan	70.2	63.280	1.411	2.450	299	0
Darbandikhan	74.4	63.982	1.068	0.456	247	0.3
Penjwin	126	98.565	1.450	3.935	534	0
Chwarta	88.3	72.284	1.084	1.497	334	0.7
Halabjah	81	64.718	1.204	2.720	342	0
Bazian	71.5	68.227	1.475	2.555	323	0
Chamchamal	51.2	58.033	1.957	5.174	301	0

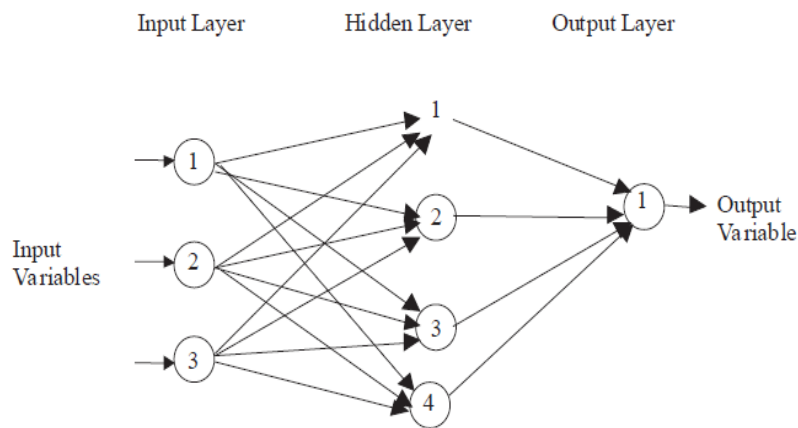
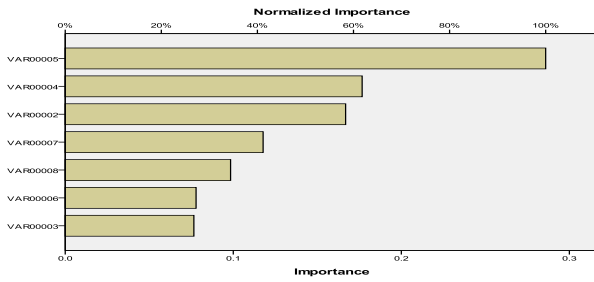


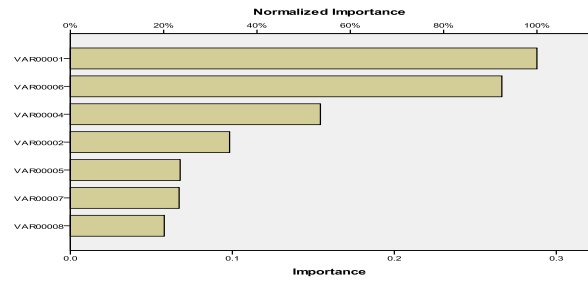
Figure 2. A 3-layer ANN architecture used for Monthly precipitation prediction.

Table 4. ANN Models for different weather stations at Sulaimani governorate.

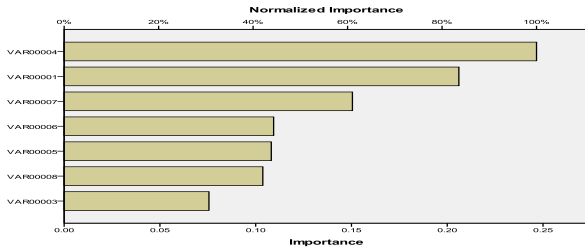
Weather Station under Prediction	Training	Testing	Holdout	No. of Hidden Nodes	Learning Rate	Momentum Factor	Correlation Coefficient
Sulaimani	44	14	6	6	0.4	0.9	97.2%
Dukan	50	12	2	6	0.4	0.9	94.3%
Darbandikhan	49	13	2	8	0.4	0.9	90%
Penjwin	52	11	1	3	0.4	0.9	96.9%
Chwarta	56	6	2	8	0.4	0.9	95.1%
Halabjah	49	5	10	10	0.4	0.9	96.0%
Bazian	46	10	8	3	0.4	0.9	95.0%
Chamchamal	52	6	6	3	0.4	0.9	94.9%



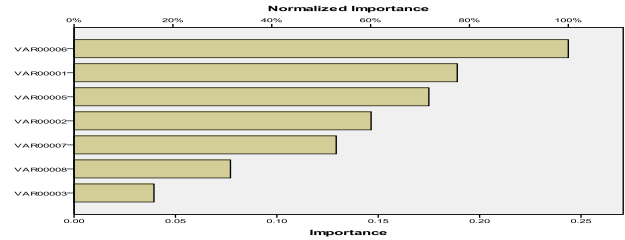
(a)



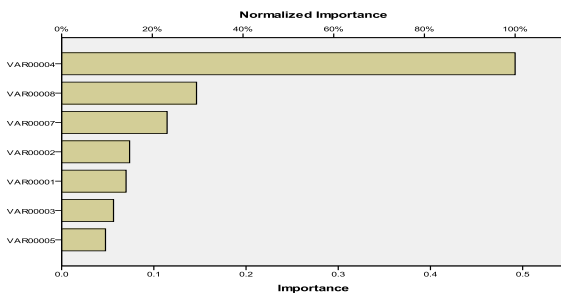
(b)



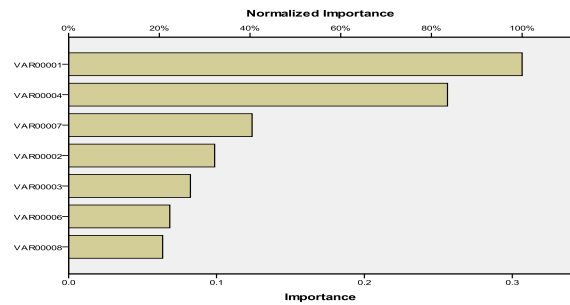
(c)



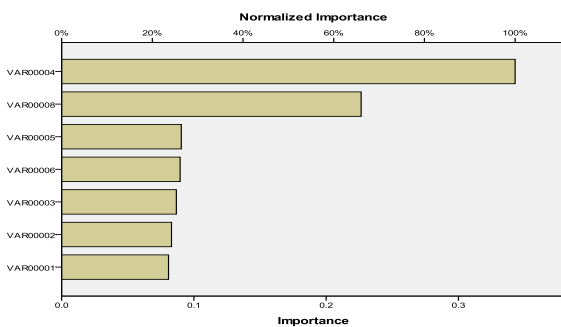
(d)



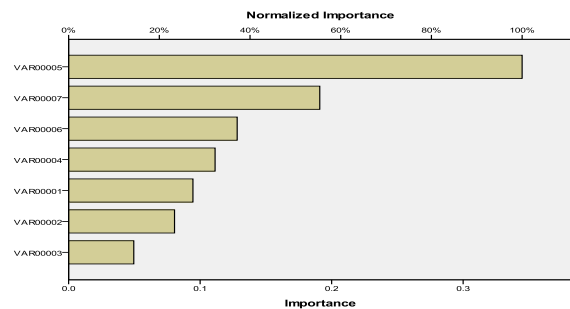
(e)



(f)



(g)



(h)

Figure 3. Normalized importance analysis for weather stations in Sulaimani governorate. a) Sulaimani, b) Dukan, c) Darbandikhan, d) Penjwin, e) Chwarta, f) Halabjah, g) Bazian, h) Chamchamal.

Figure 4. Continued (var0001:Sulaimani, var0002:Dukan,var0003Darbandikan,var0004: Penjwin,var0005:Chwarta,var0006:Halabjah,var0007:Bazian:var0008:Chamchamal).

Table 5. Normalized importance analysis in descending order with the distance and elevation of each related stations.

Model Prediction Station	Independent Importance Station	Chwarta	Penjwin	Dukan	Bazian	Chamchamal	Halabjah	Darbandikhan
Sulaimani Weather Station	Importance in descending order	100%	61.8%	58.4%	41.2%	34.4%	27.2%	26.8
	Distance from Sulaimani Station(km)	20.85	45.88	62.36	29.17	56.10	63.36	54.00
	Elevation difference from Sulaimani station	273.35	402.95	-365.15	-60.35	-170.70	-193.25	-367.65
Model Prediction Station	Independent Importance Station	Penjwin	Sulaimani	Bazian	Halabjah	Chwarta	Chamchamal	Darbandikhan
Dukan Weather Station	Importance in descending order	100%	83.6%	61%	44.3%	43.9%	42.1%	30.7%
	Distance from Dukan Station (km)	97.10	62.76	42.00	125.85	61.20	47.90	114.73
	Elevation difference from Dukan station	768.1	365.15	304.8	171.9	638.5	194.46	-2.50
Model Prediction Station	Independent Importance Station	Sulaimani	Halabjah	Penjwin	Dukan	Chwarta	Bazian	Chamchamal
Darbandikhan Weather Station	Importance in descending order	100%	92.5%	53.6%	34.1%	23.5%	23.3%	20.1%
	Distance from Darbandikhan Station(km)	54.00	28.36	61.40	114.73	68.68	73.98	90.57
	Elevation difference from Darbandikhan station	367.65	174.4	770.6	2.5	641	307.3	196.96
Model Prediction Station	Independent Importance Station	Halabjah	Sulaimani	Chwarta	Dukan	Bazian	Chamchamal	Darbandikhan
Penjwin Weather Station	Importance in descending order	100%	77.5%	71.8%	60.1%	53%	31.6%	16.2%
	Distance from Penjwin Station (km)	48.22	45.88	36.53	97.10	74.15	102.12	61.40
	Elevation difference from Penjwin station	-596.2	-402.95	-129.6	-768.1	-463.3	-573.64	-770.6

**Table 5.Continued.**

Model Prediction Station	Independent Importance Station	Sulaimani	Penjwin	Bazian	Dukan	Darbandikhan	Halabjah	Chamchamal
Chwarta Weather Station	Importance in descending order	100%	83.5%	40.5%	32.2%	26.9%	22.3%	20.7%
	Distance from Chwarta Station (km)	20.85	36.53	41.30	61.20	68.68	69.73	69.90
	Elevation difference from Chwarta station	-273.35	129.6	-333.7	-638.5	-641	-466.6	-444.04
Model Prediction Station	Independent Importance Station	Penjwin	Chamchamal	Bazian	Dukan	Sulaimani	Darbandikhan	Chwarta
Halabjah Weather Station	Importance in descending order	100%	29.7%	23.3%	15%	14.2%	11.4%	9.7%
	Distance from Halabjah Station (km)	48.22	111.05	89.50	125.85	63.36	28.36	69.73
	Elevation difference from Halabjah station	596.2	22.56	132.9	-171.9	193.25	-174.4	466.6
Model Prediction Station	Independent Importance Station	Penjwin	Chamchamal	Chwarta	Halabjah	Darbandikhan	Dukan	Sulaimani
Bazian Weather Station	Importance in descending order	100%	66%	26.4%	26.1%	25.3%	24.2%	23.6%
	Distance from Bazian Station (km)	74.15	28.41	41.30	89.50	73.98	42.00	29.17
	Elevation difference from Bazian station	463.3	-110.34	333.7	-132.9	-307.3	-304.8	60.35
Model Prediction Station	Independent Importance Station	Chwarta	Bazian	Halabjah	Penjwin	Sulaimani	Dukan	Darbandikhan
Chamchamal Weather Station	Importance in descending order	100%	55.4%	37.2%	32.3%	27.4%	23.4%	14.4%
	Distance from Chamchamal Station (km)	69.90	28.41	111.05	102.12	56.10	47.90	90.57
	Elevation difference from Chamchamal station	444.04	110.34	-22.56	573.64	170.69	-194.46	-196.96

Calculation steps for the prediction of monthly precipitation in Sulaimani governorate:

The following equations are those used for the prediction of the missed precipitation values at sulaimani station. Similar forms of equations are also available for the estimation of the missed precipitation for each of the other stations.

1. Find matrix $Zin_{(6 \times 1)}$.

$$Zin_{(6 \times 1)} = V_{obias_{(6 \times 1)}} + V_{(7 \times 6)}^T * X_{(7 \times 1)}$$

Where: $W_{obias_{(1 \times 1)}} = \begin{bmatrix} 0.837 \end{bmatrix}$, $X_{(7 \times 1)} = \begin{bmatrix} \text{Duk} \\ \text{Drb} \\ \text{Pnj} \\ \text{Chw} \\ \text{Hlb} \\ \text{Bzn} \\ \text{Chm} \end{bmatrix}$

$V_{obias_{(6 \times 1)}} = \begin{bmatrix} 1.107 \\ 0.311 \\ 1.037 \\ -0.729 \\ 0.098 \\ 0.428 \end{bmatrix}$

$V_{(7 \times 6)} = \begin{bmatrix} 0.007 & -0.035 & -0.080 & 0.207 & 0.212 & 0.321 \\ -0.864 & -0.168 & -0.526 & 0.023 & -0.191 & -0.121 \\ -0.158 & 0.339 & -0.104 & 0.298 & -0.065 & -0.209 \\ 0.116 & -0.099 & 0.383 & 0.006 & -0.047 & -0.305 \\ 0.213 & 0.373 & 0.329 & -0.534 & 0.458 & -0.327 \\ -0.064 & -0.014 & 0.560 & -0.042 & -0.642 & 0.243 \\ 0.246 & -0.422 & 0.865 & 0.447 & -0.049 & 0.009 \end{bmatrix}$

$W_{(6 \times 1)} = \begin{bmatrix} -1.242 \\ 0.745 \\ 0.851 \\ 1.074 \end{bmatrix}$



0.035

0.105

2. Find $Z_{(6 \times 1)} = \tanh(Z_{in(6 \times 1)})$
3. Find $y_{in(1 \times 1)} = W_{obias(1 \times 1)} + W_{(6 \times 1)}^T * Z_{(6 \times 1)}$
4. Find $y_{(1 \times 1)} = y_{in(2 \times 1)}$

$$= \begin{bmatrix} y_1 \end{bmatrix}$$

5. Find $Suly = y_1 * sd_{Suly} + Mean_{Suly}$

Competitive Stripping of Multi-Organic Pollutants from Contaminated Water in Bubble Column Semi-Batch

Waleed M. Salih

Department of Environmental College of
Engineering
Baghdad University
Email:waleedmsprof@yahoo.com

Ahmed A. Mohammed

Department of Environmental College of
Engineering
Baghdad University
Email:ahmed.abedm@yahoo.com

Yaseen R. Hasan

Department of Environmental College of
Engineering
Baghdad University
Email:yaseenrh1963@yahoo.com

ABSTRACT

Air stripping for removal of Trichloroethylene (TCE), Chloroform (CF) and Dichloromethane (DCM) from water were studied in a bubble column (0.073 m inside dia. and 1.08 m height with several sampling ports). The contaminated water was prepared from deionized water and VOCs. The presence of VOCs in feed solution was single, binary or ternary components. They were diluted to the concentrations ranged between 50 mg/l to 250 mg/l. The experiments were carried out in batch experiments which regard the bubble column as stirred tank and only gas was bubbled through stationary liquid. In this case transient measurements of VOC concentration in the liquid phase and the measured concentration profiles were modeled by bubble aeration model (BAM) to fit the experimental data fairly well. The results from batch experiments show that the removal efficiency of VOCs increases with increasing gas flow rate or gas holdup. It is found a pH=10 give the best removal rate, but all experiments were adjusted at pH=8 which allow to study other operating conditions. TCE is being removed faster than the other two components for all systems and a single component was removed faster than binary or ternary system. The K_{La} values were evaluated by fitting the BAM to the experimental data. It is found that K_{La} increased with increasing gas flow rate and TCE exhibits the highest K_{La} values.

Key Words: Mass transfer, Bubble column, Air stripping

الانتزاع التنافسي لخليط مركبات عضوية من الماء الملوث باستخدام برج الفقاعات في التجارب شبه الساكنة

ياسين رشيد حسن

قسم الهندسة البيئية / كلية الهندسة/جامعة بغداد

أحمد عبد محمد

قسم الهندسة البيئية / كلية الهندسة/جامعة بغداد

وليد محمد صالح

قسم الهندسة البيئية / كلية الهندسة/جامعة بغداد

خلاصة البحث:

ان الانتزاع الهوائي لإزالة مركبات التراكيلورواثيلين (TCE)، الكلوروفورم (CF) والدايكلوروميثيلين (DCM) من الماء الملوث تمت دراسته باستخدام برج فقاعات (بقطر داخلي ٠,٠٧٣م وارتفاع ١,٠٨م مزود بعدة فتحات جانبية لغرض أخذ النماذج من مادة البلكسكلاس). تم تحضير المحلول الملوث من المواد العضوية المتطايرة (VOCs) بمساعدة محلول الميثانول وتضاف الى الماء المقطر، وبعد ان يحضر المحلول يوضع في خزان التغذية. ان مركبات الـ (VOCs) المذكورة تحضر على شكل نظام فردي او ثنائي او ثلاثي. واما التراكيز المحصورة فتتراوح بين 50 ملغ/لتر الى 250 ملغ/لتر. لقد تم اجراء التجارب شبه ساكنة والذي يعتبر فيها برج الفقاعات كخزان خلط (Stirred Tank) و فقاعات الهواء تتحرك فيه من الاسفل الى الاعلى في الماء الساكن. تم احتساب تراكيز الـ (VOCs) من الطور السائل باستخدام النموذج الرياضي للفقاعات الهوائية (ABM). وقد وجد ان القيم التجريبية مطابقة بشكل جيد مع النموذج المستخدم. ان النتائج المستحصلة في التجارب اظهرت ان نسبة كفاءة ازالة المواد العضوية المتطايرة تزداد بزيادة معدل جريان الهواء او زيادة معدل التغير الحجمي للهواء (Gas Holdup). لقد وجد ان افضل كفاءة ازالة عند pH=10. كما ان التجارب اظهرت ان مركب التراكيلورواثيلين (TCE) يزال اسرع من المركبين الاخرين لكل الانظمة، وخاصة في النظام المفرد. ان قيم معامل انتقال المادة الحجمي (K_{La}) قد تم ايجادها لكل الحالات التي تم بحثها بضبط النموذج الرياضي BAM مع البيانات التجريبية. وبشكل عام فقد وجد ان قيم K_{La} تزداد بزيادة معدل جريان الهواء وان المركب TCE اظهر اعلى قيم K_{La} .

كلمات البحث الرئيسية: انتقال المادة، برج الفقاعات، الانتزاع بالهواء

1. INTRODUCTION

Ground water contamination by trace levels of volatile organic compounds (VOCs) has emerged as a major water quality issue in the last five decades. Interest in VOCs in drinking water began escalating in the mid-70s when it became possible to measure these compounds concentrations $\mu\text{g/l}$ levels. Since then, it has been recognized that volatile compounds are finding their ways into ground water, which is often used as the main source of drinking water, **Djebbar 1998**.

VOCs are organic compounds with a tendency to migrate or diffuse from the aqueous phase (water) to the gaseous phase (air), or vice-versa. They are generally highly volatile, with low molecular weight. VOCs are a widely used class of compounds employed in many types of industrial, commercial, agricultural, and household activities, **DeMarco 1983**.

These compounds find their way into the environment through industrial and municipal wastewater discharges, leachate from deficient, old waste disposal sites that received hazardous chemicals, illegal discharges, and leaks from above or underground storage tanks and pipes. Contamination of drinking water supplies may occur from any combination at relatively high concentrations, and several other compounds will be present at lower concentrations, **Dyksen et al., 1982**.

A very prevalent water pollution problem pertains to contamination by VOCs that offer potentially very important health risks, when they have a certain propensity to evaporate away from the water into air. Many of these VOCs are only partially miscible with water but in general they all present certain solubility. The problem of reducing VOCs in water applies to ground waters, surface waters, and waste waters alike. The origin of the water has some important design implications that will be discussed later. This write-up will discuss the application of air stripping for the removal of VOCs from water.

Depending on the contaminant and site characteristics, volatilization can be an important mechanism for the loss of hazardous compounds from soils and liquid waste systems. Volatilization may decrease the concentrations of the wastes at a facility or site; however, because of the law of mass conservation, contaminants will subsequently be found in the atmosphere. Therefore, air emissions, may become hazardous air pollutants (HAPs) and result in short or long-term health effects. Volatilization can also be applied as a hazardous waste treatment process to clean up contaminated ground water through air stripping and to remediate soils by soil vapor extraction. If volatilization occurs, it will do so primarily as a function of the contaminants vapor pressure (if the compound is in relatively pure form) and the Henry's Law constant (if it is in aqueous solution), **Richard, 1997**.

One of the most useful methods to remove the VOCs from contaminated water by using the dispersion aeration (bubble column technique) which include flow of air bubbles in water, and mass transfer from liquid phase to gas phase will occur (VOCs move from the water to the air as the bubbles rise through the water). Several types of air stripper technologies are currently available for removal of VOCs from water. This evaluation focuses on the capabilities and limitations of several major established and emerging air stripper technologies that are potentially applicable for VOCs removal such as Packed tower Aeration, low profile aeration, bubble diffusion aeration, spray towers, aspiration, **Andrew et al., 1995**.

Transfer of the VOCs from the water to the air can be improved by increasing the column length or by producing smaller bubbles. Its main advantages are that it is simple and that it can handle water having high levels of suspended solids, **Dwight, 2001**.

As far as published studies are concerned, the main interest is concentrated on

design and scale-up, fluid dynamics and regime analysis and characteristic parameters, especially gas holdup, bubble characteristics, mass transfer coefficient and heat transfer coefficient., the effects of superficial gas velocity, liquid properties, operating conditions, column dimensions, gas distributor design, solid type and concentrations are presented, **Nigar et al. 2004**.

Bubble columns are intensively used as multiple contactors in chemical, biochemical and petrochemical industries. They provide several advantages such as high heat and mass transfer rates, compactness and low operating and maintenance cost, **Andrews et al., 1995 and Sulaymon and Mohammed 2010**.

Investigation of design parameters characterizing the operation and transport phenomena of bubble columns have led to better understanding of the hydrodynamic properties, **Onder et al., 2004**.

2.OBJECTIVES

The main objective of this work is to investigate competitive removal of identified VOCs (TCE, CF and DCM) pollutants from water by air stripping batch wise, and to investigate stripping of dangerous VOCs from wastewater by air using bubble column from liquid phase to gas phase through single, binary and ternary systems of VOCs in water, also to determine the volumetric mass transfer coefficient K_La for a particular component as single and in the presence of other components (binary and ternary systems).

3.MATHEMATICAL MODEL

For a VOC with a Henry's law coefficient much greater than approximately (1.6×10^{-4} atm. $m^3/mole$ at $25^\circ C$), however, the gas-film resistance is negligible compared with the liquid-film resistance, **Mackay and Leimonen, 1975**.

K_La values for VOCs are not easily predicted because they are highly system dependent. However, a relative value of K_La can be computed because K_La is proportional to the VOCs diffusion coefficient in water, which is

proportional to the molar volume at its normal boiling point, **Wilke and Chang, 1955**.

As mass transfer occurs between water and air in a bubble, the VOC concentration in a bubble increases as the bubble moves through the water column to the water surface. This phenomenon was considered by **Matter-Muller et al., 1981 and Roberts et al, 1983**, who developed a kinetic model for bubble transfer with the following assumptions; the system is isothermal; mass- transfer coefficients are constant and independent of time and location, if hydraulic conditions are stable; equilibrium follows Henry's law; complete mixing occurs in the water; the change of VOC concentration in water during the retention time of a bubble in the water is insignificant compared with concentration change in a bubble; and although the upward velocity, surface area, and volume of a bubble depend on the actual depth of the bubble, use of the mean values over that total depth is acceptable.

The bubble-transfer model is based on the continuity equation for a VOC in a bubble rising through the water, **Matter-Muller et al., 1981**.

$$\frac{d}{dt} \left(\frac{P.V_b.y}{R.T} \right) = \frac{(K_L)_b}{H} \cdot \frac{A_b}{V_b} \cdot P.V_b \cdot \left(-\frac{C_L.H}{M.P} \right) \quad (1)$$

Integrating **Eq. (1)** yields a relationship between water depth and the mole fraction of VOC in the bubble phase.

$$y(Z) = \frac{1}{P \cdot \exp(-\Phi.Z)} \times \left[\frac{C_L}{M} \cdot H_c \cdot R.T. \exp(-\Phi.Z) \right] \quad (2)$$

When **Eq. (2)** applied for the entire bubble rise for typical unsteady-state gas transfer, C_L becomes a function of the aeration time (t), according to:

$$\ln \left(\frac{C_{L,i}}{C_{L,o}} \right) = -Q_G \cdot \frac{H_c}{V_L} \cdot [1 - \exp(-\Phi.Z_s)] \cdot t \quad (3)$$

The slope of the relationship between $\ln(C_{L,t}/C_{L,0})$ versus t of **Eq. (4)** is expressed as :

$$S_b = -Q_G \cdot \frac{H_c}{V_L} [1 - \exp(-\phi \cdot Z_s)] \quad (4)$$

Because ϕ in **Eq. (4)** is a function of $(K_L a)_b$, $(K_L a)_b$ of any VOC_i can

be obtained from **Eq. (5)** as rearranged to solve for $(K_L a)_{b,i}$

$$(K_L a)_{b,i} = -Q_G \cdot \frac{H_{c,i}}{V_L} \cdot \ln \left(1 - \frac{S_{b,i} V_L}{Q_G \cdot H_{c,i}} \right) \quad (5)$$

4. EXPERIMENTAL SET UP

Fig.1 the experimental set up which consists mainly of a pixglass bubble column 73 mm inside dia. and 1.08 m height with several sampling ports, the column; a feed pump, a feed tank, a stock solution tank, an air compressor and air rotameter. The distributor plate is a 1/8 in metal sheet having 50 orifices of 0.5mm in diameter arranged on a square pitch. mm polyethylene. The liquid line is a plastic pipe with nominal diameter of 1/2 inch. The column has a two 3/4 in overflow pipes, and all fittings are either PVC or galvanized steel. The gas holdup was measured according to the volume fraction of the gas phase occupied by the gas bubbles, which defined as the volume of gas phase divided by the total volume.

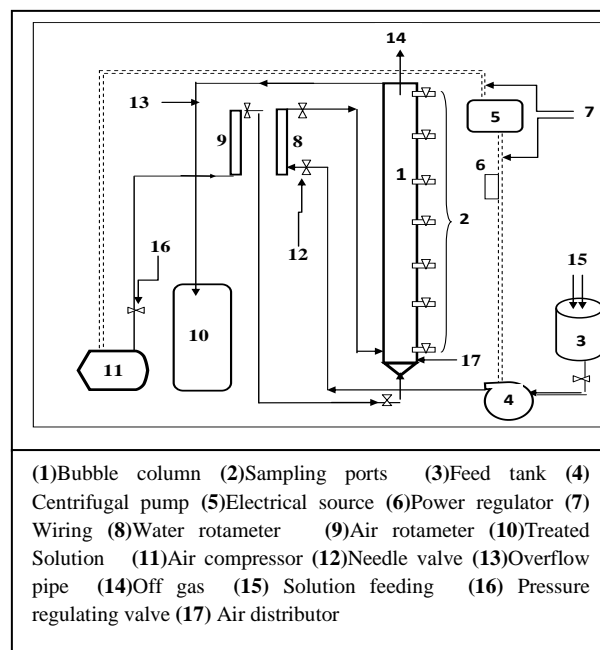


Figure 1. Experimental setup.

5. MATERIALS

VOCs used for the experiments were trichloroethylene TCE, chloroform CF and dichloromethane DCM. Alternatively DCM is known as methylene chloride. All these chemicals were of purity greater than 99.6 % and they were used without further purification. In this study deionized water was used for the preparation of the feed solution, i.e. aqueous solution of VOCs. Due to a low solubility of these VOCs in water, high purity methanol was used as a co-solvent which assisted in obtaining homogeneous solutions of VOCs in water.

The physical-chemical properties of the three VOCs used in the present work are summarized in **Table 1**.

Table 1. Physical and chemical properties of VOCs.

property	Compound		
	TCE	CF	DCM
Formula	C ₂ HCl ₃	CHCl ₃	CH ₂ Cl ₂
Molecular weight (g/mol)	131.4	119.39	84.93
Solubility in water at 20C°, (g/100mL)	0.10	0.8	2.0
Henry's constant at 20C° (dimensionless)	0.376	0.141	0.11
Density, at 20C° (g/cm³)	1.464	1.483	1.327
Wave length, λ (nm)	244	214	211

6. PREPARATION OF FEED SOLUTION

Contaminated water was used as feed solution. This was prepared by dissolving VOCs in deionized water. However, VOCs chosen for this study are of little solubility in water and consequently the aqueous solutions produced were heterogeneous.

Fatima et al, 2009, suggested the use of a co-solvent before mixing with water. Their procedure is simple, in which 1gm of a VOCs e.g TCE or CF or DCM is dissolved in 10 mL of high purity methanol e.g > 99.6% purity and the mixture is added to 10L of deionized water.

This step yielded a homogeneous aqueous solution of a single component of VOC of concentration 100 mg/l. Employing this technique, aqueous solutions of single VOC of initial concentrations of 50,100,150,200 and 250 mg/l were prepared for the experiments. By a similar method binary and ternary solution were prepared with initial concentration of 50,150 and 250 mg/L of each component. The use of methanol proved to be an effective solvent which assisted in the dissolution of VOCs in water with the result that homogenous aqueous solution were obtained. Methanol concentration is too low to have an effect on desorption performance and it's volatilization during bubble aeration processes can be neglected according to blank test.

7. ANALYTICAL TECHNIQUES

Water samples drawn from bubble column during the course of experiments were analyzed to determine VOCs concentration. Single component samples were analyzed using the UV-spectrophotometer system at 190-1100 wavelength spread. The injection volume of samples was 5 ml. For the two-component systems binary systems the spectro-photometric method is also used but the technique is different from that used for single-component systems. The bivariate calibration method presented by **Pedrol et.al, 1997**, was applied for the simultaneous determination of two VOCs components in a mixture, particularly when the two components have close wavelengths.

8. AIR STRIPPING EXPERIMENTS

All stripping experiments were carried out under isothermal conditions of temperature ranging within 22-28 C° average 25C°. The experiments were operated as semi-batch wise by allowing air to bubble through non flowing water. The experiments involved desorption of single component solutions. To investigate competitive desorption, binary and ternary experiments were done for this purpose. The removal efficiency of VOCs and values of the mass transfer coefficient K_{La} could be determined.

In these experiments, the stripping air was allowed bubble through stationary water at different rates of flow. In each run about 4L of wastewater aqueous solution of VOCs were charged into the column. Different flow rates of air were used for the experiments. The pH of solution was varied covering five values 3, 5, 7, 8, and 10 and pH was adjusted by sodium hydroxide or hydrochloric acid. After initialization the air flow water samples were withdrawn at discrete time intervals through a sampling port in the middle of the bubble column. The samples were immediately kept in sealed vials 10mL volume and placed in a cold box to prevent volatilization. The sparging process was terminated when the VOC concentration in the column was low or relatively constant. In most of the runs steady state

situation was attained within around 80 min. Variability was randomly tested by taking two samples one right after the other and their concentrations were immediately measured. **Table 2** summarizes the operating conditions used in the experiments.

Table 2. Operation conditions.

Run	O _c (l/min)	pH	Con(mg/l)
Single system			
1	3	3	250
2	3	5	250
3	3	7	250
4	3	8	250
5	3	10	250
6	1.5	8	250
7	2	8	250
8	4	8	250
9	6	8	250
10	3	8	200
11	3	8	150
12	3	8	100
13	3	8	50
Binary system			
1	3	8	250
2	2	8	250
3	1	8	250
4	2	8	150
5	2	8	50
Ternary system			
1	2	8	100
2	3	8	250
3	4	8	250
4	2	8	250
5	2	8	150
6	2	8	50

The removal rate or removal efficiency for each run was calculated as the difference between initial and residual concentrations. The results shows that a pH =8 was the most favorable value for recovering VOCs from wastewater consequently.

9. RESULTS AND DISCUSSIONS

A series of desorption tables and curves were obtained experimentally for air stripping from water of single, binary and ternary systems in a bubble column. In all experiments the overall mass transfer coefficient (K_La) was obtained by Bubble Aeration Model (BAM), the results were obtained by solving the model by using STATISTICA software computer program.

The mass transfer coefficient (K_La) assumed as an unknown parameter, was obtained from the model using the experiment data. The experimental and predicted curves are presented as plots of removal factors (C_L/Co) versus time.

Several experiments were carried out to investigate the effect of different experimental parameters on the removal efficiency of VOCs from water. The parameters studied were pH, air flow rate and the initial concentration of solutions for single, binary and ternary systems of VOCs.

1-Effect of pH The effect of pH on the removal of TCE ,CF and DCM was studied in single system as shown in figures 2, 3 and 4 respectively plotting the concentration ratio C_L/Co versus time at various pH values while the other variables remained constant. From these three figures it can be seen that concentration ratio decreases sharply at the beginning of the runs, then it began to decrease slowly with time and it was found that the best pH value for the removal of all components to be 10 highly alkaline but all experiments were adjusted at pH=8 for laboratory purposes to control experiments easily and to be easy to study another operation conditions.

2.Effect of Air Flow Rate The removal of VOCs from water was studied at different gas flow rates 1, 2, 3, 4, 6 l/min with the pH adjusted at 8, and for three systems single, binary and ternary. The results are presented in **Figs. 3, 4, and 5**, as plots of C_L/Co versus time with air flow rate as parameters. It can be seen that high removal occurs with higher gas flow rates. This is due to the fact that the hydrodynamics of bubble columns depend on superficial gas velocity U_G . If U_G increases hinder liquid flow indicating that the Liquid is getting more agitated and hence more removal. At low gas velocity, bubbles are small, and rise uniformly without much interaction with the liquid. On the other hand, at higher gas velocity, large fast-rising bubbles appear which disrupt the system contents, resulting in an increase in the liquid dispersion, Moustiri et al., 2001. Thus increasing the gas flow rate increases the removal of volatile solutes by gas transfer in

the range of interest for both surface and bubble aeration ,**Paul et al. 1985**.

The first point of significance from these plots is the systematic increase in the extent of VOCs removal with increase in air flow rate. The general shape of these curves is as expected based on the solution of the mass transfer equation BAM, it was an exponential removal rate with time. The effect of air flow rate is depicted in figures above and as found with single the binary and ternary the removal efficiency was increased with increasing air flow rate for all components in the mixture. Similarly, TCE was removed faster than the other components.

3-Competitive Desorption: To show the effect of operating conditions on desorption experiments of a component by the presence of other components in the mixture; TCE is taken as a case. **Fig. 6** and **Table 3** illustrate the removal rate of TCE as a single system, as a binary system first with CF and second with DCM and as ternary system TCE-CF-DCM. It can be seen from the curves of experiments, TCE is being removed at a faster rate in a single system in comparison with binary and ternary cases. For example, after 700 s of operation, 82% of TCE is removed in the single case, whereas 68% is removed in the presence of CF and 70% is removed in the presence of DCM. In the case of ternary system, 66% of TCE is removed over the same period of time and operating conditions. Another example taken near the end of stripping operation (nearly after 2000 s), we note that 99% of TCE is removed in the single case, 96% and 97% with CF and DCM respectively, and 93% in the ternary case. It is clear that TCE in all these cases is the components with highest tendency for removal. The closeness of the removal CF and DCM is possibly due to the closeness of their Henry's constant and their molecular weight.

Table 3.Competitive desorption of TCE in presence of CF or DCM in binary system and in presence of CF-DCM in ternary system, $Q_G=2$ l/min, $C_o=250$ mg/l, $T\approx 25^\circ\text{C}$.

TCE (C_L/C_o)				
Time (sec)	single	with CF	with DCM	with CF- DCM
0	0.993	0.997	0.997	0.994
180	0.625	0.813	0.745	0.824
360	0.419	0.638	0.557	0.673
540	0.288	0.493	0.417	0.515
720	0.183	0.361	0.34	0.32
1020	0.087	0.195	0.174	0.156
1320	0.044	0.107	0.1	0.0794
1920	0.005	0.0326	0.055	0.069
2520	0.0022	0.013	0.033	0.044
3420	0.0016	0.008	0.012	0.013
4320	0.001	0.001	0.004	0.005
5520	0.0001	0.001	0.002	0.003

4-Evaluation of the Volumetric Mass Transfer Coefficient (K_La)

The overall liquid phase mass transfer coefficient for each compound (as single, binary, and ternary systems) was evaluated by applying the experimental data to the aeration bubble model **Eqs. 4** and **5** using STATISTICA program. The results of calculations are presented in **Tables 4, 5 and 6**, for all systems investigated. **Fig. 7** presents the results for single component systems which show that K_La increases with increasing gas flow rate or gas holdup for the three VOC compounds. This result indicates the dependency of K_La on bubbling behavior created by gas flow through the liquid phase. A large number of small size bubbles observed at high gas flow rate caused the creation of large interfacial area for mass transfer and in turn this led to higher values of K_La . As can be seen from **Fig. 7**, TCE exhibits the highest value of K_La in comparison with other two VOC compound and the order is:

$$K_{LaTCE} > K_{LaICF} > K_{LaIDCM}$$

This result is probably due to difference in diffusion coefficients of VOC compounds in the liquid phase. K_La is directly proportional to the Henry's law constant and molecular diffusion in the liquid, cited by Wilke and Change, 1955, i.e.

$$K_La \propto \sqrt{D_i} \quad (6)$$

Where:

D_i is the diffusivity coefficient of VOC in the liquid phase.

And from **Table 3**, we noted that experiments of VOCs with mechanical stirring and found that K_La values increased when stirring speed increased. Mechanical stirring has improved the interfacial area by producing large number of small size bubbles. **Figs.8, 9** and **10** present the results for binary systems. As can be seen, the highest value of K_La is exhibited by the component with the highest value of Henry's constant, we note that CF and DCM exhibit weak competition, i.e. their K_La values are close and this is probably due to the closeness of their diffusion coefficients. This discrepancy in the results is possibly due to variations in experimental conditions, particularly temperature which is difficult to control. The results shown in **Fig.11** for the ternary system indicate weak competition among the three VOC compounds, particularly at low gas flow rate. At higher air rate, value.

The effect of flow rate on K_La value is in agreements with Matter-Muller et al., 1981, who carried out batch desorption.

$$u_{m1\text{ TCE}} < u_{m1\text{ CF}} < u_{m1\text{ TCE}}$$

It can be seen from **Table 1** the D_i values of DCM and CF is rather close and the diffusion coefficient in a solution could be different from that in pure solvent. The observed effect of gas flow rate on K_La is in agreements with Matter-Muller et al., 1981 who carried out batch desorption experiments of VOCs with mechanical stirring and found that K_La values increased with stirring

speed. Mechanical stirring has improved the interfacial area for mass transfer by producing large number of small size bubbles.

Table 4. K_La and gas holdup for single experiments.

VOC	$Q_G(\text{l/min})$	$K_La(\text{sec}^{-1})$	ε_G
TCE	1		0.0185
	2	0.0026	0.023
	3	0.0032	0.034
	4	0.0037	0.046
	6	0.0044	0.057
CF	1	0.0009	0.0185
	2	0.0012	0.023
	3	0.0018	0.034
	4	0.0029	0.046
	6	0.0034	0.057
DCM	1	0.001	0.0185
	2	0.00124	0.023
	3	0.00154	0.034
	4	0.0017	0.046
	6	0.00237	0.057

Table 5. K_La and gas holdup for binary experiments.

Group	VOC	$Q_G(\text{l/min})$	$K_La(\text{sec}^{-1})$	ε_G
TCE-CF	TCE	3	0.00199	0.034
		2	0.00149	0.023
		1	0.00089	0.014
	CF	3	0.00124	0.034
		2	0.0071	0.023
		1	0.0005	0.014
TCE-DCM	TCE	3	0.00134	0.034
		2	0.0011	0.023
		1	0.00087	0.014
	DCM	3	0.00087	0.034
		2	0.0007	0.023
		1	0.0005	0.014
CF-DCM	CF	3	0.0014	0.034
		2	0.001	0.023
		1	0.0008	0.014
	DCM	3	0.00146	0.034
		2	0.0012	0.023
		1	0.00058	0.014

Table 6. K_La and gas holdup for ternary-batch experiments.

VOC	$Q_G(\text{l/min})$	$K_La(\text{sec}^{-1})$	ε_G
TCE	2	0.00125	0.023
	3	0.00149	0.034
	4	0.00198	0.046
CF	2	0.00117	0.023
	3	0.00201	0.034
	4	0.00249	0.046
DCM	2	0.0014	0.023
	3	0.00215	0.034
	4	0.00252	0.046

10. CONCLUSIONS

The main goals of this work were to investigate competitive removal of identified VOCs from water by air stripping in a concurrent bubble column. The results obtained led to the following conclusions:

- From experiments it was found that the best pH value for removal of VOCs to be 10.
- High removal rates occur with high gas flow rates. The percentage removal increases proportionally with gas flow rate or gas holdup. This result can be generalized for the three systems.
- The removal efficiency affected slightly with increasing initial concentration of the solution for all systems.
- Component TCE is being removed faster than CF and DCM because of the difference in their Henry's constants. TCE has the highest value of Henry's constant and hence it is the most volatile component and the order of removal can be written as follows:
 $\text{TCE} > \text{CF} > \text{DCM}$
- The competition between the components in binary and ternary systems caused reduction in the material removed of each

solute compared with that in single solute systems.

- It is found that K_La increases with increasing gas flow rate for all systems.
- The k_La values for TCE in all systems were the highest compared with other components. This was due to its highest value of Henry's coefficients. The order of K_La values in single and ternary systems can be summarized as follow:

$$K_{La\text{DCM}} < K_{La\text{ICF}} < K_{La\text{ITCE}}$$

and for the binary system is:

$$\underline{K_{La\text{TCE}} > K_{La\text{CF}}}, \quad \underline{K_{La\text{TCE}} > K_{La\text{DCM}}}, \quad \underline{K_{La\text{CF}} > K_{La\text{DCM}}}$$

11. REFERENCES

- Sulaymon A.H. and Mohammed A. A. ,2010. *Separation and Hydrodynamic Performance of Air-Kerosene-Water System by Bubble Column*. International Journal of Chemical Reactor Engineering V8.
- Andrews, G.F., Fike R., and Wong S. ,1988. *Bubble Hydrodynamics and Mass Transfer At High Reynolds Number and Surfactant Concentration*, Chemical Engineering Science, Vol.43, No.7, 1467-1477.
- DeMacro J. ,1983. *History of Treatment of Volatile Organic Compounds in Water*. in *Occurrence and Removal of Vocs from Drinking Water*. A cooperative research report between, AWWA and KIWA, Denver, Co.
- Djebbar Y. ,1998. *Prediction of Mass Transfer Coefficients of Air Stripping Packed Towers for Volatile Organic Compounds Removal*. Ottawa –Carleton Joint Institute of Civil Engineering, University of Ottawa, Ontario, Canada.

- Dwight A. B. 2001, *Engineering and Design Air Stripping*, Department of the army U.S Army Corps of Engineers Washington, D. C, 20313-1000;.
- Dyksen J. E., Hess A. F., Barnes M. J. and Cline G. C., 1982, *The use of Aeration to Remove Vos from Groundwater*. Proceeding Annual Conference of the AWWA, pp. 965-980.
- Fatema B., Jalal S., Hesamedin S. and Jalal B. P. ,2009,. *Removal of Organic Pollutants from Waste Streams by Dissolved Air Precipitation/Solvent Sublation Technology*, Tehran, Iran, Department of Chemistry, Bu-Ali Sina University, Hameda.
- Mackay, D. and P.J. Leinonen ,1975, *Rate of Evaporation of Low Solubility Contaminants from Water Bodies to Atmosphere*, Environmental Science and Technology, Vol.9, No.13,1178.
- Matter-Mueller, C., W. Gujer, and W. Giger, 1981, *Transfer of Volatile Substances from Water to The Atmosphere*, Water Research, Vol.15, issue 11, 1271-1279.
- Moustiri S. Herbard E. Thakre S.S. and Roustand N. ,2001, *A Unified Correlation for Predicting Liquid Axial Dispersion Coefficient In Bubble Column*. J. Chemical Engineering Science. Volume 56, issue 3, Pages 1041-1047.
- Nigar K., Fahir B. and Kutlu O., 2004, *Bubble Column Reactors*, ELSEVIER, J. Volume 40, Issue 7m, Pages 2263-2283.
- Onder A., Paul A., and Anderson P. W. 2004, *Laboratory Batch Experiments of The Combined Effect Ultrasound and Air Stripping in Removing CCl₄ and 1,1,1-TCA from Water*. Journal of Hazardous Materials, Volume 120, issue 1-3, pages 149-156.
- Pedro L. L., Leticia L.M., Luis I. M. R., Katarzayna W., and Judith A. H. ,1997, *Extraction of Sunset Yellow and Tartrazine by Ion-Pair Formation With Adogen-464 and Their Simultaneous Determination by Bivariate Calibration and Derivate spectrophotometry*. Analyst Vol. 122, P: 1575-1579.
- Richard G. Zepp, 1997, *Role of Photoreactions in the Formation of Biologically Labile Compounds from Dissolved Organic Matter*, Ecosystems Research Division, National Exposure Research Laboratory, U.S. Environmental Protection Agency, Athens, Georgia 30605-2700.
- Roberts P.V. et al., 1983, *Volatilization of Organic Pollutants in Wastewater Treatment, Model studies*. EPA-R-806631, U. S. EPA Munic Environ. Res. Lab. Cincinnati Ohio.
- Wilke, C. R. and Change, P., 1955, *Correlation of Diffusion Coefficients in Dilute Solutions*, AIChE J., 1, 264-270.

10. NOTATIONS

*	Denotes equilibrium	
a	Interfacial area	m^2
A	Cross section area	m^2
A_b	Absorbency	Angstrom
b	Denote bubble	
C_G^*	Gas phase at	mg/l
C_{AI1}	Molar concentration inside the film	mole/l
C_{AO1}	Molar concentration outside the film	mole/l
C_L	liquid phase concentration at	mg/l
C_L^*	liquid concentration in equilibrium with Column inside	mg/
d	Water phase diffusion coefficient	m
Dl	Water phase diffusion coefficient	m^2/sec
G	denotes gas phase	
H	Henry's Law constant	$atm \cdot m^3/mole$
H_c	Henry's law constant	dimensionless
i,j	Subscript denote to Compound	
k_L	Low flux mass transfer coefficient	sec^{-1}
K_La	Overall mass transfer coefficient	
L	denotes liquid phase	
M	Molar weight	g/mole
o	Denotes initial	
R	Gas constant	$8.2 \cdot 10^{-5} m^3$
S	water solubility	$mole/m^3$
Sb	Denotes slope	
T	Temperature	K
t	Time	sec
U_G	Superficial gas	m/sec
U_L	Superficial liquid	m/sec
V_c	Critical volume	$cm^3/mole$
V_L	water solution volume	m^3
Z	Axial distance	m
Φ	$= ([K_La]_b \cdot V_L) / (H_c \cdot Q_G \cdot Z_s)$	1/m
ρ	Density	g/mm^3
ε_G	Gas holdup	

ε_L	Liquid holdup
ψ	High flux correlation
	Ratio of mass-transfer coefficients
ABM	Aeration bubble
CF	Chloroform
DCM	Dichloromethane
GC	Gas chromatography
TCE	Trichloroethylene
UV	Ultra-Violet spectro-photometry
VOCs	Volatile organic compounds

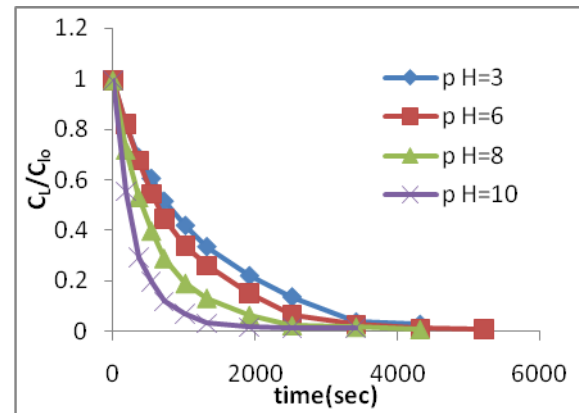


Figure 2. Effect of pH on the removal of DCM single-batch, $Q_G = 3$ l/min, $C_{Lo} = 250$ mg/l, $T \approx 25^\circ C$.

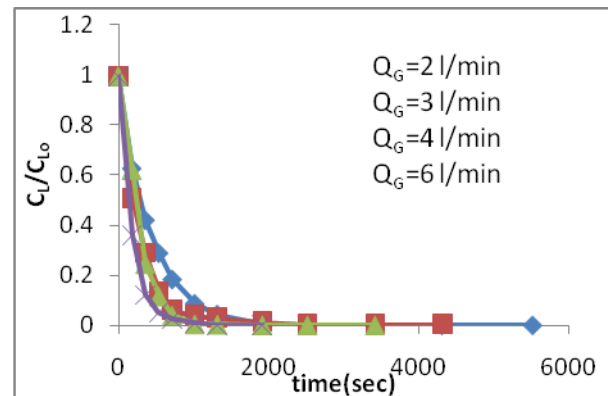


Figure 3. Effect of air flow rate on the removal of TCE single system, $pH = 8$, $C_{Lo} = 250$ mg/l, $T \approx 25^\circ C$.

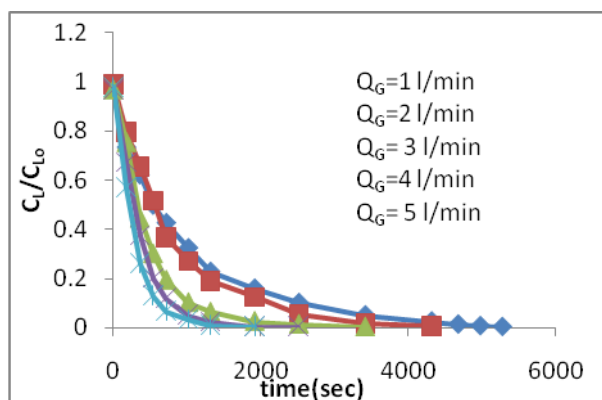


Figure 4. Effect of air flow rate on the removal of CF single system pH=8, C_{Lo} =250 mg/l, $T \approx 25^\circ\text{C}$.

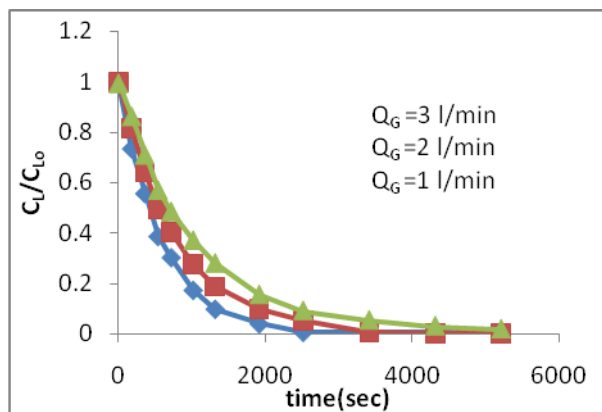


Figure 5. Effect of air flow rate on the removal of TCE in TCE-CF binary system, C_{Lo} = 250 mg/l, pH=8, $T \approx 25^\circ\text{C}$.

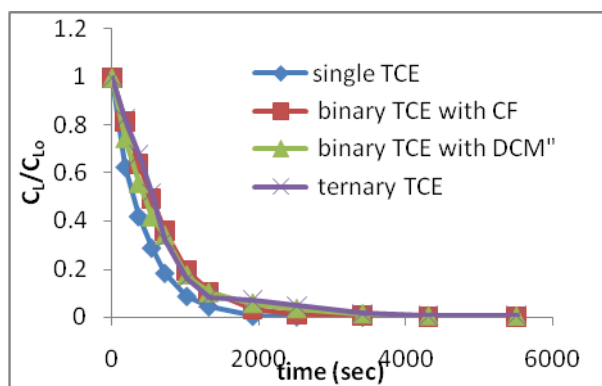


Figure 6. Competitive desorption of TCE in presence of CF or DCM in binary system and CF-DCM in ternary, Q_G =2 l/min, C_{Lo} =250 mg/l, $T \approx 25^\circ\text{C}$.

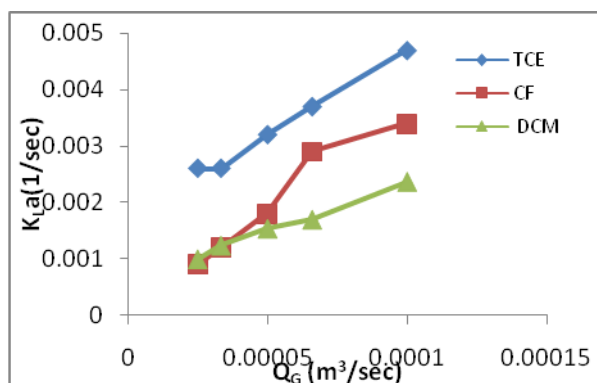


Figure 7. Effect of air flow rate on K_{La} single system component C_{Lo} =250 mg/l , pH= 8, $T \approx 25^\circ\text{C}$.

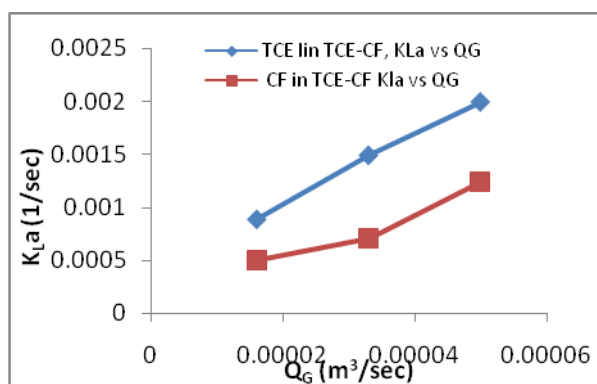


Figure 8. Effect of gas flow rate on K_{La} in binary system (TCE-CF) component, C_{Lo} =250 mg /l , pH= 8, T =25°C.

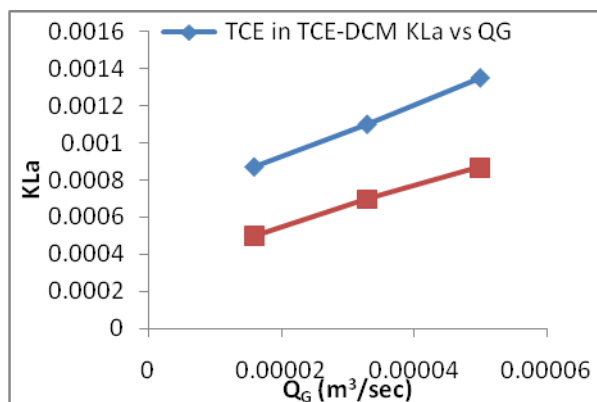


Figure 9. Effect of gas flow rate on K_{La} in binary system (TCE-DCM) component, C_{Lo} =250 mg/l pH= 8, T =25°C.

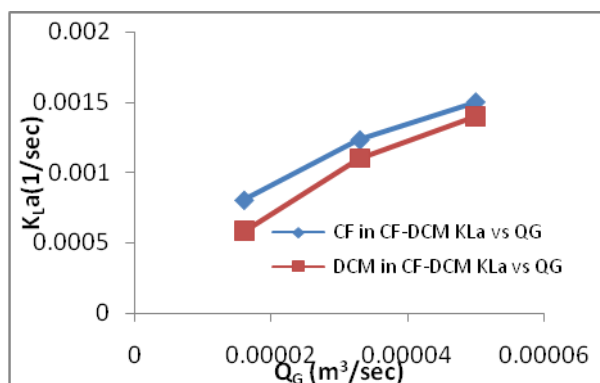


Figure 10. Effect of gas flow rate on K_{La} in binary system (CF-DCM) component, $C_{Lo}=250$ mg/l, pH= 8, $T \approx 25^\circ\text{C}$.

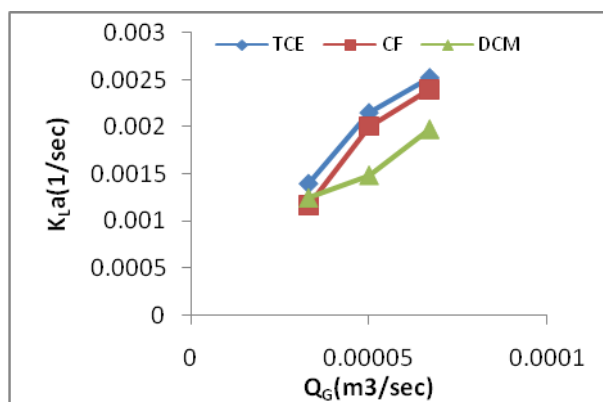


Figure 11. Effect of gas flow rate on K_{La} ternary System (TCE-CF-DCM) component, $C_{Lo}=250$ mg/l, pH=8, $T \approx 25^\circ\text{C}$.

Evaluating the Crop Coefficient for Cherries Plants in Michigan State

Sabah Anwer Dawood Almsaraf

Assistant Professor

Engineering College- Baghdad University

[E-mail:sabah_dawood@yahoo.com](mailto:sabah_dawood@yahoo.com)

ABSTRACT

Crop coefficient for cherries was evaluated by measure the water consumption in Michigan State to find its variation with time as the plant growth. Crop coefficients value (K_c) for cherries were predicated by Michigan State University (MSU) and also by Food and Agriculture Organization (FAO) according to consume of water through the season. In this paper crop coefficients for cherries are modified accordingly to the actual measurements of soil moisture content. Actual evapotranspiration (consumptive use) were measured by the soil moisture readings using Time Domain Reflectometers (TDR), and compared with the actual potential evapotranspiration that calculated by using modified Penman-Monteith equation which depends on metrological station and by using pan evaporation method. Absolut error techniques show that the predicated crop coefficient by MSU should be modified and changed from 1.0 to 1.20 during June, and from 1.02 during July and August to 1.2 to reduce the crop water stress and give better water management and perfect schedule for irrigation process.

Key words: crop coefficient, actual evapotranspiration, soil moisture, plant growth.

تقييم معامل نباتات الكرز في ولاية ميشيكان

صباح انور داود المصرف

أستاذ مساعد

كلية الهندسة - جامعة بغداد

الخلاصة

تم تقييم معامل نبات الكرز في ولاية ميشيكان من خلال قيمة استهلاك الماء لغرض ايجاد التباير في قيم المعامل مع مراحل نمو النبات. أن معامل نبات الكرز (Cherries) والمستنبط من قبل باحثين في جامعة ولاية ميشيغان و منظمة الغذاء والزراعة (فاو) يعتمد على مراحل استهلاك النبات وانتاجه خلال السنة. من اجل الحصول على دقة أعلى لتقدير قيم معامل النبات ، تم في هذا البحث أعداد مقترح لتعديل معامل النبات وذلك من خلال القياسات الحقلية للمحتوى الرطوبي للتربة وبالتالي بالامكان معرفة الاستهلاك الفعلي للنبات وذلك باستخدام مقياس مجال وقت الانعكاس (TDR). تمت مقارنة النتائج مع القيم المحسوبة من معادلة بنمان – مونتيث المعدلة (Modified Penman-Monteith equation) والتي تعتمد على قياس المتغيرات المناخية لمحطة الانواء الجوية قرب منطقة البحث وكذلك قيم التبخر من حوض التبخير (Pan evaporation). استخدمت تقنية الخطأ المطلق (Absolute Error) الاحصائية لايجاد الطريقة الافضل عند المقارنة ، فوجد أنه من المفضل تعديل معامل النبات والمستنبط من قبل جامعة ولاية ميشيكان الامريكية لشهر حزيران من ١,٠ الى ١,٢، ومن ١,٠٢ الى ١,٢ لشهري تموز وأب، وذلك للتقليل من الجهد الرطوبي ، وأيضا للحصول على إدارة افضل للمياه وجدولة مثلى لعملية الري.

1. INTRODUCTION

Crop coefficient, variety and development stage should be considered when assessing the evapotranspiration from crops grown in large, well-managed fields. Differences in resistance to transpiration, crop height, crop roughness, reflection, ground cover and crop rooting characteristics results in different crop evapotranspiration (ET) levels in different types of crops under identical environmental conditions. Due to the differences in evapotranspiration during the various growth stages, crop coefficient for a given crop will vary over the growing period. The growing period can be divided into four distinct growth stages: dormant, bloom, fruit set and development, and late season, **Allen, et al., 1998**.

Once the reference evapotranspiration (ET_0) has been determined, a crop coefficient must be applied to adjust the reference ET_0 value for local conditions and the type of crop being irrigated. Crop coefficients for Apples, Cherries, Pears and Grapes with cover crops have been segregated into months, **Water Conservation, 2001**.

The most important use of evapotranspiration information is in the irrigation scheduling where good water management requires that the irrigator apply only enough water to meet the needs for the crop plus some additional amount to compensate of the inefficiencies of the irrigation system, **Darrell, 20103**.

Crop coefficients that given by **FAO, 1998** resulted in an update of Kc values to be applied into Penman-Monteith method and procedures to arrive better estimates under various climatic conditions and crop height and expanding the range of crops and crop types, **Kassam, and Smith, 2001**.

Proper irrigation is essential to maintaining, healthy and productive Cherry orchard. Over irrigation slows root growth, increase iron chlorosis in alkaline soils, and leaches nitrogen, and sulfur out of the root zone, **Brent, 2008**. Drought stress will effect on the fruit development from the pit hardening to harvest, and typically occurs concurrently with the highest temperature of the season, **Brent, 2008**.

In this study the crop coefficients for cherries which calculated by measuring crop evapotranspiration were compared with FAO, Utah State and Michigan State recommended values.

2. AREA OF THE STUDY

The study area is located north- west of Michigan State in United State of America, called Travers City, where research center of Michigan State University (MSU) is located. Cherry of 10 years ages is used which are spaced by 6.3×6.3m. Trickle irrigation is used and one emitter per crop of capacity 3.785 l/hr is considered, see **Fig.1**. Soil texture is Loamy sand and the groundwater is the source for the irrigation.

Time Domain Reflectometer (TDR) soil moisture tools, **Fig.2**, are used in the measurement of soil moisture every fifteen minutes per day and through the growing season. Determination of water content with TDR relies on the fact that the travel time of an electromagnetic pulse through stainless steel probe (the wave guided), embedded in the soil, and is a function of the soil's water content. Total numbers of twenty four of TDR are being used to cover the studied area, where at each location two numbers of the tools are used at depth of 915mm and 1220mm, and it is distant 200mm from center of the tree.

Pan evaporation class A is used for measurement of water evaporation, made of 20 gauges galvanized welded iron of size 1207mm in diameter and 254mm in depth. It is normally installed on a wooden platform set on the ground in a grassy location. The pan is filled with water within 60mm of the top edge.

3. METHODOLOGY AND PROCEDURE

The adopted methodology in this study is first: estimate the actual evapotranspiration from measuring soil moisture content, second: calculate the potential evapotranspiration by using pan evaporation and Enviro-Weather station methods,

and finally third: calculate the actual crop coefficient from first and second steps.

3.1 Actual Evapotranspiration

Actual crop evapotranspiration (ET_c) may be estimated by measuring the soil moisture content, especially when the plant age is 10 years and the shaded area is large enough to reduce the evaporation from the ground surface. Average values of all the soil moisture measurements tools are recorded. The difference between the reading in the early day and the late hour of the day is the consumptive use of the plant, **Tables 1 and 2** show samples of soil moisture measurements for years 2010 and 2011. The estimated crop evapotranspiration can be calculated from the following **Eq. (1)**:

$$ET_c = ET_o * Kc \quad (1)$$

Where:

ET_c = Actual or crop evapotranspiration (mm/day),
 ET_o = Potential or reference evapotranspiration (mm/day), and
 Kc = crop coefficient.

3.2 Crop Coefficient (Kc)

Crop coefficient for cherries will vary over the growing season starting from April to October (growing season in Michigan State). **Fig.3** shows the comparison of the crop coefficient values developed by MSU, FAO and by Utah State University for cherries, **Brent, 2008**.

3.3 Potential (or Reference) Evapotranspiration

In this study potential evapotranspiration (ET_o) can be calculated by using the following methods:

- 1- Pan evaporation: cylindrical pan over covered ground surface is used through growing season in the area of the study.
- 2- Enviro-Weather station is used in the area near by the area of the study. Modified

Penman-Monteith equation is used which developed by, **FAO, 1998**:

$$ET_o = \frac{0.408 \Delta(Rn - G) + \gamma \left(\frac{900}{T + 273} \right) U_2 (e_s - e_a)}{\Delta + \gamma(1 + 0.34 U_2)} \quad (2)$$

Where:

ET_o = potential or reference evapotranspiration (mm/day),
 R_n = net radiation at the crop surface (MJ/m²/day),
 G = soil heat flux density (MJ/m²/day),
 T = mean daily air temperature at 2m height (C°),
 U_2 = wind speed at 2m height (m/s),
 $e_s - e_a$ = saturation vapor pressure deficit (kpa),
 γ = psychrometric constant (kpa/C°), and
 Δ = slope vapour pressure curve .

4. RESULTS AND DISCUSSION

Values of Kc which developed by FAO and by Utah State are less in early growing stage and Kc developed by FAO is more in the bloom stage and fruit set and development stage from the measured values by MSU, when the plant's evapotranspiration is increased. While Kc developed by Utah State and by MSU is almost equal in these stages. On the other hand the developed Kc by FAO and by Utah State is less in the late of the season and after, when the plant's evapotranspiration is decreased.

Fig.4 shows the comparison between different calculations of actual evapotranspiration based on Kc equals to 1.02 as developed by MSU for year 2010. The actual evapotranspiration calculated from Modified Penman-Monteith (ET_2) gives values less than that measured values (ET_4), especially during July and early days of August, and almost equals in values in mid days of August.

Table 3 shows summary of absolute error for year 2010 and 2011. The absolute error $|ET_4 - ET_2|$ for crop coefficient developed by FAO is much better than the developed one by MSU. While Absolute error $|ET_4 - ET_3|$ for crop coefficient developed by MSU gives value

less than crop coefficient developed by FAO, except for June 2011.

Fig.5 shows comparison between different calculations of actual evapotranspiration based on Kc equals to 1.20 as developed by FAO for year 2010. The potential evapotranspiration calculated from Modified Penman-Monteith equation (ET_2) gives values less than measured values (ET_4), especially during July and early days of August, and higher values during mid-days in August.

Figs.6 and **7** show comparison between different calculations of actual evapotranspiration based on different values of Kc (equals to 1.0 and 1.20) as developed by MSU and by FAO respectively for June 2011.

Absolute errors $|ET_4 - ET_2|$ and $|ET_4 - ET_3|$ are 11.42, 7.23 and 9.59, 5.01 respectively. That's mean Kc = 1.2 is the best in the comparison.

Fig.8 shows the absolute error when Kc equals to 1, 1.02, and 1.2. The absolute errors of $|ET_4 - ET_2|$ for July and August of years 2010 and 2011 were less in values than the absolute errors of $|ET_4 - ET_3|$. On other hand the absolute errors of $|ET_4 - ET_2|$ for June of years 2010 and 2011 were higher than $|ET_4 - ET_3|$.

From actual evapotranspiration measured by soil moisture content ET_4 and from ET_2 and ET_3 , modified crop coefficient (Kc) can be found by using the following equations, assuming that there is no deep percolation (drainage water):

$$Kc = \frac{ET_c}{ET_o} \quad (3)$$

The developed values of Kc from **Eq. (3)** were equal to 1.2 for June, July and August. **Table 4** shows comparison between Kc used by MSU and the modified values.

5. CONCLUSION

According to above results, crop coefficient developed by Michigan State University should be modified to be equal to 1.2 for month's stages June, July and August, which matches with values

recommended by FAO. Therefore, schedule the irrigation process according to none modified crop coefficients may be harmful on the plant growth and production under water stress.

Recommendation for further research works is to use the crop coefficient developed by MSU and study the effect of water stress on the crop growth and production to minimize the irrigation process and save water. Also crop coefficient for early months could be included in future studies.

6. ACKNOWLEDGEMENT

Many thanks to the staff of research field in Michigan State University, Travers City. Also thanks to Mr. Steve Miller in Biosystems and Agriculture Engineering Department.

7. REFERENCES

- Allen, G. A., Perera, L. S., Raes, D., and Smith, M., 1998, *Crop Evapotranspiration – Guidelines for Computing Crop Water Requirement* FAO. Irrigation and Drainage paper No.56, FAO, Rome, Italy.
- Brent, B., 2008, *Orchard Irrigation: Cherry*. Utah State University, Cooperative extension, March.
- Darrell, W., 2010, *Crop Water Use*, Crop Production Clinics Proceedings, University of Nebraska-Lincoln Extension.
- FAO, 1998, *Crop Evapotranspiration- (Guidelines for Computing Crop Water Requirements)*, Irrigation and Drainage Paper No. 56, Rome, Italy.
- Farahani, H. J., Howell, T. A., Shuttleworth, W. J., and Bausch, W. C., *Evapotranspiration: Progress in Measurement and Modeling in Agriculture*. Transactions of the ASABE, Vol. 50(5), PP. 1627-1638
- Kassam, A., and Smith, M., 2001, *FAO Methodologies on Crop Water Use and Crop Water Productivity*, Expert Meeting on crop water



productivity paper No. CWP-M07, Rome, 3 to 5 December.

Suat, I., 2009, *Estimating Crop Evapotranspiration from Reference Evapotranspiration and Crop Coefficient*, Neb Guide, University of Nebraska-Institute of Agriculture and aural Resources, paper no. G 1994.

Water Conservation Factsheet, 2001, *Crop Coefficients for Use in Irrigation Scheduling*, British Columbia, Ministry of Agriculture, Food and Fisheries, October.

Table 1. Soil moisture content as in equivalent depth for year 2010.

Date	Soil moisture content (equivalent depth mm) for depth 915mm	Soil moisture content (equivalent depth mm) for depth 1220mm
23-Jul.	2.18	2.92
24-Jul.	3.48	4.65
25-Jul.	5.49	7.32
26-Jul.	6.05	8.05
27-Jul.	5.03	6.71
9-Aug.	4.12	5.49
10-Aug.	4.48	5.97
11-Aug.	2.18	2.92
12-Aug.	3.66	4.88
13-Aug.	3.56	4.75
15-Aug.	3.66	4.88
16-Aug.	3.94	5.26
17-Aug.	3.38	4.5

Table 2. Soil moisture content as in equivalent depth for year 2011.

Date	Soil moisture content (equivalent depth mm) for depth 915mm	Soil moisture content (equivalent depth mm) for depth 1220mm
24-June	2.85	3.79
25-June	4.93	6.58
26-June	4.47	5.97
27-June	6.86	9.14

Table 3. Summary of absolute error for year 2010 and 2011.

Year	Month	Crop coefficient (Kc)	Absolute error ET4 – ET2	Absolute error ET4 – ET3
2010	July	1.02 [*]	6.98	6.67
	July	1.2 ^{**}	5.98	7.4
	August	1.02 [*]	8.12	13.67
	August	1.2 ^{**}	6.83	17.0
2011	June	1.0 [*]	11.42	7.23
	June	1.2 ^{**}	9.59	5.01

* Developed by MSU.

** Developed by FAO.

Table 4. Crop coefficients developed by MSU and the modified values.

Month	June	July	August
Kc (MSU)	1.0	1.02	1.02
Modified Kc	1.20	1.20	1.20



Figure1. Cherries field in research area- Travers City / Michigan State.



Figure 2. Location and depth of the time domain reflectometer (TDR) beside the irrigation system in the research area.

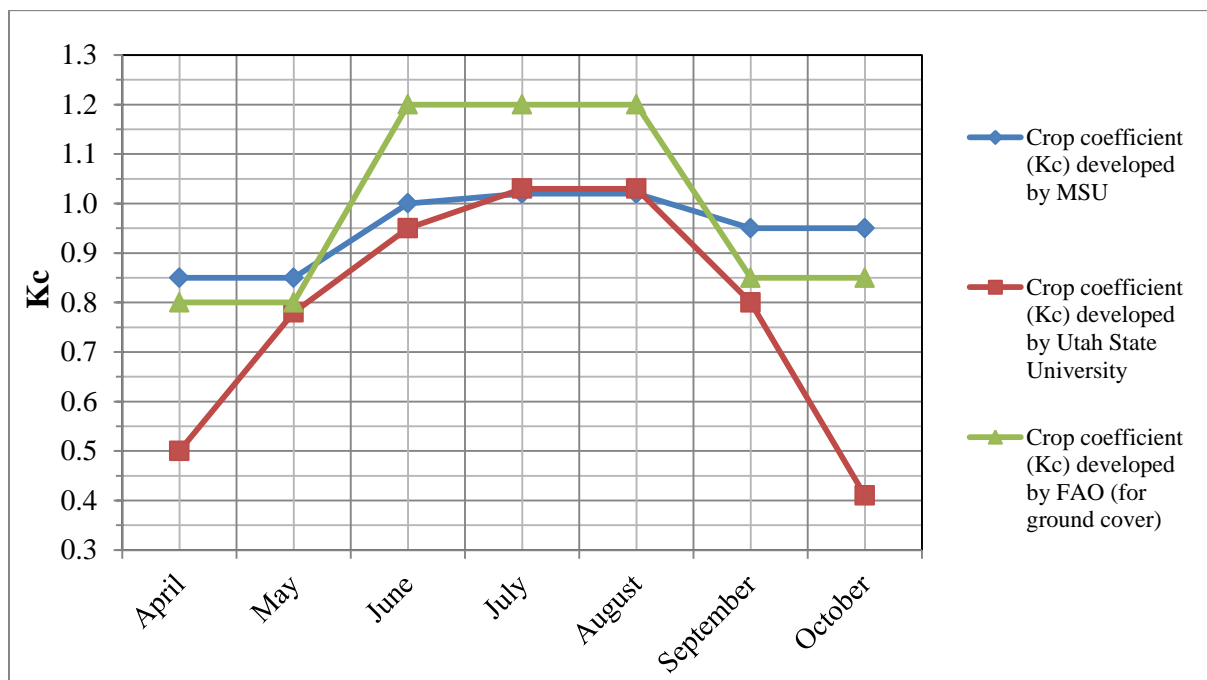


Figure3. Comparison between values of crop coefficients for Cherries.

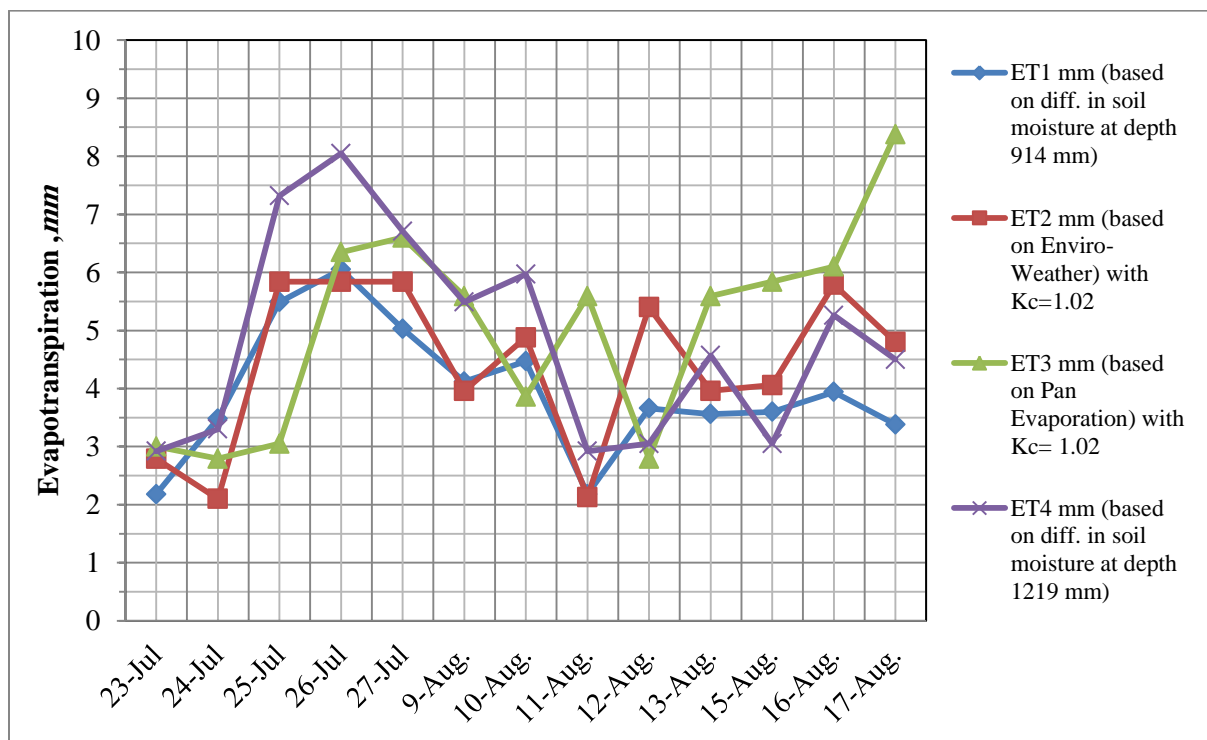


Figure 4. Calculated evapotranspiration for different approaches and methods using Kc=1.02 for Cherries in 2010.

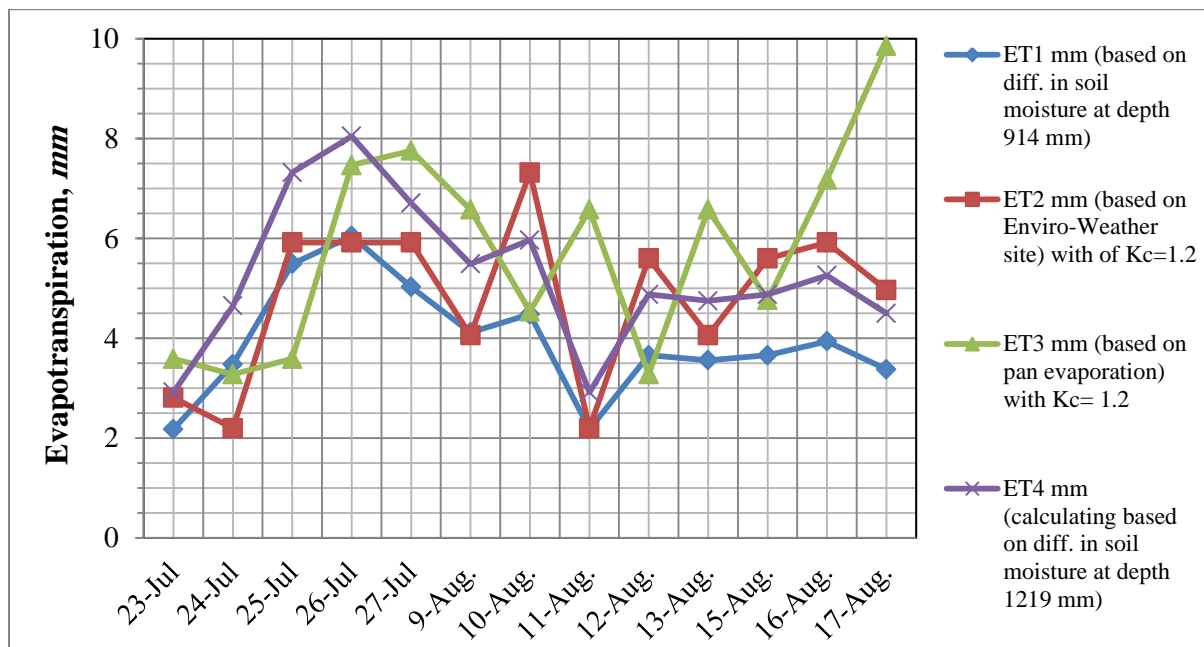


Figure 5. Calculated evapotranspiration for different approaches and methods using $K_c=1.2$ for Cherries in 2010.

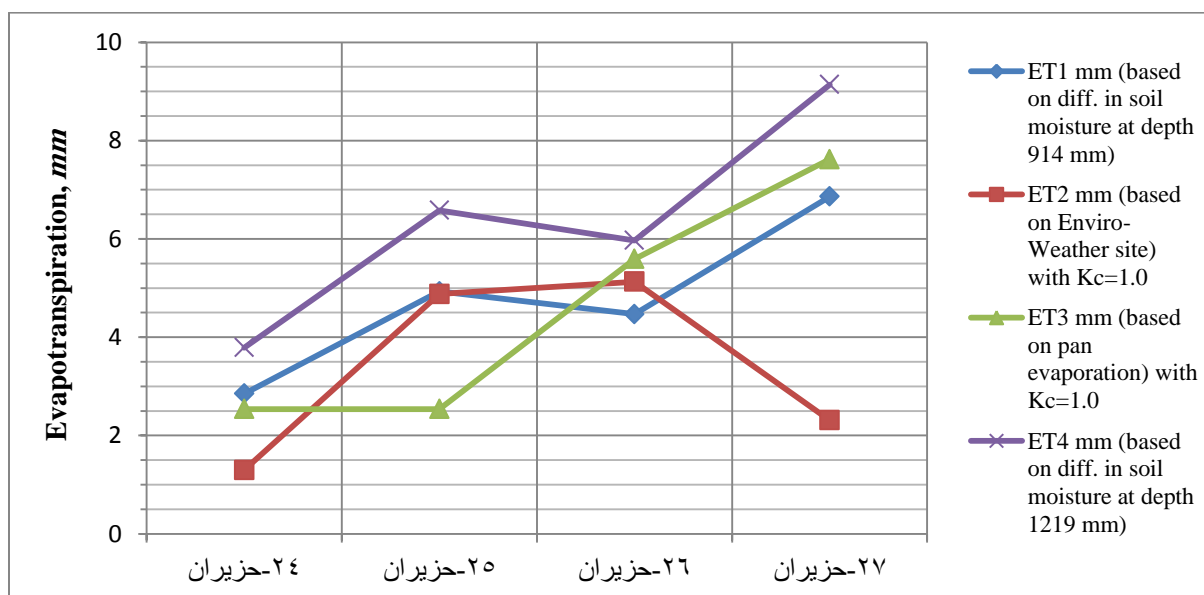


Figure 6. Calculated evapotranspiration for different approaches and methods using $K_c=1.0$ for Cherries in 2010.

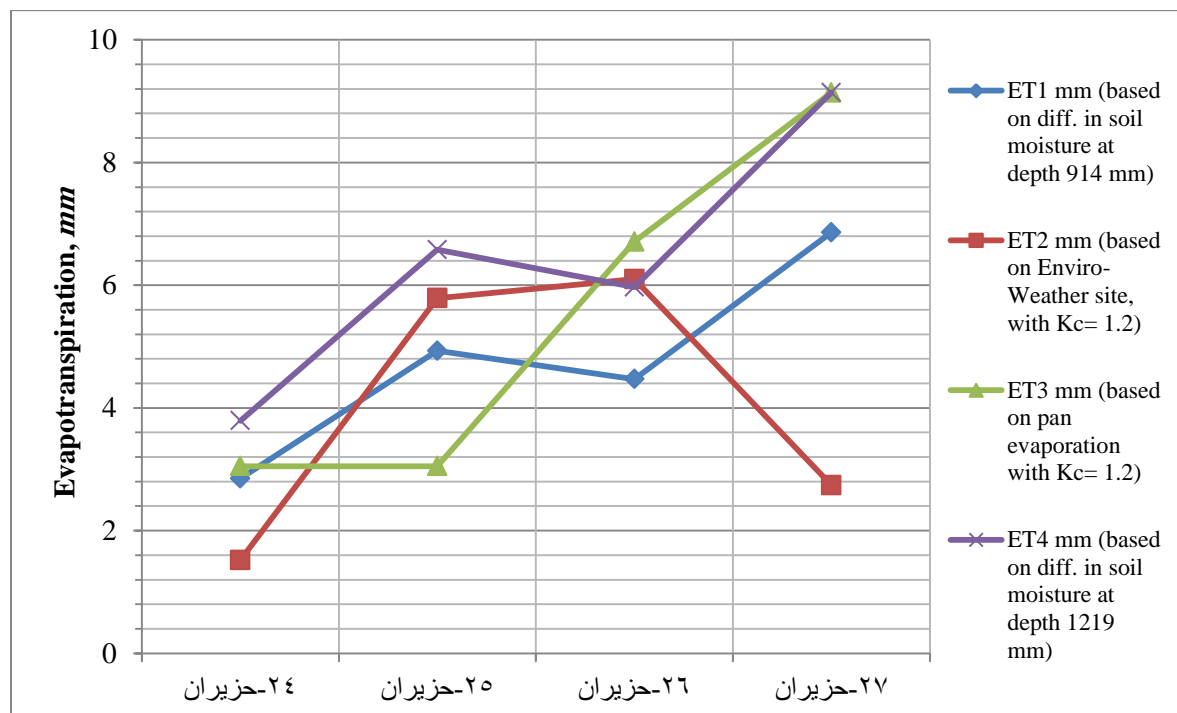


Figure 7. Comparison between different approaches and methods for calculating actual evapotranspiration using Kc=1.20 for Cherries 2011.

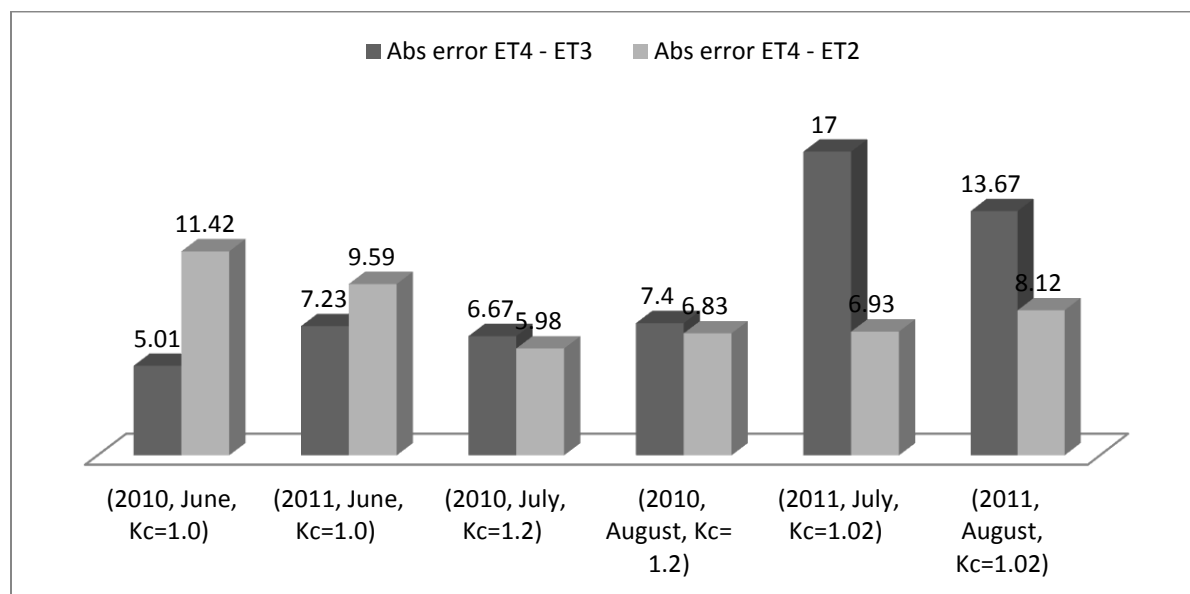


Figure 8. Absolute error for actual evapotranspiration using TDR, Enviro-Weather (modified Penman-Monteith equation) and Pan evaporation for years 2010 and 2011.

Experimental and Modeling Study of Abrasive Wear of Tungsten Carbide Drilling Bit in Wet and Dry Conditions

Asst. Prof. Dr. Fathi Al-Shammaa

Department of mechanical Eng.

College of Eng.

Baghdad university / Iraq

Email : fathi_alshamma@yahoo.com

Dr. Amar Hussein Al-Allaq

Department of mechanical Eng.

College of Eng.

McGill university / Canada

Email : amarallaq@mcgill.ca

Mohaimen Habeeb Makki

Lecturer in mechanical Eng

Email : mohaimen77@yahoo.com

ABSTRACT

The results of theoretical and experimental investigations carried out to study the effect of load and relative sliding speed on the abrasive wear behavior in drilling bit teeth surfaces of an insert tungsten carbide bit have been presented. Experimentally, an apparatus for abrasive wear tests conducted on the modified ASTM-G65 was modified and fabricated to facilitate loading and measurement of wear rate for the sand/ steel wheel abrasion test, which involves two cases of contact; first is at dry sand and second is under wet condition. These tests have been carried under varied operating parameters of normal load and sliding speed. A theoretical model based upon the Archard equation has been developed for predicting wear simulation by using ANSYS12.1 program for dry and wet abrasive wear rates. The general trend for all the results of wet tests is that an increase in the applied load as well as wheel rotational speed produces an increase in wear rate, while at the dry tests the behavior shows an increase and fluctuating in wear rate due to the transition in wear mechanism. As compared to the dry tests, the volume losses in wet tests have much higher values, that is because the presence of water which causes high adhesion between sand particles and specimen surface as well as wear-corrosion interaction which accelerate the wear rates. The percentage errors between theoretical and experimental results are more stable with the wet than dry tests due to the stability in wear rates.

Keywords : abrasive wear, WC-hardmetals, archard theory, friction, ANSYS program

دراسة عملية و نمذجة البلي بالاحتكاك لدقاق الحفر كاربيد التنجستن في الحالتين الرطبة و الجافة

الباحث مهيم حبيب
اختصاص هندسة ميكانيك
جامعة بغداد

د. عمار العلاق
قسم هندسة الميكانيك
جامعة ميكل/ كندا

د. فتحي الشماع
قسم هندسة الميكانيك
كلية الهندسة / جامعة بغداد

الخلاصة

انجاز النتائج النظرية والفحوصات العملية التي نفذت لدراسة تأثير الحمل وسرعة الانزلاق النسبية على تصرف البلي في سطوح الانسان لدقاق حفر كاربيد التنجستن. عمليا ، جهاز لاختبارات البلي والذي يكون ضمن المواصفة العالمية ASTM G65 المعدلة عدل وصنع لتسهيل التحميل وقياس مدى البليان وذلك باستخدام الرمل مع عجلة فولاذية للاختبار، والذي يتضمن اثنين من حالات الاحتكاك؛ أولاً باستخدام الرمل الجاف والثانية تحت الشرط الرطب. هذه الاختبارات اجريت تحت ظروف التشغيل المختلفة من الحمل المسلط والسرعة المنزقة. كما تم استخدام نموذج نظري مطور مستند على معادلة Archard لتوقع معدلات البلي تحت التأثير الرطب والجاف باستعمال برنامج ANSYS 12.1. إن الاتجاه العام لكل نتائج الاختبارات الرطبة تلك هي ان الزيادة في

الحمل المسلط بالإضافة إلى سرعة العجلة التدويرية تُنتج زيادة في معدل البلي، بينما في الإختبارات الجافة، يشير السلوك إلى الزيادة والتذبذب في معدل البلي بسبب التحول في ميكانيكية التآكل. بالمقارنة مع الإختبارات الجافة، خسائر الحجم في الإختبارات الرطبة لها قيم أعلى بكثير، وذلك لأن وجود الماء يسبب الالتصاق العالي بين حبيبات الرمل مع سطح العينة بالإضافة إلى تأثير التآكل الكيميائي والذي يُعجل معدل البلي. إن نسبة الخطأ المئوية بين النتائج النظرية والتجريبية أكثر استقراراً بالإختبارات الرطبة منها في الإختبارات الجافة وذلك بسبب الاستقرار في معدلات البلي.

لكلمات الرئيسية: البلي الانخلاعي، تنجستن كاربيد معدن ذو صلابة عالية، نظرية ارجارد، الاحتكاك، برنامج ANSYS 12.1

1. INTRODUCTION

Whenever surfaces move over each other, wear will occur in the form of damage to one or both surfaces, generally involving progressive loss of material. Damage-resistant surfaces are required in many engineering components to meet demanding performance requirements in contact applications. For example, in rock drilling equipment, constant rubbing action of the drilling head against the hard surfaces of rocks leads to wear and requires frequent replacement of the drilling head. In the process of design of machine elements and tools operating in contact conditions, engineers need to know areas of contact, contact stresses, and they need to predict wear of rubbing elements. These examples illustrate the critical need for new and improved materials and design methods for better wear resistant surfaces, **Mandar Rajiv Thakare 2008**.

2. ARCHARD'S EQUATION

Archard has set his formula in 1957 and it is based on the previous work of Holm made in 1946. Archard equation is used for the analysis of wear when the deformation of the specimen is plastic. This equation gives a relation between the volume of wear, the normal load and the sliding distance. Archard's equation is defined by, **Mandar Rajiv Thakare, 2008**:

$$Q = \frac{V}{L} = \frac{KW}{H} \quad (1)$$

Where Q is the wear rate, V is the wear volume, L is the sliding distance, K is a constant known as dimensionless wear coefficient, W is the total applied normal load and H is the surface hardness. **Mandar Rajiv Thakare, 2008** mentioned that this

equation is exactly same as the Archard's equation, which was originally derived for sliding wear of metals. Tatjana Lazovic, Radivoje Mitrovic and **Mileta Ristivojevic, 2003** explained

that the surface roughness is not a factor in this measure of wear because the wear is assumed to be severe enough that surface roughness difference is insignificant.

Archard's wear equation states that the wear rate Q in any contact is directly proportional to the load applied W and inversely proportional to the

surface hardness of the wearing material H . Since the knowledge of the dimensionless wear coefficient and the hardness of the top layer of the surface may not be known with certainty, a more useful term is defined by taking the ratio K/H , which is known as the *specific wear rate* (κ , *SWR*) with the units of $\text{mm}^3\text{N}^{-1}\text{m}^{-1}$ and represents wear volume (mm^3) per unit sliding distance (m) per unit normal load (N). The modified Archard's wear equation is given by **Mandar Rajiv Thakare, 2008**:

$$\kappa = \frac{V}{WL} = \frac{K}{H} \quad (2)$$

Where V is the wear volume in mm^3 , W is the total applied load in N , L is the sliding distance in m , K is the dimensionless wear coefficient and H is the surface hardness of the material.

It has been shown experimentally that the loss of material is proportional to the sliding distance except for short tests where the non-linear running-in periods are significant. However, proportionality between wear rates and normal loads is found less often. Abrupt transitions from



low to high wear rates and sometimes back again are often found with increase in load. This is due to the transition between wear mechanisms observed with change in applied loads. Also no mention has been made of the velocity of sliding or the apparent area of contact in the equation 1, suggesting that the wear rate Q should be independent of these factors as, **Mandar Rajiv Thakare, 2008 mentioned.**

3. WEAR SIMULATION ANALYSIS

John M. Thompson and Mary Kathryn Thompson, 2006 put a proposal to calculate wear by using creep formula in ANSYS program.

This proposal shows that the starting point for any discussion of wear on the macro scale is the Archard equation, which states that:

$$\Delta V = \kappa \times S \times L \quad (3)$$

Where ΔV is the change in volume due to wear, L is the sliding distance, S is the normal contact stress and κ is the wear per unit pressure (or unit normal load, as in equation 2) per sliding distance. Archard says "[κ] may be described as the coefficient of wear and, in a series of experiments with the same combination of materials; changes in [κ] denote changes in surface conditions".

The Archard equation assumes that the wear rate is independent of apparent area of contact. However, it makes no assumptions about the surface topography (surface roughness effects are encompassed by the experimental wear coefficient) and it also makes no assumptions about variations with time. It must also be stated that although it is widely used, the Archard equation only provides for an order of magnitude estimate and is a true calculation of wear.

A method proposed for calculating wear is included into a finite element program where wear will be calculated in the solution processor instead of in the post processor.

Consider a modified form of the Archard equation:

$$\Delta V = \kappa \times S^{C_2} \times R_o^{C_3}$$

Where ΔV is the change in volume, κ , C_2 and C_3 are equation constants to account for such things

as the materials in contact, S is the stress created by the contacting pair and R_o is the number of repetitions of the load (one sliding pass, for example). If ΔV represents the change in volume of the element due to wear, then we can define wear strain as the change in volume divided by the original (initial) volume and rewrite the wear equation as:

$$e_{wr} = c_1 \times S^{C_2} \times R_o^{C_3} \quad (4)$$

Where e_{wr} is the wear strain, C_1 is equal to κ divided by the volume. This strain is similar to volumetric strain which has the form

John M. Thompson and Mary Kathryn Thompson 2006.

$$e = \Delta V / V_i = \frac{1}{3} \times (e_1 + e_2 + e_3) \quad (5)$$

Where e_1 , e_2 and e_3 are the principal strains and V_i is the initial volume (before wear). Often only one of these strains is present for wear as it is expected that wear will occur perpendicular to the surface of the component. But that is not a requirement and wear strain may be a vector quantity in a manner similar to any other type of strain. Loads that are applied oblique to the surface may generate wear that is not perpendicular to that surface and provisions should be made for including this type of wear. The principal difference between wear strain and any other strain quantity is that wear strain represents material that is removed from the system. Wear strain as proposed here is different from wear as proposed by Archard.

The Archard equation is a systems approach where the applied load is assumed to be distributed over the entire loading area. Wear would be expected to occur uniformly over the entire surface. The wear strain proposed here is a function stress and load repetitions. This implies that where load is applied to the surface, wear will occur and that parts of the surface which are currently unloaded will not experience change due to wear. This definition of wear strain also considers the local effect of stress and permits wear to be different at different locations on the surface. This does not change the fact that the approach presented here is only a systems level estimate of the wear and that

detailed calculations at specific locations on a surface should not be relied upon.

This form of the wear equation, **Eq. 4**, is similar to creep equations that have a material constant (C_1), a stress contribution (S and C_2) and a third factor, creep strain or time in the case of creep equation and repetitions in the case wear. This suggests that creep may be used to simulate wear until such time as wear is directly calculable in ANSYS. Explicit creep is used since the plan is to calculate the wear strain based upon the final configuration of the surface at the end of the load step. In ANSYS, the explicit creep calculation is performed after the elastic and plastic calculations are completed; this is the approach used for wear. The strain hardening creep equation that is programmed into ANSYS has the form:

$$de_{cr}/dt = c_1 \times stress^{c_2} \times e_{cr}^{c_3} \times \exp(-c_4/T) \quad (6)$$

Where C_1, C_2, C_3 and C_4 are constants that are supplied by the user. For each time increment, the incremental creep strain is calculated using this equation, then incremental creep strain is multiplied by the incremental time and added to the previous creep strain. A similar procedure can be used to calculate wear. The incremental wear strain can be calculated in a similar manner. For each load step, the incremental wear strain is calculated multiplied the load step time and added to the previous wear strain.

4. CALCULATION OF FRICTION FORCE

We derived a mathematical model, as explained below, to calculate the friction force from the difference in electrical power absorbed before and after the contact between the specimen and the rotating wheel (ΔP) which is taken from a three phase powermeter device.

$$\Delta P = P_2 - P_1 = \Delta t_r \times \Omega \quad (7)$$

$$\Omega = \frac{2\pi N}{60}$$

$$F_f = \frac{\Delta t_r}{R} = \frac{\Delta P / \Omega}{R} = \frac{60 \Delta P}{2\pi N R} \quad (8)$$

Where F_f is the friction force (N), Δt_r variation in torque (N.m), R radius of rotating wheel (m), ΔP variation in power absorbed (watt), Ω angular

velocity of the rotating wheel (rad/sec), N revolution per minute (rpm) for the rotating wheel, P_1 power absorbed before the contact and P_2 is the power absorbed after the contact.

5. COEFFICIENT OF FRICTION

The friction force is the resisting force tangential to the interface between two bodies when, under the action of an external force, one body moves or tends to move relative to the other and the coefficient of friction is the ratio of the force resisting tangential motion between two bodies (F_f) to the total applied normal load (W), the definition is represented by the following equation.

$$COF = \frac{F_f}{W} \quad (9)$$

Also it is an appropriate way to describe the resistance to relative motion between surfaces, but it is not a material property, nor is it a physical constant like the speed of light in a vacuum or Avogadro's number or the elementary charge on the electron as mentioned, by **Ameer Hussein Ali 2008**.

6. EXPERIMENT

6.1 Experimental Material

The samples are teeth which were taken from an insert tungsten carbide $8_{1/2}$ " tri-cone drilling bit. The specimen considered has a cone of 6.78 mm bottom radius and 3.5 mm upper radius and depth of 1mm with cylindrical base of 6.78 mm radius and 20 mm height, **Fig. 17a**. The area of contact (A) is equal to (πr_i^2) , $r_i = 3.5$ mm, and then $A = 38.48 \text{ mm}^2$. The roughness (R_a) of the contact surfaces is found to be $R_a = 5.583$ to $7.808 \text{ }\mu\text{m}$.

6.2 Materials Properties

X-ray diffraction (XRD) test shows that the material of the tooth is based upon WC-based hardmetal; by X-ray fluorescence (XRF) test, it was observed that the specimen contain Pt (11.2646%) and Ni (0.7253%). And from micro hardness test we found that the average hardness of the tooth is 1532 HV. Also it was found that

the Young's modulus (E) of tooth material can be 601 Gpa. The density of the samples' material is calculated by taking a piece of sample and weighting it, then by using a tube and filling it with water and then pull out the water to know its volume, after that we put the piece of the sample in the tube and filling it again with the water and then pull out the water to know its volume, the difference in water volume before and after putting the sample's piece in the tube represents the sample's piece volume, then by dividing sample's piece weight on its volume to get the density of the sample's material which was found to be 13.3 g/cm^3 . The average microhardness of the steel wheel is 271.15 HV.

6.3 Test Apparatus

Abrasive wear tests were performed using the steel wheel high abrasion stress with diameter of 229 mm. The test set-up of the modified ASTM-G65 test is shown in figure 1. Basically, this standard uses the rubber wheel as the counterface, K. Elalem and D.Y. Li 2001, and this case of contact known as "low abrasion stress". Some researchers used both the rubber wheel and steel wheel for their studies ,Wirojanupatump and Shipway 2000. The wheel is driven by a nominally 1.4 kW (2 hp) AC motor through a 10/1 gear box to ensure that full torque is delivered during the test. The abrasives are fed between the wheel and the sample from a hopper by a nozzle. The sample is pressed against the wheel by a loaded lever. The test is run for a set period and the wear is measured by calculating the volume of material lost through weight loss and density measurements. Silica sand of 1mm, as maximum size, is used as abrasives during these tests. The machine shall be equipped with a revolution counter that will monitor the number of wheel revolutions as specified. It is recommended that the incremental counter have the ability to shut off the machine after a preselected number of wheel revolutions.

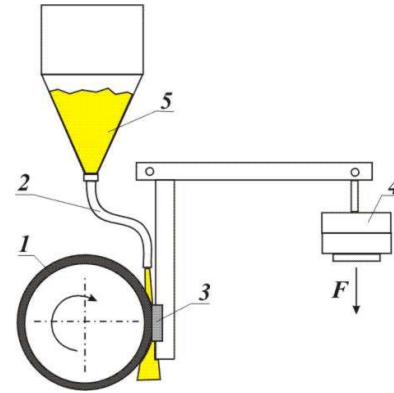


Figure 1. Schematic representation of the test apparatus.

The test apparatus mainly consists from the following parts, **Fig. 1**:

1. The wheel.
2. Sand nozzle.
3. Specimen Holder and Lever Arm
4. Applied weight.
5. Sand hopper.

6.4 Test Procedure

The test time is selected to be as 15 minute. The speeds of rotation for the wheel were selected to be 160 rpm, 220 rpm and 300 rpm. The effective applied load and contact pressure at each rotating speed are illustrated in **Table 1**. The abrasives flow rate which was used in dry tests, **Fig. 16a** was 350 g/min and of 200 g/min in wet tests, **Fig. 16b**, with water flow rate of 125 g/min. When the wheel rotation will be started, the lever arm automatically will be lowered to allow the specimen to contact the wheel. When the test has run at the desired time, the specimen automatically will be lifted away from the wheel and then we have to stop the sand/slurry flow and wheel rotation. The abrasive wear was determined from the mass loss results, which were measured with 0.001 g resolution, converted to volume loss by the following equation:

$$\text{Volume loss (mm}^3\text{)} = \frac{\text{mass loss (g)}}{\text{density (}\frac{\text{g}}{\text{cm}^3}\text{)}} \times 1000 \quad (10)$$

7. RESULTS AND DISCUSSION

7.1 Wear Performance

The effects of the effective applied load on the performance characteristics of wear rates were examined by analyzing five different weights during each rotational speed. The graphs of applied pressure versus wear volume loss are shown in **Figs. 2 and 3**. It shows at dry tests that there was a fluctuating in the volume loss as the applied load was increased, but more stability in wear volumes at wet tests. A phenomenon was observed by **A.J. Gant and M.G. Gee 2001 and X. Ma, R. Liu and D.Y. Li 2000** on the wear loss of D2 steel by ASTM-G65 device using silica sand as abrasive material. It shows that the damage to the abrasive sand particles was markedly increased at the higher sliding speed. The severe damage to the abrasive sand explains why at higher sliding speeds, the volume loss of the samples was lower than that at lower sliding speeds. This happened because the relatively brittle SiO_2 sand could not withstand increased impact at higher sliding speeds when interacted with hard but relatively tougher D2 steel. Generally, under higher loads, the damage to the sand particles considerably increased, leading to less wear of the sample. This reason explains the variations in the relation between the wear losses of the tested materials and the applied load. The damage to sand under high loads was so high that a decrease in the volume loss of the target material could occur as the applied load was increased.

The same reason above can be suggested as one reason responsible for the decreasing in volume loss as the sliding speed or the applied load was increased.

The results of COF versus load with dry and wet tests at each rotational speed are illustrated in **Figs. 4 and 5**. Generally, the COF have the highest values at 220 rpm at the dry and wet tests. Friction, through a heating effect, can affect

material properties, which in turn can influence wear behavior. In addition, friction modifies the contact stress system by introducing a shear or traction component, which can also be a factor in wear behavior. Because of these aspects, friction and wear must be generally considered as related phenomena, but not equivalent phenomena, **Raymond G. Bayer, 2004**. The general trend is that the behavior of the COFs shows a fluctuating response with respect to the applied pressure as well as to the wheel rotational speed due to the transition in wear mechanism.

Figs. 6 and 7 illustrate the temperature evaluations along with cases of contact by using laser thermometer. These temperatures represent the maximum values obtained at the end of the test time. It shows that the temperatures have the highest values at dry tests and it is proportional to the applied load and sliding speeds. Comparison between dry and wet tests, it was observed that at wet tests the temperatures have less sensitive to the applied load, which was happened due to the use of water during these tests.

Figs. 8 and 9 illustrate the SWRs behavior. At the dry tests wear coefficients or the specific wear rates (SWRs) have fluctuating values as the applied load increased and its values are decreased with an increase in the sliding speed at most loads levels. While at the wet tests the SWRs are proportional to the sliding speed and have its highest values at the minimum applied load. That is due to probability damage to the sand particles which is increasing as the applied load increased as well as increasing in the relative sliding speed. Transition in wear mechanism can produce such behavior. Comparisons between dry and wet tests we observed that the wear coefficients or SWRs are much higher at the wet than dry tests; this is due to the wear-corrosion interaction effects which can accelerate the volumes losses. Another factor can influence the volume losses during wet tests that the presence of water produces high cohesion between sand particles and high adhesion between the specimen and those particles which were accumulated above the contact surface and fall down slowly. The SWRs were calculated according to the equation ($V = k W$) at each effective applied load. Where V is the wear

volume loss per unit sliding distance (mm^3/m), k is the SWR ($\frac{\text{mm}^3}{\text{N}}$ /m) and W is the total applied normal load (N). Also it was observed that the grooves created at the worn surface of the specimen are more clearly at wet tests than dry ones, **Figs. 17b** and **17c**, that is happened due to the difference in wear mechanism between them.

7.2 Simulation Results

The ANSYS program is used to simulate the wear results by using explicit creep equation. Explicit creep equation uses the wear strain phenomenon to describe the wear rate behavior. The experimental wear strains are calculated by dividing the wear volume loss, **Eq. 10**, by V_i value supposed volume before wear. Simulation wear strain and experimental wear strain results versus applied pressures are plotted as shown in **Figs. 10 to 15**. The percentage errors (PE) have been taken between the simulation results and a linear fitting to the experimental ones. Fluctuating in wear rates at the dry tests has large effects on the PE values. Very high PE over experimental in case of dry sand-300 rpm as well as at dry sand - 200 rpm are supposed to be caused by the damage in abrasive sand particles which reduces the wear loss of the specimen. Stability of wear rates at wet tests has direct effect on the stability of PE as compared to the dry ones.

8. CONCLUSIONS

The main task of this work is to investigate the wear behavior of an insert tungsten carbide tooth material under the dry and wet sand / steel wheel abrasion conditions, and in particular, the responses of the materials to variations in the applied load and the sliding speed. It was demonstrated by the abrasion tests that the tested material showed different responses to the variations in the applied load and the sliding speed.

1. The abrasive wear rate was generally proportional to load, that is an increase in the applied load / pressure produces an increase in wear rate of the bit tooth in both dry and wet conditions.

2. The general trend for all the results of wet tests is that an increase in wheel rotational speed produces an increase in wear rate of the bit tooth. Compared in dry tests, the wear rate is decreased.

3. The abrasive wear rates were significantly altered by the presence of an aqueous carrier. High adhesion and wear-corrosion interaction produced high wear rates; it is observed that the wear coefficients (SWRs) in wet tests were approximately 10 times higher than those in the dry condition.

4. Presence of water have no effects at the COFs as compared between dry and wet tests at the rotational speeds of 160 and 220 rpm. Variations to the COFs are observed at the speed of 300 rpm, that the COFs are higher in wet than dry tests after the applied load of 64.525 N.

5. It is possible to analyze the wearing phenomenon by using ANSYS program. The percentage errors have more stability at the wet tests than dry ones due to the stability in wear rates.

9. REFERENCES

A.J. Gant and M.G. Gee ,2001, *Wear of Tungsten Carbide–Cobalt Hardmetals and Hot Isostatically Pressed High Speed Steels under Dry Abrasive Conditions*, Wear 908–915.

Ameer Hussein Ali ,2008, *Using Universal Material Tester to Study Effect of the Porosity on Wear Behavior*, Master Thesis, University of Baghdad.

G. Raymond Bayer ,2004, *Mechanical Wear Fundamentals*, Second Edition, Vestal, New York.

K. Elalem and D.Y. Li 2001, *Variations in Wear Loss with Respect to Load and Sliding Speed under Dry Sand/Rubber-Wheel Abrasion Condition: A Modeling Study* , Wear 59–65.

Mandar Rajiv Thakare, 2008, *Abrasion-Corrosion of Downhole Drill Tool Components*, Ph.D. Thesis, University of Southampton.

M. John Thompson and Mary Kathryn Thompson, 2006, *A Proposal for the Calculation of Wear*, Mechanical Engineering Dept, MIT G. Raymond

Bayer, 2004, *Mechanical Wear Fundamentals*, Second Edition, Vestal, New York.

S. Wirojanupatump and P.H. Shipway, 2000, *Abrasion of Mild Steel in Wet and Dry Conditions with the Rubber and Steel Wheel Abrasion Apparatus*, Wear 91–101.

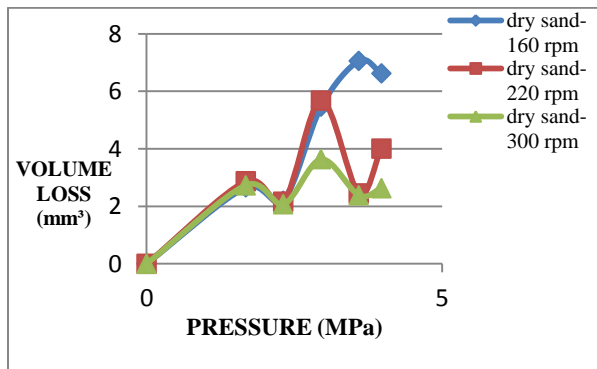


Figure 2. Overall plot of volume loss versus pressure applied in three cases of contact represent dry sand tests of 160, 220 and 300 rpm wheel rotational speeds.

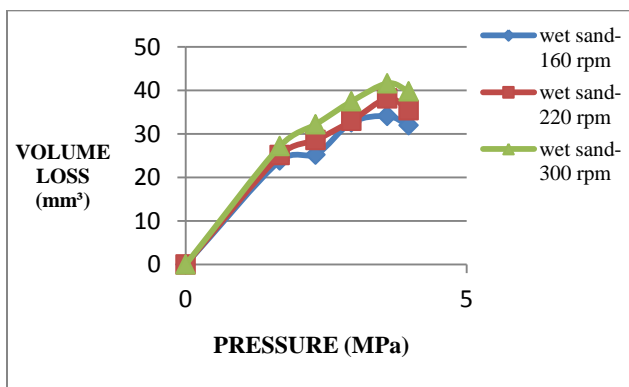


Figure 3. Overall plot of volume loss versus pressure applied in three cases of contact represent wet sand tests of 160, 220 and 300 rpm wheel rotational speeds.

Tatjana Lazovic, Radivoje Mitrovic and Mileta Ristivojevic, 2003, *Influence of Abrasive Particle Geometry and Material on the Abrasive Wear Mode*, University of Belgrade.

X. Ma, R. Liu and D.Y. Li, 2000, *Abrasive Wear Behavior of D2 Tool Steel with Respect to Load and Sliding Speed under Dry Sand/Rubber Wheel Abrasion Condition*, Wear 79–85.

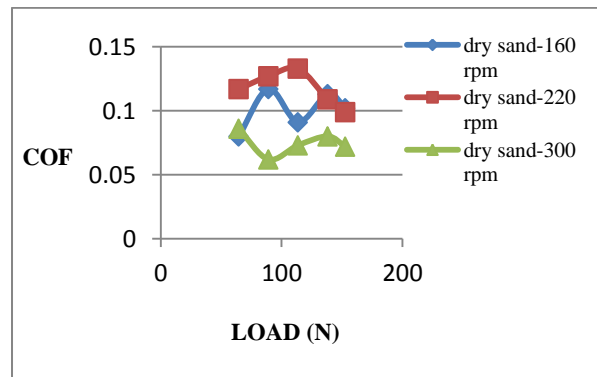


Figure 4. Overall plot of coefficient of friction versus applied load represent dry contact at 160, 220 and 300 rpm wheel rotational speeds.

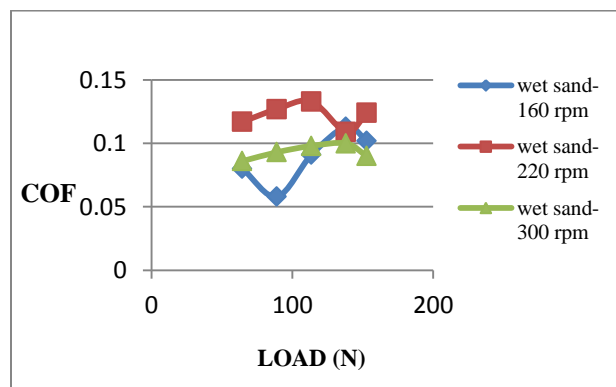


Figure 5. Overall plot of coefficient of friction versus applied load represent wet contact at 160, 220 and 300 rpm wheel rotational speeds.

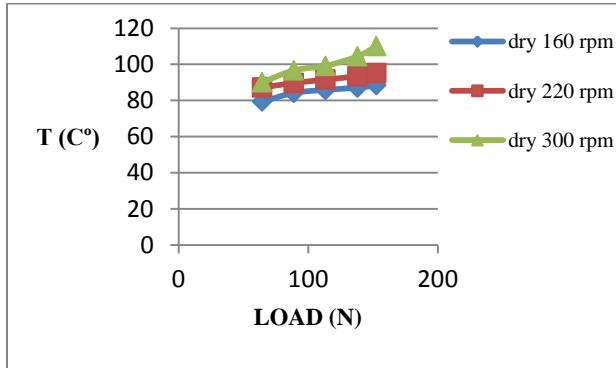


Figure 6. Comparisons of temperatures were evaluated at 160, 220 and 300 rpm wheel rotational speeds /dry condition.

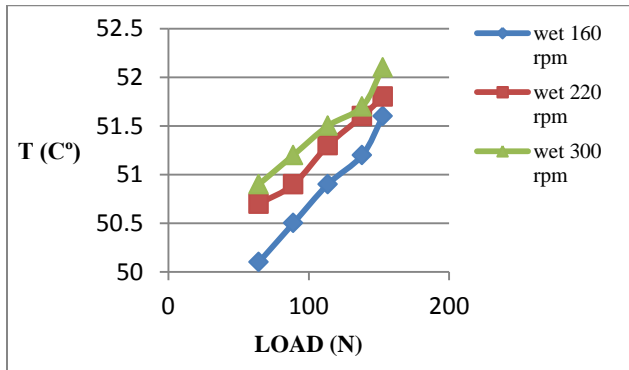


Figure 7. Comparisons of temperatures were evaluated at 160, 220 and 300 rpm wheel rotational speeds /wet condition.

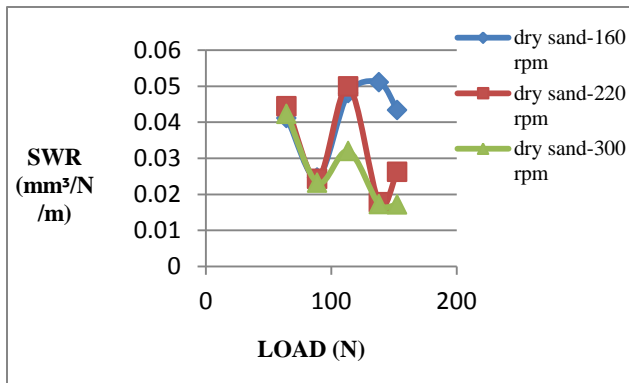


Figure 8. Comparisons of specific wear rates were evaluated at dry condition among 160, 220 and 300 rpm wheel rotational speeds.

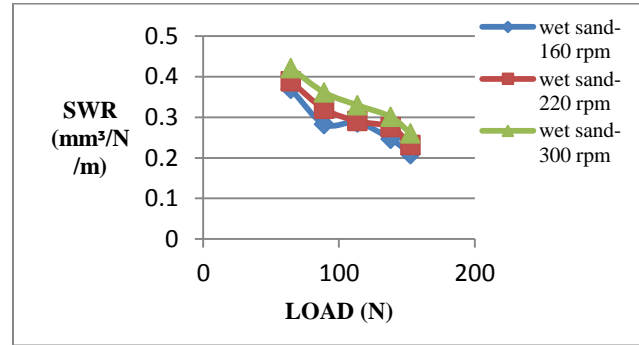


Figure 9. Comparisons of specific wear rates were evaluated at wet condition among 160, 220 and 300 rpm wheel rotational speeds.

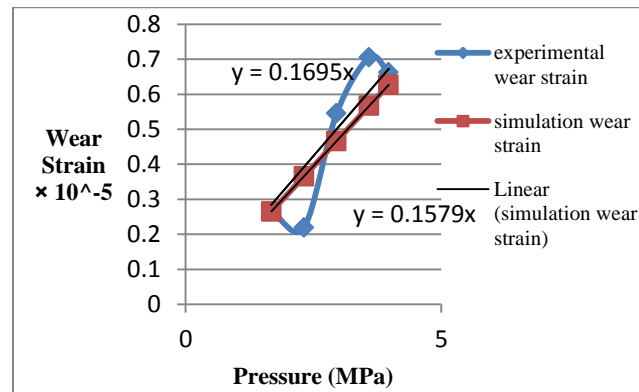


Figure 10. Plot of experimental wear strain and simulation wear strain versus applied pressure at dry sand condition and 160 rpm wheel rotational speed.

$$\text{Percentage error (PE)} = \frac{|y_{\text{experimental}} - y_{\text{simulation}}|}{y_{\text{experimental}}} \times 100\% \quad (11)$$

$$\text{PE}_{\text{dry-160 rpm}} = \frac{|0.1695 - 0.1579|}{0.1695} \times 100\% = 6.843\% \quad (\text{under experimental}).$$

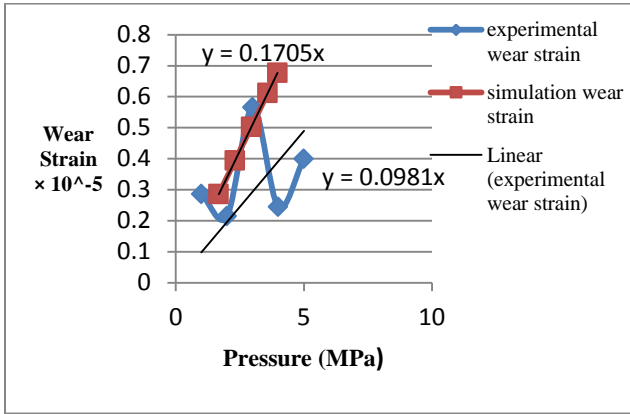


Figure 11. Plot of experimental wear strain and simulation wear strain versus applied pressure at dry sand condition and 220 rpm wheel rotational speed.

$$PE_{\text{dry-220 rpm}} = \frac{|0.0981 - 0.1705|}{0.0981} \times 100\% = 73.802\% \text{ (over experimental).}$$

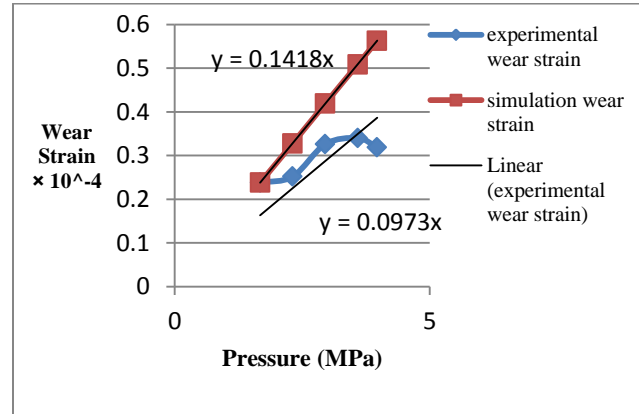


Figure 13. Plot of experimental wear strain and simulation wear strain versus applied pressure at wet sand condition and 160 rpm wheel rotational speed.

$$PE_{\text{wet-160 rpm}} = \frac{|0.0973 - 0.1418|}{0.0973} \times 100\% = 45.734\% \text{ (over experimental).}$$

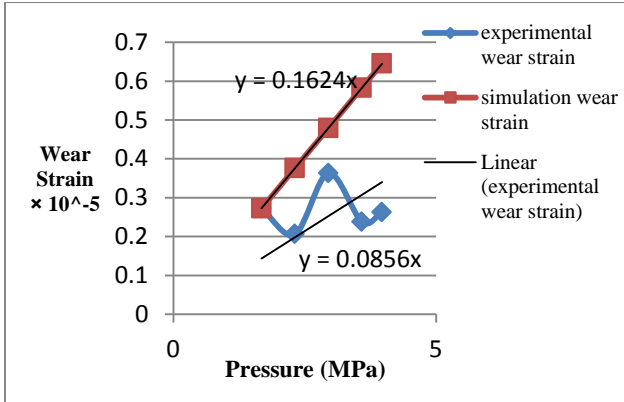


Figure 12. Plot of experimental wear strain and simulation wear strain versus applied pressure at dry sand condition and 300 rpm wheel rotational speed.

$$PE_{\text{dry-300 rpm}} = \frac{|0.0856 - 0.1624|}{0.0856} \times 100\% = 89.719\% \text{ (over experimental).}$$

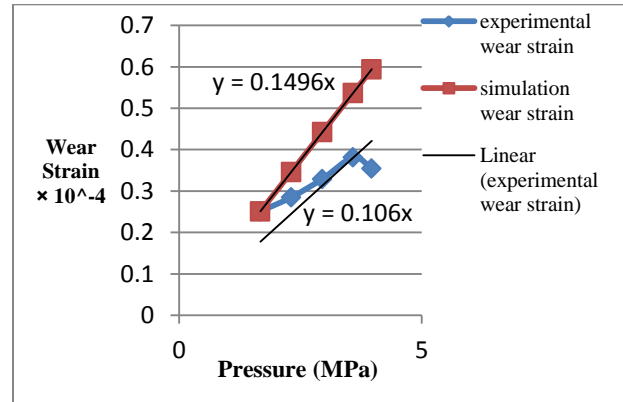


Figure 14. Plot of experimental wear strain and simulation wear strain versus applied pressure at wet sand condition and 220 rpm wheel rotational speed.

$$PE_{\text{wet-220 rpm}} = \frac{|0.106 - 0.1496|}{0.106} \times 100\% = 41.132\% \text{ (over experimental).}$$

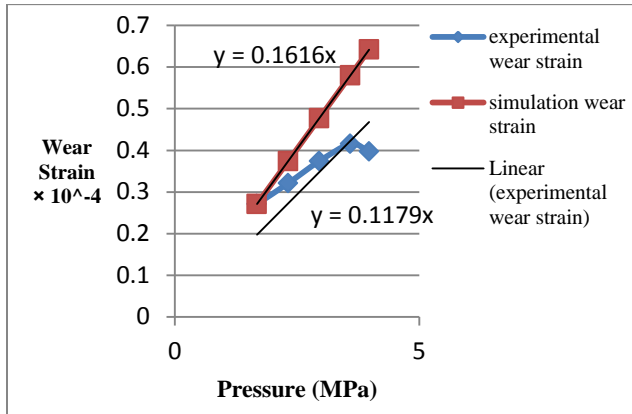


Figure 15. Plot of experimental wear strain and simulation wear strain versus applied pressure at wet sand condition and 300 rpm wheel rotational speed.

$$PE_{\text{wet-300 rpm}} = \frac{|0.1179 - 0.1616|}{0.1179} \times 100\% = 37.065\% \quad (\text{over experimental}).$$

Table 1. The effective applied loads and contact pressures with respect to rotational speeds associated at each contact condition.

Contact condition	Wheel rotational speed (rpm)	Effective applied Load (N)	Contact pressure (MPa)
Dry sand/ Wet sand	160	64.525	1.676845
	220	89.05	2.314189
	300	113.575	2.951533
		138.1	3.588877
		152.815	3.971283



(a)



(b)

Figure 16. (a) -The dry sand test and (b) –The wet sand test.



(a)

(b)

(c)

Figure 17. Contact surface; (a) - before the test, (b) - after dry test and (c) - after wet test, (b) and (c) are at load of 138.1 N and 300 rpm.

Improving Fatigue Life of Bolt Adapter of Prosthetic SACH Foot

Prof. Muhsin J. Jweeg

Applied Mechanics, Al-Nahrain
University

Asst.Prof. Kadhim K. Resan

Applied Mechanics, Head of Materials
Engineering Department, Al-Mustansiriya
University

Ali Abdulameer Najm

Applied Mechanics, Engineering College,
Al-Nahrain University
Email: aliulameer@gmail.com

ABSTRACT:

In this research an analysis for improving the fatigue behavior (safety factor of fatigue) of non-articular prosthetic foot (SACH) in the region (Bolt Adapter). The laser peening was carried to the fatigue specimens to improving the fatigue properties of bolt's material. The tests of mechanical properties and fatigue behavior were carried for material that the bolt manufacture from it, a region where the failure occur and inserted of these properties to the program of engineering analysis (Ansys) to calculate the safety factor of fatigue. The results showed that the safety factor after hardening by laser is increased by 42.8%.

Keywords: SACH, bolt, foot, prosthetic, safety factor, fatigue, adapter, laser peening.

تحسين عمر الكلال للولب القدم الصناعية نوع SACH

طالب الماجستير : علي عبد الامير نجم

جامعة النهرين /كلية الهندسة /قسم الهندسة
الميكانيكية

أ.م. كاظم كامل رسن

جامعة النهرين /كلية الهندسة /قسم الهندسة
المواد

أ. محسن جبر جويج

جامعة النهرين /كلية الهندسة /قسم الهندسة
الميكانيكية

الخلاصة:

في هذا البحث تم تحليل و تحسين سلوك الكلال (عامل الامان للكلال) للقدم الاصطناعية غير مفصلي (SACH) في منطقة الالولب. عملية التصليد بالليزر قد اجريت لعينات الكلال لتحسين خواص الكلال لمادة الالولب. اختبارات الخواص الميكانيكية و سلوك الكلال اجريت لمادة التي صنع منها الالولب، المنطقة التي يحصل بها الفشل و ادخال هذه الخواص لبرنامج التحليل الهندسي (SACH) لحساب عامل الامان للكلال. النتائج اظهرت ان عمر الكلال بعد التصليد بواسطة الليزر قد ازداد بنسبة ٤٢,٨ %.

الكلمات الرئيسية : SACH ، لولب ، قدم ، طرف صناعي، عامل الامان ، الكلال ، adapter، التصليد بالليزر.

1.INTRODUCTION

In the development of prostheses, all prosthetic assemblies and components are subjected to structural acceptance tests which include static and fatigue tests. Static tests are required to determine the structural strength of the foot to ensure performance and safety. These are carried out on a universal testing machine. While this is important, fatigue tests to reveal the fatigue strength of the components must also be performed. Fatigue tests are designed to study performance under load for the equivalent of the expected service life during normal use (TOH, et al., 1993).

Fig.1 shows a schematic diagram of the mechanism by which laser peening generates residual stress. Irradiation by a strong laser pulse, exceeding the abrasion threshold, on a material submerged in water converts the material surface to plasma and generates high pressure plasma on the surface. Under water, the inertia of the water prevents the plasma from expanding, which consequently concentrates the laser energy in small area (Sakino, 2009). The plasma absorbs subsequent laser energy and generates a heat-sustained shock wave, which impinges on the material with an intensity of several gigapascals, far exceeding the yield strength of the material (Standard Test Methods, 2003). As a result, the plasma pressure becomes 10-100 times larger than in atmosphere and reaches Gpa levels. This pressure generates a shock wave that passes in the material. The shockwave causes plastic deformation of the material, and the restraint from the surrounding non-deformed spots generates compressive residual stress on the surface. The residual stress can be generated evenly and without scattering by continuously irradiating the object by moving the laser beam (Sakino, 2009).

Laser peening changes tensile residual stress to compressive. So it seems that laser peening will be very effective in enhancing the fatigue strength, because tensile residual stress is one of the most important factors to reduce fatigue strength. Recent studies have revealed that laser peening dramatically improved the fatigue properties of austenitic stainless steel (Murdhi, 2013).

2.LASER PEENING

The laser peening test was carried out at (University of Technology) by using (Q-switched neodymium – YAG laser) that has the following parameters:

- 1- Laser wavelength is about 1.065 μm .
- 2- Pulse duration 7 Nano seconds.
- 3- Pulse energy 300 mJ .
- 4- The laser spot is typically (4-7) mm in diameter.
- 5- The deep water to the area that treated is typically (5-10) mm.

The selection 300 mJ of plus energy of laser peening because this gave best fatigue characteristic (Murdhi, 2013)

Fig. 2 shows (Q-switched neodymium –YAG laser system) used in the following work.

The specimens are coated by using the dark paint as shown in **Fig.3**.

3.GAIT ANALYSIS AND GROUND REACTION FORCES:

In order to understand the behavior of lower limb prosthetics, the act of walking must be understood. The process of walking is broken down into a series of repeated events in which a person's weight is supported by one leg while the other leg moves forward, with the weight being transferred between the two. This sequence of actions, occurring on one leg, is called the gait cycle.

The gait cycle is broken into two periods, the stance period and the swing period. The term stance refers to the “period of time that the foot is on the ground.” The term swing refers to the “time that the foot is in air for limb advancement” .The gait cycle can also be subdivided into three main tasks: weight acceptance, single limb support, and limb advancement. These main tasks are accomplished through the eight distinct phases that occur within the gait cycle.

4. FAILURE ANALYSIS

The failure is breaking the sample into two parts. The failure occurs as a result of load that be in heel and toe of foot in intermittent periods and regular during the phases of gait and that lead to alternating moment and opposite directions about the point A

.Where at heel strike phase as shown in **Fig.4** the ground reaction force applied on the heel of the foot upward vertically and the axis of the foot is italic so that the force analyze to two components, the first parallel to the axis of the screw and its operating moment in clockwise about the point A in distance L_1 and the second perpendicular to the axis of the screw and its operating share stress and its small amount so its neglected, while at toe off phase as shown in **Fig.5** which be vertical upward to the foot and analyze to two components, the first parallel to the axis of the screw and its operating moment in anticlockwise about the point A in distance L_2 and the second operating share stress and its small amount so its neglected too. From **Figs. 4 and 5** noted that the L_2 larger than L_1 so that the moment in toe off phase larger than the moment in heel strike phase.

5.MODELING THE SACH FOOT BY AUTOCAD

In order to conduct the finite element analysis, all of the components needed to be modeled. All of the components to be tested were modeled in Pro/AutoCAD 2011, as shown if **Figs. 6-9**.

6. FINITE ELEMENT ANALYSIS

ANSYS Workbench was chosen as the FEA software package because of its ability to accept a 3D computer aided design (CAD) model and assembly of high complexity. The program also allows for the accurate placement of angled pressures and loads, in addition to the modeling of contact surfaces and large deflection.

In the modeling of SACH foot, the standard tetrahedral elements were used because the elements have plasticity, hyper elasticity, stress stiffening, creep, large deflection, and large strain capabilities. The automatic size control was used to mesh the model as shown in **Fig.10**, with refined meshing at the notches of the bolt.

The total number of elements was (46889 elements) with total a number of nodes of (81263 nodes.).

Applied the same boundary conditions (constraints and loads) that taken from the GRF test. The tip of

the adapter was selected as fixed support for the four sides at all time. a vertical upward pressure of 310 Kpa was applied to the bottom surface of the heel from 0% to 21% of gait cycle and 310 was applied to the bottom surface of the toes from 69% to 100% of gait cycle as shown in **Fig. 11**.In this work SOLID 185 as in **Fig.12** is used. SOLID185 is used for 3-D modeling of solid structures.

7.EXPERIMENTAL

The fatigue performance of a material is determined by testing a number of similar test specimens at different levels of maximum stress. A fatigue-testing machine of type rotating bending was used to execute all fatigue tests. The fatigue test of material specimens was carried out at (AL-Kufa University) as shown in **Fig. 13** .The specimens were subjected to an applied load from the right side of the perpendicular to the axis of specimen, developing a bending moment. Therefore, the surface of the specimens is under tension and compression stresses when it rotates.

8. RESULTS AND DISCUSSION:

I. Chemical Analysis:

Chemical analysis of the alloy was carried out at the Specialized Institute using x-rays method by using the device shown in the **Fig. 14**. The results are listed in the **Table 1**, which are compared to the American Society for Testing and Materials specifications (ASTM) (A 479 316 stainless steel) (**American Society for Testing and Materials, 2007**).

II. Mechanical Properties:

Tensile specimens had been examined at room circumstances conditions and the specimens after test shown in the **Fig.15**.The results of the mechanical properties of bolt material are shown in **Table 2**, which are compared to the American Society for Testing and Materials specifications (ASTM)(**American Society for Testing and Materials, 2007**).

The tensile specimen's geometry and dimensions knew by using standard (A370)(**Standard Test**

Methods, 2003) which was specified for metals (Stainless steel) are shown in **Fig. 16**, and the dimensions of the specimen shown in **Fig. 17**.

III. Fatigue Results (S-N Curve)

The specimens hardened by laser peening are presented in the form of table as shown in **Table 3** while the description are in curves as shown in **Fig. 18**.

In comparison the fatigue result with reference (**Jweeg, et al., 2014**) the key benefits achieved in most application with laser peening are significant increase in fatigue life and fatigue strength. **Fig. 19** shows a comparison of fatigue properties for stainless steel specimens subjected to laser peening and dry fatigue. It is clear that, the fatigue performance of 300mJ with water is the best one compared with dry fatigue. The reason is that water generates high pressure plasma, and the strength of material surface is improved owing to the impact force by the plasma (SaKino, et al., 2009).

9. THE RESULT OF THE NUMERICAL ANALYSIS AND DISCUSSION

To increasing the life of bolt adapter in reference (**Jweeg, et al., 2014**), the Laser peening (LP) is a surface enhancement technique that has been applied to improve fatigue. Behavior The ability to use a high energy laser pulse to generate shock waves, inducing a compressive residual stress field in metallic materials (**Singh, 2009**).

The aim of this analysis is to investigate the equivalent (Von-Mises) stress and safety factor of fatigue of prosthetic SACH foot.

According to the Von-Mises theory that considers the yield stress as criteria; ($\sigma_e < \sigma_y$, safe), ($\sigma_e = \sigma_y$, critical) and ($\sigma_e > \sigma_y$, failed).

Where, (σ_e) is the equivalent stress, and (σ_y) is the yield stress.

The safety factor for fatigue will be safe in design if the safety factor about or more than (1.25) (Miller, 2002).

Figure (20) shows the equivalent stress-safety factor for the prosthetic SACH foot. From noted that the safety factor of fatigue after laser peening increased

by 42.8% as shown in **Fig. 21** and this increment due to formed layer of compressive residual stress which inhibits both crack initiation and propagation this lead to life longer of bolt and more safety factor.

10. CONCLUSIONS:

- 1-An improvement in fatigue life by 42.8% due to laser peening.
- 2-The fatigue limit of bolt material was improved by 19.7% at 10^7 cycles under the laser treatment.
- 3-The results showed that good agreement was found when comparing the experimental and numerical data.
- 4-The minimum equivalent stress-safety factor is located in bolt at interface region between adapter and foot at notch because the cross section is minimum at notch.

11. REFERENCES

- S. L. TOH, J. C. H. GOH, P. H. TAN and T. E. TAY, 1993, *Fatigue Testing of Energy Storing Prosthetic Feet*.
- Yoshihiro Sakino, 2009, *Effect Of Laser Peening Pn Improving Fatigue Strength of Welded Rib of High-Strength Steel*.
- Standard Test Methods for Tension Testing of Metallic Materials*, 2003, (Metric), ASTM A370.
- Samer S.Murdhi, 2013 *Fatigue Behavior under Shot Peening and Laser Peening Stainless Steel Turbine Shaft*, thesis in Materials Engineering Department, AL-Mustansiriyah University, Iraq.
- American Society for Testing and Materials, 2007, specifications (ASTM) Volume 01.03 steel, wire, stainless steel bar "Specification for Stainless Steel Bars and Shapes, Data Modified.
- Muhsin J. Jweeg, Kadhim K. Resan and Ali Abdulameer Najm, 2013, *Study and Analysis of Failure Mechanism of Bolt Adapter in Prosthetic SACH Foot*, submitted to Eng. & Tech. Journal, under publication.
- Y.SaKino, K.Yoshikawa, Y.sano and Y-c kim, 2009, *Effect of Laser Peening on Residual Stress and Fatigue Life of Welded Joints of High Strength Steel*.

Gulshan Singh, ,2009. *Effective Simulation and Optimization of a Laser Peening Process.*

Brett A. Miller, 2002, *Failure Analysis and Prevention, Fatigue Failures, ASM International Handbook.* Vol. 11.

Sakino Yoshihiro,Sano Yuji and Kim You-Chul, 2007.*Residual Stress of Steels for Structure and Fillet Weld Zone after Laser Peening*

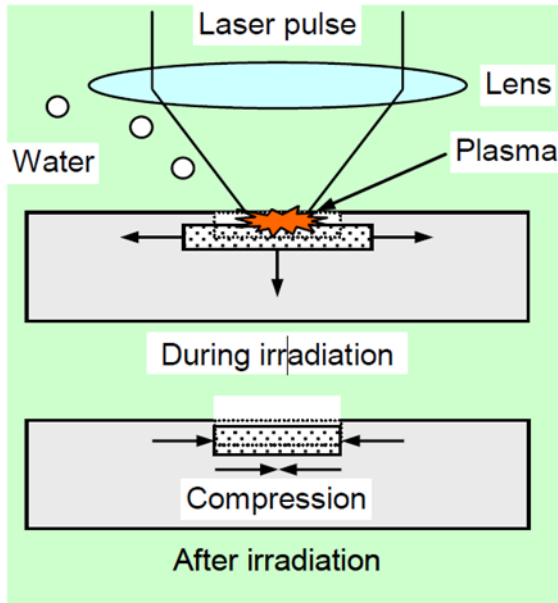


Figure 1. Basic process of laser peening (Yoshihiro, et al., 2007).

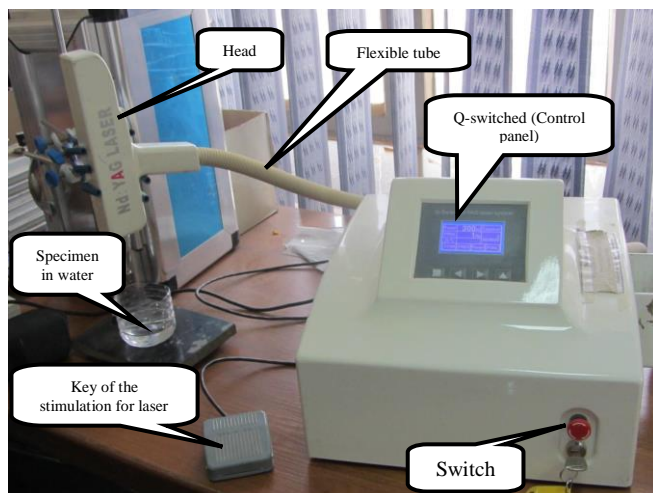


Figure 2. Details of laser peening test rig in University of Technology (Laser and Electoptical Engineering Department) (Murdhi, 2013).



Figure 3. The fatigue specimens test after coating.

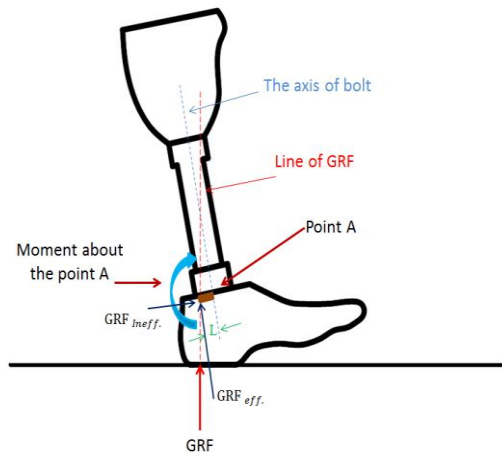


Figure 4. GRF at heel strike phase.

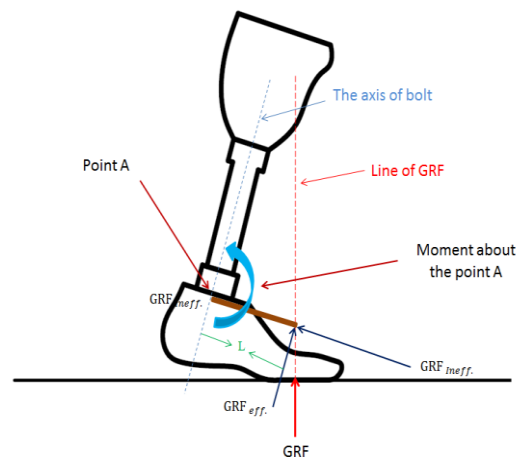


Figure 5. GRF at toe off phase.



Figure 6 . Final solid model of KEEL OF SACH foot.

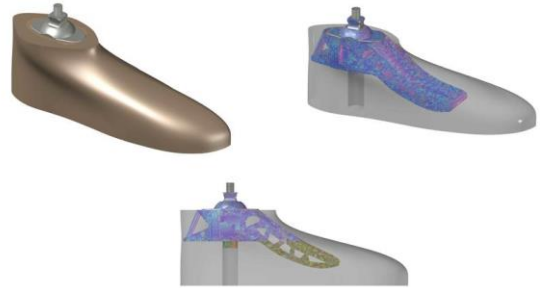


Figure 9. Multiple views of final model of SACH foot and bolt adapter.



Figure 7. Simplified SACH foot.

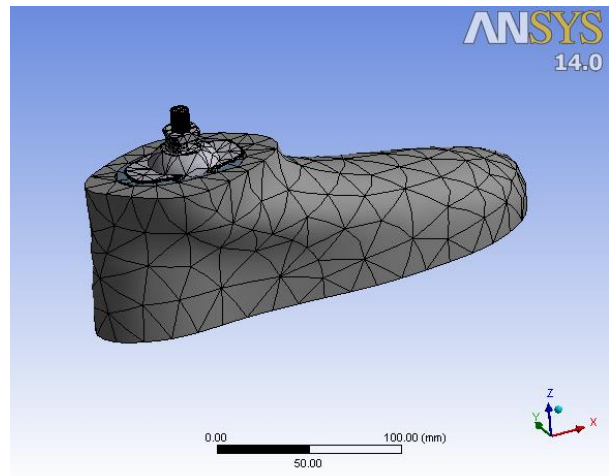


Figure 10. Meshed SACH foot models.

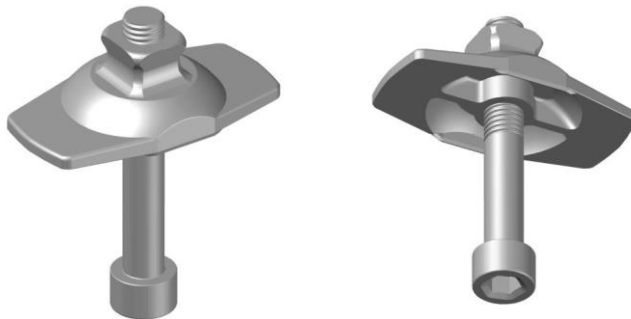


Figure 8. Final bolt adapter model.

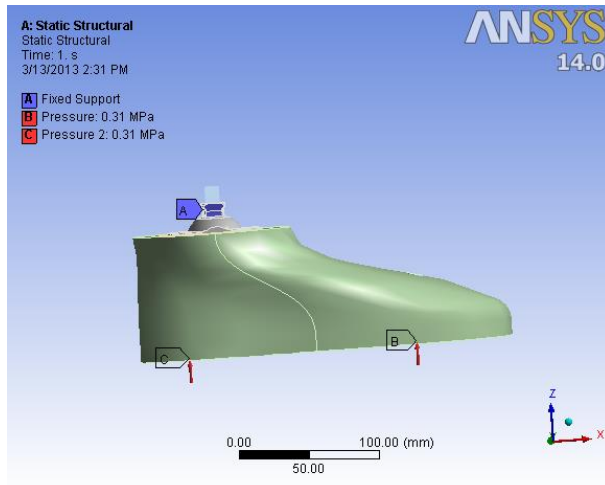


Figure 11. FEA model constraints and loads.



Figure 13. Fatigue Testing Machine.

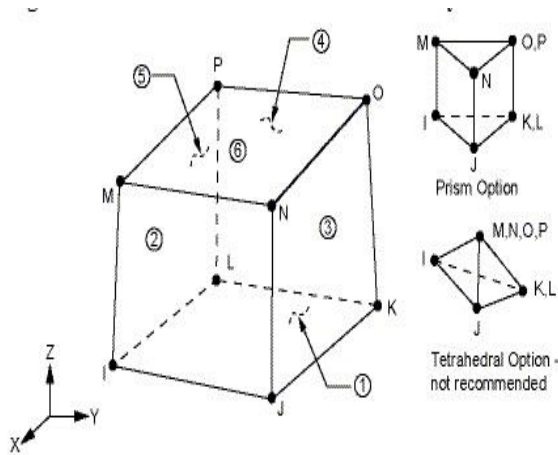


Figure 12. Solid 185.

Table 1. Chemical composition wt%

Material	C	Si	Mn	Cr	N i	Other elements
bolt (experimental)	0.00 89	0.8 67	0.4 75	13. 48	3. 6	----
Key to steel (standard) American Society for Testing and Materials, 2007)	0.00 8	1	2	16	1 0	----



Figure 14. X-ray fluorescent (XRF).

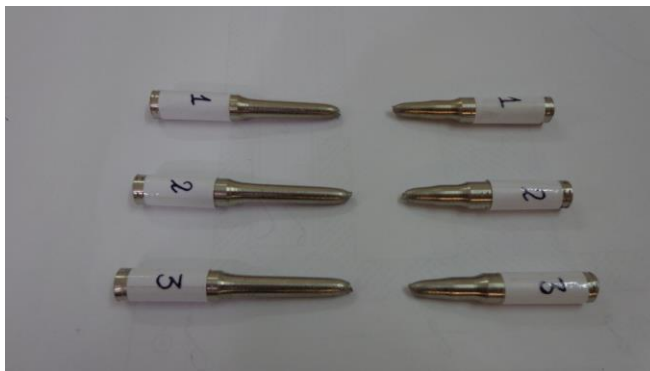


Figure 15. Tensile test specimens after test.

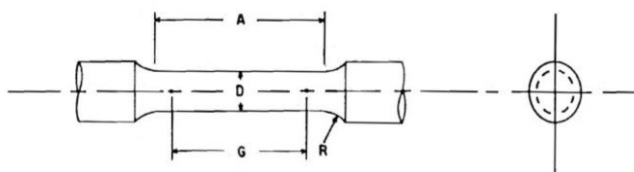


Figure 16. Circular cross section tensile test specimen according to ASTM (A370) (Standard Test Methods, 2003).

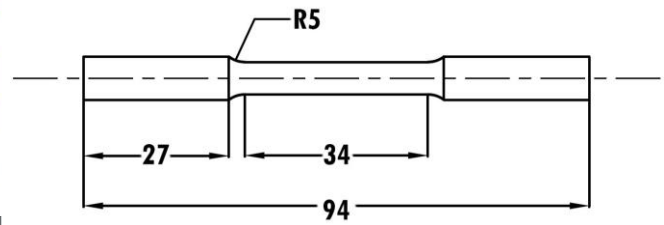


Figure 17. Tensile test specimen (all dimensions in millimeters).

Table 2. The mechanical properties of material bolt (stainless steel).

Material	Young's Modulus (GPa)	Yield Stress (MPa)	Ultimate Stress (MPa)
Experimental	185	483	570
Standard (American Society for Testing and Materials, 2007)	195	450	585

Table 3. S-N fatigue tests.

Test	σ_f (MPa)	No. of cycles (cycle)
1	400	1000000*
2	420	6511000
3	460	4254000
4	480	1948000
5	500	1229000
6	520	320000
7	540	102000
8	560	4000

* didn't failed specimen

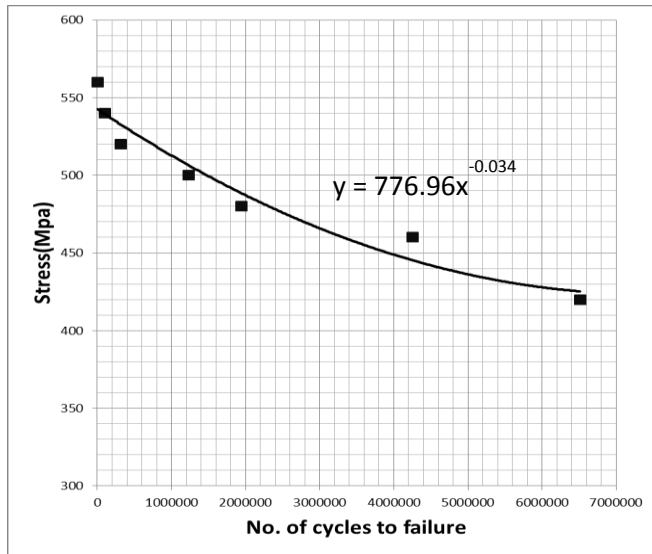


Figure 18. S-N fatigue tests curve.

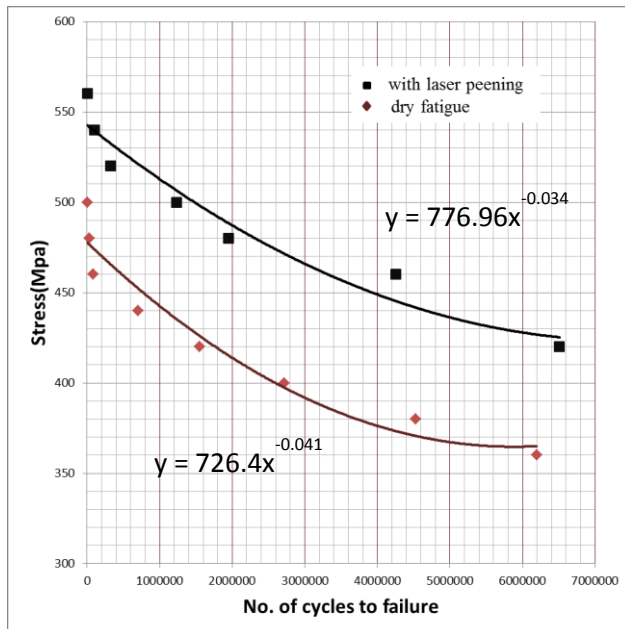


Figure 19. Comparison between the fatigue behavior with laser peening and without laser peening.

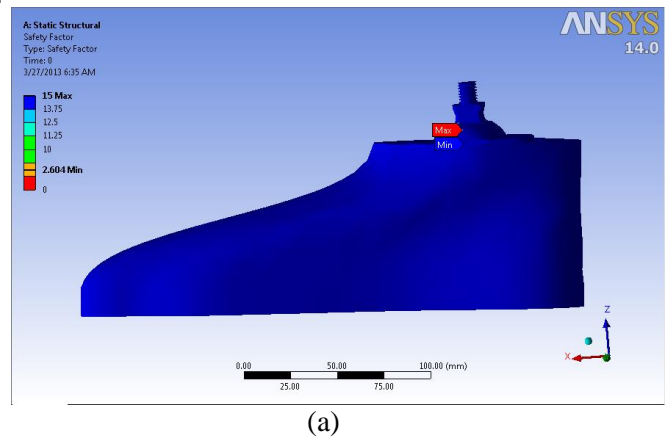
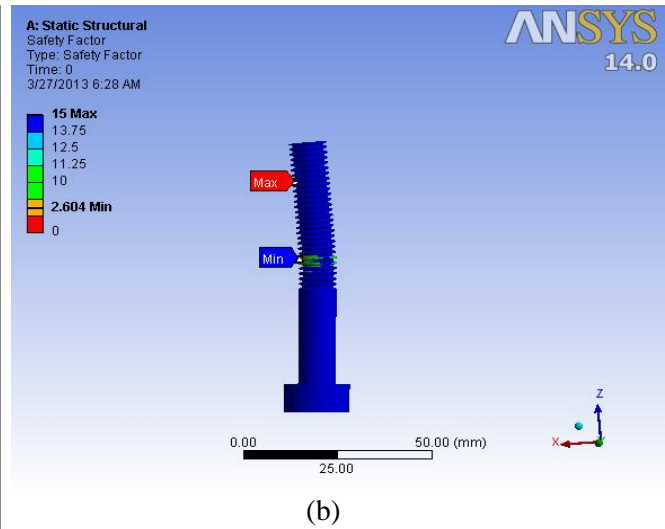


Figure 20. The equivalent stress-safety factor for fatigue of the prosthetic SACH foot.

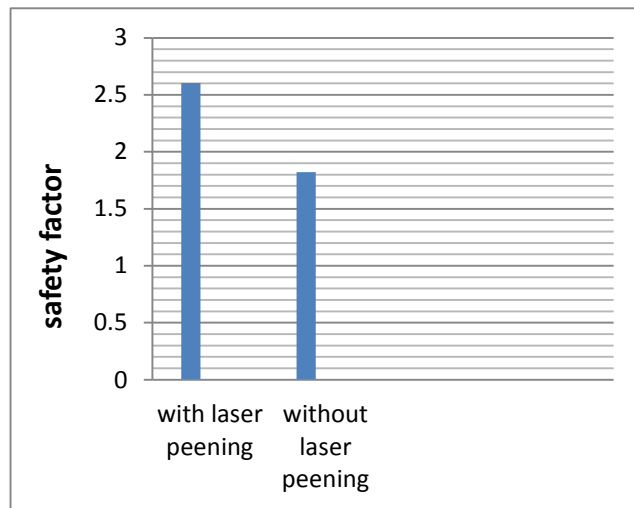


Figure 21. Comparison between the fatigue improvement factor for fatigue with laser peening and without laser peening.

Numerical Simulation of 3D- Flow Structure and Heat Transfer for Longitudinal Riblet Upstream of Leading Edge Endwall Junction of Nozzle Guide Vane

Prof.Dr.Najdat Nashat. Abdulla
College of Engineering
E-mail najdat_abdulla@yahoo.co.uk

Asst.Prof.Dr.Ikhlas Mohammed Fayed
University of Technology
E-mail ikhlase 60 @ yahoo. com

Asst.Lecturer Kareem Khalf Ali
Technical Instituted-Baquba
E-GEml Kareemkhalf72@Google .com

ABSTRACT

The simulation have been made for 3D flow structure and heat transfer with and without longitudinal riblet upstream of leading edge vane endwall junction of first stage nozzle guide vane .The research explores concept of weakening the secondary flows and reducing their harmful effects.Numerical investigation involved examination of the secondary flows ,velocity and heat transfer rates by solving the governing equations (continuity , Navier -stokes and energy equations) using the known package FLUENT version (12.1).The governing equations were solved for three dimentional, turbulent flowe, incompressible with an appropriate turbulent model ($k-\omega, SST$) .The numerical solution was carried out for 25 models of V-groove riblet with wide ranges of height (h) and space (s). The results indicated that, the riblet endwall junction was a powerful tool for controlling the flow structure , reducing secondary flow formation,and elimination the effect of heat transfer at leading edge and passage . The drag reduction produced by riblet was proportional with their height and space. V-groove riblet with dimension of (h=1.35mm and s=2.26mm) was found to be the most effective in reduction of drag (2.7%) and heat transfer (21%) so it was selected as an optimum dimension of riblet model. The results also showed that the drag reduction produced by riblet was proportional to their size. The riblet model had a great effect in elimination spanwise ,pitchwise velocities ,but strength the streamwise velocity .At leading edge ,the effect of secondary flow was extended up to 23% from span height and 35% upstream leading edge .The riblet model caused an increase in momentom at a region very close to leading edge and to move stagnation point very close to the leading edge.

المحاكاة العددية لتكوين جريان وانتقال الحرارة ثلاثي البعد وباستخدام حزم طولية في مقدمة اتصال الحافة الامامية لريش التوربين الثابتة

م.م كريم خلف علي

أ.م.د أخلص محمد فياض

أ.د نجدة نشأت عبد الله

الخلاصة :

تم اجراء التحليل العددي لجريان ثلاثي الابعاد وانتقال الحرارة ولحالي وجود وعدم وجود الحزم الطولية في مقدمة الحافة الامامية للريش الموجه الثابتة والمرحلة الاولى .البحث الحالي إستكشف طريقة لإضعاف الجريان الثانوي ويُخَفِّضُ تأثيراتهم الضارة . تضمن التحليل العددي اختبار الجريان الثانوي والسرعة ومعدل انتقال الحرارة من خلال حل المعادلات الحاكمة (الاستمرارية ونافيرستوك والطاقة) باستخدام البرنامج الجاهز (FLUENT) اصدار (١٢,١) . تم حل المعادلات الحاكمة بثلاث ابعاد ولجريان مضطرب ولاانضغاطي وباستخدام نموذج اضطراب ($k-\omega, SST$) . شمل الحل العددي ٢٥

نموذج للحزوز ولمدى واسع للارتفاع (h) والخطوة (s). النتائج المستحصلة تشير ان الحزوز في منطقة الاتصال تعمل كاداة فعالة للسيطرة على الجريان والتقليل من الجريان الثانوي والحد من تأثير درجة الحرارة عند الحافة الامامية للريشة وكذلك الممر. ان انخفاض الكبح المتحقق بوسطة الحزوز يتناسب مع الارتفاع والخطوة للحزوز. ان النموذج ذو البعد (h=1.35mm) و (s=2.26mm) كان الاكثر تأثيرا في خفض الكبح بمقدار (٢,٧%) والحرارة (٢١%) لذلك تم اختياره كافضل نموذج للحزوز. تشير النتائج ايضا الى ان الحزوز الطولية فعالة جدا في تقليل مركبات السرعة العرضية باتجاه الارتفاع والخطوة ولكن تزيد من مركبة السرعة المحورية. عند الحافة الامامية كان تأثير الجريان الثانوي يمتد الى (٢٣H%) وكذلك (٣٥C_{ax}%) قبل الحافة الامامية للريش. والحزوز ايضا تزيد الزخم في المنطقة القريبة جدا من الحافة الامامية وتحرك موضع نقطة الركود الى نقطة اقرب الى الحافة الامامية.

1.INTRODUCTION

The flow at endwall junction is very complex and it is well known that three - dimensional secondary flows in endwall junction of inlet guide vane can dramatically affect the performance of gas turbine. Consequently, there is a strong need for computation model/tools that would allow an accurate prediction of the secondary flow effect on both the pressure losses and heat transfer. Recent advances in flow control have the potential for significant impact on the design and performance of modern gas turbine engines, weakening secondary flow, delaying separation, reducing drag and creating virtual shape with modifying.

The present work focus on riblet of longitudinal groove with streamwise direction locates before the leading edge of airfoil as shown in **Fig. 1**. There are two types of flow control technique, active and passive. Active flow control method requires an energy input such as suction or blowing to delay transition and modify the fluid viscosity with polymers and film cooling. While the passive control method not require energy and it is a low cost method such as a longitudinal riblet ,leading edge fillet and three dimension contour endwall junction.

A number of researches had investigated endwall modification in the past .As a tool of reducing secondary flows and losses, many techniques have been approved numerically to pursue drag reduction. To create a method of horseshoe vortex reduction elimination, first it is necessary to understand the reason for the formation of the vortex. **Sieverding , 1985**, gave a comprehensive review of the secondary flow structure which produce losses in several ways : first of these flows is the extraction of energy

from the main flow and create aerodynamic losses. Second, their rotation can bring the hotter gas from the main passage to the endwall creating high heat transfer regions. **Medic and Durbin, 2002**, improved turbulent model (k- ω ,k- ϵ ,V²-f) that can be used in any particular application. This analysis is dealing with transonic compressible flow through a gas turbine blade cascade. The results showed that a good predictions for the case of using k- ϵ model. In all models, the turbulent intensity T_u was high at the stagnation point and in the near wake region. **Galzada and Alonso,2003**, Investigated the mechanism of the flow and heat transfer in separated flows particularly in separation and reattachment points .Also, they studied the influence of inlet flow angle, Reynolds number, Mach number on the heat transfer mechanism. The result showed that both the local Stanton number and the local heat transfer coefficients drop approaching the separation point and rose rapidly up to the region where flow reattaches. **Saha and Acharya,2008**, Investigated the modification design of endwall for reduction of heat transfer and total pressure losses .Various non-axisymmetric endwalls were studied using three-dimensional numerical simulations .The results showed that the total pressure loss was also low and the average heat transfer reduced by about 8% compared to the flat endwall. Local reduction in heat transfer was significant. **Sonoda et al, 2009**, Investigated the effect of three types endwall contouring: 1 only hub contour 2 only tip contour 3 hub and tip contours on the aerodynamic performance for the low -aspect ratio transonic turbine inlet guide vane IGV. Also they investigated the secondary flow mechanisms to show whether there were difference between the secondary flow models. The result showed that all types of endwall contouring reduce the mass averaged

overall loss by 4% for type 1, 5% for type 2 and 10% for type 3 as compared to the base line. Also, the flow mechanism in the small size full annular ultralow-AR transonic turbine IGV was different from the secondary flow model obtained from the low speed linear cascade.

There were some researches available on modification of endwall junction flow by passive modification to control flow by using fillet upstream leading edge and three-dimension 3D endwall contour. But a few researches were found on modification of the junction flow using riblet upstream leading edge. Based on the past studies, there is a clear need to investigate further the secondary flow losses and heat transfer characteristic of the endwall junction of a modern day stator vane.

The present work aims to explore concept of weakening the secondary flows and reducing their harmful effects by using a numerical technique to predicate the optimum dimensions of riblet by testing different riblet geometries. A theoretical formulation is used to examine secondary flow and drag reduction with longitudinal riblet upstream leading edge vane, by using the known package FLUENT version 12.1. Continuity and Navier-Stokes equations are solved in turbulent regime with an appropriate turbulent model SST, $k-\omega$ in three-dimension. Numerical solution will be carried out for 25 riblet models type V-groove with various riblet heights, spaces and geometries on junction flow.

2. COMPUTATIONAL ASPECTS

An accurate simulation of flow over riblet required that each riblet cross-section be represented by at least several grid points in addition to accurately simulate analysis. The turbulent flow passage width and length should be greater than the size of characteristic turbulent flow structure such as boundary layer streaks and quasi-stream wise vortices. All these parameters are taken into the consideration in simulation process. The model facility is shown in **Fig. 2** and consists of one passage between two adjacent vanes. The model consists of inlet section, vane endwall junction hub, outer endwall junction casing and outlet section. The inlet section is located at one chord length upstream of airfoil leading edge, while the outlet

section at one chord length downstream trailing edge.

2.1 Vane Airfoil and Riblet Geometry

The airfoil profile of guide vane of gas power plant Unit PG9171E is found by using **Gambit** program, as shown in **Fig. 3**, with the dimensions as given in **Table 1**. The riblets types V-riblet with different dimensions are used in the present work and found by using **Gambit** program as given in **Table 2**.

2.2 Mesh Topology

For unstructured mesh, FLUENT uses unstructured solver with internal data structures to assign an order to the cells, faces, and grid points in a mesh and to maintain contact between adjacent cells. This gives the flexibility to use the best grid topology for complex geometry. The solver does not force an overall structure or topology on the mesh (i.e., it does not require i, j, k indexing to locate neighboring cells). FLUENT code uses different element types for mesh topology. The type of element specifies the number of mesh nodes and the node pattern associated with element shapes.

The model will be meshed by using tetrahedral element as shown in **Fig. 4**. Although many mesh generation codes, Fluent & Ansys, support mesh generation of solid geometry and three-dimensional models from a single phase with minimum input the user **Fig. 5**, but it is more durable to divide this process into subsequent steps including two major issues for further controlling of the mesh, and are as follows:-

(I) Surface mesh generation:

Surface mesh is created for the vane-endwall junction geometry including the riblet, airfoil, and other boundaries as follows:

- Edges are meshed by assigning an interval size for each boundary comprising a closed loop of area.
- Edges meshes are controlled by specifying a grading scheme for each individual edge.
- Once all edges are meshed, a triangular element is used to generate a three-dimensional unstructured surface mesh.

(II) Volume meshes generation:

As far as all surfaces for each individual area have been meshed, volume mesh can be created for each zone comprising a closed loop

of area using T-Grid, **Gambit** scheme .Building the mesh required fine cells in area near the riblet , vane and endwall junction surface ,so that it is convenient for turbulent flow characterized with wake and separation .Therefore ,the mesh should be manipulated and controlled manually to keep smooth mesh transition and maintain accurate mesh for a three-dimensional model with a minimum computational expense .This was achieved by applying the size function.

Size functions are used to control the size of mesh intervals for edge and mesh elements for faces or volumes and thus to keep smooth transition of mesh from fine mesh near the nozzle vane-endwall junction surface to coarse mesh far away at the undisturbed boundaries .

2.3 Computational Method

In order to examine secondary flow and drag reduction, continuity and Navier-Stokes equations will be solved by using the known package FLUENT version 12.1. Continuity and Navier –Stokes equations are solved in turbulent regime with an appropriate turbulent model SST, k- ω in three-dimension .Numerical solution will be carried out for 25 riblet models type V-riblet with taking into account the effect of riblet height ,space and geometry on junction flow.

A-Flow Field Characteristics:

The most important aerodynamic characteristics in this study are drag, local skin and static pressure coefficients, turbulent intensity and secondary flow.

•Drag coefficients are calculated as follows:

$$C_d = \frac{F}{1/2 \rho U_\infty^2} \quad (1)$$

Where F is the resultant force and divided into two components,

1-Pressure force acts on airfoil and riblet.

2-Viscous force acts on airfoil, riblet, bottom endwall junction hub and outer endwall junction casing.

•Local skin –friction coefficient (C_f). **Calzada and Alonso, 2003.**

$$C_f = \frac{\tau_w}{1/2 \rho U_\infty^2} \quad (2)$$

•Static pressure coefficient (C_p). **Barringer and Thole, 2009.**

$$C_p = \frac{(p_{stat} - p_{stat,ref})}{1/2 \rho U_\infty^2} \quad (3)$$

•Turbulent intensity

$$T_u = \frac{u_{rms}}{U} \quad (4)$$

•Secondary flow formation

The average secondary kinetic energy of the secondary flow is defined as: **Aunapu et al, 2000.**

$$SKE = \sqrt{v^2 + w^2} \quad (5)$$

B- Heat Transfer Characteristics:

The most important heat transfer characteristics in this research are the Stanton number and Nusselt number.

•Stanton number is calculated as follows.

Levchenya, 2007.

$$St = \frac{h_c}{\rho C_p U_\infty} = \frac{q_w}{\rho_{ref} U_\infty C_p (T_w - T_\infty)} \quad (6)$$

•Nusselt number (N_u) is given by: **Barringer and Thole, 2009.**

$$N_u = \frac{h_{local} \times C_{ax}}{k_f} \quad (7)$$

3. RESULTS AND DISCUSSION

3.1 Selection the Best Model of Riblet

The effect of riblet ratio h/s on drag reduction behavior for V-groove riblet models

are presented in **Figs. 6 up to 10**, taking into account the effect of riblet spacing and height as in **Table 2**. Peak angles for riblet model are selected based on data given by, **Stalio and Nobile, 2003**.

Generally, as shown in figures that the riblet at upstream leading junction has an effective upon drag reduction. Drag reduction occurs for all V-riblet models. The trend of increase in total drag can be attributed to an increase of effectiveness of riblet in adverse pressure gradient. Maximum drag reduction occurs at riblet model with peak angle of 80° and ratio of $h/s=0.595$ for all ranges of h 1-2mm. The models number Mo.2, Mo.7, Mo.12, Mo.17 and Mo.22, have the most effect in reduction of drag and heat transfer upon the others as shown in **Table 3**. One can find that, all these models have an effect on heat transfer reduction. Behavior of drag and heat transfer reduction are shown in **Fig.11** and indicates that, Mo.12 and Mo.17 are the most effective on drag and heat transfer reductions.

The selection of optimum dimensions are based on a maximum drag reduction and acceptable heat transfer reduction, therefore Mo.12 is considered to be the best model. It is manufactured to present the structure of flow field. The drag results indicate that there are an average skin-friction reduction for V-groove riblet model which has a specified dimensions of space s and height h .

3.2 Structure of Flow Field

3.2.1 Structure of flow field at leading edge endwall junction

The velocity vectors, streamline pattern, velocity gradient and secondary flow contour and vector in the same flow domain of interest are presented in **Figs. 12,13,14,15** and **16**. The velocity vectors in **Fig. 12** are parallel to each other in the region far away from the base wall indicating a uniform incoming flow. As the endwall boundary layer approaches vane, the flow stagnates as shown in **Fig.13**. The fluid velocity increases with distance from endwall, this creates a static pressure gradient along the span. In other word, a pressure difference exists in the spanwise direction and a minimum static pressure exists at the endwall. The streamline

patterns and velocity gradient at the leading edge as shown in **Figs.14** and **15** illustrate how the free stream and near wall fluid migrates toward the endwall junction as a result of the relatively low static pressure which exists at junction. In addition, the streamlines close to the endwall demonstrate that the incident flow, first turns towards the wall then reverses and moves upstream. This explains the origin of the circulation associated with the horseshoe vortex system. The relationship between the axial velocity and secondary flow can be characterized by pumping action of the mean horseshoe vortex structure at work. The mechanism which brings the high momentum fluid into the junction and ejects low momentum from the near wall region can be shown in **Fig.16** at a region approximately 32% H of the span height and 35% C_{ax} upstream of the leading edge near van-wall interaction. The flow is directed outward from the vane with negative flow angle, then changes direction of the secondary flow with positive flow towards the vane to base which resulted in clockwise vortex. The secondary flow structure near the base wall, tends to be flattened into an elliptical shape and the contribution of velocity V_y at pitchwise in secondary velocity is larger than the velocity V_z at spanwise resulting clockwise motion. In that region, the horseshoe vortex wraps around the leading edge and splits into two legs, first leg of horseshoe vortex moves toward the pressure side of the vane and second moves toward the suction side of the vane and is called the suction side leg.

– Effect of riblet on the secondary flow structure

The effect of riblet on leading edge are shown in **Figs. 17,18,19** and **20**. The position of saddle point moves toward the leading edge as shown in **Fig. 18** and separation line pattern is different. Since the region between the saddle point and the leading edge where the flow separates to yield horseshoe vortex is short for the riblet wall, this implies that the size and extent of the leading edge horseshoe vortices are small for riblet case. The orientation of the streamlines for the riblet changes in flow direction and this is not the case for the smooth surface. Thus yaw angle of the flow near the wall will be reduced as shown in **Fig.19** which

in turns will reduce the development of the passage vortex. Also, the riblet reduces the size of secondary flow vortex and with a velocity gradient at endwall as shown in **Fig. 20**.

3.2.2 Pressure distribution at endwall

Static pressure coefficient distributions at endwall (hub) around the vane surface from the leading edge to the trailing edge are presented in **Figs. 21 and 22** with and without riblet surface modification of leading edge. Near the endwall, the flow is complex, being affected by the interaction of plate and vane boundary layers and by the horseshoes vortex.

As shown in figures, the minimum pressure occurs on the suction side due to the high fluid acceleration on this side. While the maximum pressure occurs on the pressure side due to the low fluid velocity on this side. Therefore, there is a pressure gradient from pressure side towards the suction side, which result in cross flow from pressure side to suction side of passage and this cross flow increases the formulation of secondary flow. The negative values of pressure coefficient extends to the suction side reaches to the lower with a value of -5.5 in the throttle region at $X/C_{ax}=88\%$ till trailing edge. The positive values of pressure coefficient extends near the pressure side then changes its sign to a negative. Also, there is a reduction in the wake region reaches up to the value of -4.5. The higher negative value of pressure coefficient in the center of passage vortex results in a peak turbulent kinetic energy.

In the passage, there is a minimum static pressure location a long suction surface of the vane and an attenuated suction side leg of the horseshoe vortex still exists. A high magnitude value of the loss coefficient in the suction side and trailing region of vane reaches up to a wake region. It can be observed that a strong adverse pressure gradient upstream at vane leading edge causes flow separation in this region.

- Effect of riblet on pressure coefficient, C_p distribution at endwall junction

From **Fig.22** it can be seen that, the pressure coefficients with the riblet are greater in magnitude than the corresponding points without riblet. There are an increase in pressure

coefficient in the region very close to leading edge endwall junction. It seems that, when the riblets are placed in the location of the separation point on the endwall surface, there is an increase in momentum in this region. The stagnation streamlines move to location closer to leading edge resulting in an increase in momentum in the corner, also, with riblet less pressure losses occurs across the passage. Reduction in pressure gradient from pressure side to suction side leads to reduction in cross flow, where a maximum reduction occurs in throttle region.

3.3 Structure of Heat Transfer.

3.3.1 Heat transfer distribution at leading edge

The leading edge of vane experiences very high load, there are some regions with a higher heat transfer than others. **Fig. 23** illustrates the distribution of Stanton number at the leading edge junction flat plate endwall junction. Stanton numbers begins to increase dramatically at a location upstream of the leading edge vane approximately 15% of the chord $X/C_{ax} = -0.15$. It is related to the position where the flow separates from the endwall, which occurs at approximately $X/C_{ax} = -0.12$, the heat transfer continues to increase till the flow approaches the vane. The leading edge and endwall platforms of the vanes are areas with highest thermal loads for two reasons; firstly, the vertical flows increase the transport of relatively hot flow from the mid-span towards the endwall juncture. Second, because the platform is affected by secondary flows, it experiences an increase in heat transfer coefficients, **Radomsky and Thole, 2000**. Stanton number levels decrease as the thermal boundary layer thickens and then increases as the stagnation region is approached. The high heat transfer rates in this region are consistent with the horseshoe vortex, where formulation of vortex system in this region increases with mixed process. The trend of the results was in consistent with measurement of **Radomsky and Thole, 2000**.

One can notice that, the high heat transfer regions at leading edge with the stagnation region near leading edge of the vane, the highest

Stanton number values occur nearest to the vane surface. This peak value occurs because the secondary flows bring the high speed mainstream fluid down towards the endwall, thereby thinning the boundary layer.

—Riblet effects on the heat transfer structure

Fig. 24 shows the main effect of riblet sheet at upstream vane on distribution of heat transfer. The figure shows that the location of very hot spots is shifted away from leading edge to another location in the passage that lead to weaken the heat load on the front of leading edge. The riblet controls the flow direction through reducing the turning angle of hot stream toward the endwall. Reduction in heat transfer rate in the leading edge and endwall is obtained by using of riblet surface.

3.3.2 Endwall junction heat transfer distribution

-Stanton number, (St) distribution at endwall

The heat transfer coefficients given in **Fig. 25** represents in terms of a non-dimensional Stanton number $st \times 1000$. In the region upstream of the vanes, a high heat transfer region is occurred between the stagnation point and the reattachment point of the flow on the suction side of the airfoil where the Stanton number is reached to the value of 4.5. This is the area which experiences a very high acceleration. But the local Stanton number drops approaching the separation point, as the flow moves through the passage. It is apparent that the location of the peak Stanton numbers peak heat transfer is being swept from the outer pressure surface towards the suction side of the central vane causes high heat transfer along the suction side of vane. The favorable static pressure gradient, which moves away from the stagnation region and the pressure surface, tends to drive the separation line for the inlet boundary layer toward the suction surface.

This lowest heat transfer region is contained with the convergence of the separation streamline from suction surface leg of the horseshoe vortex and the separation streamline due to the roll up of the pressure

surface leg of the horseshoe vortex by the passage vortex.

Downstream from the trailing edge of the vanes, the influence of the wake is appeared on the endwall heat transfer with lower value on the pressure surface than the trailing suction surface.

- Riblet effect on Stanton number, (St) distribution

Fig. 26 illustrates the effect of riblet on distribution of Stanton number on endwall junction. With riblet surface, the distribution of Stanton number changes upstream of leading edge where the riblet surface has low heat transfer rate which leads to decrease heat transfer in region very close to leading edge endwall junction. The riblet shifts the location of high heat transfer to points furthest from junction. High heat transfer rates are still presented in the stagnation region and downstream from the trailing edge of the vane but the effect of the separation streamline is not apparent.

4. CONCLUSIONS

1-The effect of secondary flow on endwall junction flow extends up to 23% H from span height and 35 % C_{ax} upstream leading edge.

2-The drag reduction produced by riblet is proportional to their sizes. These sizes represent height h , space s and riblet cross-section area.

3- The maximum drag reduction obtained is 2.7% for the V-groove riblet type which has a height $h=1.35$ mm, space $s=2.26$ mm and peak angle of 80° . The other sizes have lower drag reduction.

4-The effect of riblet causes a reduction of secondary flow formation in the region very near to the endwall junction as well as a reduction in the average of secondary flow formation near pressure side.

5-Significant effects of riblet endwall on pressure distribution in hub from leading edge to trailing edge are observed. The riblet reduces cross-flow from pressure side to suction side and leads to weaken of secondary flow formation.

6-With riblet there is an increase in momentum in the region very close to leading edge endwall junction in turn leads to move stagnation point to location close to leading edge.

7- A maximum reduction in average heat transfer near the leading edge-endwall juncture is obtained. The riblets shift the location of high heat transfer to upstream furthest from junction .While; a little reduction is obtained in the downstream portion of the passage.

8-The amount of heat transfer reduction in the leading edge is due to reduction in secondary flow formulation at leading edge junction.

9-The riblet surface controls the flow direction in the boundary layer and reduces the thickness of boundary layer by increasing the momentum in streamwise direction.

5- Nomenclatures

C_{ax} axil chord (mm)
 h locale heat transfer coefficient .
 I current (A).
 K_s surface thermal conductivity .
 $k-\omega$ turbulent model.
LDV laser Doppler velocimeter.
 R reynolds number.
SST shear stress transport.
 T_∞ locale free stream temperature (K).
 T_w locale wall temperature (K).
 u axil velocity component in X-direction (m/s).
 U_∞ free stream velocity (m/s).
 V voltage (V).
 ρ density (kg/m^3).
IGV Inlet guide vane.
 C_d drag coefficient .
 C_f skin- friction coefficient
 τ_w wall shear stress.
 C_p static pressure coefficient .
 T_u turbulent intensity (%)
 q_w wall heat flux.

6- REFERENCES

Calzada P.D.L, and Alonso A, 2003, *Numerical Investigation of Heat Transfer in Turbine Cascades with Separated flows* ASME, Journal of Turbo- Machinery , Vol.125, April.

Medic G.,and Durbin P.A, 2002, *Toward Improved Prediction of Heat Transfer on Turbine Blades*. ASME, Journal of Turbo- Machinery ,Vol. 124,PP 187, April.

Program, 2009, *Ansys CFX,Version 12* Ansys Inc.,.

Program ,2009, *Tecplot 360,version 12.0.0.3116"*, Tecplot Inc.

Radomsky R.M.and Thole K.A, 2000, *Flow Field Measurements for a Highly Turbulent Flow in a Stator Vane Passage*. ASME, Journal of Turbomachinery, Vol.122, April.

Radomsky R.M.and Thole K.A,2000, *High Free-Stream Turbulence Effects on Endwall Heat Transfer for a Gas Turbine Stator Vane*. ASME, Journal of Turbo-Machinery, Vol.122,October ,2000.

Saha A.K and Acharya S2008, *Computation of Turbulent Flow and Heat Transfer through a Three-Dimensional Nonaxisymmetric Blade Passage*. ASME, Journal of Turbo- Machinery, Vol. 130/031008-1, July..

Sonoda T.,Hasenjäger M.,Arima T.and Sendhoff B, 2009, *Effect of Endwall Contouring on Performance of Ultra-low Aspect Ratio Transonic Turbine Inlet Guide Vanes* ASME, Journal of Turbo Machinery, Vol. 131, January.

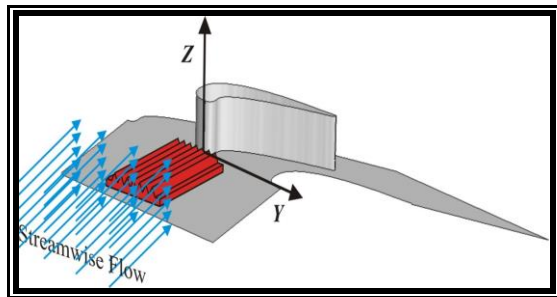


Figure 1.Position of leading edge riblet.

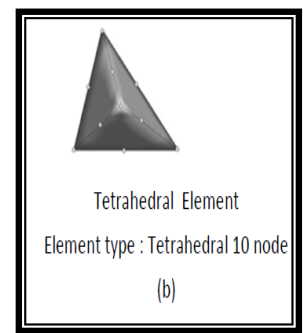
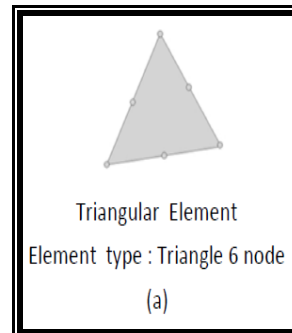


Figure 4. (a)Triangular elements type, (b) Tetrahedral elements type.

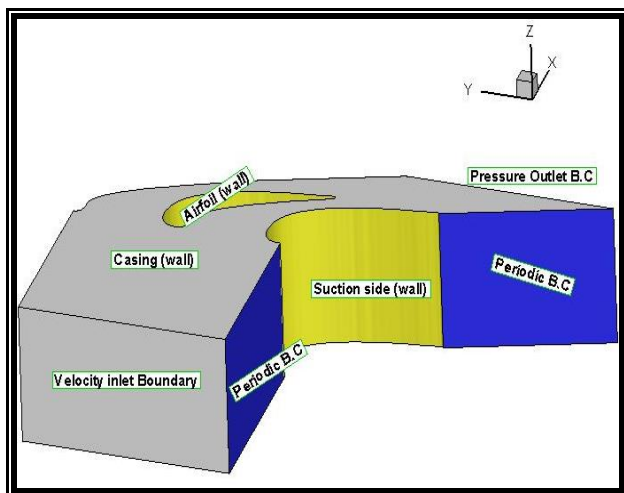


Figure 2. Facility of model with one passage on inlet guide vane.

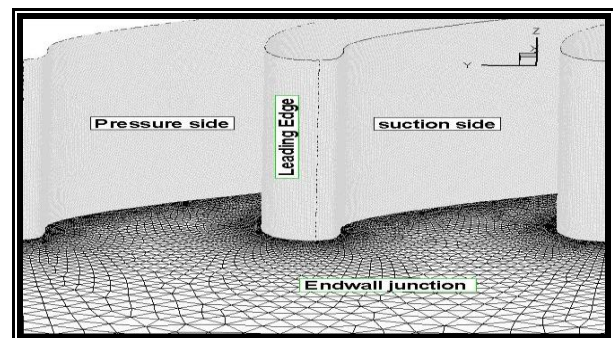


Figure 5. Fine mesh near the nozzle vane-endwall junction surface.

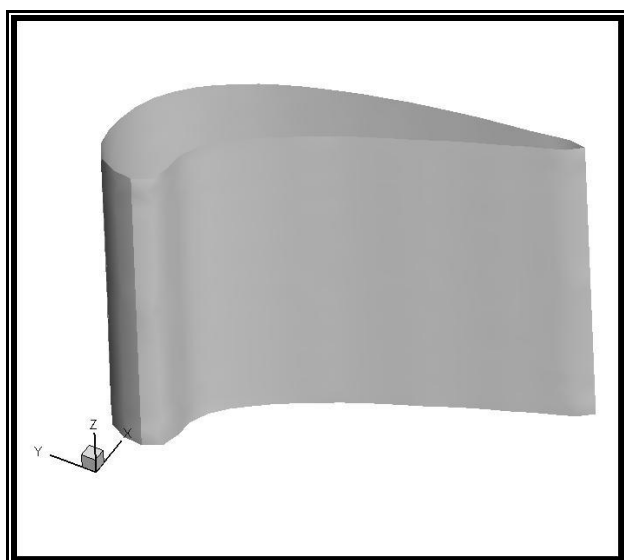
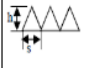


Figure 3.Vane airfoil profile by use of Gambit program.

Table1.Dimensions of guide vane of gas power plant (unit PG9171E).

1	Span or vane height (H)	210 mm
2	Pitch or vane spacing (S)	175 mm
3	Chord length (C)	280 mm
4	Axial chord length (C_{ax})	145.12 mm
5	Inlet flow angle (β_1)	0° degree
6	Outlet flow angle (β_2)	72.8° degree
7	Stagger angle (λ)	56.4° degree
8	Inlet velocity (U_{ref})	19 m/s
9	Inlet turbulent Intensity (T_u)	3.0 %
10	Chord Reynolds number (Re)	3.38853×10^5
11	Length of suction side (Lss)	334 mm
12	Length of pressure side (Lps)	275 mm

Table ٢. Riblet models dimensions.

Riblet configuration	Model No.	Height (h)mm	Peak angle (θ)degree	Space (s)mm	Ratio h/s
 Space (s) Height (h)	Mo.1	2.00	90	4.00	0.500
	Mo.2	2.00	80	3.35	0.595
	Mo.3	2.00	70	2.80	0.714
	Mo.4	2.00	60	2.30	0.869
	Mo.5	2.00	53	2.00	1.000
	Mo.6	1.68	90	3.36	0.500
	Mo.7	1.68	80	2.82	0.595
	Mo.8	1.68	70	2.35	0.714
	Mo.9	1.68	60	1.94	0.869
	Mo.10	1.68	53	1.67	1.000
	Mo.11	1.35	90	2.70	0.500
	Mo.12	1.35	80	2.26	0.597
	Mo.13	1.35	70	1.89	0.714
	Mo.14	1.35	60	1.55	0.871
	Mo.15	1.35	53	1.35	1.000
	Mo.16	1.23	90	2.45	0.500
	Mo.17	1.23	80	2.10	0.595
	Mo.18	1.23	70	1.72	0.714
	Mo.19	1.23	60	1.42	0.860
	Mo.20	1.23	53	1.22	1.000
	Mo.21	1.00	90	2.00	0.500
	Mo.22	1.00	80	1.67	0.595
	Mo.23	1.00	70	1.40	0.714
	Mo.24	1.00	60	1.15	0.860
	Mo.25	1.00	53	1.00	1.000

Numerical Simulation of 3D- Flow Structure and Heat Transfer for Longitudinal Riblet Upstream of Leading Edge Endwall Junction of Nozzle Guide Vane

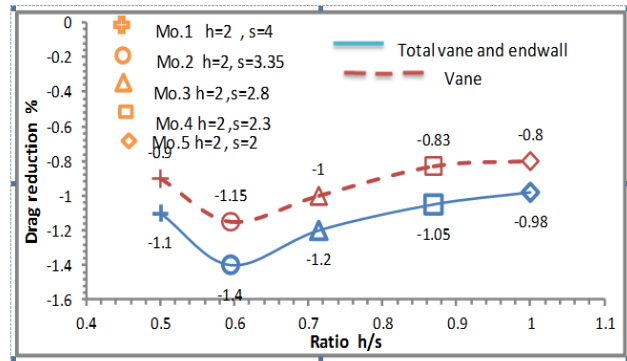


Figure 6. Drag reduction for different ratio h/s at (h=2mm).

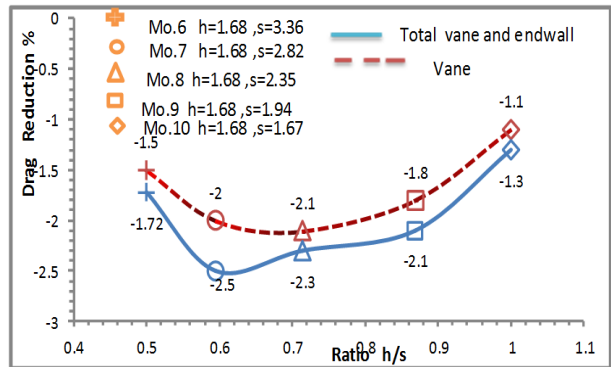


Figure 7. Drag reduction for different ratio (h/s) at (h=1.68mm).

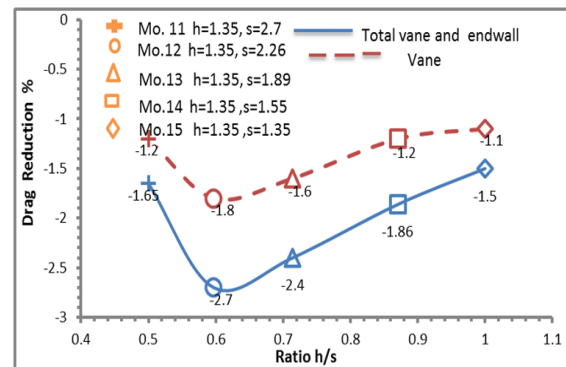


Figure 8. Drag reduction for different ratio (h/s) at (h=1.35mm).

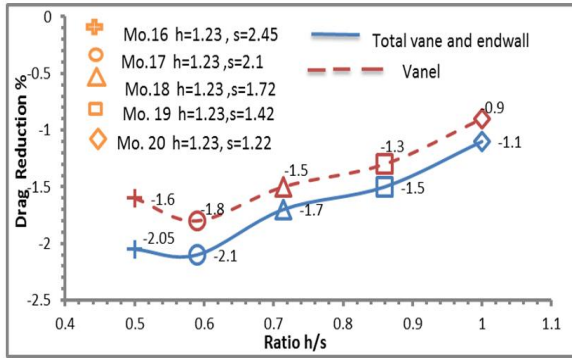


Figure 9. Drag reduction for different ratio (h/s) at (h=1.23mm).

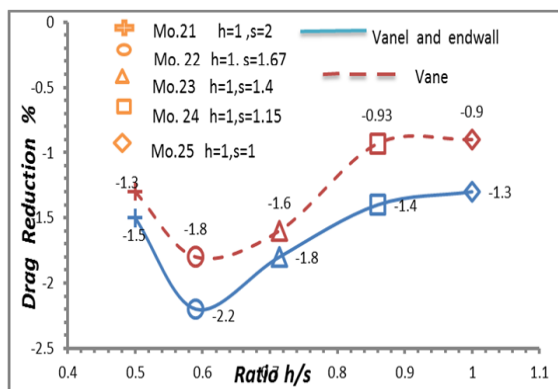


Figure 10. Drag reduction for different ratio (h/s) at (h=1mm).

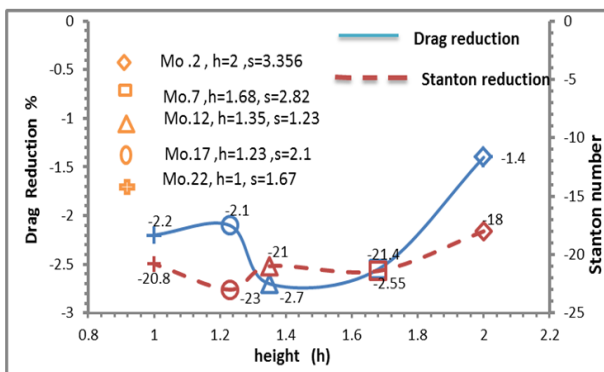


Figure 11. Drag and heat transfer reduction of riblet surface.

Table 3. Maximum effect of riblet on drag and heat transfer at peak angle(80°).

Model No.	Height (h mm)	Space (s mm)	Ratio h/s	Airfoil drag reduction %	Total drag reduction (DR) %	Total Stanton number reduction (st ×1000) %
Mo.2	2.00	3.35	0.595	-1.15	-1.40	-18.0
Mo.7	1.68	2.82	0.595	-2.00	-2.55	-21.4
Mo.12	1.35	2.26	0.595	-2.15	-2.70	-21.0
Mo.17	1.23	2.10	0.595	-1.70	-2.10	-23.0
Mo.22	1.00	1.67	0.595	-1.73	-2.20	-20.8

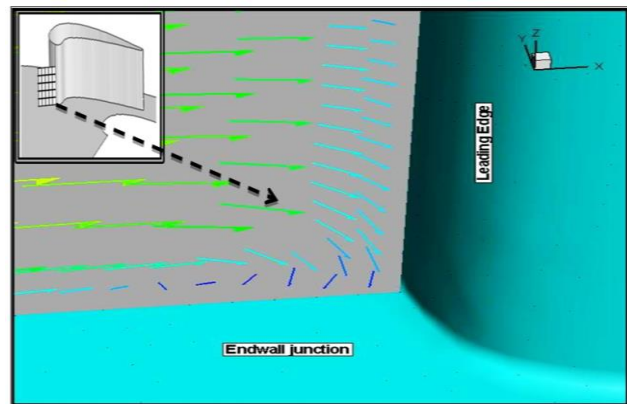


Figure 12. Velocity vector at the leading edge endwall junction without riblet.

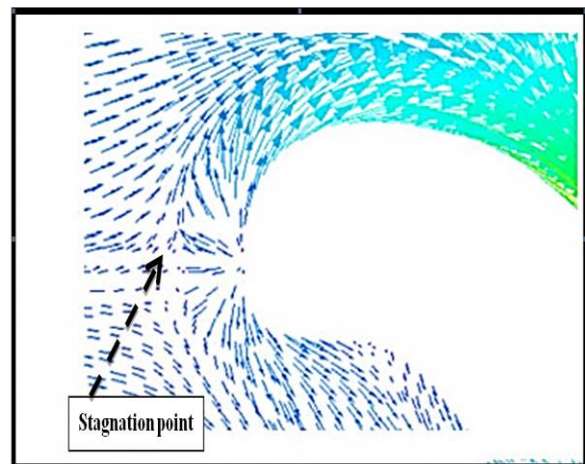


Figure 13. Velocity vector at the leading edge.

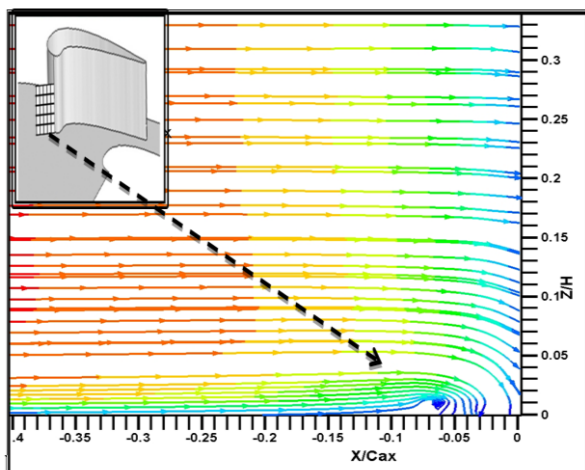


Figure 14.Streamline show horseshoe vortex at the leading edge junction without riblet.

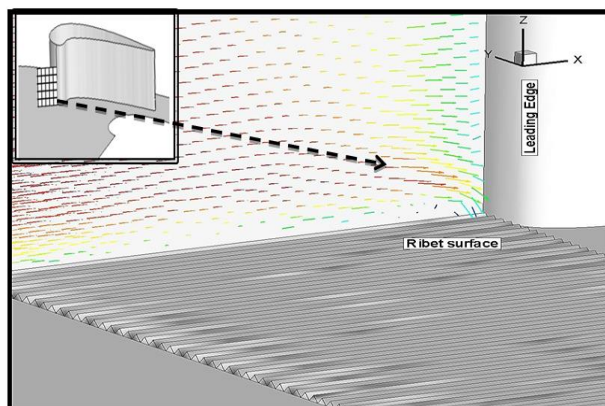


Figure 17.Velocity vector at the leading edge endwall junction with riblet.

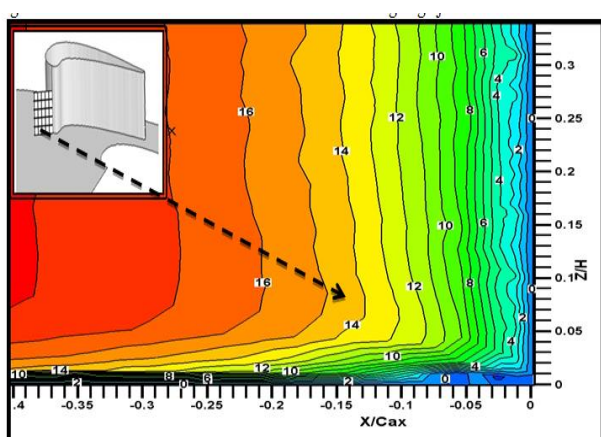


Figure 15.Velocity contour at the leading edge junction without riblet.

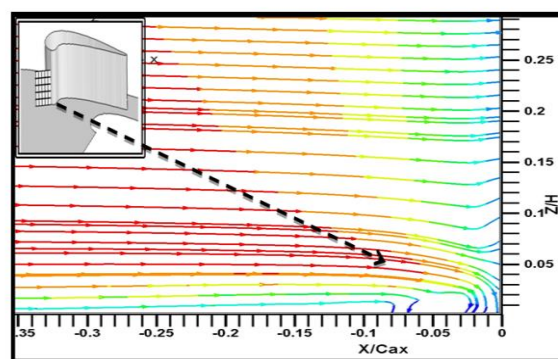


Figure 18. Horseshoe vortex at the leading edge junction with riblet.

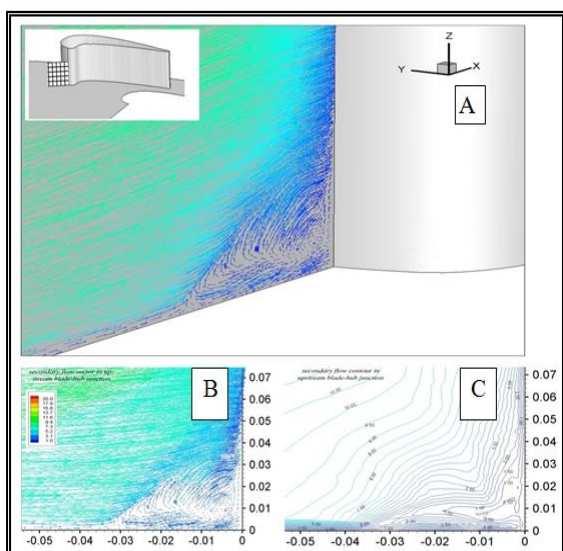


Figure 16. Secondary flow vector and contour in upstream vane-hub junction.

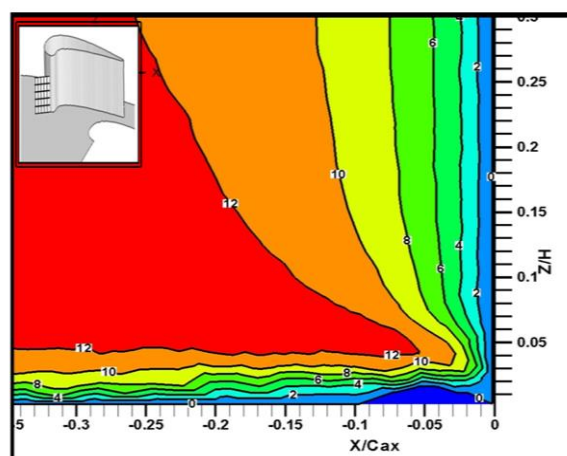


Figure 19.Velocity contour at the leading edge with riblet.

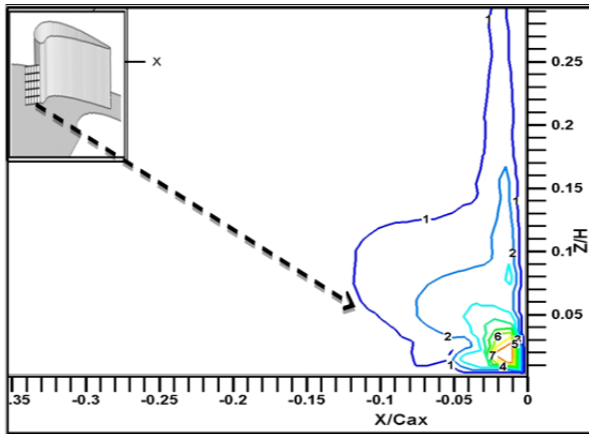


Figure 20. Scondary flow vector and contour in upstream vane endwall junction.

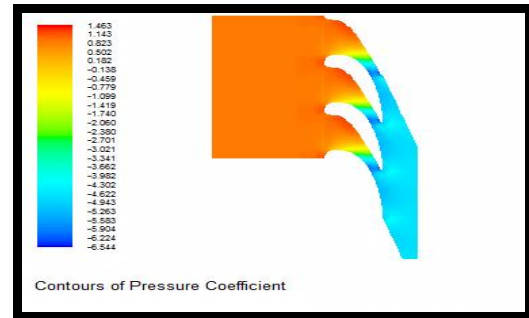


Figure 22. Contour of static pressure coefficient distribution on the endwall junction for gas turbine nozzle guide vane with riblet upstream leading edge. A-Filled contour, B-Line contour.

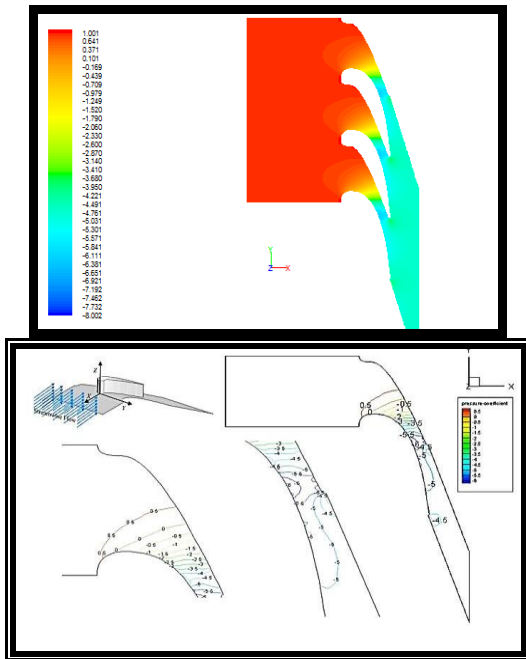
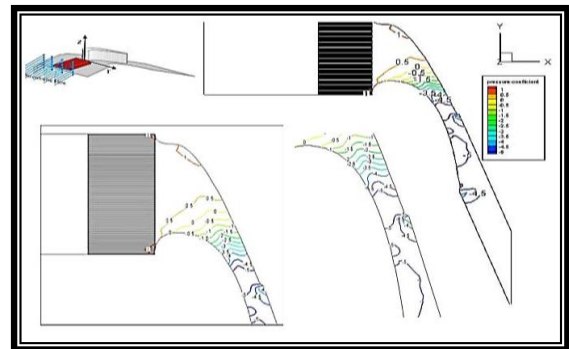


Figure 21.Contour of static pressure coefficient distribution on the endwall junction for gas turbine nozzle guide vane without riblet. A- Filled contour, B-Line contour.



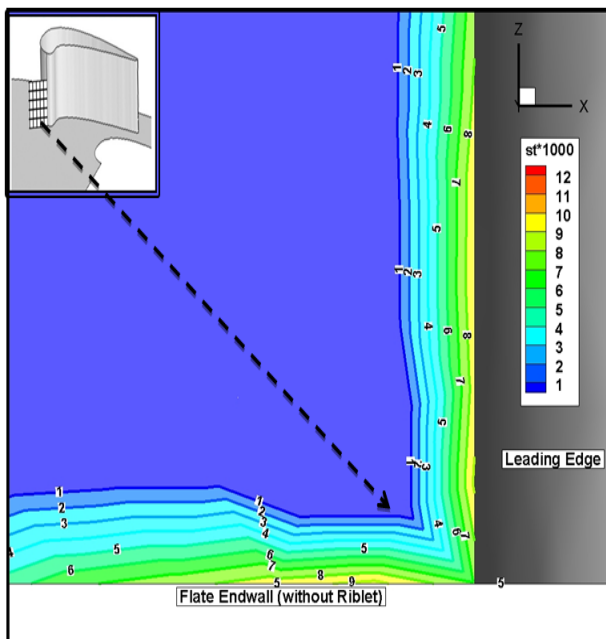


Figure 23.Stanton number distribution at the leading edge without Riblet.

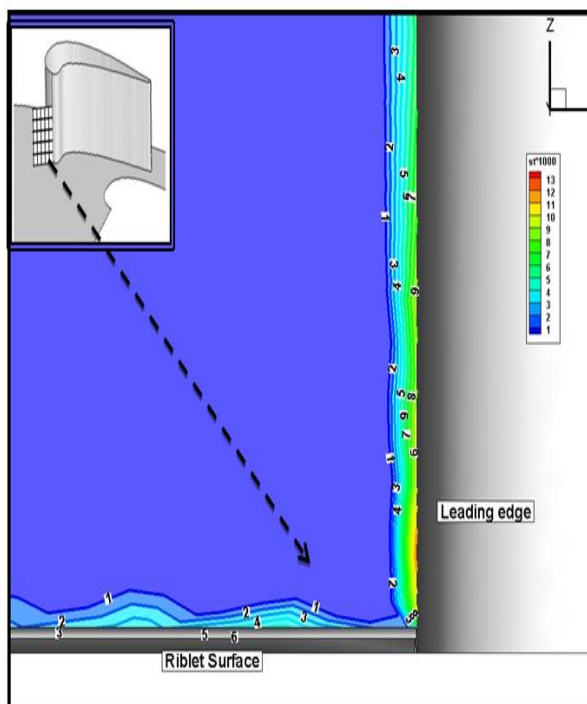


Figure 24.Stanton number distribution at the leading edge with Riblet.

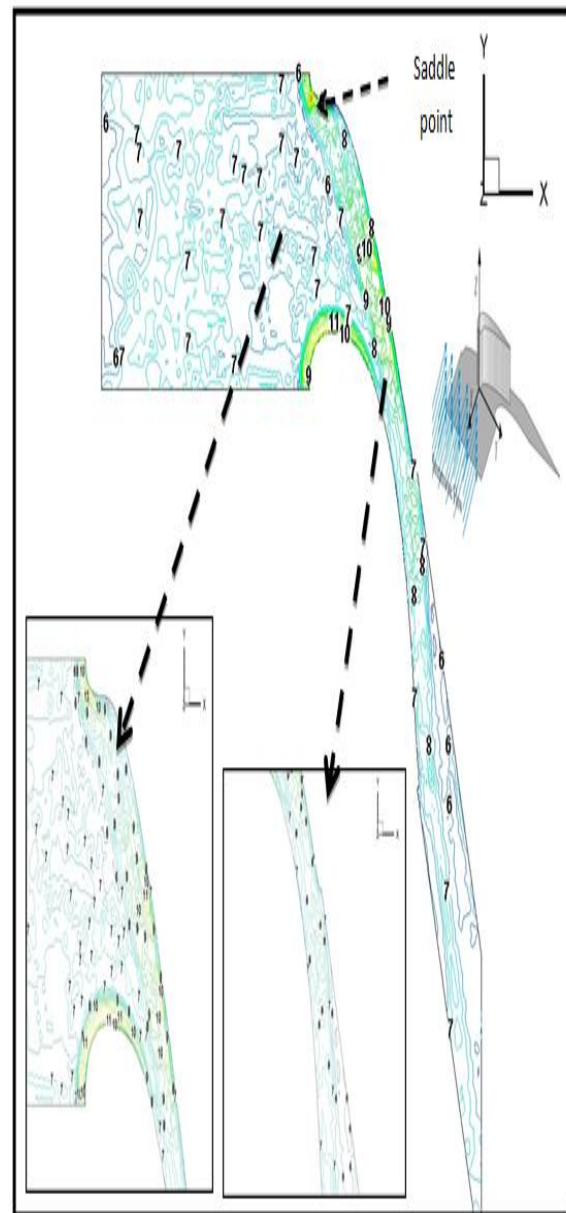


Figure 25.Stanton number distribution on the endwall junction without riblet.

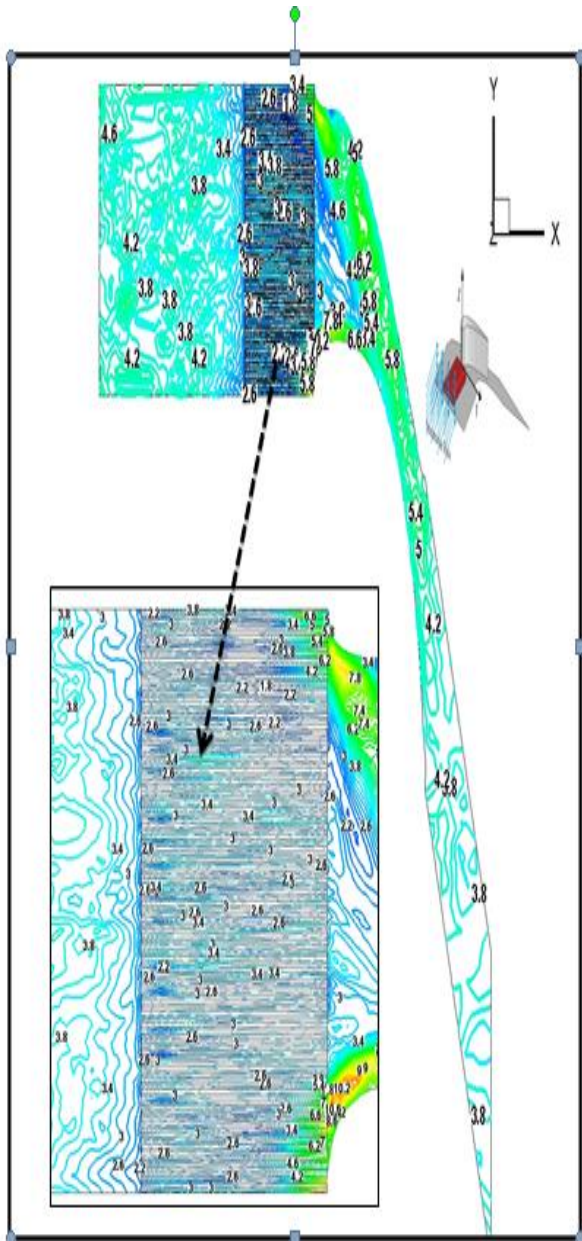


Figure 26. Stanton number distribution on the endwall junction with riblet.

Experimental Study for Materials Prosthetic above Knee Socket under Tensile or Fatigue Stress with Varying Temperatures Effect

Asst. Prof. Dr. Hatem Rahim Wasmi
Department of Mechanical Engineering
College of Engineering
Baghdad University
Email: hatemrwa@yahoo.com

Asst. Prof. Dr. Jumaa Salman Chiad
Department of Mechanical Engineering
College of Engineering
Al-Mustansiriya University
Email: jumaachiad@yahoo.com

M. Sc. Student: Adawiya Ali Hamzah
Department of Mechanical
College of Engineering
Baghdad University
Email: dr_majidhabeeb@yahoo.com

ABSTRACT

The residual limb within the prosthesis, is often subjected to tensile or fatigue stress with varying temperatures. The fatigue stress and temperatures difference which faced by amputee during his daily activities will produces an environmental media for growth of fungi and bacteria in addition to the damage that occurs in the prosthesis which minimizing the life of the prosthetic limb and causing disconfirm feeling for the amputee.

In this paper, a mechanical and thermal properties of composite materials prosthetic socket made of different lamination for perlon/fiber glass/perlon, are calculated by using tensile test device under varying temperatures (from 20°C to 60°C), also in this paper a device for measuring rotational bending fatigue stress under varying temperatures was designed, manufactured, and calibrated (this device is not available in Iraq), to achieve S – N curves for different lamination of perlon/fiber glass/perlon composite materials of prosthetic above knee socket.

In this paper, the mechanical and thermal properties set (E , σ_y , σ_{ult} , K , and α) results of the above composite materials are decreased when the temperatures are increased.

The S–N curves results of rotational bending fatigue for these lamination of composite materials are decreased when the temperatures are increased, also the endurance limit stresses (σ_e) are decreased with the increasing of number of perlon, and increasing temperatures, generally after about 10^7 cycles.

Key words: socket materials, tensile test, fatigue stress, mechanical and thermal properties.

دراسة عملية لمواد وقب طرف سفلي صناعي أعلى الركبة تحت تأثير أجهاد الشد أو الكلال عند مختلف درجات الحرارة

طالبة الماجستير: عدويه علي حمزه
قسم الهندسة الميكانيكية
كلية الهندسة / جامعة بغداد

أ.م.د. جمعه سلمان جواد
قسم الهندسة الميكانيكية
كلية الهندسة / الجامعة المستنصرية

أ.م.د. حاتم رحيم وسمي
قسم الهندسة الميكانيكية
كلية الهندسة / جامعة بغداد

الخلاصة

يتعرض متبقي العضو المبتور الى اجهاد شد أو كلال متكرر مع اختلاف في درجات الحرارة بشكل دائم. ان تعرض الطرف المبتور الى اجهاد كلال متكرر ودرجات الحرارة المختلفة يسبب في كثير من الأحيان بيئة لنمو الفطريات والبكتيريا ناهيك عن الضرر الذي يتعرض له متبقي الطرف المبتور بالإضافة الى الضرر الذي يحدث في الطرف الصناعي مما يسبب عدم راحة ذوي الاحتياجات الخاصة بالإضافة الى قصر عمر الطرف الصناعي.

في هذا البحث تم أستخراج الخواص الميكانيكية والحرارية للمواد المركبة الداخلة في تصنيع وقب طرف سفلي صناعي أعلى الركبة مصنع من البرلون/ألياف الزجاج/البرلون ذو طبقات مختلفة وذلك بأستخدام جهاز اختبار شد معرض الى درجات حرارة مختلفة (من ٢٠ الى ٦٠ درجة مئوية). كذلك تم في هذا البحث تصميم وتصنيع ومعايرة جهاز اختبار كلال أنحناء دوراني حراري (الجهاز غير متوفر في العراق) وذلك لغرض أستخراج منحنيات الأجهاد – عدد الدورات للوصول الى الفشل لطبقات مختلفة من المواد المركبة برلون / ألياف الزجاج / برلون المصنوع منها وقب الطرف الصناعي. أن نتائج الخواص الميكانيكية والحرارية التي أستخرجت في هذا البحث مثل (معامل المرونة وأجهاد الخضوع وأجهاد الشد الأعظم والمتانة ومعامل التمدد الحراري) للمواد المركبة التي ذكرت أعلاه تقل مع أرتفاع درجات الحرارة. كذلك وجد بأن نتائج منحنيات الأجهاد – عدد الدورات للوصول الى الفشل من خلال اختبار أجهاد كلال الأنحناء الدوراني لصفائح المواد المركبة المذكورة تقل مع أرتفاع درجات الحرارة. كذلك وجد أن اجهادات حد التحميل تقل مع زيادة عدد طبقات البرلون وأرتفاع درجات الحرارة بعد حوالي عشرة ملايين دورة.

الكلمات الرئيسية: مواد الوقب، اختبار الشد، إجهاد الكلال، الخواص الميكانيكية والحرارية.

1. INTRODUCTION

A limb prosthesis can be prescribed an attempt to replace the lost functionality of an absent limb as a result of amputation or a birth defect. The lower limb prosthesis is generally used to aid much basic functions such as standing and walking (Lafortune, and Henning, 1992).

In general, prosthesis for individuals with above knee amputation are comprised of four major components specifically: a socket interface to the residual limb, a knee joint, a shank, and foot assembly as illustrated in Fig.1, (Lafortune, and Henning, 1992).

The study of tensile or fatigue failure under varying temperatures is very complex. The fatigue performance of a materials is determined by testing a number of similar test specimens at different levels of maximum stress and with either a complete reversal of stress of a lower stress of zero.

A more recent study evaluating the fatigue testing of energy storing prosthetic feet by (Toh et al., 1993).

Van et al. 1995, understood the mechanical properties of the prosthetic foot on different aspects of gait and briefly attempted to explain how a difference in stiffness and hysteresis of the prosthetic foot would alter the gait cycle.

Zhichao, 2007, carried out high temperature stress controlled tests for interaction behavior.

Four fatigue – creep fracture character maps have been established. It was found that the fracture life will decrease rapidly and the fracture ductility will reach its minimum.

The manufacturing of above knee prosthesis by using different weighted materials such as perlon, nylon, carbon fiber, and fiber glass which was used in design and manufacturing the above knee prosthetic socket by a lamination consisting of a mixture of some of these materials embedded with an acrylic resin (Dianyin, and Rongqia, 2009) and (Pierce, 2010).

2. EXPERIMENTAL WORKS

The work steps of this work will be summarized as:

a) Materials part which describing the method of manufacturing socket made of perlon/fiber glass/perlon from different four laminations lay- up (3-2-3, 4-2-4, 5-2-5, and 6-2-6) respectively.

b) Preparing dies to make about (20) different standard flat specimens from different four laminations of composite said in para.(a), for testing by static digital tensile device under varying temperatures (from 20°C to 60°C), to calculate a mechanical and thermal properties of these materials specimens.

c) Design and manufacturing a rotational bending fatigue stress under varying

temperatures device for measuring (S – N) curves.

d) Making about (250) different standard hollow circular specimens from different four laminations of composite said in para. (a), for testing by a device validity of para. (c), to achieve S-N curves under varying temperatures (from 20°C to 60°C).

2.1 Materials

In this work, the materials needed in the lamination of the above knee socket are as follows and shown in **Fig.2**.

- a)** Perlon stockinet white (Ottobock health care 623 T3).
- b)** Fiber glass stockinet (Ottobock health care 616 G3).
- c)** Lamination resin (80:20) polyurethane proterhand icap technology).
- d)** Hardening powder (Ottobock health care 99 B71).
- e)** Materials for Jepson mold.

2.2 Procedure of Laminations

All laminations were performed under vacuum with the following procedures:

- a)** Mount the positive mold at the laminating stand.
- b)** Put the perlon stockinet and fiber glass stockinet according to the laminating lay up given in **Table 1**.
- c)** Mix the lamination resin 80:20 polyurethane with the hardener.
- d)** Maintain constant vacuum until the composite materials becomes cold and then lift the resulting lamination as shown in **Fig. 3**.

2.3 Tensile Test under Varying Temperatures

The tensile specimens were machined at the (Baghdad Center for Prosthetic and Orthotic Workshop). Twenty samples for each lamination were machined according to ASTM D638 (**Zhichao, 2007**), with 80mm original length and 13mm the width, while thickness varied with the type of the lay-up, these samples as shown in **Fig. 4**.

All the specimens were tested by using the universal testing instrument for tensile under varying temperatures (from 20°C to 60°C), to find mechanical and thermal properties of different composite laminations said in **Table 1**. These specimens are tested in the Materials Laboratories of the Ministry of the Science and Technology. **Fig.5** shown specimen under tensile test with and without temperatures, and **Tables 2, and 3** give the mechanical and thermal results.

2.4 Design and Calibration of Rotational Bending Fatigue Device

The main parts of the rotational bending fatigue under varying temperatures as shown in **Fig. 6** are:

- a)** Electric speed change motor.
- b)** Digital speed controller.
- c)** Rotational shaft with bearings.
- d)** Drill chuck.
- e)** Electronic stress meter.
- f)** Thermal chamber.
- g)** Thermometer control gauge.
- h)** Tachometer.
- i)** Change level frame.
- j)** Proximity sensor.

This device has been calibrated by the Central Organization for Standard Dization

and Quality Control at room temperature (20°C), with error rate about (7%).

2.5 Rotational Bending Fatigue Test under Varying Temperatures

The rotational bending fatigue specimens were machined at the (Baghdad Center for Prosthetic and Orthotic Workshop) according to ASTM D1043-02. Two hundred fifty samples for each lamination were machined according to the ASTM D638, with 100mm original length while diameter varied with the type of the lay up, these samples as shown in Fig.7.

All the specimens were tested by using a rotational bending fatigue under varying temperatures (from 20°C to 60°C) device as design, manufacturing, and calibrating in this study (this device is not available in Iraq) as shown in Fig. 6. These specimens are tested at the Strength of Materials Laboratory of Baghdad University/College of Engineering /Mechanical Department, and the S – N curves results for different laminations with varying temperatures as shown in Figs. from 8 to 12

3. RESULTS ANALYSIS AND DISCUSSION

The mechanical and thermal properties results of each sample as shown in Tables 2, and 3 can be calculated and by taking the average value of these properties (E, σ_y , σ_{ult} , K, and α) under varying temperatures (from 20°C to 60°C), these properties results for all laminations, with constant fiber glass layer in the lamination, the mechanical properties (E, and K) are increasing with the increasing perlon layers at constant temperature, especially for high number of perlon layers, also the mechanical and thermal properties (σ_y , σ_{ult} , and α) are decreasing with the increasing perlon layers, especially for high number of perlon layers at constant

temperature. While in general for all laminations, the mechanical and thermal properties are said above are decreasing with the increasing temperatures.

The S – N curves results of each sample as shown in Figs. from 8 to 12 can be calculated and by taking the average value of the failure stress with number of cycles under varying temperatures (from 20°C to 60°C), these S – N results for all laminations, with constant fiber glass layer in the lamination, the failure stress results are decreasing with the increasing perlon layers, while the number of cycles to reach the failure points are increasing with the increasing perlon layers at constant temperature. Also, from the S – N curves results as shown in Figs. from 8 to 12, for all laminations, the failure stresses are decreasing and the number of cycles to reached to the failure points are increasing with the increasing temperatures. Also, Table 4 shows the results of endurance stress limit for laminations under varying temperatures, from these results the endurance limit stresses (σ_e) are decreased with the increasing of number of perlon, and increasing temperatures.

4. CONCLUSIONS

In this paper, the following mean summarized conclusions:

- 1) When the temperatures are increased, the mechanical and thermal properties are improved with the decreasing of number of perlon with two fixing layers of fiber glass.
- 2) When the number of perlon layers are increased, the mechanical properties (E, and K) are clearly improved with two fixing layers of fiber glass, at constant and changed in temperatures.
- 3) The mechanical and thermal properties (σ_y , σ_{ult} , and α) are decreased when the temperatures are increased for all laminations.



4)The failure stresses are decreased and the number of cycles to reach the failure points are increased when the temperatures are increased for all laminations.

5)The endurance limit stresses (σ_e) are decreased with the increasing of number of perlon, and increasing temperatures.

6)The maximum error difference in results at room temperature (20°C) between a rotational bending fatigue is designed in this paper with the same standard device are about 7%.

7)A good conformability between the mechanical properties results of this work with these of the Reference [9] results at room temperature (20°C), with maximum differences about 5%.

8)A good agreement between the S-N curves results at room temperature (20°C) of a device in this work with that in the Central Organization for Standardization and Quality Control, with error rate about (7%).

5. REFERENCES

Alaneme, K. K., 2011, *Design of a Cantilever Type Rotating Bending Fatigue Testing Machine*', Akure, PMB 704, Nigeria, Vol. 10, No. 11, PP. 1027-1039, (this paper from IVSL).

Dianyin, H., and Rongqiao, W., 2009, *Experimental Study on Creep – Fatigue Interaction Behavior of GH4133B Super Alloy*', Volume 515, Issues 1-2, 25 July, PP. 183-189.

Dunmin, L., Daoxiang, G., Tian, Y., and Aiping X., 2011, *Mechanics and Dynamics of Active and Passive Knee Joint of Above Knee Prosthesis*', IEEE, (this paper from IVSL).

Lafortune, M. A., and Henning, E. M., 1992, *Cushioning Properties of Footwear During*

Walking : Accelerometer and Force Platform Measurements', No.7: PP.181-184.

Muhsin, J. J., Shaker, S. H., and Jumaa, S. CH., 2009, *Analysis and Design Optimization of the Above Knee Prosthetic Socket*', Thesis.

Pierce, C. J., 2010, *Creep and Fatigue Interaction in the PWA1484 Single Crystal Nickel – Base Alloy*', Volume 527, Issues 29-30, 15 November, PP. 7484 – 7489.

Toh, S. L., Goh J. C. H., Tan P. H. and Tay T. E., 1993, *Fatigue Testing of Energy Storing Prosthetic Feet*'. *Prosthetics and Orthotics International* No.17: PP.180-188.

Van Jaarsveld, H. W. L., Grootenboer, H. J., De Vries, J., and Koopman, H. F. J. M., 1995, *Stiffness and Hysteresis Properties of Some Prosthetic Feet*'. *Prosthetics and Orthotics International* No.14:PP. 117-124.

Zhichao, F., 2007, *Fatigue-Creep Behavior of 1.25 Cr 0.5 Mo Steel at High Temperature and its Life Prediction*', *International Journal of Fatigue*, Vol.29, Issue 6, June, PP.1174-1183.



Figure1. The prosthesis components (Lafortune, and Henning).

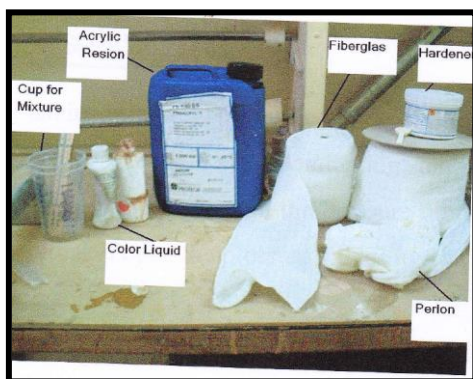


Figure2. Materials for above knee socket.



Figure3. Positive mold before and after lamination lay-up.

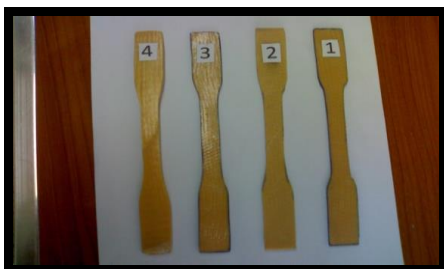


Figure4. Tensile test specimens.



a) without temp.



b) with temp.

Figure5. Tensile test device without and with temperatures.



motor.



shaft with bearings.



frame.



thermal chamber, and thermal control gauge.

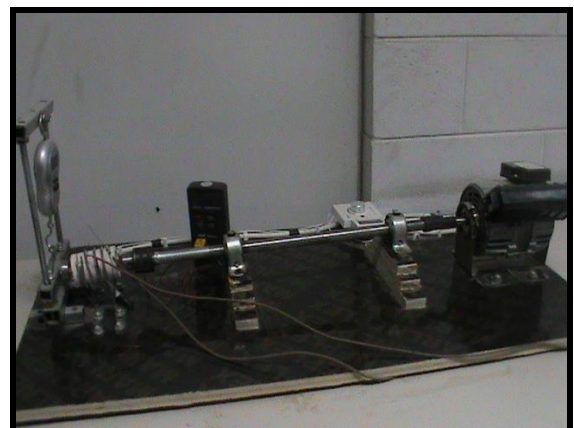


Figure6. Parts and device of rotational bending fatigue under varying temperatures.



Figure7. Rotational fatigue test specimens.

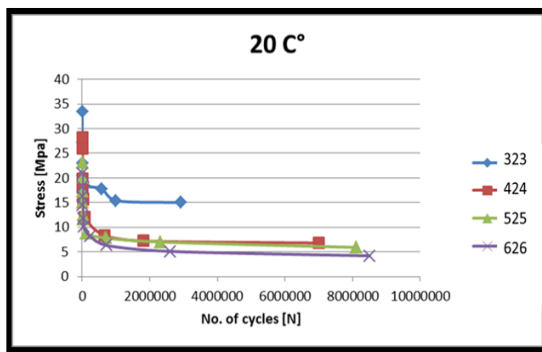


Figure8. S-N curves for laminations at 20°C.

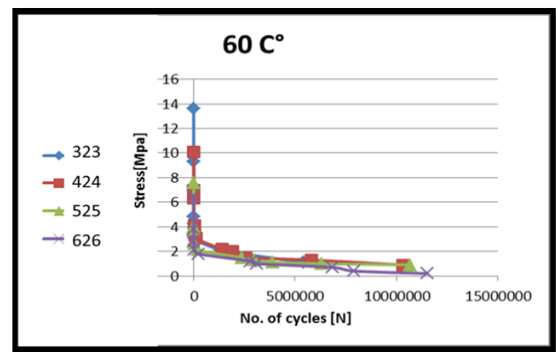


Figure12. S-N curves for laminations at 60°C.

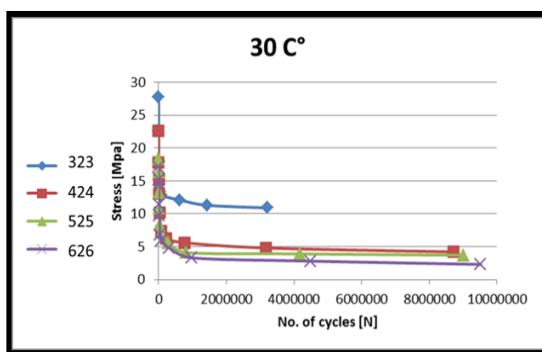


Figure9. S-N curves for laminations at 30°C.

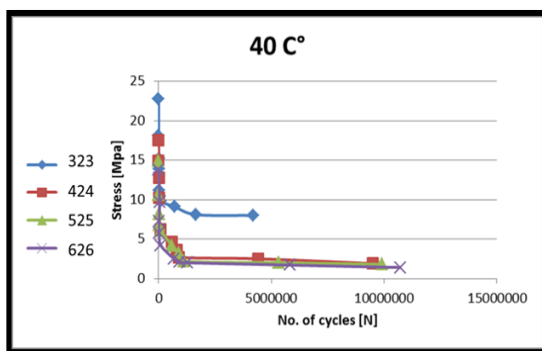


Figure10. S-N curves for laminations at 40°C.

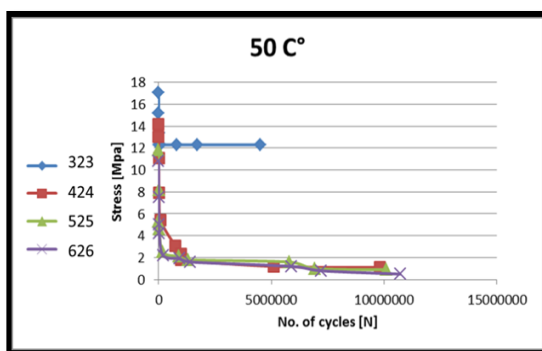


Figure11. S-N curves for laminations at 50°C.

Table 1. Laminations lay-up.

No. of lamination	Lay up	No. of layers	Thickness (mm)	Description layers
1	3-2-3	8	2.41	(3Perlon+2fiber glass+3perlon)
2	4-2-4	10	2.92	(4Perlon+2fiber glass+4perlon)
3	5-2-5	12	2.96	(5Perlon+2fiber glass+5perlon)
4	6-2-6	14	3.37	(6Perlon+2fiber glass+6perlon)

Table 2. Mechanical properties results for all laminations.

T (C°)	No. of lamination	Lay-up	σ_{yield} (Mpa)	σ_{ultimate} (Mpa)	Modulus of elasticity E(Mpa)	Stiffness K(N/mm)	Poisson's ratio(ν)
20	1	3-2-3	58.2	73.1	0.857	1317.3	0.390
	2	4-2-4	41.2	50.3	0.924	1602.8	0.371
	3	5-2-5	37.4	45.5	0.979	1841.7	0.362
	4	6-2-6	33.9	44.8	1.027	2121.3	0.353
30	1	3-2-3	57.2	72.2	0.843	1309.2	0.383
	2	4-2-4	40.1	48.3	0.911	1600.2	0.368
	3	5-2-5	36.9	44.1	0.965	1840.3	0.356
	4	6-2-6	32.2	42.7	1.011	2119.1	0.348
40	1	3-2-3	56.6	71.6	0.821	1301.3	0.381
	2	4-2-4	39.4	46.5	0.903	1593.7	0.367
	3	5-2-5	35.8	42.5	0.933	1821.5	0.354
	4	6-2-6	31.4	41.4	1.007	2101.8	0.347
50	1	3-2-3	54.2	69.3	0.803	1295.8	0.380
	2	4-2-4	36.5	44.2	0.888	1585.0	0.366
	3	5-2-5	31.9	41.1	0.912	1812.7	0.353
	4	6-2-6	29.8	40.2	0.882	2088.1	0.345
60	1	3-2-3	51.8	65.4	0.794	1278.3	0.374
	2	4-2-4	34.2	42.8	0.834	1501.4	0.364
	3	5-2-5	30.4	40.2	0.905	1773.0	0.352
	4	6-2-6	27.5	38.4	0.977	1997.2	0.343



Table3. Coefficients of thermal expansions results (α) for laminations with different temperatures (ΔT).

No. of laminations	α ($1/^\circ\text{C}$) * 10^{-8}	ΔT ($^\circ\text{C}$)
3-2-3 4-2-4 5-2-5 6-2-6	3.24 2.81 2.66 2.45	from 20 to 30
3-2-3 4-2-4 5-2-5 6-2-6	3.11 2.78 2.63 2.43	from 20 to 40
3-2-3 4-2-4 5-2-5 6-2-6	3.08 2.76 2.62 2.39	from 20 to 50
3-2-3 4-2-4 5-2-5 6-2-6	3.02 2.74 2.60 2.37	from 20 to 60

Table4.Endurance stress limit results (σ_e) with varying temperatures (T).

No. of laminations	Endurance stress limit σ_e (Mpa)	Temperatures ($^\circ\text{C}$)
3-2-3 4-2-4 5-2-5 6-2-6	15.0 7.20 6.20 4.10	20
3-2-3 4-2-4 5-2-5 6-2-6	12.6 4.30 3.20 2.50	30
3-2-3 4-2-4 5-2-5 6-2-6	7.80 2.90 2.10 1.80	40
3-2-3 4-2-4 5-2-5 6-2-6	2.0 1.60 1.20 0.60	50
3-2-3 4-2-4 5-2-5 6-2-6	1.60 1.40 0.80 0.40	60

An Experimental Study of the Effects of Coolant Fluid on Surface Roughness in Turning Operation for Brass Alloy

Suhair Ghazi Hussein

Assistant Lecturer

Engineering College-Baghdad University

Email: suhairaaffmm@yahoo.com

ABSTRACT

The effect of different cutting fluids on surface roughness of brass alloy workpiece during turning operation was carried out in this research. This was performed with different cutting speed, while other cutting parameters had been regarded as constants (feeding rate, and depth of cut). Surface roughness of machined parts that will be tested by electronic surface roughness tester. The results show that the standard coolant gives the best values of surface roughness for fixed cutting speed, followed by sun flower oil that has approximately the same effect, while the air stream as a coolant gave unsatisfied results for the evaluation of surface roughness. In the other hand the best values of surface roughness were recorded for maximum cutting speed with all other types of cutting fluids.

Keywords: turning operation, cutting speed, cutting fluid, surface roughness

دراسة عملية لتأثير سوائل التبريد على خشونة الاسطح في عملية الخراطة لسبيكة البراص

سهيير غازي حسين

مدرس مساعد

كلية الهندسة / جامعة بغداد

الخلاصة

تضمن البحث دراسة وتقييم تأثير سوائل قطع مختلفة على خشونة الاسطح لعينات من البراص مشغلة بعملية الخراطة. حيث تضمنت خطوات العمل اخذ خمسة انواع من سوائل التبريد اضافة الى حالة القطع الجاف ودراسة تأثيرها على القطع المشغلة مع تغيير قيم سرعة القطع للماكينة حيث تم اخذ ست سرعات مختلفة حسب امكانية ماكينة الخراطة المستخدمة للدراسة اما بقية عوامل القطع الاخرى فقد تم تثبيتها في الدراسة، تم فحص الاسطح بواسطة جهاز قياس الخشونة. اظهرت النتائج ان استخدام سائل التبريد القياسي اعطى افضل نتائج من حيث نعومة السطح مع ثبوت سرعة القطع للماكينة يتبعه زيت الطعام حيث اعطى نتائج مقاربة، بينما استخدام التبريد بالهواء المضغوط اعطى اسوأ النتائج من حيث نعومة الاسطح. من ناحية اخرى اظهرت الدراسة ان افضل نعومة للاسطح سجلت عند استخدام اعلى سرعة للقطع لكل انواع سوائل القطع التي استخدمت بالدراسة.

الكلمات الرئيسية : عملية الخراطة، سرعة القطع، سوائل التبريد، خشونة الاسطح.

1. INTRODUCTION

The machining processes have an important place in the traditional production industry. Cost effectiveness of all machining processes has been eagerly investigated. This is mainly affected selection of suitable machining parameters like cutting speed, feed rate and depth of cut according to cutting tool and workpiece material. The selection of optimum machining parameters will result in longer tool life, better surface finish and higher material removal rate. During machining process, friction between workpiece-cutting tool and cutting tool-chip interfaces cause high temperature on cutting tool. The effect of this generated heat decreases tool life, increases surface roughness and decreases the dimensional sensitiveness of work material. This case is more important when machining of difficult-to-cut materials, when more heat would be observed, **M.B. Da Silva ,1998**. Various methods have been reported to protect cutting tool from the generated heat. Choosing coated cutting tools are an expensive alternative and generally it is a suitable approach for machining some materials such as titanium alloys, heat resistance alloys etc. The application of cutting fluids is another alternative to obtain higher material removal rates. **O. Çakır and etal,2007**.

Cutting fluids consist of those liquid and gases that are applied to the tool and the material being machined to facilitate the cutting operation. Vast quantities are used annually to accomplish a number of objectives: 1-To prevent the tool from overheating , i.e. so that no temperature is reached where the tool's hardness and resistance to abrasion are reduced, thus decreasing the tool life. 2- to keep the work cool so preventing machining that results in inaccurate final dimensions . 3- To provide a good surface finish on the work. 4-To wash away the chips / clear the swarf from the

cutting area . 5- To prevent corrosion of work , the tool and machine(University of Pretoria) .

Surface roughness is a commonly encountered problem in machined surfaces. It is defined as the finer irregularities of surface texture, which results from the inherent action of the production process. Consequently, surface roughness has a great influence on product quality, **Mohd Zulhilmi,2010**.

The product quality depends very much on surface roughness. Decrease of surface roughness quality also leads to decrease of product quality. In field of manufacture, especially in engineering, the surface finish quality can be a considerable importance that can affects the functioning of a component, and possibly its cost. Surface roughness has been receiving attention for many years in the machining industries. It is an important design feature in many situations, such as parts subject to fatigue loads, precision fits, fastener holes and so on. In terms of tolerances, surface roughness imposes one of the most crucial constraints for the machines and cutting parameters selection in process planning, **Mohd Zulhilmi,2010**.

Dry machining means machining the material without any fluids at all, and only atmospheric air surrounding the cutting zone. Dry machining is elimination on the use of cutting fluids. The interest in dry machining is often related to the lower cost, healthy issues and environmentally friendly .

Dry machining requires less power. Cutting dry, the chips will move across the rake face of the tool and so take the point of maximum heat a way back from the tool tip. The tool will get hot, but there is a larger bulk of tool in which to dissipate the heat. In dry machining, bringing the point of maximum heat much closer to the point of cut where there is less material to conduct away the heat; the tool life decrease, **Fig.1** shows an example on dry machining, **Mohd Zulhilmi,2010**. In wet machining, both the tool and the workpiece are cooled using large quantities of lubricant. The

coolant is subsequently cleansed and used again, **Fig.2** shows an example on wet machining, Rohaida, 2008.

Raviraj Shetty, et al studies a comparative experiments were carried out in cutting AA6061-15vol.%SiC (25 μ m particle size), with cubic boron nitride insert KB-90 grade under conditions of compressed air, oil water emulsion-steam as coolant and lubricant, and dry cutting, respectively. The experimental results show that, with steam as coolant and lubricant, the friction coefficient and surface roughness value are decreased respectively,

Raviraj Shetty, et al, 2008.

Mohd Zulhimi bin Rifin studied minimum quantity of lubrication (MQL) in machining is an established alternative to completely dry or flood lubricating system from the viewpoint of cost, ecology and human health issues. Hence, it is necessary to select MQL and cutting conditions in order to enhance machinability for a given work material. This thesis describes experimental investigations on influence of different lubrication conditions such as minimum quantity lubrication (MQL), dry machining and wet machining on surface roughness. The surface roughness was examined with Perthometer. Three different materials had been chosen as work material. It was found that, minimum quantity lubricants produced better surface finish as compared to dry and wet machining. The result can significantly reduce cost and environmental pollution by using minimum quantity lubrication, **Mohd Zulhimi, 2010.**

*L B Abhang and M. Hameedullah, 2010 used minimum quantity of lubrication of boric acid mixed with base oil SAE 40 has proved to be a feasible alternative to the conventional cutting fluid. In the present work 10% boric acid by weight mixed with base oil SAE 40 is used as a MQL in turning process. Variations in cutting (lubricant) force, cutting temp, chip thickness and surface roughness are studied under different machining conditions. The results indicated that there was a considerable improvement in machining performance with MQL assisted machining compared to dry machining, **L B Abhang, 2010.**

Ahmad Dziauddin bin Mohamed, 2010, investigated the different cutting tool length parameter effect of surface roughness in CNC Turning boring operation for an aluminium 6061 workpiece. A fractional factorial design is used to evaluate the effect of five (5) independent variables (cutting speed, feed rate, depth of cut, tool length and diameter of boring bar) on the resulting first cut surface roughness (Ra). This study found that using short tool length always produce a good surface roughness and that only slight improvement on surface roughness can be achieved by properly controlling the cutting parameters and/or the diameter size of boring bar.

Suleiman Abdul-kareem, et al., 2011, investigated the influence of the three most important machining parameters of depth of cut, feed rate and spindle speed on surface roughness during turning of mild steel. The individual parameters effect as well as effect of interactions between the machining parameters on the surface roughness height Ra is analyzed using various graphical representations. Using multiple linear regressions, mathematical models correlating the influence of machining parameters on the surface roughness Ra during the machining process were developed.

2. SELECTION OF SUITABLE CUTTING FLUIDS

The selection of cutting fluids in machining processes depends on various factors. The selection of cutting fluids is carried out according to factors mentioned below:

- a. Type of machining processes
- b. Type of machined workpiece material
- c. Type of cutting tool material

The most important parameter in the selection of cutting fluids is the characteristics of machining process.

In turning, milling and grinding machining processes water based cutting fluids are more suitable due to using new cutting tool materials such as hard metals and high cutting speeds. The contact period between

Cutting tool and workpiece material is small when high cutting speeds are used. Therefore penetration of cutting fluid will not be sufficient. The type of crater wear on cutting tool can be seen more often. Water based cutting fluids will reduce the effect of generated heat on cutting tool wear, **S. Ebbrell, et al, 2000**.

The other factor for selection of suitable cutting fluids in machining processes is the type of workpiece material. The application of emulsion cutting fluids or thin mineral oils should be selected for copper and copper based alloys machining. High pressure additive cutting oils are preferred for brass machining, **S. Ebbrell, et al, 2000**.

The third influential parameter for selection of cutting fluid in machining processes is the cutting tool material. Various cutting tool materials are commercially available for all kind of machining processes. High speed steel cutting tools can be used with all type of cutting fluids. However waterless cutting fluids are preferred when difficult-to-cut materials are machined.

3. EXPERIMENTAL WORK

In this research, a series of experiments was done to study the effect of cutting speed and type of lubricants on resulting surface quality. The turning machine in workshop was used with brass alloy workpiece material chemical composition shows in **Table 1**, dimension of the workpiece was 10mm diameter \times 20mm. Carbide tools were used in the machining trials. see **Fig. 3**.

The cutting speeds were chosen that ranged from the available on the machine in three levels as shown in **Table 2**, only one level of feed rate 0.2mm and depth of cut was applied to the limited effect of the axial depth of cut on the surface roughness in the turning operation. Six types of conditions were chosen in turning trials: dry condition, wet condition contains: water, soluble water, water and soap solution in percentage (3) soap to (10) water, sun flower oil, standard coolant, and air stream. For

every condition of cutting we use the variable values of cutting speed to examine the effect of the cutting fluids with cutting speed on surface roughness.

After turning operation was accomplished the work piece had been taken to measure its surface roughness by Electronic surface roughness tester as shown in **Fig. 4**. The measuring device was calibrated with the standard sample.

The readings of each measured value are repeated three times and the average was taken.

4. RESULTS AND DISCUSSION

The surface roughness of the machined pieces was recorded, (Ra) : this parameter is known as the arithmetic mean roughness value, AA (arithmetic average) or CLA (center line average). Ra is universally recognized and the most used international parameter of roughness, **Dr. Mike, et al, 1998**.

a. Cutting speed affecting on surface roughness:

Figs. 5 to 10 show the surface roughness for dry, water, soluble water, oil, standard coolant, and air stream for brass alloy turning respectively. It was clearly revealed that in every condition decrease in surface roughness with increase in cutting speed, because it is generally well known that an increase in cutting speed improves machine ability. This may be due to the continuous reduction in the build up edge formation as the cutting speed increases, **Mohammad T. Hayajneh, et al., 2007**.

b. Coolant affecting on surface roughness

Figs. 11 to 16 show the relation ship between the surface roughness and cutting fluid in every cutting speed. It was noticed that the maximum reduction in surface roughness was observed to be in standard coolant condition, followed it the sun flower oil, after these the soluble water. This is because the reduction metal cutting forces. The decrease in surface roughness due to standard coolant can be



considering interest lubricating properties; this reduces frictional forces at the chip-tool interface and tool work piece interface. This decrease the temperature at the cutting zone and results in surface quality improvement.

5. CONCLUSIONS

In this study, the effected of cutting fluid on surface roughness has been carried out . The surface roughness has been recorded by surface roughness measurement device, the following conclusions can be drawn:

1. The standard coolant is found to be the best choice of cutting fluid to obtain finer surface roughness, followed by sun flower oil that has the same affecting, so it can be use the sun flower oil instead of standard coolant to give the same results with lowest cost .
2. Machining with high cutting speed decreases the surface roughness with all types of cutting fluids ,and with dry cutting ,too.
3. The best results of surface roughness has been obtained with (2200 rpm) ,standard coolant , this value is (.125 μm).

6. REFERNCES

- Ahmad dziauddin bin Mohamed,2010, *Effect of Process Parameters on Surface Roughness Produced by Turning Boring Operation Aproject Report Submitted in Partial Fulfillment of The Requirement for the Award of Degree of Master of Engineering* .
- Dr. Mike S.Lou, Dr. Joseph C.Chen & Dr.Caleb M.Li, 1999, *Surface Roughness Prediction Technique for CNC End-Milling*,volume15, Number 1- November 1998 to January .
- LB Abhang and M.Hameedullah, 2010, *Experimental Investigation of Minimum Quantity Lubricants in Alloy Steel Turning*. International Journal of Engineering Science and Technology Vol.2(7).
- M.A. El Baradie, Cutting Fluids, 1996, *Part I:Characterisation, Journal of Materials Processing*. Technology 56 ,786-797
- M.B. Da Silva, J. Wallbank, 1998, *Lubrication and Application Method in Machining*, Lubrication and Tribology 50 , 149-152 .
- Mohd Zulhimi bin Rifin, 2010, *Effect of Lubrication Condition on Surface Roughness in Turning Operation*.
- Mohammed T.Hayajneh, Montasser S.Tah At , Joachim Bluhm, 2007,*A Study of The Effects of Machining Parameters on the Surface Roughness in the End-Milling process*.Volume1,Number 1,Sep.
- O.Cakir, A. Yardimeden, T. Ozben, E. Kilickap, 2007, *Selection of Cutting Fluids in Machining*. processVolume 25 Issue 2 December .
- Raviraj Shetty,etal ,2008, *Steam as Coolant and Lubricant in Turning of Metal Matrix Composites*, journal of Zhejiang, University Science A .
- Rohaida binti Mohd, 2008 , *Effect of Lubrication Condition on Surface Croughness By Using Lathe Machine* .
- S. Ebbrell, N.H. Woolley, Y.D. Trimidas, D.R. Allanson, W.B. Rowe, 2000, *The Effects of Cutting Fluid Application Methods on the Grinding Process*, International Journal of Machine Tools and Manufacture. Vol40 , 209-223
- Suleiman- Abdulkareem1, Usman Jibrin Rumah1 and Apasi Adaokoma1, 2011, *Optimizing Machining Parameters during Turning Process*, International Journal of Integrated Engineering, Vol. 3 No. 1 , p. 23-27

Table 1. Chemical composition of alloy .

Items	Cu	Al	Fe	Pb	Ni	Si	Sn	Zn
Percentage	58	.8	.7	1.5	.8	.05	1.2	36

Table 2. Cutting parameters.

Cutting parameters	1	2	3	4	5	6
Feed (mm)	0.2					
Speed (RPM)	325	420	575	925	1400	2200

Table 3 . Surface roughness of machined pieces in variable conditions.

Condition	level	speed (Rpm)	Ra (μm)	condition	level	speed (Rpm)	Ra (μm)
DRY	B	325	13.32	OIL	B	325	2.421
	C	420	10.52		C	420	1.652
	A	575	6.22		A	575	1.141
	A	925	4.75		A	925	0.882
	C	1400	3.54		C	1400	0.661
	C	2200	2.33		C	2200	0.432
WATER	B	325	8.95	S.COOLANT	B	325	0.736
	C	420	6.64		C	420	0.4995
	A	575	4.134		A	575	0.338
	A	925	3.182		A	925	0.264
	C	1400	2.346		C	1400	0.202
	C	2200	1.556		C	2200	0.125
WATER & SOAP	B	325	6.211	AIR	B	325	11.145
	C	420	4.659		C	420	8.353
	A	575	2.845		A	575	5.175
	A	925	2.12		A	925	3.94
	C	1400	1.634		C	1400	2.956
	C	2200	1.083		C	2200	1.954



Figure1. Dry machining ,Mohd Zulhilmi,2010.



Figure2.Wet machining, Rohaida ,2008.



Figure 3 .Turning machiene with work piece.

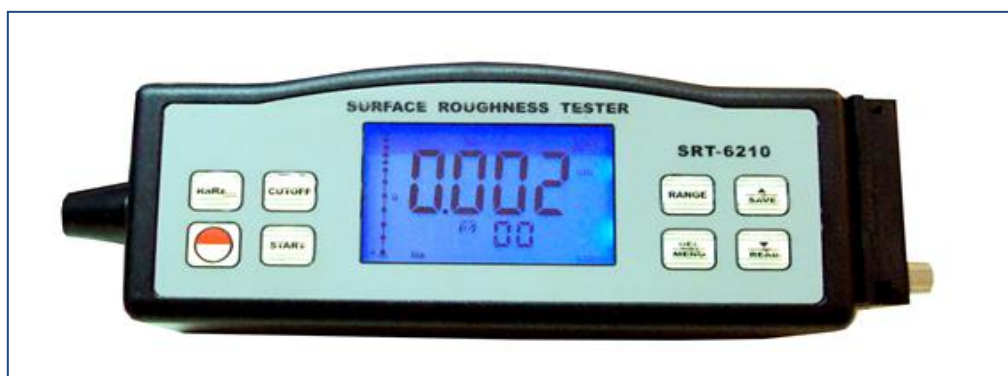


Figure 4. Electronic surface roughness tester.

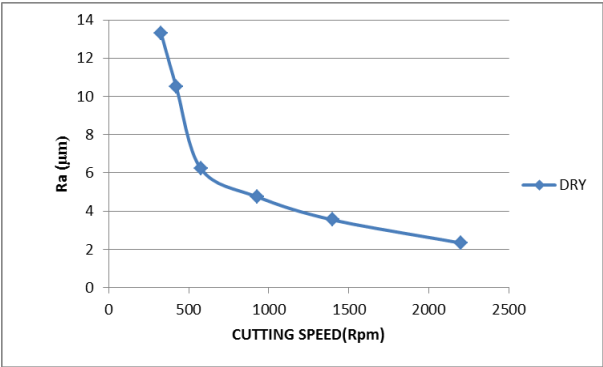


Figure 5. Cutting speed effective on surface roughness in dry condition.

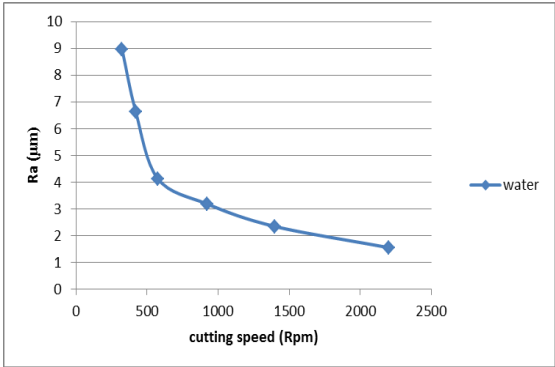


Figure 6. Cutting speed effective on surface roughness in water condition.

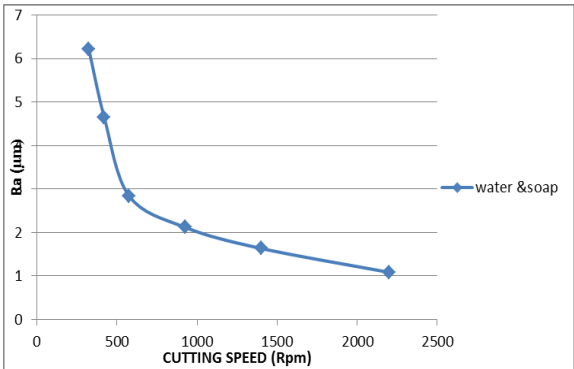


Figure 7. Cutting speed effective on surface roughness with water & soap.

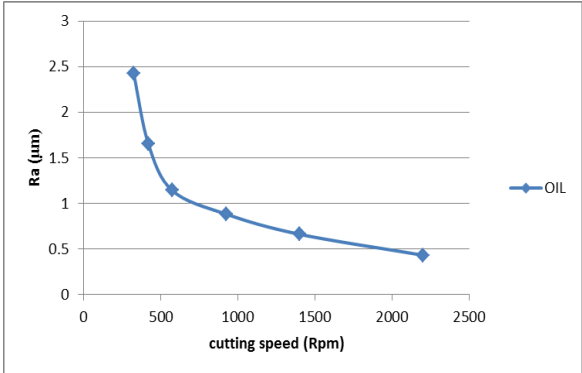


Figure 8. Cutting speed effective on surface roughness with oil

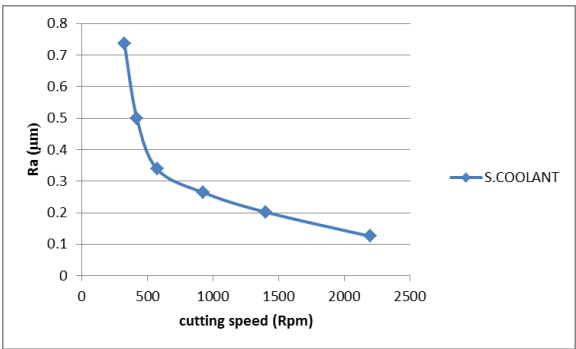


Figure 9. Cutting speed effective on surface roughness with s. coolant.

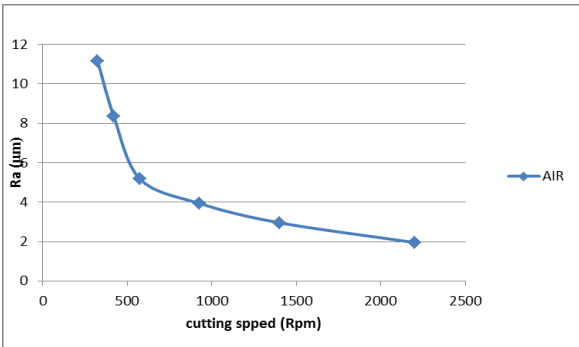


Figure 10. Cutting speed effective on surface roughness with air.

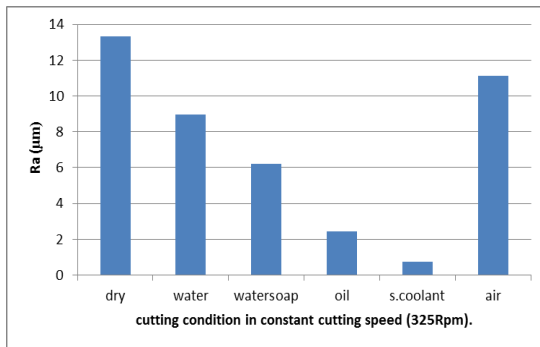


Figure 11. Effect of cutting fluid on surface roughness with fixed cutting speed (325Rpm).

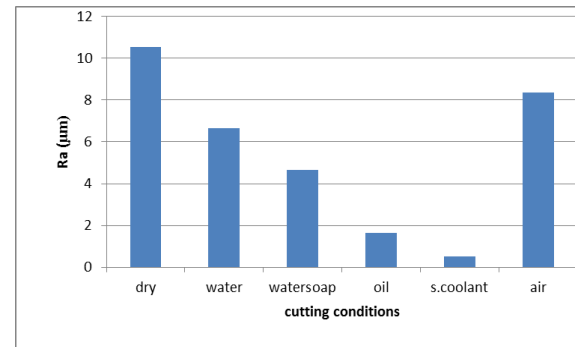


Figure 12. Effect of cutting fluid on surface roughness with fixed cutting speed (420Rpm).

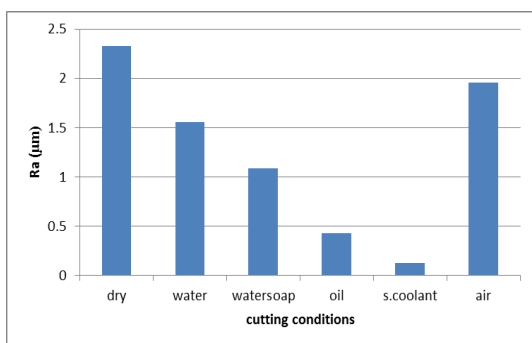


Figure 13. Effect of cutting fluid on surface roughness with fixed cutting speed (2200rpm).

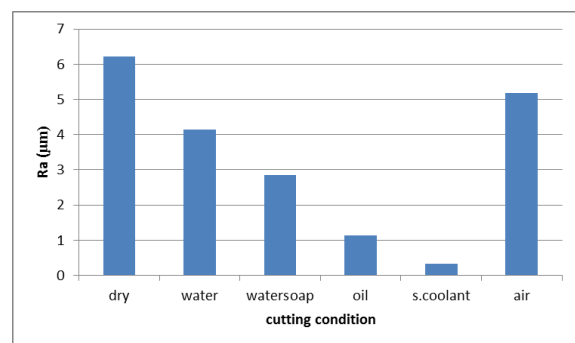


Figure 14. Effect of cutting fluid on surface roughness with fixed cutting speed (575rpm).

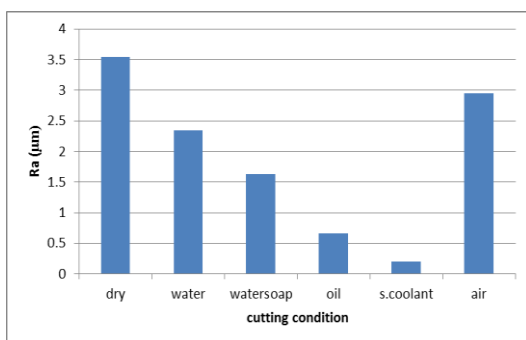


Figure 15. Effect of cutting fluid on surface roughness with fixed cutting speed (1400rpm).

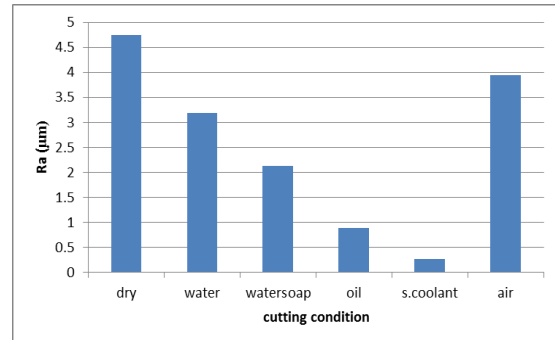


Figure 16. Effect of cutting fluid on surface roughness with fixed cutting speed (925rpm)

A Modified Strength Pareto Evolutionary Algorithm 2 based Environmental /Economic Power Dispatch

Asst. Prof. Dr. Hassan Abdullah Kubba

Department of Electrical Engineering
College of Engineering/Baghdad University
Email:hassankubba@yahoo.com

Saif Sabah Sami

M.Sc. Electrical Engineering
College of Engineering/Baghdad University
Email:saif2007@yahoo.com

ABSTRACT

A Strength Pareto Evolutionary Algorithm 2 (SPEA 2) approach for solving the multi-objective Environmental / Economic Power Dispatch (EPPD) problem is presented in this paper. In the past fuel cost consumption minimization was the aim (a single objective function) of economic power dispatch problem. Since the clean air act amendments have been applied to reduce SO_2 and NO_x emissions from power plants, the utilities change their strategies in order to reduce pollution and atmospheric emission as well, adding emission minimization as other objective function made economic power dispatch (EPD) a multi-objective problem having conflicting objectives. SPEA2 is the improved version of SPEA with better fitness assignment, density estimation, and modified archive truncation. In addition fuzzy set theory is employed to extract the best compromise solution. Several optimization run of the proposed method are carried out on 3-units system and 6-units standard IEEE 30-bus test system. The results demonstrate the capabilities of the proposed method to generate well-distributed Pareto-optimal non-dominated feasible solutions in single run. The comparison with other multi-objective methods demonstrates the superiority of the proposed method.

Keywords: genetic algorithm, multi-objectives optimization, power generation dispatch, power generation economic, pareto distributions

خوارزمية التطور باريتو ٢ لحل ارسالية القدرة الاقتصادية والبيئية

سيف صباح سامي
قسم الهندسة الكهربائية
كلية الهندسة/جامعة بغداد

أ.م.د. حسن عبدالله كبة
قسم الهندسة الكهربائية
كلية الهندسة/جامعة بغداد

الخلاصة:

ان الخوارزمية التطورية الفعالة بمفهوم برتو ٢ تقدّم في هذا البحث لحلّ مشكلة إرسال القدرة بالصورة الاقتصادية متعددة الدوال الرفيعة بالبيئة. في الماضي كان تحقيق الحد الأدنى للتكلفة الوقود المستهلك الهدف (دالة) موضوعية وجيدة من مشكلة إرسال القدرة بالصورة الاقتصادية. منذ أقرار قانون الهواء النظيف الذي فرض تخفيض انبعاثات غازات SO_2 و NO_x من محطات إنتاج القدرة الكهربائية، غير القائمين على ادارة هذه المحطات ستراتيبياتهم لكي يتم تخفيض هذه الانبعاثات وتلوث جو أيضاً، مضيفين بذلك تحقيق الحد من هذه الانبعاثات كدالة موضوعية أخرى و جاعلين إرسال القدرة بالصورة الاقتصادية مشكلة متعددة الدوال الموضوعية ذات أهداف متعارضة. ان الخوارزمية التطورية الفعالة بمفهوم برتو ٢ هي النسخة المحسنة من الخوارزمية التطورية الفعالة بمفهوم برتو بقبالة افضل على تحديد لياقة كل فرد وتقدير كثافة (توزيع) افضل لكل فرد (حل) مع آلية معدلة لتقليص حجم الأرشيف. بالإضافة

لاستخدام نظرية المجموعات الضبابية (المضبضة) لإستخلاص أفضل حلّ مساومة" بين الدوال. تم عمل عدّة محاولات لتحقيق الأمثلية باستخدام الطريقة المُقترحة على النظام ذي الثلاثة وحدات توليدية والنظام ذي الست وحدات توليدية (نظام IEEE ذي الثلاثون ناقل قدرة القياسي) الاختبارية. النتائج توضح قابليات الطريقة المُقترحة لتوليد حلول عملية ليست تحت الهيمنة موزعة بشكل جيد مثالية بمفهوم بريتو في محاولة واحدة لتحقيق الأمثلية. المقارنة بالطرق المتعددة الاهداف الأخرى تظهر تفوق الطريقة المُقترحة.

الكلمات الرئيسية: الخوارزمية الجينية -التضئيل متعدد المعايير - ارسالية قدرة التوليد- توليد القدرة الاقتصادية- توزيعات باريتو

1. INTRODUCTION

The objective of Economic Power Dispatch EPD of electrical power system is to schedule the committed generating unit outputs so as to meet the load demand plus real power transmission loss at minimum operating cost while satisfying all units and system equality and inequality constraints.

The increasing public awareness of environmental protection and the passage of the U.S clean air act amendments of 1990 have forced utilities to modify their design or operational strategies to reduce pollution and atmospheric emission of thermal power plants, **Abido, 2001**.

Strategies as switching to lower emission fuels or installation of pollutant clearing equipment requires considerable capital outlay, while considering emission as a constraint to be satisfied in EPD problem solution, or minimization of emission side by side with fuel cost requires modifying existing dispatching programs to include emission, **Talaq et al, 1994**. During recent years the last idea received much attention due to development of a number of multi-objective techniques.

Linearly combined fuel cost and the amount of emission as a weighted sum convert the multi-objective EEPD problem to a single-objective optimization problem, **Perez-Guerrero, 2005**. By varying the weights a set of potential solutions Pareto-optimal set were found, unfortunately this requires many runs as many as number of Pareto-front individuals to form the Pareto-optimal solutions as well as the diversity of Pareto-optimal set along Pareto-front depend on the diversity of the weights. Alternatively, many attempts to solve the EEPD were done by handling emission minimization as another objective function using stochastic multi-objective approaches. M. Abido used NSGA, **Abido, 2001**, NPGA, **Abido, 2003a** and SPEA **Abido, 2003** to solve EEPD problem and obtained the better results using SPEA, although T.F. **Robert, King et al, 2004**, and S. **Agrawal, Agrawal et al, 2008** obtains a better

results less fuel cost than SPEA using NSGA-II, FCPSPSO respectively but the corresponding emission amount increased due to conflicting objectives. An extensive evaluation may be done by inserting a real penalty price factor the tax legislated to calculate the overall cost and helping to state the better solution.

SPEA2 which is used in this paper is the improved version of SPEA to solve the multi-objective EEPD problem, SPEA2 uses an archive to store the non-dominated individuals, fitness assignment which takes into account both dominated and dominating other individuals and archive truncation to maintain a constant archive size with good diversity, **Zitzler et al, 2001**. A fuzzy-based mechanism is used to extract a Pareto-optimal solution as the best compromise solution. Two test systems were used to compare and state the superiority SPEA2 with other multi-objective approaches.

2. PROBLEM FORMULATION

The EEPD, involves the simultaneous optimization of fuel cost and emission amount as multi-objective conflicting problem, is generally formulated as follows.

2.1 Problem's Objectives

1. Minimization of fuel cost: The generator consumption fuel cost curves are represented by quadratic functions where the total consumed fuel cost $F(PG)$ in (\$/h) can be expressed as

$$F(P_G) = \sum_{i=1}^n a_i + b_i P_{Gi} + c_i P_{Gi}^2 \quad (1)$$

Where n is the number of generators, a_i , b_i , and c_i are cost coefficients of the i^{th} generator, and P_{Gi} is the real power output of the i^{th} generator, **Abido, 2001**.

2. Minimization of emission amount: The total emission $E(PG)$ in (ton/h) of atmospheric pollutants such as sulfur oxides SO_x or nitrogen oxides NO_x caused by fossil-fueled thermal generating units may be expressed as, **Perez-Guerrero, 2005**.

$$E(P_G) = \sum_{i=1}^n \alpha_i P_{Gi}^2 + \beta_i P_{Gi} + \gamma_i \quad (2)$$

Or

$$E(P_G) = \sum_{i=1}^n \alpha_i + \beta_i P_{Gi} + \gamma_i P_{Gi}^2 + \zeta_i \exp(\lambda_i P_{Gi}) \quad (3)$$

Where $\alpha_i, \beta_i, \gamma_i, \zeta_i$ and λ_i are i^{th} generator emission coefficients and P_G is the vector of real power outputs of system generators so,

$$P_G = [P_{G1}, P_{G2}, \dots, P_{Gn}]^T \quad (4)$$

2.2 Problem's Constraints

1. Generator capacity constraints: The real power output of each generator is restricted by the lower and upper limits as follows:

$$P_{Gi}^{\min} \leq P_{Gi} \leq P_{Gi}^{\max} \text{ for } i=1, 2, \dots, n \quad (5)$$

2. Power balance constraint: The total generated real power should exactly cover the total demand PD and real power loss in transmission lines PL as follows, Abido, 2001,

$$\sum_i^n P_{Gi} - PD - PL = 0 \quad (6)$$

2.3 The EEPD Problem Formulations

The EEPD problem is formulated as:

$$\text{Minimize } [F(P_G), E(P_G)]$$

Subject to:

$$g(P_G) = 0 \quad (\text{equality constraint})$$

$$h(P_G) \leq 0 \quad (\text{inequality constraint})$$

The real power loss in transmission lines PL can be considered as another objective function which needs to be minimized, Abido, 2001.

3. MULTI-OBJECTIVE OPTIMIZATION

3.1 Basic Concepts

Multi-objective optimization (MOP) to several objective functions (which are often competing and conflicting objectives) simultaneously obtains a set of optimal solutions (instead of one solution) since none of them are considered better with respect to all objectives. The MOP to N_{obj} objective function can be formulated as, **Abraham et al, 2005**:

$$\text{Minimize } [f_1(x), f_2(x), \dots, f_{N_{obj}}(x)]$$

Subject to the m equality constraints:

$$g_i(x) = 0, \text{ for } i = 1, 2, \dots, m \quad (7.a)$$

And the p inequality constraints:

$$h_i(x) \leq 0, \text{ for } i = 1, 2, \dots, p \quad (7.b)$$

Where $x = [x_1, x_2, \dots, x_n]^T$ is the vector of decision variables. The Pareto-optimality is explained as follows: a vector $x^* \in \mathcal{F}$ is Pareto-optimal if for every other vector $x \in \mathcal{F}$

$$\begin{aligned} f_i(x^*) &\leq f_i(x) && \text{for all } i=1, 2, \dots, N_{obj} && \text{and} \\ f_j(x^*) &< f_j(x) && \text{for at least one } j. \end{aligned}$$

Where \mathcal{F} is the feasible set (its elements satisfy **Eqs. (7.a) and (7.b)**), the vector x^* is called non-dominated since there is no such x which dominate it, all non-dominated solutions (vectors) forms Pareto-optimal set.

3.2 The Strength Pareto Evolutionary

Algorithm 2 (SPEA2)

E. Zitzler, M. Laumanns, and L. Thiele, had developed SPEA in 1999, Zitzler and Thiele, 1999, yet in 2001 they published SPEA2, **Zitzler et al, 2001** as enhancement version, by fixing (improving) the potential weakness in fitness assignment, density estimation and archive truncation. Like the earlier SPEA, SPEA2 has external archive to store non-dominated individual and only these individuals form the mating pool. The SPEA2 has an overall algorithm as follow:

Step1: Initialization: Generate an initial population P_0 and create the empty archive (external set) $\bar{P}_0 = \emptyset$; Set $t = 0$.

Step 2: Fitness assignment: Calculate fitness values of individuals in P_t and \bar{P}_t , each individual i in the archive \bar{P}_t and the population P_t is assigned a strength value $S(i)$, representing the number of solutions (individuals) which it dominates:

$$S(i) = |\{j | j \in (P_t + \bar{P}_t) \wedge i \succ j\}| \quad (8)$$

Where $|\cdot|$ denotes the cardinality of a set (the number of elements in a set), $+$ stands for multi-set union, $>$ corresponds to Pareto dominance relation ($i > j$ refers to that individual i which dominates individual j) and $i, j \in \bar{P}_t + P_t$.

On the basis of the S values, the raw fitness is determined by the strengths of its dominators in both archive and population, The raw fitness $R(i)$ of an individual i is calculated:

$$R(i) = \sum_{j \in Ag + \bar{Ag}, j > i} S(j) \quad (9)$$

Since the non-dominated individuals would have the same raw fitness value $R(i)=0$, while a high $R(i)$ value means that individual i is dominated by many individuals. Therefore additional density information is incorporated to discriminate between individuals having identical raw fitness values. The density estimation technique used in SPEA2 is an adaptation of the k^{th} nearest neighbor method, Zitzler et al, 2001, for each individual i the distances (in objective space) to all other individuals j in archive and population are calculated and stored in a list. After sorting the list in ascending order, the k^{th} element gives the distance sought. As a common setting, k equal to the square root of the entire population size $= \sqrt{N + \bar{N}}$. Where N is a population (P_t) size and \bar{N} is an archive (\bar{P}_t) size.

The distance between the individuals i and k is denoted as σ^k_i . Density $D(i)$ corresponding to i is defined by

$$D(i) = \frac{1}{\sigma^{k_i+2}} \quad (10)$$

By adding $D(i)$ to the raw fitness value $R(i)$ of an individual i yields its fitness $F(i)$:

$$F(i) = R(i) + D(i) \quad (11)$$

Step 3: **Environmental selection:** Copy all non-dominated individuals in P_t and \bar{P}_t to \bar{P}_{t+1} . If size of \bar{P}_{t+1} exceeds \bar{N} then reduce \bar{P}_{t+1} by means of the modified truncation operator, so, at each iteration the individual i which has the minimum distance to another individual j and $\sigma^k_i < \sigma^k_j$ is chosen for removal; otherwise if size of \bar{P}_{t+1} is less than \bar{N} then fill \bar{P}_{t+1} with dominated individuals in P_t and \bar{P}_t , by

sorting the multi-set $P_t + \bar{P}_t$ according to the fitness values and copy the first $N - |P_t + 1|$ individuals i with $F(i) \geq 1$ from the resulting ordered list to \bar{P}_{t+1} .

Step4: **Termination:** If $t = T$ (maximum number of generations) then stop.

Step5: **Mating selection:** Perform binary tournament selection with replacement on \bar{P}_{t+1} in order to fill the mating pool.

Step6: **Variation:** Apply recombination and mutation operators to the mating pool and set \bar{P}_{t+1} to the resulting population. Increment generation counter ($t = t + 1$) and go to step 2.

3.3 Real-Valued (Coded) Genetic Algorithm

The calculations of objective functions many times in the process of the simulation computer program make coding and decoding individuals from and to binary-coded time consuming as well as coding one individual of 3-unit system having the same accuracy obtained in real-valued string needs 3×20 bits, since there are 3 variables of P_G and each variable needs at least 4 digits of 0, 1, assuming the population size is 5. Therefore the genetic algorithm string is represented in a vector of real-valued of power outputs of system generators as:

$$P_G = [P_{G1}, P_{G2}, \dots, P_{Gn}]^T$$

1. **Recombination (crossover):** A blending crossover operator has been employed. This operator recombines the i^{th} parameter (gene) values of individuals x, y (selected for recombination), the offspring appear as follows:

$$x = [x_1, x_2, \dots, x'_i, y_{i+1}, \dots, y_n]$$

$$y = [y_1, y_2, \dots, y'_i, x_{i+1}, \dots, x_n]$$

Where the offspring are:

$$x'_i = x_i + \beta(y_i - x_i)$$

$$y'_i = y_i - \beta(y_i - x_i)$$

And β is a randomly generated number between 0 and 1.

2. **Mutation:** a non-uniform mutation operator is employed in this study, Michalewicz, 1996, the new

value x_i'' of the parameter x_i after mutation at generation t is given as:

$$x_i'' = \begin{cases} x_i + \Delta(t, P_i^{max} - x_i) & \text{if random binary digit is 0} \\ x_i - \Delta(t, x_i - P_i^{min}) & \text{if random binary digit is 1} \end{cases} \quad (12)$$

$$\Delta(t, y) = y * \left(1 - rand^{(1 - \frac{t}{T})^b}\right) \quad (13)$$

Due to the imprecise nature of the decision maker's judgment, the i^{th} objective function of a solution in the Pareto-optimal set Fi is represented by a membership function μ_i which is a Z-function asymmetrical polynomial curve, defining by:

$$\mu_i = \begin{cases} 1 & Fi \leq F_i^{min} \\ \frac{F_i^{max} - Fi}{F_i^{max} - F_i^{min}} & F_i^{min} < Fi < F_i^{max} \\ 0 & Fi \geq F_i^{max} \end{cases} \quad (14)$$

Where F_i^{max} and F_i^{min} are the maximum and minimum values of the i^{th} objective function, respectively.

For each non-dominated solution h , the normalized membership function μ^h is calculated as:

$$\mu^h = \frac{\sum_{i=1}^{Nobj} \mu_i^h}{\sum_{h=1}^M \sum_{i=1}^{Nobj} \mu_i^h} \quad (15)$$

Whereas M is the number of non-dominated solutions. The best compromise solution is the one having the maximum value of μ^h . By arranging all solutions in Pareto-optimal set in descending order according to their membership function will provide the decision maker with a priority list of non-dominated solutions. This will guide the decision maker in view of the current operating conditions. The implementation flow chart of the proposed approach is shown in **Fig.1**

Where $rand$ is a random number generator between (0,1), t is iteration index, T is maximum number of iterations and $b=5$, Michalewicz, 1996.

3.4 Best Compromise Solution

The solutions obtained for best (minimal) fuel cost and for best (minimal) emission amount were giving an image about the optimized objective functions, but in order to adopt one solution as the best compromise solution to the decision maker's judgment, the proposed approach presents a fuzzy-based mechanism to extract a Pareto-optimal solution as the best compromise solution, Abido, 2003.

4. IMPLEMENTATION OF THE PROPOSED METHOD

To satisfy the problem constraints, the following steps had been made:

(a) The initial population is generated within a capacity limit of each generator as well as the recombination and mutated elements are as follows:

$$P_{Gi} = (P_{Gi}^{max} - P_{Gi}^{min}) * rand + P_{Gi}^{min} \quad (16)$$

Whereas $rand$ is a random number generator between (0, 1).

(b) The power balance constraint is satisfied as follows, the traditional B-matrix loss formula is used to calculate the real power transmission loss

$$PL = \sum_{i=1}^n \sum_{j=1}^n P_{Gi} B_{ij} P_{Gj} + \sum_{i=1}^n B_{io} P_{Gi} + B_{oo} \quad (17)$$

By choosing the r^{th} unit randomly, it's assumed that the r^{th} reference unit power output is responsible of bucking up the remaining load after the other $(n-1)$ units have been assigned theirs output power,

$$P_{Gr} = PD + PL - \sum_{\substack{i=1 \\ i \neq r}}^n P_{Gi} \quad (18)$$

Rewriting eq. (18) in order to form a polynomial with P_{Gr} is the variable as follows:

$$PL = aP_{Gr}^2 + bP_{Gr} + c \quad (19)$$

Where a , b , and c represent parameters depending on the B-matrix coefficients of the power loss equation of the test system used and on the powers of the $(n-1)$ generators.

Substituting PL from **Eq. (19)** in **Eq. (18)**, yields

$$aP_{Gr}^2 + (b-1)P_{Gr} + \left(c + PD - \sum_{i \neq r}^n P_{Gi}\right) = 0 \quad (20)$$

The roots of the eq. (20) represent the value of P_{Gr} satisfying equality constraint, if neither roots located within unit power capacity limit, other generator is randomly chosen as r^{th} reference unit also, if all units were failed to backup the remaining load another individual is generated randomly to replace this one. After recombination and mutation process each individual is checked for equality constraint violation, it is worth to mention that this process works as another mutation operator. Since, it may vary the value of one gene (generating unit) to achieve equality constraint satisfaction, or it may be the reason of destroying the recombination operator process (if the recombination gene is chosen to be the first or the last in the individual string).

(c) Archive truncation modification

By formulating (a distance matrix) with size $[\bar{P}_{t+1} \times \bar{P}_{t+1}]$, this matrix contains each possible pair of two individuals in archive set \bar{P}_{t+1} (before truncation process), reducing the dependency on the k^{th} nearest neighbor method, the process is as follows:

Step1: form the distance matrix, calculating the distance σ_j^i between each pair of non-dominated individuals (i,j) in multi-objective space.

Step2: searching the matrix for smallest element σ_j^i (represents the minimum distance between any two individuals i,j).

Step3: If $\sigma_i^k < \sigma_j^k$, individual i would be eliminated from archive and its row and column would be eliminated too, else the individual j is chosen for elimination and the size of \bar{P}_{t+1} and distance matrix reduced by one.

Step4: If $\bar{P}_{t+1} = \bar{N}$ then stop, else go to step 2.

5. RESULTS AND DISCUSSION

In this research two systems were adopted in order to investigate the effectiveness and applicability of the proposed method, several simulations runs were done for each test and an identical population and archive sizes were used, **Zitzler et al, 2001**, the parameters used for all cases are as follows: 200 individuals for each population size and archive size for case (1) and 100 individuals for each population size and archive

size for case (2) and the simulations were run for 1000 generations, crossover and mutation probabilities were 1(100%) and 0.01 respectively.

Case (1): Three Generating Units System

The three generators test system whose data are given in **Tables 1, 2 and 3, King, 2003**, the system demand is 850 MW, and the system transmission losses are calculated using a simplified loss expression, **King, 2003**:

$$PL = 0.00003P_{G1}^2 + 0.00009P_{G2}^2 + 0.00012P_{G3}^2 \quad (21)$$

The coefficients of eq. (19) are

$$a=B_{rr}, b=0 \text{ and } c = \sum_{i \neq r}^N \sum_{j=1}^N P_{Gi} B_{ij} P_{Gj}$$

It is important to maintain that the cross-point in the proposed approach applied to solve this test system is fixed in the second gene (second generating unit position) to grantee new individuals generated next population.

Test (1): Fuel Cost and SO₂ Emission Objective Functions:

In this test fuel cost with SO₂ emission were taken as objective functions to be minimized, **Tables 4, 5, and 6** show the simulation results obtained in one run for best (minimum) fuel cost, minimum emission and best compromise solution in the Pareto front respectively, as compared to TABU search and NSGA-II, while the Pareto-front were plotted in **Fig. 2**.

Table 4 shows a reduction in the consumption fuel cost by more than 100 \$ per year than the results obtained by NSGA-II approach. While, **Table 5** shows a reduction in SO₂ harmful emission by 5.6 ton per year than the results obtained by NSGA-II approach for this small system.

The minimum fuel cost and minimum emission solutions were drawn against generations (iterations) in **Fig. 3**. The average simulation run time for this test is 550 second.

The convergence of non-dominated solutions to the true Pareto-optimal front region was done in early stages of the search process (20-30 % of the maximum generations limit), as shown in **Fig. 3**, the later stages is for convergence to the exact solutions (fine tuning).

Test (2): Fuel Cost and NO_x Emission Objective Functions:

In this test fuel cost with NOx were taken as objective functions to be minimized, **Tables 7, 8, and 9** shows the simulation results obtained in one run as compared to TABU search and NSGA-II, while the Pareto-front was plotted in **Fig. 4**. The average simulation run time for this test is 550 second.

Test (3): Fuel Cost, SO₂ Emission and NO_x Emission objective functions:

In this test fuel cost with SO₂ emission and NO_x emission were taken as objective functions to be minimized **Tables 10, and 11** shows the simulation results obtained in one run as compared to NSGA-II, while the Pareto-front was plotted in **Fig. 5**. The average simulation run time for the test is 780 second.

Although NSGA-II is a new powerful multi-objective technique, the results in the previous tables show that SPEA 2 gave not only better results but also with less population size and less maximum generations number, NSGA-II has population size 500 individuals and was run for 20000 generation, **King, 2003**.

Case (2): Six Generating Units System

The standard 30-bus IEEE test system with 6-generating units, King, 2004 is used with load demand 2.834 p.u. (100 MW power base), since this system has been already solved and validated by several multi-objective optimization techniques the comparison of SPEA2 with such techniques can show the potential of the proposed method, system data listed in **Tables 12, and 13**.

Test (1): Fuel Cost and Emission Objective Functions (Real Power Transmission Loss is neglected):

In this test, fuel cost with harm emission were taken as objective functions to be minimized, the system is considered as lossless and the equality constraint is as follows:

$$\sum_i^n P_{Gi} - PD = 0$$

Tables 14, 15, and 16 show the simulation results obtained in one run as compared to other approaches, while the Pareto-Optimal front was plotted in Figure 6. The average simulation run time for the test is 70 second.

The minimum fuel cost and minimum emission solutions were drawn against generations (iterations) in **Fig. 7**.

The results obtained in **Tables 14 and 15** are clearly demonstrated the superior of SPEA 2 over other multi-objective GA methods and also over the new multi-objective-PSO approach (FCPSO) with reduction in consumption fuel cost more than 190 \$ per year than FCPSO approach (table IXV), also the fuel cost corresponding to minimum emission in table XV is less than the fuel cost corresponding to minimum emission FCPSO approach.

Test (2): Fuel Cost and Emission objective functions (transmission loss is included):

The exact value of the system losses can only be determined by means of a power flow solution, but in this research the B-coefficient matrix from, Perez-Guerrero, 2005 is used:

$$B_{ij} = \begin{bmatrix} 0.1382 & -0.02299 & 0.0044 & -0.0022 & -0.0010 & -0.0008 \\ -0.0299 & 0.0487 & -0.0025 & 0.0004 & 0.0016 & 0.0041 \\ 0.0044 & -0.0025 & 0.0182 & -0.0070 & -0.0066 & -0.0066 \\ -0.0022 & 0.0004 & -0.0070 & 0.0137 & 0.0050 & 0.0033 \\ -0.0010 & 0.0016 & -0.0066 & 0.0050 & 0.0109 & 0.0005 \\ -0.0008 & 0.0041 & -0.0066 & 0.0033 & 0.0005 & 0.0244 \end{bmatrix}$$

$$B_{io} = [(-0.0107 \ 0.0060 \ -0.0017 \ 0.0009 \ 0.0002 \ 0.0030)]$$

$$B_{oo} = 9.8573 \times 10^{-4}$$

the coefficient of eq. (19) is

$$a = B_{rr}, \quad b = \sum_{i=1}^n P_{Gi} B_{ir} + \sum_{j=1}^n B_{rj} P_{Gj} + B_{ro}$$

$$\text{and } c = \sum_{i=1}^n \sum_{j=1}^n P_{Gi} B_{ij} P_{Gj} + \sum_{i=1}^n B_{io} P_{Gj} + B_{oo}$$

Tables 17, 18, and 19 show the simulation results obtained in one run as compared to other approaches, while the Pareto-front was plotted in **Fig. 8**. The average simulation run time for the test is 70 second. Other researches use load flow solution approach to determine the transmission loss instead of B-coefficient matrix approach, the transmission loss obtained by load flow solution depends on the accuracy of the load flow solution such as in FCPSO approach for example, while the accuracy of the transmission loss obtained by the B-coefficient matrix approach is within 0.25 % of the load demand, which may be accepted when is taking into consideration the computational time which is spent in load flow

solution approach compared to those which is using B-coefficient matrix approach.

Test (3) Fuel Cost, Emission and Transmission Loss Objective Functions:

In this test real power transmission loss, fuel cost and harm emission were taken as objective functions to be minimized, **Table 20** shows the three objective functions optimization results as compared with reference ,Wang, 2008, results. While, **Table 21** shows the best compromise solution. The Pareto-front was plotted in **Fig. 9**. The average simulation run time for the test is 90 second.

It is important to mention that the research in ,Wang, 2008, neglects the linear coefficient *Bio* and the constant coefficient *Boo* of the B-matrix used to calculate the power loss *PL* then, in order to obtain a good comparison results these coefficients are neglected in the obtained results in this test only.

All the simulation results obtained in this research were implemented on personal computer Pentium 4, 3.59 GHz with 1GB RAM using MATLAB version 7 programming language.

6. CONCLUSIONS

This paper presents multi-objective environmental/economic power dispatch (EPPD) solutions using the proposed Strength Pareto Evolutionary Algorithm 2 (SPEA2). The proposed method has a diversity-preserving mechanism to find widely different Pareto-optimal solutions. A distance matrix technique is implemented to provide the decision maker with diverse and manageable Pareto-front without destroying the shape and the boundary of the trade-off front. Moreover, a Fuzzy-based mechanism is employed to extract the best compromise solution over the trade-off curve as in Fig. 1. The Fuzzy system contains a fuzzy inference system, fuzzy controller with a rule base, and a defuzzifier. A triangular membership function is used. The results show that the proposed method is efficient for solving multi-objectives optimization whereas multiple Pareto-optimal solutions can be found in one simulation run. The simulation results of all the tests which were done reveal that SPEA2 presents low computational time (less population size and less generations) and is suitable for on-line EPPD solutions. The proposed method has reliable convergence, high accuracy of solution, and better results than other multi-objective

optimization techniques with good Pareto-front diversity regardless of the number of objective functions used.

7. REFERENCES

- Abido M. A., 2001, *A New Multi-objective Evolutionary Algorithm for Environmental/Economic Power Dispatch*, Power Engineering Society Summer Meeting, IEEE, Volume 2, Pages:1263–1268.
- Talaq J. H., El-Hawary F. and El-Hawary M. E., 1994, *A Summary of Environmental/Economic Dispatch Algorithms*, IEEE Transactions on Power Systems, Volume 9, No. 3, Pages: 1508–1516.
- Perez-Guerrero R. E., Cedeno-Maldonado J. R. , 2005, *Differential Evolution Based Economic Environmental Power Dispatch* power Symposium, proceedings of the 37th Annual North American, Pages: 191-197.
- Abido M. A., 2003a, *A Niche Pareto Genetic Algorithm for Multi-Objective Environmental/Economic Dispatch*, International Journal of Electrical Power & Energy Systems, Elsevier, Volume 25, No. 2, Pages: 79–105.
- Abido M. A., 2003, *Environmental/Economic Power Dispatch using Multi-Objective Evolutionary Algorithms*, IEEE Transactions on Power Systems, Volume 18, No. 4, Pages:1529–1537.
- Ah. King R. T. F., Rughooputh H. C. S. and Deb K., 2004, *Evolutionary Multi-Objective Environmental/Economic Dispatch: Stochastic vs. Deterministic Approaches*, KanGAL Report number 2004019.
- Agrawal S., Panigrahi B. K. and Tiwari M. K., 2008, *Multiobjective Particle Swarm Algorithm with Fuzzy Clustering for Electrical Power Dispatch*, Evolutionary Computation, IEEE Transactions on Evolutionary Computation, Volume 12, Issue 5, Pages:529 - 541.
- Zitzler E., Laumanns M., and Thiele L., 2001, *SPEA2: Improving the Strength Pareto Evolutionary Algorithm*, TIK-Rep.



Abraham A., Jain L. and Goldberg R., 2005, *Evolutionary Multi-Objective Optimization: Theoretical Advances and Applications*, Springer-Verlag, London.

Zitzler E. and Thiele L., 1999, *Multi-Objective Evolutionary Algorithms: A Comparative Case Study and the Strength Pareto Approach*, *IEEE Transactions on Evolutionary Computation* Volume 3, no. 4, Pages:257-271.

Michalewicz Z., 1996, *Genetic Algorithms + Data Structures = Evolution Programs*, 3rd ed., Springer-Verlag, Berlin.

R.T.F.A King and Rughooputh H.C.S. , 2003, *Elitist Multi-objective Evolutionary Algorithm for Environmental/Economic Dispatch*, *Evolutionary Computation*, IEEE, Volume 2, pages: 1108-1114.

Wang L. F. and Singh C., 2008, *Stochastic Economic Emission Load Dispatch Through a Modified Particle Swarm Optimization Algorithm* Elsevier, *Electric Power Systems Research*, Volume 78, Issue 8, Pages:1466-1476.

Table 1. Fuel cost coefficients.

Unit i	a_i	b_i	c_i	P_{Gi}^{min} (MW)	P_{Gi}^{max} (MW)
1	561	7.92	0.001562	150	600
2	310	7.85	0.00194	100	400
3	78	7.97	0.00482	50	200

Table 2. SO₂ (Sulfur oxide) emission coefficients.

Unit i	α_{iN}	β_{iN}	γ_{iN}
1	1.4721848e-7	-9.4868099e-5	0.04373254
2	3.0207577e-7	-9.7252878e-5	0.055821713
3	1.9338531e-6	-3.5373734e-4	0.027731524

Table 3. NO_x (Nitrogen Oxides) Emission Coefficients.

Unit i	α_{iN}	β_{iN}	γ_{iN}
1	1.4721848e-7	-9.4868099e-5	0.04373254
2	3.0207577e-7	-9.7252878e-5	0.055821713
3	1.9338531e-6	-3.5373734e-4	0.027731524

Table 4. Best fuel cost.

Unit i (MW)	TABU search (King, 2003)	NSGA-II (King, 2003)	SPEA2
P_{G1}	435.69	436.366	435.2538
P_{G2}	298.828	298.187	299.6112
P_{G3}	131.28	131.228	130.9553
Losses(MW)	15.798	15.781	15.8203
Fuel cost(\$/h)	8344.598	8344.606	8344.5935
Emission (ton/h)	9.02146	9.02083	9.0219

Table 5. Best SO₂ emission.

Unit i (MW)	TABU search (King, 2003)	NSGA-II (King, 2003)	SPEA2
P_{G1}	549.247	541.308	551.4131
P_{G2}	234.582	223.249	219.9989
P_{G3}	81.893	99.919	93.10592
Losses(MW)	15.722	14.476	14.5179
Fuel cost(\$/h)	8403.485	8387.518	8395.8514
Emission(ton/h)	8.974	8.96655	8.9659

Table 6. Best compromise solution.

Unit i (MW)	NSGA-II (King, 2003)	SPEA2
P_{G1}	485.886	493.2324
P_{G2}	263.67	259.8824
P_{G3}	115.381	111.7609
Losses(MW)	14.937	14.8757
Fuel cost(\$/h)	8354.419	8357.442
Emission(ton/h)	8.98383	8.9801

Table 7. Best fuel cost.

Unit i (MW)	TABU search (King, 2003)	NSGA-II (King, 2003)	SPEA2
P_{G1}	435.69	435.885	435.2475
P_{G2}	298.828	299.989	299.751
P_{G3}	131.28	129.951	130.8251
Losses(MW)	15.798	15.826	15.8236
Fuel cost (\$/h)	8344.598	8344.598	8344.593
Emission(ton/h)	0.09863	0.09860	0.098694

Table 8. Best NO_x emission.

Unit <i>i</i> (MW)	TABU search (King, 2003)	NSGA-II (King, 2003)	SPEA2
P_{G1}	502.914	505.810	508.1853
P_{G2}	254.294	252.951	250.7858
P_{G3}	108.592	106.023	105.7796
Losses(MW)	15.8	14.784	14.7507
Fuel cost(\$/h)	8371.143	8363.627	8364.8956
Emission(ton/h)	0.0958	0.09593	0.095924

Table 9. Best compromise solution.

Unit <i>i</i> (MW)	NSGA-II (King, 2003)	SPEA2
P_{G1}	470.957	464.4353
P_{G2}	280.663	286.072
P_{G3}	113.675	114.9137
Losses (MW)	15.294	15.421
Fuel cost(\$/h)	8349.722	8348.1913
Emission(ton/h)	0.09654	0.096768

Table 10. Comparison of results for three objective functions.

Unit <i>i</i> (MW)	Best fuel cost		Best SO ₂ emission		Best NO _x emission	
	NSGA-II (King, 2003)	SPEA2	NSGA-II (King, 2003)	SPEA2	NSGA-II (King, 2003)	SPEA2
P_{G1}	431.68	433.73	538.53	552.05	508.37	508.57
P_{G2}	302.93	300.86	227.82	219.62	250.44	250.48
P_{G3}	131.31	131.26	98.185	92.857	105.93	105.70
Losses (MW)	15.919	15.858	14.528	14.518	14.745	14.747
Fuel cost (\$/h)	8344.65	8344.6	8385.1	8396.4	8364.9	8365.1
SO₂ Emission (ton/h)	9.0254	9.0234	8.9667	8.9659	8.9737	8.9737
NO_x Emission (ton/h)	0.0989	0.0988	0.0963	0.0968	0.0959	0.0959

Table 11. Best compromise solution for three objective functions.

<i>Unit i (MW)</i>	NSGA-II (King, 2003)	SPEA2
P_{G1}	496.328	492.5533
P_{G2}	260.426	259.9366
P_{G3}	108.144	112.3851
<i>Losses (MW)</i>	14.898	14.8749
Fuel cost (\$/h)	8358.896	8357.1467
SO₂ emission (ton/h)	8.97870	8.9804
NOx emission (ton/h)	0.09599	0.096076

Table 12. Fuel cost coefficients.

Unit <i>i</i>	<i>ai</i>	<i>bi</i>	<i>ci</i>	P_{Gi}^{min} (p.u.)	P_{Gi}^{max} (p.u.)
1	10	200	100	0.05	0.5
2	10	150	120	0.05	0.6
3	20	180	40	0.05	1.0
4	10	100	60	0.05	1.2
5	20	180	40	0.05	1.0
6	10	150	100	0.05	0.6

Table 13. Emission coefficients.

Unit <i>i</i>	<i>ai</i>	β_i	γ_i	ζ_i	λ_i
1	4.091e-2	-5.554e-2	6.490e-2	2.0e-4	2.857
2	2.543e-2	-6.047e-2	5.638e-2	5.0e-4	3.333
3	4.258e-2	-5.094e-2	4.586e-2	1.0e-6	8.000
4	5.326e-2	-3.550e-2	3.380e-2	2.0e-3	2.000
5	4.258e-2	-5.094e-2	4.586e-2	1.0e-6	8.000
6	6.131e-2	-5.555e-2	5.151e-2	1.0e-5	6.667

Table 14. Best fuel cost.

nit <i>i</i> (p.u.)	NPGA (Abido, 2003a)	SPEA (Abido, 2003)	NSGA-II (King, 2004)	FCPSO (Agrawal, 2008)	SPEA2
P_{G1}	0.1080	0.1062	0.1059	0.1070	0.10978
P_{G2}	0.3284	0.2897	0.3177	0.2897	0.2993
P_{G3}	0.5386	0.5289	0.5216	0.525	0.52433
P_{G4}	1.0067	1.0025	1.0146	1.015	1.0162
P_{G5}	0.4949	0.5402	0.5159	0.530	0.52457
P_{G6}	0.3574	0.3664	0.3583	0.3673	0.35981
Fuel Cost (\$/h)	600.259	600.15	600.155	600.131	600.109
Emission (ton/h)	0.22116	0.2215	0.22188	0.2223	0.22215

**Table 15.** Best emission.

Unit i (p.u.)	NPGA (Abido, 2003a)	SPEA (Abido, 2003)	NSGA-II (King, 2004)	FCPSO (Agrawal, 2008)	SPEA2
P_{G1}	0.4002	0.4116	0.4074	0.4097	0.40607
P_{G2}	0.4474	0.4532	0.4577	0.455	0.45898
P_{G3}	0.5166	0.5329	0.5389	0.5363	0.53785
P_{G4}	0.3688	0.3832	0.3837	0.3842	0.38308
P_{G5}	0.5751	0.5383	0.5352	0.5348	0.53785
P_{G6}	0.5259	0.5148	0.5110	0.514	0.51017
Emission (ton/h)	0.19433	0.1942	0.1942	0.1942	0.1942
Fuel Cost (\$/h)	639.182	638.51	638.269	638.357	638.264

Table 16. Best compromise solution.

Unit i (p.u.)	NPGA (Abido, 2003a)	SPEA (Abido, 2003)	SPEA2
P_{G1}	0.2696	0.2785	0.11044
P_{G2}	0.3673	0.3764	0.30004
P_{G3}	0.5594	0.5300	0.52349
P_{G4}	0.6496	0.6931	1.0159
P_{G5}	0.5396	0.5406	0.52406
P_{G6}	0.4486	0.4153	0.36009
Fuel Cost(\$/h)	612.127	610.254	600.1115
Emission(ton/h)	0.19941	0.2005	0.22209

Table 17. Best fuel cost.

Unit i (p.u.)	NPGA (Abido, 2003a)	SPEA (Abido, 2003)	NSGA-II (King, 2004)	FCPSO (Agrawal, 2008)	SPEA2
P_{G1}	0.1245	0.1086	0.1182	0.1130	0.12048
P_{G2}	0.2792	0.3056	0.3148	0.3145	0.28649
P_{G3}	0.6284	0.5818	0.5910	0.5826	0.5822
P_{G4}	1.0264	0.9846	0.9710	0.9860	0.99335
P_{G5}	0.4693	0.5288	0.5172	0.5264	0.5248
P_{G6}	0.3993	0.3584	0.3548	0.3450	0.3523
Fuel Cost (\$/h)	608.147	607.807	607.801	607.786	605.998
Emission (ton/h)	0.22364	0.22015	0.21891	0.2201	0.22076

Table 18. Best emission.

Unit i (p.u.)	NPGA (Abido, 2003a)	SPEA (Abido, 2003)	NSGA-II (King, 2004)	FCPSO (Agrawal, 2008)	SPEA2
P_{G1}	0.3923	0.4043	0.4141	0.4063	0.41072
P_{G2}	0.4700	0.4525	0.4602	0.4586	0.46356
P_{G3}	0.5565	0.5525	0.5429	0.5510	0.54474
P_{G4}	0.3695	0.4079	0.4011	0.4084	0.39033
P_{G5}	0.5599	0.5468	0.5422	0.5432	0.54446
P_{G6}	0.5163	0.5005	0.5045	0.4974	0.5155
Emission (ton/h)	0.19422	0.19422	0.19419	0.1942	0.19418
Fuel Cost (\$/h)	645.984	642.603	644.133	642.896	646.190

Table 19. Best compromise solution.

Unit i (p.u.)	NPGA (Abido, 2003a)	SPEA (Abido, 2003)	SPEA2
P_{G1}	0.2227	0.2594	0.12048
P_{G2}	0.3787	0.3848	0.28649
P_{G3}	0.5560	0.5645	0.5822
P_{G4}	0.7147	0.7030	0.99335
P_{G5}	0.5500	0.5431	0.5248
P_{G6}	0.4424	0.4091	0.3523
Fuel Cost (\$/h)	615.097	616.069	605.9986
Emission (ton/h)	0.20207	0.20118	0.22076

**Table 20.** Comparison of results of three objective functions optimization.

Unit i (p. u.)	Minimum Fuel Cost		Minimum Emission		Minimum Transmission Loss	
	MOPS (Wang, 2008)	SPEA2	MOPS (Wang, 2008)	MOPS (Wang, 2008)	SPEA2	MOPS (Wang, 2008)
P_{G1}	0.1789	0.1115	0.3606	0.1789	0.1115	0.3606
P_{G2}	0.2888	0.2906	0.4568	0.2888	0.2906	0.4568
P_{G3}	0.5776	0.5807	0.5100	0.5776	0.5807	0.5100
P_{G4}	0.9388	0.9940	0.5184	0.9388	0.9940	0.5184
P_{G5}	0.4973	0.5245	0.5598	0.4973	0.5245	0.5598
P_{G6}	0.3770	0.3556	0.4657	0.3770	0.3556	0.4657
Losses (p. u.)	0.0233	0.0231	0.0313	0.0233	0.0231	0.0313
Fuel cost (\$/h)	606.54	605.42	633.70	606.54	605.42	633.70
Emission (ton/h)	0.2002	0.2209	0.1953	0.2002	0.2209	0.1953

Table 21. Best compromise solution.

Unit i (p. u.)	SPEA2
P_{G1}	0.13811
P_{G2}	0.25129
P_{G3}	0.90012
P_{G4}	0.60386
P_{G5}	0.56767
P_{G6}	0.39051
Losses (p. u.)	0.017558
Fuel cost (\$/h)	620.3921
Emission (ton/h)	0.21193

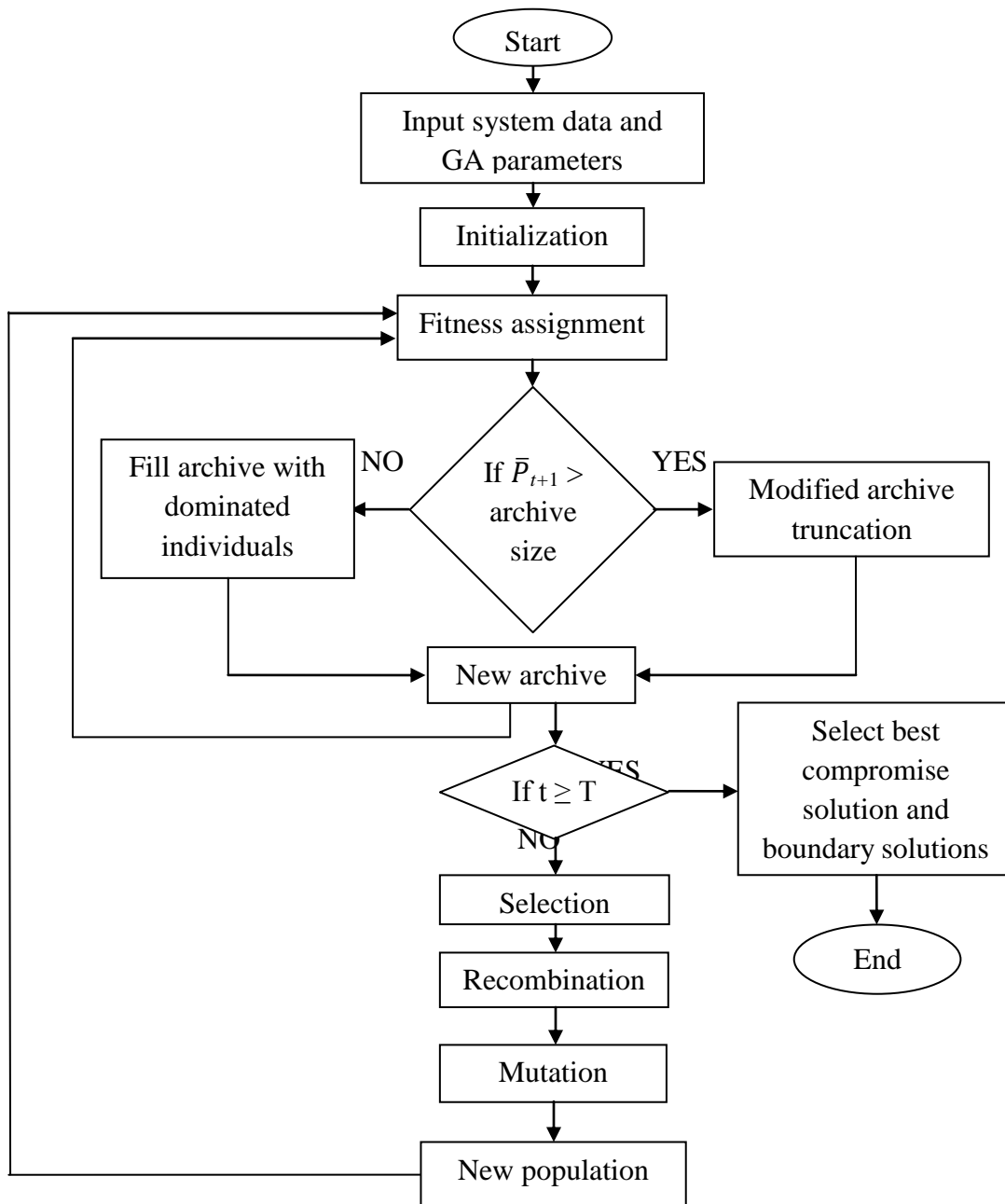


Figure1.The strength pareto evolutionary algorithm 2 flow chart.

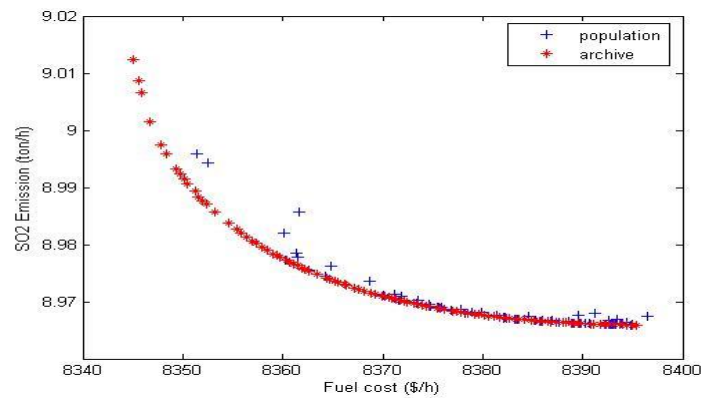


Figure2. Pareto –optimal front for case (1) test (1).

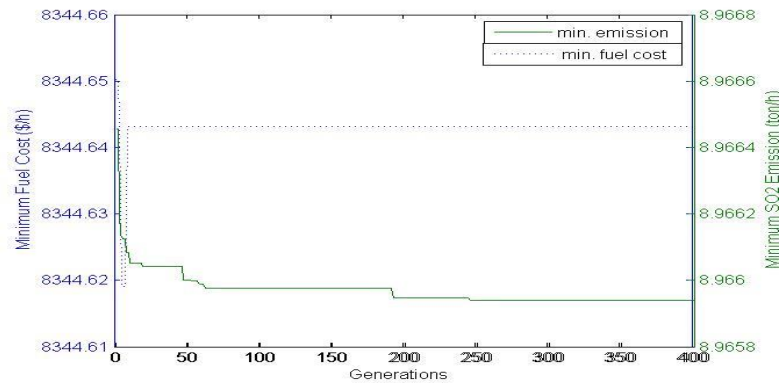


Figure3. Convergence of min. fuel cost and min. emission of the proposed method for system (1), test (1).

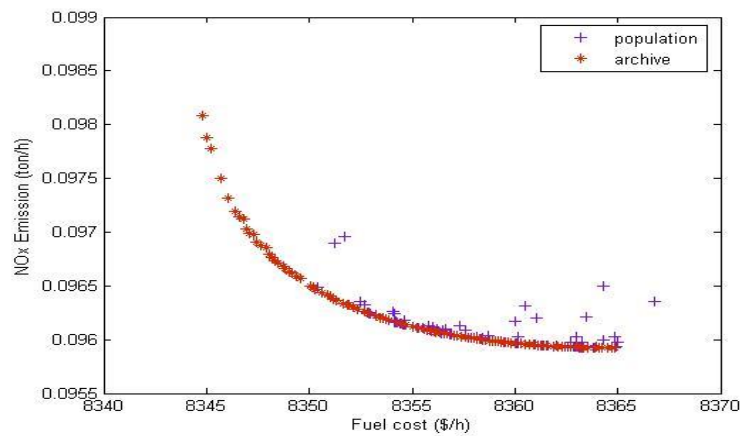


Figure4. Pareto-optimal front for case (1) test (2).

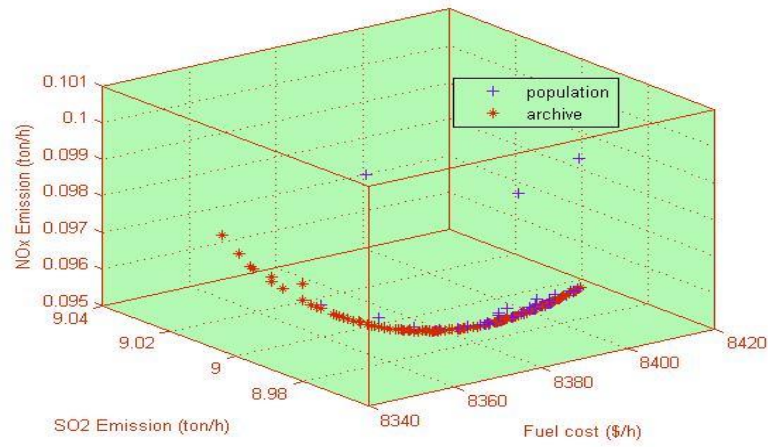


Figure5. Pareto-optimal front for case (1), test (3).

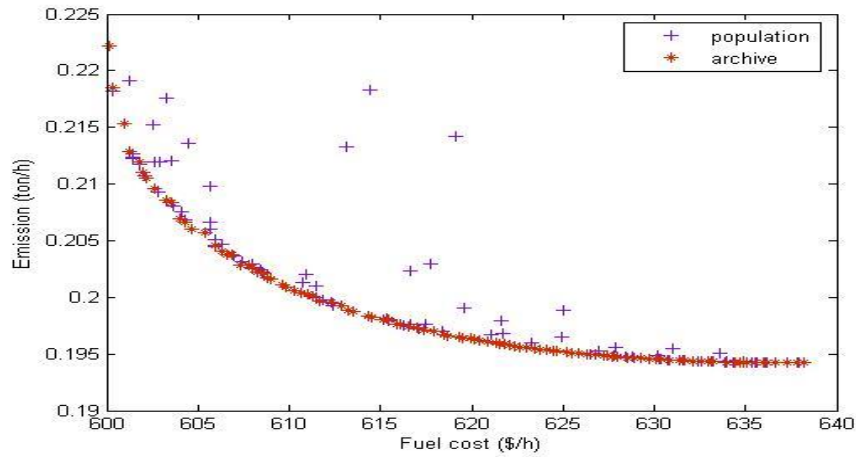


Figure6. Pareto-optimal front for case (2) test (1).

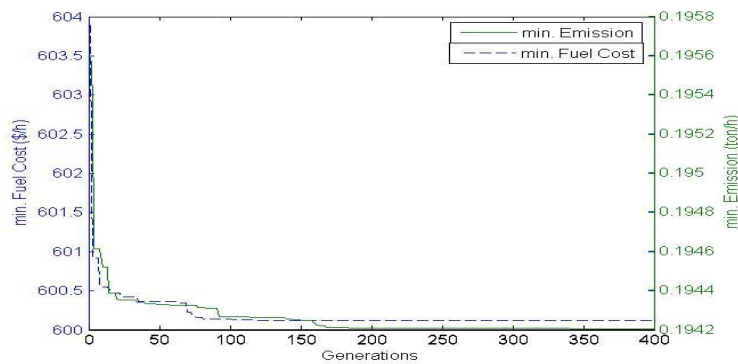


Figure7.Convergence of min. fuel cost and min. emission of the proposed method for system 2, test (1).

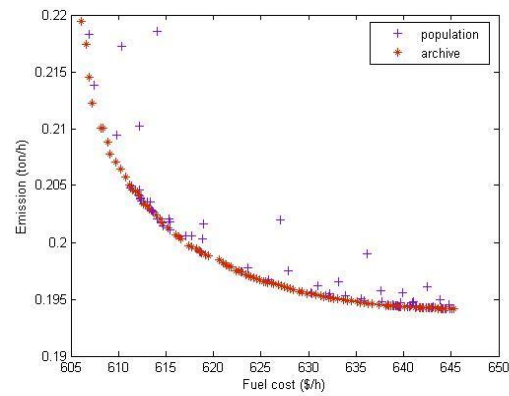


Figure8. Pareto-optimal front for case (2), test (2).

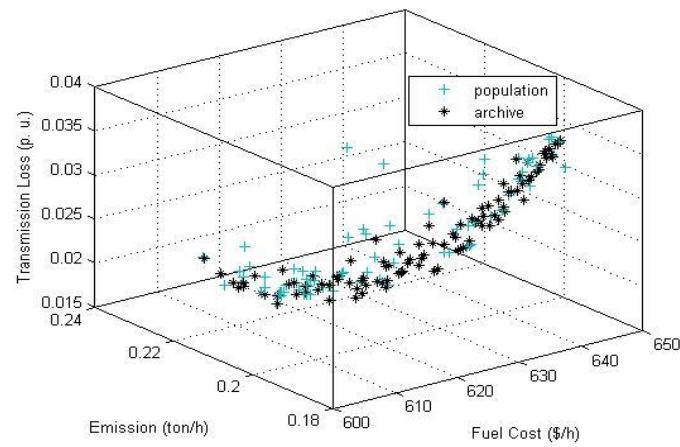


Figure9. Pareto-optimal front for case (2) test (3).

Estimation of Some Mechanical Soil Properties from Static and Dynamic Plate Load Tests

Hayder Alwan Mahdi Al-Zayadi
Ass. Lecturer, Eng. College-Civil Dept.
Baghdad University
Email: civil_hayder1974@yahoo.com

ABSTRACT

When the depth of stressed soil is rather small, Plate Load Test (PLT) becomes the most efficient test to estimate the soil properties for design purposes. Among these properties, modulus of subgrade reaction is the most important one that usually employed in roads and concrete pavement design. Two methods are available to perform PLT: static and dynamic methods. Static PLT is usually adopted due to its simplicity and time saving to be performs in comparison with cyclic (dynamic) method. The two methods are described in ASTM standard.

In this paper the effect of the test method used in PLT in estimation of some mechanical soil properties was distinguished via a series of both test methods applied in a same site. The comparison of the test results between both methods showed that the dynamic (cyclic) method gives lower values of soil properties than the static one does.

Key words: Plate load test, modulus of subgrade reaction, dynamic, static.

تخمين بعض خصائص التربة الميكانيكية من فحصي تحميل الصفيحة الاستاتيكي والديناميكي

حيدر علوان مهدي الزياي
مدرس مساعد

الخلاصة

عندما يكون عمق التربة المجهدة قليل نسبياً يصبح فحص تحميل الصفيحة أكثر الفحوص فعالية لتخمين خصائص التربة للأغراض التصميمية. ومن بين هذه الخصائص يعتبر معامل رد الفعل الأرضي الأهم والذي عادة ما يستعمل في تصاميم الطرق والبلاطات الخرسانية. وتتوفر طريقتان لأنجاز فحص تحميل الصفيحة: الطريقة الإستاتيكية والطريقة الديناميكية. وغالباً ما يتم تبني الطريقة الإستاتيكية في فحص تحميل الصفيحة لسهولة ولغرض التوفير بالوقت إذا ما قورنت بالطريقة الدورية (الديناميكية)، علماً أن الطريقتان موصوفتان في مواصفات الجمعية الأمريكية للفحص والمواد (ASTM).

في هذا البحث تم التعرف على تأثير الطريقة المستعملة في انجاز فحص تحميل الصفيحة على القيم المخمنة لبعض خصائص التربة الميكانيكية من خلال اجراء سلسلة من فحوص تحميل الصفيحة باستعمال كلا الطريقتين في نفس الموقع. من خلال مقارنة نتائج الفحوص بكلا الطريقتين تبين أن طريقة الفحص الديناميكي (الدوري) تعطي قيم أقل لخصائص التربة من تلك المستخلصة من طريقة الفحص الإستاتيكي.

الكلمات الرئيسية: فحص تحميل الصفيحة، معامل رد الفعل الأرضي، ديناميكي، إستاتيكي.

1. INTRODUCTION

Plate Load Test (PLT) is one of the tests that usually performed in situ to estimate some of the soil properties within shallow depths. The influenced depth (depth of stressed soil) in this test depends directly on the size of the plate used. This finding comes from the fact of bulb of stress beneath any loaded footing. Generally, the test can give an accurate estimation of mechanical properties of underneath soil in a range of about twice of plate diameter, **ASTM D1194, 2012**. However, the following empirical relation that given by, Bowels, 1988 may be used to explore load-test results to full size footings in cohesionless (sandy) soils:

$$q_{ult.} = q_{plate} \left(\frac{B_{footing}}{B_{plate}} \right) \quad (1)$$

Where,

$q_{ult.}$ = ultimate bearing capacity of the soil under footing.

$q_{plate.}$ = ultimate bearing capacity from PLT.

$B_{footing}$ = footing width.

B_{plate} = plate diameter.

On the other hand, for clay soils, since it is common to note that the BN_γ term is zero, so that it is concluded that $q_{ult.}$ Is independent of footing size, i.e.:

$$q_{ult.} = q_{plate} \quad (2)$$

Several soil properties can be predicted from PLT such as modulus of subgrade reaction, modulus of deformation, rebound (elastic) and residual (plastic) settlement as well as allowable bearing capacity.

PLT may have static and dynamic features. Static PLT is the conventional test and used widely through the world. **ASTM D1194, 2012**, standard test method may be used to perform this test sufficiently. Dynamic PLT may be subdivided into two categories: impact and cyclic PLT. The former can be executed according to the test method specified in, **ASTM D1195, 2012**. This test is conducted using the same apparatus used in static

test. The only difference is in applying incremental pressure as will be detailed hereafter. Impact PLT can be performed according to German specification TP BF-StB part B 8.3, Technical Test Provisions of Soil and Rock in Road Construction, 2003 using the Light Falling Weight Device (LFWD). The apparatus of this technique is shown in **Fig.1**.

Adam and Adam, 2003, suggested a simple and efficient mechanical model of the dynamic load plate test with the LFWD to allow the numerical simulations of the test. The motion of the device is characterized by a mass-spring-dashpot system as shown in **Fig. 2**. The mechanical properties of the spring-damper element were modeled as a Kelvin-Voigt body, i.e. a linear spring with stiffness k , and a viscous damper with damping coefficient, **Adam and Adam, 2003**.

A series of PLTs on a loam fill were carried out by **Matsuzawa et. al., 2006** via employing three loading methods: static, cyclic and rapid (dynamic) PLTs to estimate a static load-settlement relation from the rapid PLT results. They aimed to minimize the time consumed for assessment of mechanical properties of the tested ground. The rapid (dynamic) tests were conducted using the spring-hammer (SH) load test method shown in **Fig.3** which is essentially a dynamic test method.

In this work, static and cyclic PLT methods according to, **ASTM D1194, 2012** and, **ASTM D1195, 2012** were adopted. A typical assembly for conducting both static and cyclic load test is illustrated in **Fig.4**.

2. EXPERIMENTAL WORKS

Four PLTs were carried out on 0.5 m compacted subbase layer in the location of storage tank and turbines at 2.0 below ground level in Al-Haydaria Gas Power Plant. Two of these tests were static tests and others were conducted near the locations of the static tests adopting the cyclic (repetitive) PLT method. The procedure of both above methods can be seen in the following brief:

Static PLT method

As mentioned in the previous section, **ASTM D1194, 2012** is adopted to perform the conventional static PLT. The test procedure can be summarized as follows:

1. A load is applied on the plate of 305mm in diameter and settlements are recorded from a dial gage accurate to 0.01mm. The load increment was taken approximately one fifth of the estimated bearing capacity of the soil. Time intervals of loading were taken one hour for all the load increments.
2. The test was continued until one of the following is achieved:
 - (a) A total settlement of 25mm is obtained.
 - (b) The maximum soil bearing capacity is reached.
 - (c) The capacity of the testing apparatus is reached.

Cyclic (Repetitive) PLT method

On the other hand, **ASTM D1195, 2012** is taken a guide to execute cyclic (repetitive static) PLT:

1. After the equipment has been properly arranged, the total assembly (plate, jack and loading column) is seated by quick application and release of a load sufficient to produce a deflection of not less than 0.25mm or more than 0.50mm. After This release, the plate is resealed by applying one half of the recorded load that produced (0.25-0.50) mm. When the dial needle has again some to rest it is set accurately to its zero mark.
2. A load giving a deflection of about 1.0 mm is applied and maintained approximately constant until the rate of deflection is 0.03 mm/min. or less for three successive minutes. Then the load is completely released and the rebound is observed until the rate of recovery is 0.03 mm/min. or less for three successive minutes.
3. The load application and release is repeated in the same manner six times. The reading of dial gage resting on the bearing plate just before the application and release of load for each repetition is recorded.
4. The load is increased to give a deflection of about 5.0 mm and the procedure given in (2) and (3) above is repeated. Similarly, the method of load application and release is conducted for load increment giving more deflection or until the load capacity of testing apparatus or the maximum bearing capacity of the soil is reached. Keeping in mind that the standard end point of each

loading or release in each repetition for each load increment is 0.03 mm/min. or less for three successive minutes.

3. RESULTS AND DISCUSSION

The plots of applied load against the corresponding plate settlement are given in **Figs. 5 - 8**.

For the nonrepetitive plate load test, the following procedure is followed to predict coefficient of subgrade reaction and the modulus of deformation (Young modulus):

- (a) The yield point, see **Fig.9**, is obtained at intersection of the straight lines tangent to load-settlement curve from which the ultimate applied load (P_{ult}) in kN is assessed.
- (b) Calculate the allowable applied load (P_{all}) in kN from:

$$P_{all} = \frac{P_{ult}}{F.S.} \quad (3)$$

Where, F.S = Factor of safety usually taken 2.5.

- (c) Read δ which is the corrected settlement corresponding to applied load.

$$\delta = \text{observed settlement} - \delta_c \quad (4)$$

Where, δ_c = to be estimated by backward projection of arithmetic load-settlement curve to zero load.

- (d) Calculate Coefficient of subgrade reaction K_s as:

$$K_s = \frac{P_{all}}{A_p \delta} \text{ in kN/m}^3 \quad (5)$$

Where, A_p = area of plate used in the test in meters.

δ = the corrected settlement at the P_{all} .

- (e) Calculate the modulus of deformation (Young modulus) E from, UFC, 2005:

$$E \approx 1.5 \times R_p \times K_s \quad (6)$$

Where R_p is the radius of the plate used.

The results of the nonrepetitive plate load tests can be seen in **Table 1**.

For the repetitive plate load test which has a different feature compared with the nonrepetitive

test, the final settlement and rebound of each load increment after six cycles of loading and unloading is recorded. The test includes inducing a settlement and keeping the load produced this settlement constant and recording the observed settlement. Then the load is vanished and the rebound settlement is recorded. This cycle of loading unloading is repeated six times. For each load increment an assessment of coefficient of subgrade reaction and modulus of deformation can be made adopting the final observed settlement.

The results of the repetitive plate load tests can be seen in **Table 2** and **Table 3**.

It is clear that repetitive PLT method gave lowest values of soil properties (modulus of subgrade reaction and modulus of deformation). This may be attributed the effect of cyclic (or hysteresis) stress loop that causes a continuous rearrangement of the skeleton of soil particles. In other words, the strain energy that expected to be stored in the soil skeleton was dissipated due to soil particle rearrangement. This finding may has an importance in practice of machine foundation problem in which cyclic (or repetitive) loading is expected.

4. CONCLUSIONS

The following conclusion can be drawn from this study:

1. A considerable decrease in values of soil properties (modulus of subgrade reaction and modulus of deformation) was found using the repetitive PLT in the same site where the static PLT have been used.
2. Repetitive PLT is recommended in prediction of soil properties when the practice involve a fluctuated or repetitive loading such as rotating machine foundation

or tanks subjected to cyclic operations of filling and voiding.

5. REFERENCES:

- Adam, C. and Adam, D, 2003, *Modelling of The Dynamic Load Plate Test with Light Falling Weight Device*. Asian Journal of Civil Engineering (Building and Housing) Vol. 4, Nos. 2-4, Pages (73-89).
- ASTM D1194 2012, *Test Method for Bearing Capacity of Soil for Static Load and Spread Footing*, Annual Book of ASTM Standards, vol.04.08. New York, USA.
- ASTM D1195 2012, *Standard Test Method for Repetitive Plate Load Tests of Soils and Flexible Pavement Components for Static Load and Spread Footing*, Annual Book of ASTM Standards, vol.04.08. New York, USA.
- Bowels, J.E., 1988, *Foundation Analysis and Design*, McGraw-Hill Book Company, New York, Fourth Edition.
- Matsuzawa, K., Sakihama, H., Nemoto, H. and Matsumoto, T. 2006, *Size and Loading Rate Effects Observed in Plate Load Tests on A Fill*, International network: (http://www.spring-hammer.com/files/DFI2006_Matsuzawa.pdf)
- Technical Test Provisions for Soil and Rock in Road Construction TP BF – StB, Part B 8.3: , 2003
- Dynamic Plate Compression Test with the Light Falling Weight Device*, Cologne.Forschungsgesellschaft fuer Strassen-und Verkehrswesen. Germany.
- UFC, Unified Facilities Criteria, 2005, *Soil Mechanics*, UFC 3-220-10N, electronic copy

Table1. Nonrepetitive plate load tests results.

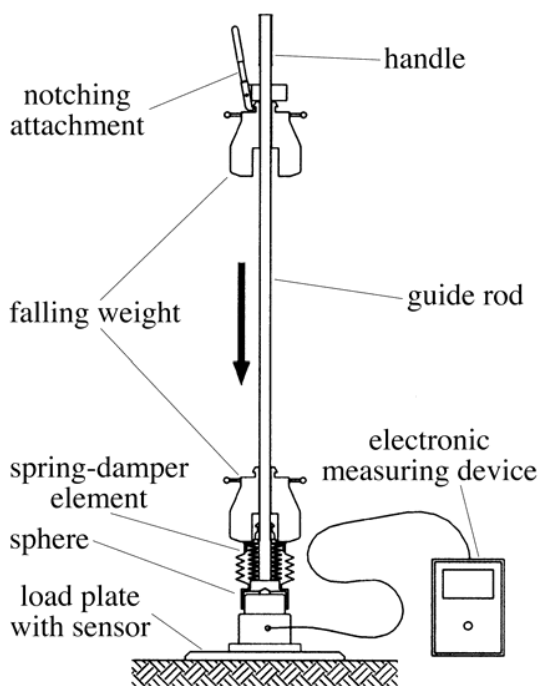
No.	Point location	Depth m	Modulus of sub- grade reaction, Ks (kN/m ³)	Modulus of deformation, E (MPa)
1	Storage Tanks	2	378462	86.6
2	Turbines	2	300000	68.6

Table2. Repetitive plate load tests results.

No .	Point location	Depth m		Incr.1 producing 1mm sett.	Incr.2 producing 5mm sett.	Incr.3 producing 10mm sett.
1	Storage tanks	2	Load, kN	20	92	125
			Final sett. mm	1.16	6.5	9.7
			Rebound mm	1.02	6.1	7.8
2	Turbines	2	Load, kN	10	30	40
			Final sett. mm	4.65	12.35	13.3
			Rebound mm	3.87	11.05	11.20

Table3.Summary of repetitive plate load tests results.

No.	Point location	Depth m	Modulus of sub-grade reaction, K_s (kN/m ³)	Modulus of deformation, E (MPa)
1	Storage tanks	2	43294	2.90
2	Turbines	2	2581	0.68


Figure 1.Components of the light falling weight device (LFWD).

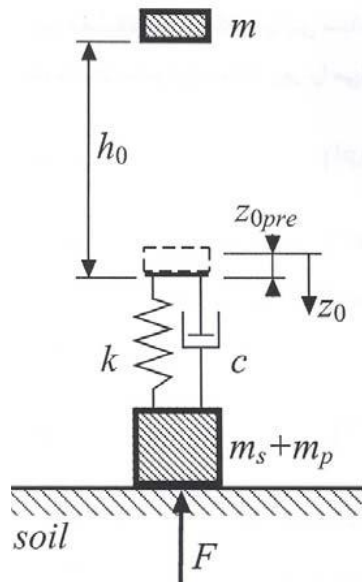


Figure 2. Mechanical model of the LFWD.

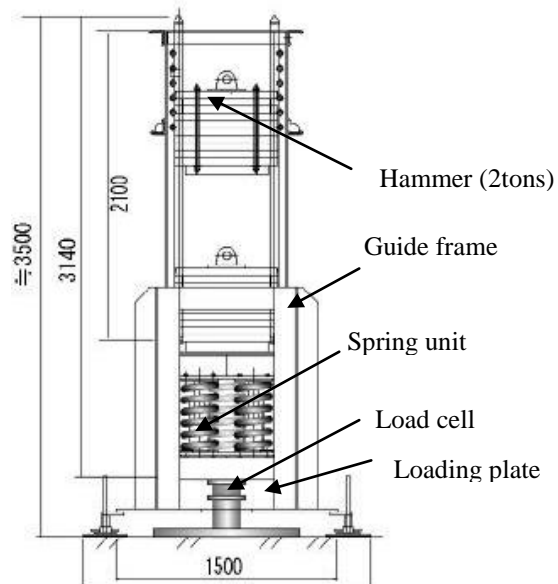
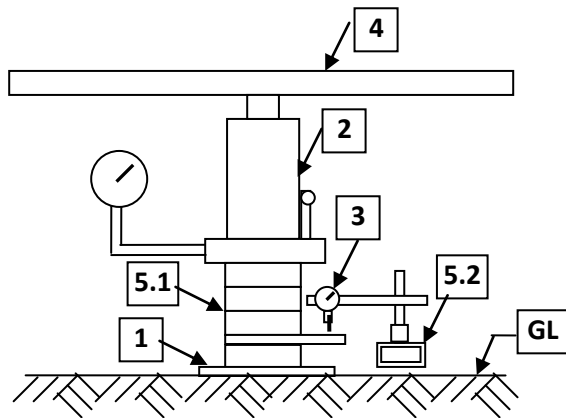


Figure 3. Spring hammer (SH) loading device.

**Plate loading apparatus**

The loading apparatus is consisted of the following parts:

1. Bearing plate:
Circular steel bearing plate 30 mm thickness and 305 mm diameter is used.
2. Hydraulic jack:
Hydraulic jack capacity is 35 ton (350kN).
3. Settlement recording devices:
Dial gauge, capable of measuring settlement of the loaded plate to an accuracy of 0.01 mm.
4. Reaction beam (chassis of a full loaded truck).
5. Miscellaneous apparatus Includes.
 - 5.1. Compression post
 - 5.2. Reference beam steel stands



Figure 4. Typical assembly of PLT apparatus.

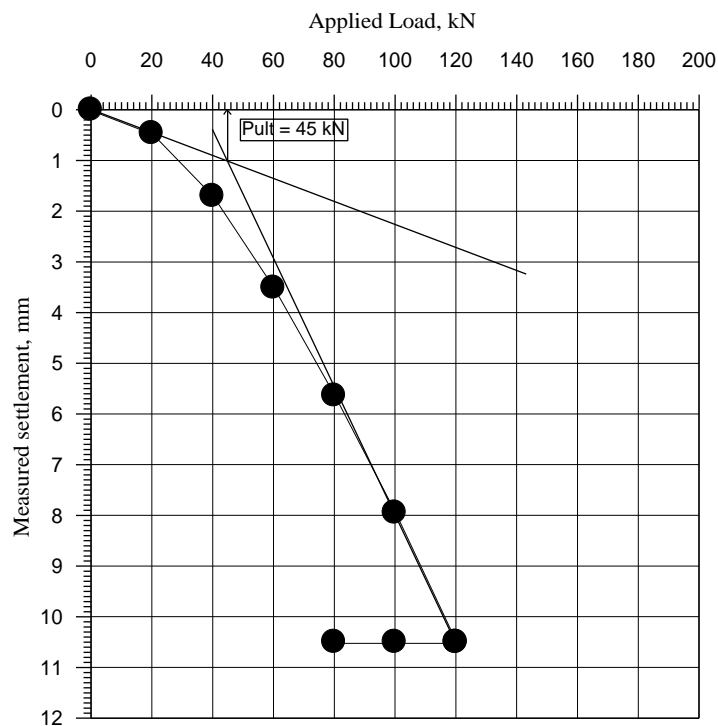


Figure 5. Static plate load test results for a point in storage tanks area.

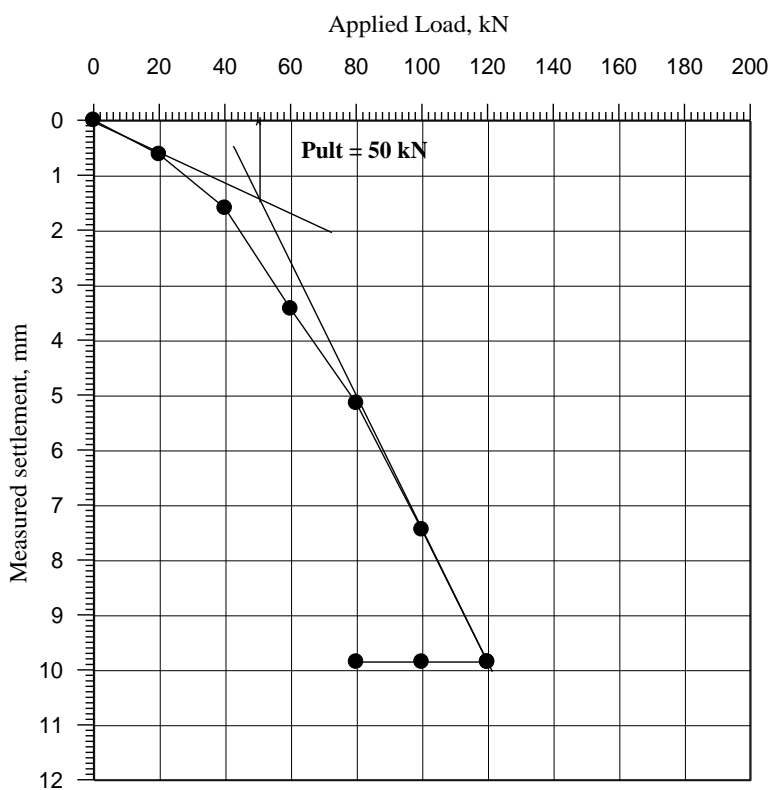


Figure6. Static plate load test results for a point in turbine area.

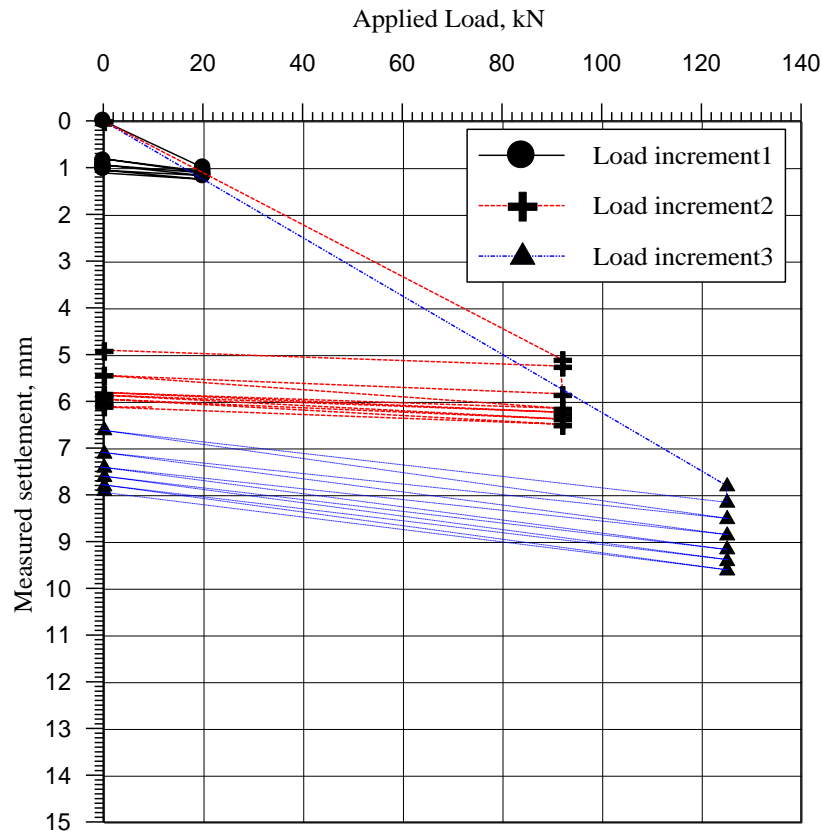


Figure7. Repetitive (dynamic) plate load test results for a point in storage tanks area.

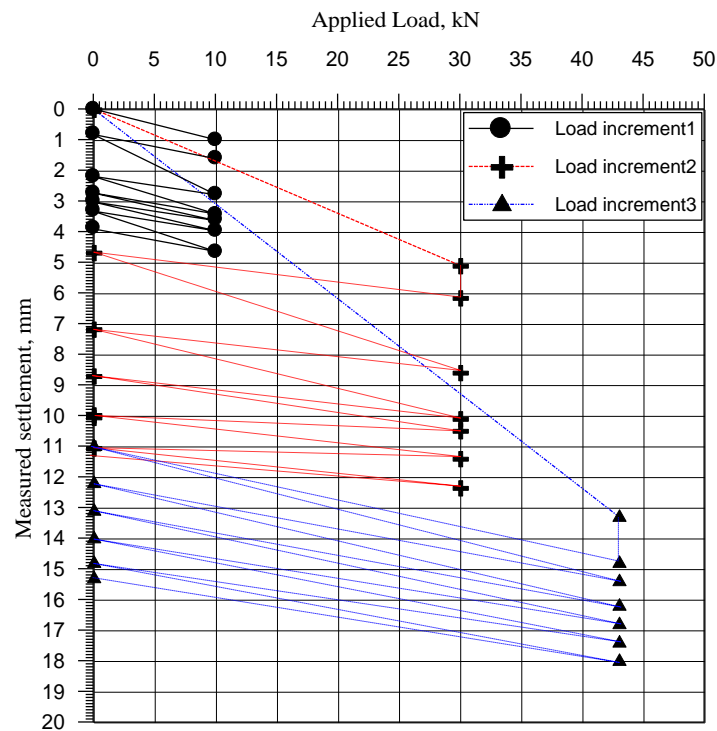


Figure8. Repetitive (dynamic) plate load test results for a point in turbine area.

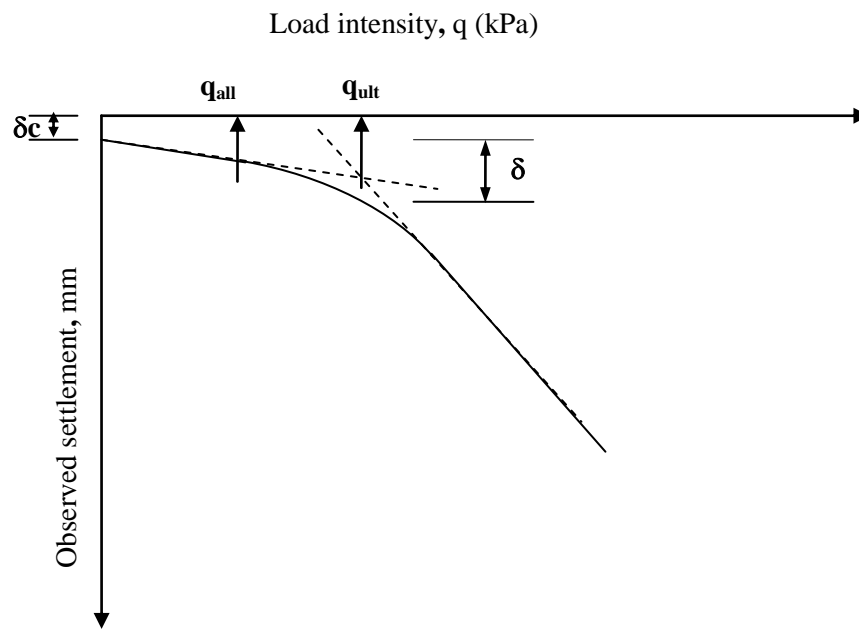


Figure 9. Method of calculation.

قائمة المحتويات

القسم العربي:

الصفحة

21 - 1

العنوان

أثر تنوع الأنماط الهيكلية والشكلية للبيئة الحضرية في تحقيق
التماسك الحضري لعناصر النسيج الحضري الكثيف

أ.م. د. أريج كريم مجيد السدخان
م. د. خنساء غازي رشيد النعيمي

أثر تنوع الأنماط الهيكلية والشكلية للبيئة الحضرية في تحقيق التماسك الحضري لعناصر النسيج الحضري الكثيف

م.د. خنساء غازي رشيد النعيمي
دكتورة هندسة معمارية
قسم هندسة العمارة
الجامعة التكنولوجية

أ.م.د. أريج كريم مجيد السدخان
دكتورة هندسة معمارية
القسم المعماري
كلية الهندسة / جامعة بغداد

خلاصة البحث :

يتطلب التخطيط لمدينة تحمل الهوية الانسانية الأخذ بالحسبان أولاً احتياجات الانسان التي كانت تحققها قيم التنوع في المدن التقليدية والتي كان من السهل خلق المكان فيها ولكن على العكس من هذا تنتهك المدن المعاصرة هذه القيم مما ينعكس كنقص ملحوظ في الصفات الانسانية لعناصر النسيج الحضري مما يترك الانسان في حالة بحث عن خلق المكان . وقد تطلب البحث عن مفهوم التماسك الحضري توفير فرشة معرفية ضمن طروحات النظرية الحضرية تركزت حول تحولات التوجهات المورفولوجية التنظيمية في تعاملها مع عناصر النسيج الحضري ومن خلالها توضحت المشكلة البحثية الآتية :
عدم وجود تصور واضح لعوامل تحقيق التماسك الحضري لعناصر النسيج الحضري الكثيف على المستويين التركيبي والشكلي. ومنها تحددت فرضية البحث كالاتي : الأنماط المتنوعة لعناصر النسيج الحضري الكثيف التي تعكس الثوابت والاختلافات المجتمعية وتعطي خيارات شكلية متنوعة للفهم والتأويل والتعبير، تصبح وسط لتحقيق التماسك الحضري شمولياً مع اختلاف أنماط التوزيع الهيكلية وموضوعياً مع اختلاف الأنماط الشكلية .

وقد استكشف البحث جوانب تحقيق التكامل لعناصر النسيج الحضري الكثيف بنائياً والتي تضمنت (التكامل الوظيفي والتكامل الشكلي والتكامل الموقعي) واختلاف هذه الجوانب مع تنوع أنماط التوزيع الهيكلي للبنية الفضائية بين نمط التوزيع العضوي للمدينة التقليدية ونمط التوزيع الشبكي للمدينة المعاصرة ، ولغرض التحقق من فرضية البحث تم تطبيق الاطار النظري المستخلص على أربعة عينات بحثية لعقدة ومحور عند النسيج العضوي لمدينة London والنسيج الشبكي لمدينة New York .

وتوصل البحث الى مجموعة استنتاجات تلخص في فكرة: أن هوية المدينة تتكامل ويتحقق تماسك الكل الموحد لنسيجها الحضري حين تحمل اجزائها رمزية ضمن سياقها أولاً من خلال تميز عناصرها المعمارية والحضرية ضمن هوية محلية سواء تقليدية او حديثة معاصرة ، في حين تعمل الرمزية النصيبية على منح المدينة هوية عالمية بينما تعمل الرمزية الوظيفية على تحقيق هوية المدينة محلياً وعالمياً ضمن إطار الدور الذي تلعبه المدينة في الاقتصاد العالمي الجديد .

The Impact of Varying of Structural & Formal Urban Types on the Coherence of Elements of Dense Urban Fabric

Asst.Prof.Dr.Areej Kareem Majeed
College of Engineering
Baghdad University

Lect..Dr. Khansaa' Ghazi Al Nuaymi
Department of Architecture Engineering
University of Technology
Email: Khansaa_rasheed@yahoo.com

ABSTRACT

Planning for a city with human identity considers the needs of human being that exist in the traditional cities where it was so easy creating place there, on the other hand, modern cities refuse these values and reduce the human characters of urban fabric elements , and the searching for the concept of " Urban Coherence " considers the knowledge about urban theory, especially Morphological attitudes finding three sides of making the coherence of

dense urban fabric which are " Functional Complementarily , Formal Complementarily , Contextual Complementarily " and the differentiation of these sides within the variety of spatial structural patterns between the organic type of traditional city and the gridiron type of modern city . To approve the hypothesis of the research, the theoretical frame was

1. المقدمة

الكفاءة لآخرين تدور حول كيفية تطابق المدينة مع المتطلبات الاجتماعية والاقتصادية والثقافية للحياة اليومية. ونظراً لسعة الطروحات حول جوانب النظرية الحضرية المتعددة، فقد ركّز البحث على تناول وتحليل التوجهات المورفولوجية في النظرية الحضرية وتحولاتها في إستكشاف جوانب المشكلة البحثية وبناء قاعدة نظرية حول مفهوم " التماسك الحضري URBAN COHERENCE "كونها تتمحور حول الجوانب الوظيفية والشكلية للبيئة الحضرية والمؤثرة بصورة مباشرة في موضوع البحث.

يعتبر هذا البحث مستقلاً من إطروحة الدكتوراه الموسومة "أثر ظاهرة الزحام الحضري في تغيير أنماط البيئة الحضرية في المدن العالمية الكبرى" والمقدمة الى مجلس كلية الهندسة في جامعة بغداد للعام 2010. يعتمد تقييم كفاءة البيئة الحضرية على اوجه المعايير المتبعة ، فبالنسبة للبعض فإن المدينة هي قيم جمالية مع اختلاف رؤية الناس لها، والمدينة للبعض الاخر هي مكان لاعمال محددة فتعتمد كفاءتها على قدرتها على التوسع لاستيعاب التضخم في حجم الاعمال هذه ، لكن

2. التوجهات المورفولوجية التنظيمية

تغطي الطروحات المورفولوجية التوجهات التي تصنف وتدرس الهيئة الحضرية للمدينة وفقاً لاشكالها وعملية تحولها عبر الزمن وآليات مقارنة البنيات الحضرية لمدن مختلفة. وفي هذا الاطار اشار القيسي الى ان شكل البيئة الحضرية ينتج من تفاعل ثلاثة مكونات اساسية: الانسان من خلال حاجاته ومتطلباته، والبيئة الثقافية الاجتماعية وهي المكونات الديناميكية في التكوين، ثم العوامل الثابتة التي تمثل المحددات في تكوين الهيئة الحضرية مثل الانماط والقواعد الحضرية، وان تفاعل هذه العوامل هو الذي يحدد الكيفية التي تتشكل بها البيئة الحضرية وهذا يعني تكامل العوامل واستمراريتها وعدم امكانية فصلها. تناولت طروحات النظريات المورفولوجية أنماط البيئة الحضرية وعمليات التحول فيها من تأثير تطور المدينة وإتساعها وبالتالي تأثيرات هذه التحولات على إستمرارية جوانب تحقيق التماسك للعناصر الفيزيائية للبيئة الحضرية من خلال توجهات ثلاثة:

1.2. متغيرات شكلية

تتحكم في طبيعة العلاقات بين عناصر النسيج الحضري وهذا ما دعى Lynch في كتابه "The Image of the City" الى التمييز بين مستوى التعقيد في تفاصيل البنية الحضرية على مستوى المقياس الصغير micro scale مقارنة بالبساطة في تكوينها على المقياس الكبير macro scale، وربط بين درجة وضوحية البيئة الحضرية والاتجاهية في توجيه الفرد وعدّها أساساً في الإحساس بالأمان والألفة. كما أشار الى إن إدراك الكل الموحد يعتمد على تحقيق الاحساس بالوحدة في النسيج الحضري المتماسك في علاقات العناصر الخمسة مع بعضها حيث تعمل الممرات "paths" على التمهيد الى القطاعات "districts" وترتبط العقد "nodes" المختلفة فيما بينها وتشير الى الحافات "edges" التي تحدد بدورها حدود القطاعات والعلامات الدالة "landmarks" التي تؤشر للعقد وتحدد لنقاط مهمة في إدراك النسيج الحضري .

وضمن هذه المتغيرات الشكلية حلل Gordon Cullen من خلال كتابه "Townscape" عناصر البنية الحضرية مؤكداً على وضوح أجزاء البنية الحضرية على المستوى

هذا المشهد من خلال التناقض والتنوع وتحفيز الذاكرة في كل من الطرز والانماط المعمارية والمقياس والمواد واللون والملبس وخصائص أخرى للمكان سواء كعقدة أو شارع حركي ، وهو بهذا يؤكد على ضرورة تكامل القيم الشكلية والتركيبية في تحقيق الوحدة والاستمرارية البصرية بالتأكيد على إستمرارية الكتل المحيطة بالشارع في

المكانية بين الكتل البنائية ومجاوراتها تشير الى امكانية التنبؤ بالبنية الشمولية والمنظومة الحضرية بصورة عامة.

ويتضح تأثير هذه المتغيرات عند Salingeros في كتابه "Principles of Urban Structure" في أن فهم المحيط الفكري للنظام الفضائي الحضري يساعد على توليد فضاء حضري متميز ولو جزئياً ، حيث يشمل النظام الحضري تفاعلات حركية وثابتة مترابطة مع بعضها بشكل معقد جدا للنظام الحضري بأجزائه الثلاثة (المسالك Path والفضاءات Spaces وتصميم الأبنية المحيطة له Mass)

3.2. متغيرات وظيفية

تتحدد من خلالها كفاءة المدينة في توفير متطلبات حياة المجتمع وزيادة حيوية البيئة الحضرية وهذا يتضح عند نظرة Hillier للمدينة على أنها نتاج في مزيج فيزيائي ووظيفي في كتابه "Space is The Machine" ، حيث تمثل المدينة فيزيائياً خزين الأبنية المترابطة مع بعضها مكانياً بواسطة النظام الحركي والبنى التحتية، أما وظيفياً فهي تدعم مجموعة من العمليات الاجتماعية والاقتصادية والحضرية والبيئية، ويأتي الخلل في البيئة الحضرية للمدينة من عدم فهم طبيعة العلاقة بين التركيب الفيزيائي للمدينة ووظيفتها. وتتضح أهمية الوظيفة عند Krier في كتابه "Choice of Fate" في إستكثاره لتأثيرات البعد الاقتصادي الاجتماعي في تحول روحية المورفولوجية الحضرية منذ القرن التاسع عشر ومؤكداً بل مؤسساً للطراز الكلاسيكي الذي احبته مابعد الحداثة، والعودة الى فكرة المحليات متعددة الوظائف.

فيما ركز Billson على أهمية فهم المجال المعلوماتي لكي يعمل على خلق نسيج حضري متماسك عندما تُوظف هذه المعلومات ضمن لغة نمطية لأن من الضروري ان تكون العناصر مؤثرة في بعضها وظيفياً وليس جمالياً فقط كي

التركيب للمقياس الكبير للمدينة) كنمط التوزيع الهيكلي سواء كان عضوي أو شبكي أو مختلط من الاثنين معاً) أو وضوحية العناصر الحضرية في هذه الاجزاء والعلاقات بينها من خلال منظومة الاشارات التي تقدمها على المستوى الدلالي للمقياس الصغير في المدينة ، فتظهر البنية الحضرية كمشهد متسلسل serial vision من الاستمرارية البصرية للمحور الحركي الطويل او الفضاء المفتوح وإظهار جماليات تنظيم عناصر البيئة الحضرية .

فيما ناقش Arthur van Billson في دراسته "Complexity and Urban Coherence" بنية النسيج الحضري للمدن الحديثة على أساس الخطأ في العلاقات البنوية إذ قسّم الحياة في البيئة الحضرية الى أجزاء بين تأثيرات مبدأ التطبيق للوظائف ، والعلاقات بين الأجزاء وعزل الفعاليات المختلفة والذي ادى الى تجزئة نسيج المدينة وبين التأكيد على مركزية النمو الحضري من خلال خمسة مكونات أساسية في بنية النسيج العضوي للمدينة التقليدية وهي (المباني ومحاور حركة المشاة والفضاءات المفتوحة "الحدائق العامة" وشوارع الحركة، ومواقف السيارات) معتمداً اللغة النمطية في تحقيق التوازن بين حاجات اجزاء البيئة parts as منفردة وحاجات الكيان ككل as a whole .

2.2. متغيرات موقعية

تتحدد من خلالها هوية المدينة وموقعها ضمن النظام العالمي المعاصر نجدها في قراءة Rossi للمدينة من خلال ذاكرتها "The Architecture of the City" ، فكل مدينة تاريخها واستمراريتها وهويتها التي تجسدها ذاكرتها الجمعية، كما انه لكل مدينة اخفاقاتها في أنماطها على مستوى مقياسها الكبير أو في تشكيل مناطق السكن الخاصة من أماكن عامة ومباني عامة وفضاءات ونصب وبنيتها التحتية وحتى هذه الإخفاقات تكون جزء من ذاكرتها.

كما أكد Hillier في طروحاته المتعددة منها "The Social Logic of Space" على التكامل بين الخصائص الشمولية والموضعية للبنية الحضرية وركز على الكيفية التي يتشكل بها النظام الشمولي من الخصائص الموضعية إذ تلعب دور كبير في تحديد وضوحية نمط هيكلي النسيج الحضري سواء ذو النمط الشبكي او العضوي، وإن العلاقات

يتحقق انطباع بصري إيجابي بالإضافة إلى الراحة العاطفية لدى المستعمل.

يتضح من مجمل الطروحات التي تم التطرق إليها بأن موضوع التماسك الحضري أخذ مديات واسعة في النظريات المتعلقة بالبيئة الحضرية و قادت مجملها إلى تحديد مجال لمشكلة معرفية :

مشكلة البحث : عدم وجود تصور واضح لعوامل تحقيق التماسك الحضري لعناصر النسيج الحضري الكثيف على المستويين التركيبي والشكلي.

أما فرضية البحث : الأنماط المتنوعة لعناصر النسيج الحضري الكثيف التي تعكس الثوابت والاختلافات المجتمعية وتعطي خيارات شكلية متنوعة للفهم والتأويل والتعبير، تصبح وسط لتحقيق التماسك الحضري شمولياً مع اختلاف أنماط التوزيع الهيكلية وموضعياً مع اختلاف الأنماط الشكلية

من أجل الاحاطة بجوانب المشكلة البحثية كان لابد للبحث أن يستعرض العناصر الأساسية للنسيج الحضري والمظاهر والمجالات المتعلقة به والتحويلات الشكلية في أجزائه بتأثير من تطور المدينة وزيادة كثافة النسيج الحضري .

3. عناصر النسيج الحضري للمدينة الكبرى

تعتمد الإرتباطات بين عناصر النسيج الحضري على عدة خصائص هي: الشكل shape والموقع position والوظيفة function وكل واحدة من عناصر النسيج الحضري يجب أن تقوي العناصر الأخرى بصرياً أو هندسياً أو بنوياً أو وظيفياً أو كل هذه القوى معاً من أجل تحقيق التماسك الحضري (p.90, Salingeros, 2005). وسيتناول البحث عناصر النسيج الحضري بالإضافة إلى التحويلات التي ظهرت عليها في المدينة المعاصرة :

1.3. الفضاء الحضري Urban Space

يعني الفضاء الحضري الحيوي " الفضاء المُستعمل والذي هو الفضاء الذي يُغذي المتلقي عاطفياً "، وبالتأكيد فإن استعمال الفضاء الحضري مرتبط بالمجال المعلوماتي الذي توفره السطوح المحيطة بالفضاء وعلى

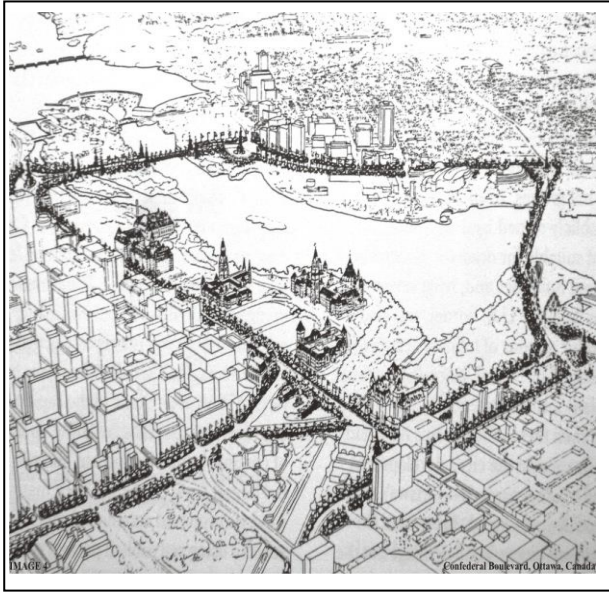
سهولة التقاط المشاهد لهذه المعلومات ، ورغم أن كفاءة الفضاء تُعرف من خلال التواصل والتفاعل مع الناس، إلا أنه ومنذ أواخر القرن العشرين أصبح تعامل الأفراد مع الفضاء وكأنه حجم خالي ليس لخصائصه الفيزيائية أي أهمية عندهم، فلم يعد المتلقي يلعب أي دور في الفضاء، وبالتالي أصبح الفضاء مجرداً وكأنه جزء من معادلة رياضية مستقلاً عن البنات المحيطة به وإنما أصبح فضاءً متجهاً نحو السماء (Salingaros, 2005, p.41) فنجد أن المصمم الحضري اليوم يركز على الشكل الهندسي المجرد للمخطط متجاوزاً أشكال الفضاءات الحضرية التي تُخلق ضمن هذا المخطط ، وبالتالي يبدو أن البنية الحضرية المعاصرة تُضعف أو تقلل من أهمية الفضاءات البارزة وعلامات الدلالة التي كانت الأصل في تعريف شخصية الفضاءات في المدينة. تُجمع جميع الدراسات الحضرية على تصنيف الفضاء الحضري تبعاً لخصائصه الوظيفية والحركية إلى:

أولاً- الشوارع والجادات الخطية الطولية Boulevards & Avenues

عملت الشوارع الخطية العريضة والمستقيمة على تحويل النظام العضوي للمدينة الأوروبية التقليدية إلى نظام فضائي يشق المدينة إلى أجزاء ويربط الشواخص في كل اتجاه وهذا ما عكس التداخلات الشمولية للمدن الكلاسيكية (Broadbent, 1990, p.117-119)

وهنا تحولت متاهات النسيج العضوي للمدينة إلى نسيج مُجزء ذو طبيعة خطية مستقيمة.

أدت الحاجة إلى تضخيم مقياس العناصر الحضرية في فترات المدن الهيلنستية حتى فترة متأخرة من عصر النهضة إلى زيادة الكثافة البنائية بزيادة إرتفاع المباني ونمى النسيج الحضري بانتشار ساحات التجمع مع إستمرارية الشوارع المستقيمة الطولية بواجهات مستمرة ومباني متساوية الارتفاع والاروقة المعقدة على طرفي الشارع كسمة جمالية متميزة إستمرت إلى مدن Baroque. كما أن إزاحة البنات والواجهات الحضرية للشوارع الرئيسية في مدن بدايات القرن العشرين عن وظائفها باتجاه الوظيفة التجارية وعن شكلها الحجري إلى الواجهات الحديدية والارتفاعات العالية، هذا عَرَف هوية



الشكل (1) ترابط العقد الحضرية للمدينة التقليدية

الساحات تبدو كمتنزه صغير لكنها بعد القرن الثامن عشر اكتسبت الطابع الرومانسي فأخذت هذه الفضاءات تبدو كأماكن للراحة لكنها أيضا كانت مواقف للعربات ثم للسيارات من بعدها (Mumford, 1961, p.395)، وحتى هذه الفترة كان الفضاء الحضري كما اشار Krier عبارة عن جسم هندسي بسيط ضمن نسيج المدينة هلال او دائرة او مربع او بيضوي محاط بحاجز من الأبنية ومحيط بمنطقة خضراء في الوسط، أما الشارع كفضاء حضري فيبدو كمحور بواجهات موحدة بمواد بناء طابوق وحجر وارتفاع موحد وعناصر متكررة مثلاً: شبابيك وابواب واعمد وزخارف وكورنيش. وعمل استخدام النسيج الشبكي Gridiron pattern كشوارع متعامدة على توفير الحد الأدنى من الفضاء العام المفتوح وكأنه مخطط قاحل جاف خالٍ من الروح حين اقتصرت وظيفة فضاءات العقد في المدينة كنقاط تغيير اتجاهات الحركة (او ما يطلق عليها بنقاط interchange في المدن العالمية المعاصرة) وقصورها في اداء وظيفتها الأساسية كمكان حضري في نسيج المدينة.

مميزة وجديدة للشوارع الرئيسية (كوظيفة تجارية لشركات عالمية) وينصب جديدة تتمازج فيها جمال عصر النهضة مع الهياكل المزججة للحدثاء. (1994, p.133, Johnson,

رغم أن التدفق خلال أماكن محددة على طول الخطوط المستقيمة العريضة وبالإستمرارية الطولية للشوارع التجارية في المدن المعاصرة هو ظاهرة لاحيوية ضمن بنية النسيج، لكن عندما تكون هذه الشوارع وبفعالية تجارية جزءاً من المراكز التاريخية للمدينة فإنها تصبح رموز Icons لتاريخ وهوية المدينة عالمياً، فتظهر ذاكرتها كنصوص أدبية ووصفات إستعارة تاريخية تصبح جزء من الاقتصاد السياحي.

ثانياً - العقدة Node

عادة ما تكتسب العقدة طاقتها من باقي اجزاء المدينة ففي اي مدينة حية ترتبط كل عقدة بباقي العقد وبالتالي فإن عناصر العقدة تتأثر بحجم النظام ككل .

وهنا يُعرّف Billson الحياة الحضرية Urban life لأية مدينة بأنها مجموعة التفاعلات المحتملة الناتجة من ارتباط عقد المدينة مع بعضها بشكل مباشر أو لا مباشر (Billson, 1995, p.150)، وخلال التاريخ الطويل لتطور المدينة لم تختفي الساحة المفتوحة (الفضاء المفتوح لتجمع العامة) لكنها تغير استخدامها ليس كلية لخدمة المشاة وإنما أصبحت مكان للتجمع الطبقي (لفئات معينة من سكان المدينة على خلاف ماكانت تمثله الساحات من مكان لذويان الطبقات كتجمع للأغنياء والفقراء في المدينة القديمة) وشكلها كانت هذه

الساحات plazas المفتوحة ربما تكون بدون بنايات أو جدران تحدد سطوحها وبدون استلام أي معلومة عن جوانب الطريق، وبالتالي لا يمكن اعتبارها فضاءات حضرية حتى مع توفر المباني البرجية المرتفعة فهي لم تعد سطحا مولداً للمعلومة كما كانت عليه الواجهات التقليدية التي مهما حاولنا استبدال المواد المستخدمة لتقليل المجال المعلوماتي سيكون هناك تجديد دائم للتأثير الأصلي بينما السطوح المعمارية المعاصرة قشرية وعاكسة بزوايا حادة ومفاجئة وهذا الأسلوب التصميمي ربما يحاكي الموصفات الظاهرية للفضاء الحضري ولكنها تنقذ للموصفات الجوهرية له.

(Salingaros,2005,p.60-62)

رغم ان السطوح الحضرية كانت تتمثل في الحافات العمودية للمحاور الحركية vertical edges سواء كمسالك أو فضاءات ، لكن أصبح من المتعذر تعريف الحدود المكانية للفضاء الحضري للمدينة المعاصرة بسبب انقطاعات هذه السطوح لأن أي بناية منتصبة بشكل مكعب معزول عن المحيط المجاور أو كأنها أحجام مجردة لا يمكن لها ان تعمل كسطح معزف لحدود المكان أو الفضاء الذي يحويه.

4.3. الأبنية النصبية Monumental building

يؤكد Fishman على حاجتنا للنصب، حين يشير الى أن لكل حضارة الحق في الحصول على النصب التي تستحقها. وإن عمارة أي حضارة تطلعنا على الثقافة التي انتجتها . ويظهر الابداع الذي حققته الرأسمالية البرجوازية في تعمدها خلق الاتحاد بين التكنولوجيا والريح الإقتصادي في الهياكل الحديدية الضخمة وقاعات المعارض والجسور المعلقة وناطحات السحاب. (Fishman ,1987,p.17)

ولكن الثقافة الجديدة المعاصرة للمدينة جلبت نصب جديدة كبديل عن النصب القديمة. فأصبحت البنوك رمز لقوة المال وتأثيره في المجتمع ومراكز الإتصالات رموز معمارية ولكن منقطعة أو معزولة عن المجتمع لأنها لا تخدم الهدف من فكرة النصبية للمجتمعات في حين كانت



الشكل (2) تداخل الفضاء الحضري التقليدي ضمن البنية

2.3. الكتل الحضرية Urban Blocks

تعتبر الكتلة البنائية الحضرية Urban blocks الوحدة الأساسية للجغرافية الحضرية لأي مدينة. ويعتقد Meyer أن الكتل الحضرية هي العنصر الأساسي في أي نسيج حضري حيث تنتظم بواسطتها العلاقات بين القطاعات الخاصة والعامة بإعتماد المقياس كجوهري لنمطية العلاقات بين هذه الكتل وبالتالي فإن اختفاء الكتل الحضرية المحيطة للشارع التقليدي ضمن التوجهات الحضرية الجديدة ينتج عنه إختفاء "عمارة المدينة واختفاء العلاقات المتميزة بين المجالين العام والخاص. ويبدو أن ظهور المجتمع الكبير في مدن القرن التاسع عشر حدد هوية البلوك البنائي في النسيج الحضري في توفير كثافة بنائية تستوعب زحام المدينة فلم يعد البلوك يأخذ وظيفة سوى وحدات اسكانية مزدحمة غير قادرة على اعطاء رسائل ذاتية وانما تقلل من ملامح هوية المدينة وتسلبها رموزها المعنوية . (Unger , p.410)

3.3. السطوح Surfaces

تشكل السطوح الأرضية الحضرية التي نتحرك فيها وأيضاً الواجهات العمودية vertical facades للكتل الصلدة التي تؤطر الشوارع وتحددها. وعلى الرغم من ضرورة تكامل الفضاء الحضري المفتوح والمسالك المؤدية اليه فهي تعمل على تقوية بعضها البعض الا أن بعض

تحقيق التماسك الحضري بصورة مباشرة مع تحقيق الإرتباطية في جميع مقاييس النسيج الحضري .
(Billson, 1995, p.86-88)

حاول البحث إستخلاص عوامل تحقيق التماسك الحضري لعناصر النسيج الحضري الكثيف ليتوصل في إستقراءه لهذه العوامل الى أن هذا يتطلب التعامل مع عناصر النسيج الحضري على ثلاثة مستويات :

- التكامل الوظيفي للقوى المؤثرة في البيئة الحضرية (الاجتماعية والبيئية والاقتصادية) وهذه ترجمت الى علاقات وظيفية لاجزاء النسيج والكيفية التي ترتبط بها هذه الاجزاء في كل موحد لتحقيق شمولية المدينة بحيوية جميع اجزائها .

- التكامل الشكلي الذي يتمثل بتحقيق تكامل المكونات الفيزيائية للنسيج الحضري ضمن خصائصها التركيبية في المقياس الكبير او خصائصها الشكلية في المقياس الصغير ولكن وفق اطار مجموعة من العلاقات

- التكامل الموقعي الذي يرتبط بالخصائص السياقية التي يحملها النسيج الحضري مؤكداً على أن تحقيق هذا التكامل للمدينة العالمية الكبرى يجب أن يأخذ غطاء الهوية المحلية العالمية glocality .

1.4. التكامل الوظيفي للنسيج الحضري الكثيف

يعتمد التماسك الحضري على تحقيق التكامل الوظيفي للنسيج الحضري الذي يعاني من التجزؤ والتشظي والعزل لقطاعات المدينة ، وقد أكد Alexander على فكرة التكامل الوظيفي للمركز الحضري الذي تتداخل فيه الفعاليات، اذ يظهر التكامل على المقياس الكبير macro scale في مراكز المدن التاريخية بينما تبني المدن الحديثة على وفق تكامل على المقياس الصغير micro scale فيكون الكل مجموع من اجزاء موضعية ولايمتلك كياناً خاصاً مميزاً. (Alexander, 1987, p.93)

يشير Krier الى ان المدن المعاصرة اصبحت تعاني من إفراط الاشكال المتنوعة نتيجة التوسع الاحادي

الكاتدرائيات هياكل عظمية نراها في أي مكان في المدينة وفي نفس الوقت تمثل مكانات لتجمع الناس ضمن ساحات عامة مفتوحة في المدينة ولكونها مكان للتواصل والتفاعل الاجتماعي فهي نصب رمزية عكست قوة العمارة المجتمعية (Doxiadis,)Architecture of society (1974, p.238-240) .

إن أي مدينة تقليدية خلقت أبنيتها النصيبية عبر الزمن ومن خلالها ذاكرتها الجمعية فكان من الصعب فهم الرمز او النصب اذا ما نقل من مدينة الى أخرى لإختلاف الثقافة التي أنتجت هذا الرمز بينما رموز المدينة اليوم أصبحت عالمية لأن المدينة نفسها خضعت لثقافة عالمية ذابت خلالها هويتها المحلية مثلاً برج دبي هو واحد من الرموز العالمية المهمة اليوم . واذا لم يعد في الإمكان تحديد شكل الأبنية النصيبية للمدينة في المستقبل فهذا لأنها انقطعت عن الهدف من وجودها، فلو عادت المدينة لتعمل بهدف خدمة الإنسان فإن المجتمع سيكون قادراً على ايجاد نصبه الجديدة او حتى أن يحب نصبه الجديدة ضمن النظام الحضري المعاصر .

4. تحقيق التماسك الحضري لعناصر النسيج الحضري الكثيف

يعتمد تماسك النسيج الحضري على حالة التوازن التي تتحقق للنظام ككل و يتأثر شكل المدينة وتنظيمها بمتطلبات الوظيفة function والحركة circulation والطوبوغرافية topography وتبدو هذه العناصر مترابطة في أي نظام متماسك بحيث يؤثر احدهم بالآخرين بطريقة ما وبالتالي ينشأ مجال مورفولوجي للتواصل مع أي عنصر مستقل او منفرد وهذا التواصل يمكن ان يكون سلبياً اوايجابياً حيث يكون شكل وموقع اي عنصر منفرد متأثراً بباقي عناصر الكل الموحد (Alexander, 2002,)

ولأن اي مدينة تتشكل من مزيج العناصر الثانوية التي تُعرف تدريجياً على مقاييس مختلفة لذا تحتاج المدينة الى وجود انماط مختلفة من الترابطات التي تربط عناصر مختلفة الحجم مع بعضها من جهة وتربط كل عنصر مع غيره من العناصر من جهة اخرى ولهذا يرتبط

الوظائف monofunctional overexpansion بدلاً من النمو العضوي التراكمي في البنية الصغرى للمدينة في المراكز التقليدية. (Krier, 1997, p.97) إن تحقيق التماسك على المستوى الوظيفي يقتضي تكامل عوامل القوى الوظيفية الأساسية للمدينة (الاجتماعية والاقتصادية والبيئية) للوصول الى الاداء الحضري المتكامل ، وسيتناول البحث أبعاد تحقيق التكامل الوظيفي من خلال القوى هذه:

أولاً - التكامل الوظيفي للاستعمال المختلط

يُعرف الاستعمال المختلط بأنه فعاليات مختلفة تتعايش معاً ويتقارب لتسمح للعيش والعمل بأن يتكاملوا معاً، ورغم انها مفردة تُطلق على مجموع الفعاليات المختلطة ضمن المبنى المنفرد الا ان الطروحات الحضرية بدأت تتناول هذه الفكرة على مستوى وحدة الحيرة وصولاً الى مراكز المدينة الكبرى. ويتضمن الاستعمال المختلط على مستوى المقياس الصغير micro scale درجة ملائمة من الارتباطية والامان مع التأكيد على حركة المشاة وتقليل حركة السيارات والتأكيد على تفعيل وظائف تجارية من محلات ومطاعم ومباني ادارية ضمن حركة المشاة وبعيد لايزيد 400m عن الوحدة السكنية. (Frank et al, 2003, pp.146,) (180)

اثبت Gehl & Gonze واستناداً الى دراسات عملية وجود علاقة بين نوعية الفضاءات المفتوحة وكمية الاستعمالات التي تجتذبها، فأثبتوا ان البيئة العامة عالية النوعية مع تجانس ملائم مع سياقها تؤدي الى زيادة وتكثيف في المهن والفعاليات، بينما تظهر الفعاليات الضرورية فقط في المساحات الخارجية ذات النوعية الفقيرة ولكن اضافة مكان عالي النوعية وهكذا سياقات سيكون نقطة جذب للسكان وسيؤدي الى تنوع اكبر للفعاليات. (Gehl, 2001, p.13)

ثانياً - التواصل الوظيفي عبر المقياس الانساني

تحاول البيئة الفيزيائية باستمرار خلق التواصل مع متلقيها مرسله بمعلومات الى حواسنا ، ويعتمد نجاح هذا

التواصل على وضوحية هذه البيئة. وقد وضع كلاً من Lynch 1960 و Gibson 1974 اساسيات عملية ادراك هذه المعلومات من خلال التوجه نحو المظهر الهندسي لعناصر هذه البيئة والتأكيد على اهمية النسيج الشبكي في تحقيق هذه الوضوحية ، فيما تضمنت دراسات اخرى مثل Appleyard 1969 و Spector 1978 العناصر الثقافية والرمزية والذاتية لهذه المعلومات مثلاً العناصر التذكارية للبيئة (Salingaros, 2005, p.39) ، ولطالما كانت المباني التاريخية مصدر لإشارات بصرية تحوي الكثير من المعلومات مثلاً واجهات الأبنية من جدران منمقة واروقة معقدة ومماشي وباقي عناصر التكوين الحضري التي توفر بكليتها محددات لعقد المشاة ومسالكهم (ibid, p.41)

تمثل العمارة إمتداد لعقل الإنسان باتجاه البيئة حوله لكي يتمكن من التواصل معها وتوسيع وعيه بالمحيط فأذا لم يتحقق هذا التواصل فإن الفرد يجد نفسه في بيئة غريبة ، وقد ساعد التركيز التقليدي للأبعاد في مركز المدينة الأجيال القديمة في فهم المدينة حولهم لكن توسيع إمتداد هذه الأبعاد الى حدود كبيرة في المدن الكبرى تجعل من الصعب الإستمتاع بالمشهد الحضري. (Grava, 2002,) (p.226)

هذا التواصل المعقد بين الإنسان والبيئة الفيزيائية التقليدية لم تستطع المدينة المعاصرة تحقيقه لعدم قدرة الطرق السريعة والشوارع والجسور ومواقف السيارات تحديد اي فضاء حضري بسبب ضعف المجال المعلوماتي الذي تولده. فالمشكلة الأكبر التي خلقتها المدينة الكبيرة في طبيعة الرسائل التي يستلمها الفرد من بنية المدينة التي يقتصر فيها التواصل المباشر مع الإنسان في مراكز تسوق المشاة التي تتكامل معها ضمن بيئة حضرية منظمة بشبكة نقل مُغذية لهذه المراكز متجاهلة الإنتعاش العاطفي الذي تمثله البيئة الحضرية الفيزيائية بالنسبة للإنسان.

بمقياس 1-3m تبعاً لحجم حركة المشاة ، وتعزل أجسام أخرى كالسيارة مثلاً لتحقيق التماسك الحضري اعتماداً على المقياس الإنساني. (Salingaros,2005,p.92)

ثانياً - تنوع المقاييس الحضرية

تلعب المقاييس دوراً كبيراً في كفاءة التصميم لأنها تُسهل عملية الإدراك عند المتلقي حين يقوم عقله بتجميع الأجسام المتماثلة ذات الحجم المتساوي في مستوى منفرد من المقياس وهذا يقلل من كمية المعلومات المُقدمة للمتلقي ضمن أية بنية معقدة ويصبح العقل قادراً على تخمين عدد الأجسام المتماثلة في كل مقياس ونجد أن فلسفة سياسات النمو الحضري المعاصرة تتركز حول المقياس الكبير والتوزيع المجاميعي وتجاهل المقاييس المتوسطة والصغيرة لدرجة أُعتبرت فيها أي بناية بهذا مقاييس غير مبدعة ولا اقتصادية (Salingaros, 2005, p.72) وقد أشارت Jacobs بأن التنوع في النسيج الحضري يخلق مشكلة فقط عندما تكون العناصر الحضرية بأحجام غير متلائمة خاصة على مستوى المقياس الأصغر (حيث يجب أن تكون الوحدات بنفس الحجم). لذا فإن أي بناية بحجم كبير ممكن أن تحتل واجهة الشارع ستعجز عن تحقيق الاندماج مع باقي الأبنية بسبب اللاتوازن في الحجم وهذا اللاتوازن هو ما يتسبب في منع التجمع للمقياس الصغير. (Jacobs, 1961, p.234) حيث يتم التضحية بالعناصر على المقياس الصغير وتجهيز العناصر الأكبر أولاً وبصبح عندئذ من الصعب إجراء التغيير لتحقيق التكيف مع البيئة الفيزيائية المحيطة لأن "العناصر الكبيرة تحوي العديد من البنيات الثانوية داخلها" ومن السهل إجراء التغيير على عناصر المقياس الصغير (Habraken,1998)

3.4. التكامل الموقعي للنسيج الحضري الكثيف

عرّف Barry التكامل كحماية للهوية الثقافية وتحقيق

2.4. التكامل الشكلي للنسيج الحضري الكثيف

ويعني التكامل بين المكونات الفيزيائية للبيئة الحضرية للوصول الى الكل الموحد وتُدرَك هذه العناصر من خلال خصائصها التركيبية على المقياس الكبير وخصائصها البصرية الشكلية على المقياس الصغير. ويعتمد التكامل الشكلي للنسيج الحضري الكثيف للمدن الكبرى المعاصرة على طبيعة العلاقات بين هذه العناصر، وسيركز البحث على شكل التحولات التي حدثت في هذه العلاقات وصولاً الى القواعد التي تحكم عناصر النسيج الكثيف لمدن اليوم المزدهمة.

أولاً - التجزئة والتشظي Fragmentation

تُظهر الإنجازات المعمارية للإنسان والمتباينة من الأبنية الصغيرة حتى ناطحات السحاب ثم المدن ككل مدى واسع ومتنوع من التجزئة ، فأى جسم من صنع الإنسان او كما هو في الطبيعة يتركب من وحدات اصغر مترابطة تُعرَف الكل . وتصنف هذه الوحدات اعتماداً على " الحجم والشكل واللمس واللون وغيرها . وقد بقي الافتراض بأن هذه الخصائص تُقرّر بشكل عشوائي بالإعتماد على معايير ذاتية ومستقلة يمكن ان تُستنبط هذه القواعد من الفن التقليدي والعمارة الكلاسيكية التي كانت تحقق الترابط مع المتلقي الذي يدركها وكأنها نظام رياضي كوحدة ثانوية تتكرر مع بعض التوزيع وهذا مشابه لقانون الطبيعة في خلق بنيات فرعية متماثلة (West, 1994, p.68-70)

إبتعدت التكوينات الحضرية الجديدة عن اشكال النمو العضوي للمدينة حين أنكرت الكسرية التجزئية العضوية للمدينة التقليدية واستبدلتها بكتل حضرية ومعمارية ضخمة لكنها غير حية وتحوي فضاءات حضرية غير مستعملة. وتوصف الهندسية الحضرية التقليدية بأنها كسرية لأن عناصرها كالأروقة وصفوف الأعمدة والمحلات مع إنقطاعات لمسالك وشوارع فرعية للحافة الحضرية وتعمل السطوح المجزئة الانتقالية هنا كصفات مسامية ، فتعطي الحرية للحركة الفيزيائية لبعض الأجسام كالمشاة مثلاً اذا ما كانت هذه الإنقطاعات والفجوات

الصفات الفنية والبصرية بين الفترتين يصبح من الصعب نقل هذه الاشكال من عصر لآخر من دون تنسيق او تعديل للشكل ليتوافق مع التغييرات في المجالات التاريخية والسياسية والاجتماعية للرؤية المعاصرة.

(Boyer, 1994, p.2-7)

ظهر شكل المدن الكبرى الحديثة في اوائل القرن العشرين كتنظيم بصري فوضوي اشبه بمنظر عام مفتوح وواسع تحكمه قوى التحول للفضاء والزمان فتحول بالمقابل مشهد المدينة الى سلسلة من التعبيرات السريعة واللقاءات الخاطفة وتمزيق الایحاءات الرمزية والاستهانة بالمعنى التاريخي، فأستبدلت الهيئة التصويرية pictorial image للمدينة كعمل فني الى المدينة كمنظر عام شامل، فهي مدينة ناطحات السحاب المرتفعة والتوسع والانتشار الحضري ، مدينة تأخذ خصائصها كنظام فضائي فقط من منظور " عين الطائر bird's eye perspective " ، وهنا يبدو أن الأشكال التمثيلية للمدينة تتغير مع انحراف وتغير بنية المدينة عبر الزمن ، حيث تحوي كل مجموعة من الاشكال (وفي فترات منفصلة) نظام مكاني يصبح صورة جامدة تلتقط اسلوب ادراكها من حاضرها، عندها ترتبط الاشكال التمثيلية كتسجيلات مختصرة للواقع الحاضرة فيه " روح العصر " .

ثانياً - تحولات الوعي الاجتماعي المعاصر حول العمارة الحضرية

تعرف العمارة الحضرية بأنها " الشبكة الفعالة من الافراد والمؤسسات التي تُكرس لخلق الأبنية والأماكن المنسجمة والإنسانية التي تحترم التقاليد المحلية"، حيث امتدت العمارة ضمن هيكل الفضاء الخدمي للمدينة لزمن طويل إلا أن هذا الدور كان دائماً ذاتياً ولم يتضمن مشاكل واقعية ، اذ لم يكن من الممكن تجريد الأشياء من معانيها وقياسها منفصلاً ، يرى Curtis بأن التنظير الاجتماعي استمر بشكل مباشر في الحركة الحديثة بتأثيرات من تداخل الأخلاقيات الحضرية في عمق النظرية المعمارية مع كتابات Ruskin و Viollet-le-duc فارتبط الوعي الاجتماعي مع الأجندة الأخلاقية الشخصية لأي معماري (Johnson, 1994 , p.59) .

الترابط بين أفراد المجتمع على إختلاف توجهاتهم الجمالية نحو البيئة الحضرية حولهم بهدف توظيف التعددية الثقافية للحفاظ على التمايز في الثقافات .

إن التحولات التدريجية في هوية البيئة الحضرية التقليدية التي تتجسد مادياً في التحولات الشكلية للعناصر الحضرية والعلاقات بينها كانت تخضع لقوانين سياقها الاجتماعي والاقتصادي والحضاري بشكل يحقق التواصل بين الماضي والحاضر ، لكن نظام القواعد المحدودة التي أظهرت التحول القسري نتيجة إقحام عناصر حضرية غريبة على البيئة الحضرية للمدن الكبرى المعاصرة عكست توجهات غريبة عن السياق الحضري مما تسبب في حدوث الانقطاع عن الهوية المميزة للمدينة وتجزئة نسيجها . إن محاولة خلق التواصل بين أجزاء المدينة بتنوع هويتها المعمارية تحتاج الى تواصل هذه الاجزاء أولاً مع روح العصر والانفتاح على السياق العالمي ، ويمكن وضع جوانب تحقيق تنوع هوية المدينة بين التقليدية وتطورات روح العصر كما يأتي :

أولاً - الذاكرة الجمعية Collective memory

مثّلت المدينة مولد واقعي ومجرد للشكل الحضري اللاحق وأمكن توقع التنظيم المكاني للمدينة نفسها حيث تقوم الاماكن والنصب بنقل المعنى والمعرفة عبرالاجيال فتصبح اجزاء محدودة في المدينة موضوعاً

مستمراً عبر الفترات التاريخية التي مرت بها مثلاً: نصبها او نمط شوارعها او اجزاء من مخططها الاصلي وهذه الحقيقة تولد الذاكرة الجمعية والاسلوب المدني لاي مجتمع (Rossi, 1984, p.50-55) ومثلت عمارة القرن التاسع عشر نسخة احتفالية وصورة اكثر عمومية للمجتمع متمثلة في مآثرها النصبية وحجمها الصناعي الضخم، وترجمت صورة القرن التاسع عشر الى نظرة معاصرة للمدينة - حين التحدث عن المدن شبيهة بالمتاحف والتجوال عبر الزمن خلال الجدران المرسومة كسيناريو لمشاهد الحياة في القرن التاسع عشر - لكن تبدو هذه الاستعارات ملفقة لانها ابتعدت عن فهم التنظيم التاريخي لهذه الصور البصرية في محتواها او سياقها المكاني والزمني، ونظراً لاختلاف

الاختلافات بين مجموعة محلية وأخرى يزيد التنوع في شخصية المدينة والتعبير. (Rapoport, 1997, p.7) ،
الا ان الاعتقاد بقيمة الشخصية المحلية يجب أن
يُصاحبه المرونة لإضافة وتقبل عناصر جديدة للبيئة
الفيزيائية لتنشيط تطوير " السياق المستقبلي "لحاجة
المدينة لإعادة خلق وإبداع نفسها باستمرار، حيث يشير
Rogers إلى أن الأبنية التاريخية تتكيف دائماً ويعاد
توظيفها وتزيينها لإعادة توازنها خلال الحياة . ويظهر من
هذا ان وسيلة قياس تماسك وكفاءة اداء النسيج الحضري
الكثيف بنائياً تكون من خلال التقييم العملي لوصولية
وحبوبة هذا النسيج كشرطين اساسيين لتحقيق جوانب
التكامل الثلاثة التي أشر لها البحث في إطاره النظري
، وقد ركز على المفردات التي تمكّن من تحديد مقياس
للخصائص الشكلية بثلاثة أبعاد وعلى مستوى المقياس
الصغير (كعلاقات وعناصر لعقدة ومحور حركي) وهذه
المفردات هي :

يشير Dubos الى أنه مادامت المجتمعات تخلق
عمارتهما تبعاً لقيم أساسية للحياة، فإن جمود وقبح العديد
من المدن الحديثة يعبر عن المجتمعات المريضة التي
أنجبتها (Dubos, 1981, p.6) وفي هذا الإطار نقّتبس
من Nietzsche " أننا لم نعد قادرين على فهم العمارة ،
فقد توسّعنا خارج حدود رمزية الخطوط والأشكال وبرز
تأثير لامحدود من الأبنية الرمزية كحجاب سحري أصبح
معه دخول العناصر الجمالية لهذا النظام عرضياً".

تأتي الرغبة في تماسك شخصية المكونات الحضرية
من ميل المجتمع للاحتفاظ بالقيمة المعنوية للمكان وهذا
يظهر على مستويات متعددة تمتد من منطقة معينة إلى
المستوى الواسع للمدينة إلا ان الشخصية المحلية تبدو
أقوى على مقياس أحياء منفردة ، حيث يشير
Rapoport الى قدرة السكان على تجسيد الشخصية
على مستوى منفرد أو مجموعة مما يمكنهم من أن ينشئوا
هوية جماعية والتعبير عن الأفضليات وخلق اختلافات
ظاهرة وتعقيدات في المدينة ، وأن إحداث هذه

1. الارتباطية Connectivity كبنية تنظيمية

تُعرف الارتباطية بأنها " التقارب النسبي للفعاليات والاتجاهات "، كما أنها أداة تعريف شمولية للنسيج الحضري ضمن اطار
الحيزيات المعاصرة الواسعة، حين تُعرف الشمولية totality بأنها " درجة الارتباطية الممنوحة من شبكة الامتدادات المنقطعة
غير المستمرة من خلال تكاملية علاقة كتلة-فراغ. جدول رقم 1

2. التشظي Fragmentation

اعتبرت حالة التشظي ظاهرة سلبية في اي مدينة معاصرة، لكن سيعتمد البحث حالة التشظي هذه كآلية لتحديد الهويات
المختلفة للأجزاء وبطريقة مورفولوجية وفهم علاقاتها مع بعضها لتحديد الهوية الشمولية لنسيج المدينة، وزيادة المعرفة
بصفتها الداخلية كمجموعة من البنيات والعلاقات النمطية لكل جزء. جدول رقم 2

3. التجانس الشكلي بين تكرار الشبكة والاستمرارية العضوية Repetition & Continuity

اي تحليل للنسيج الحضري الكثيف مورفولوجياً يجب ان يأخذ بالحسبان انماط النمو و التحول الحاصل في المبادئ
التنظيمية للبنيات الجزئية في المدينة، وعادة ما تنمو المراحل الاولى لبنية النسيج الشبكي وصولاً الى الشكل الموحد للبنية
الشمولية للمدينة الشبكية التنظيم من خلال آليات التكرار مما يعطي تنبؤ بالتطورات المستقبلية لبنية المدينة، حيث تماثل
علاقة الاجزاء بالمنظومة الشمولية للمدن الشبكية نمط للتكرار وبمختلف المقاييس في الكثير من المدن المعاصرة. جدول

رقم 3

الجدول (1) المتغيرات المتعلقة بالإرتباطية كبنية تنظيمية

المفردات الثانوية	المتغيرات التفصيلية	القيم الممكنة
تحقيق ترابط النسيج مورفولوجيا	ترابط ابنيته مكانياً	ابنية نقطية متقطعة
		واجهة بلوك حضري مستمرة
	ترابط سطوحه	حافة حضرية متقطعة بمحاور حركية
		سطوح حضرية
	ترابط محاوره الحركية	تغير قليل في الحركة
		فضاءات حركية متقطعة
تحقيق ترابط النسيج نمطياً	ضمن النمطية المعاصرة	عند اختلاف التوزيع النمطي
		تكرار مستمر للنمط (محاور وتقاطعات)
	ضمن النمطية التقليدية	امكانية توقيع نماذج خطية مع تكوينات متعددة
		سلسلة مترابطة (عقد ومسالك)
	عند اختلاف التوزيع النمطي	مرونة تسمح بالتمازج مع نمط توزيع اخر
		انماط اولية prototype
		انماط ثانوية متعددة
		انماط جديدة مع تغير المجال المعلوماتي
		انماط متكررة ومتشابهة
	عند الامتداد البصري	فضاءات متقاربة الجهتين كثيفة الحركة
		شوارع بإمتدادات طويلة مع تغيير بالحركة
		شوارع بإمتدادات قصيرة دون تغيير بالحركة

الجدول (2) المتغيرات المتعلقة بالبنية الكثيفة المجزئة كبنية انسانية

المفردات الثانوية	المتغيرات التفصيلية	القيم الممكنة
تحقيق التواصل عبر المقياس الانساني	بنية ذات ابعاد تجزئية	تعطي مقياس اكثر انسانية
	بنية ذات ابعاد كتل شاهقة	تعطي مقياس بعيد انسانياً
	ابعاد هندسية تجزئية	تعطي مقياس اكثر انسانية
	تفاصيل تجزئية بتكنولوجيا حديثة	تقريب للمقياس الانساني
تحقيق التواصل من خلال الاستغلال الافضل للارض	فضاءات حضرية بأحداث للتواصل	حدث مسترفي شوارع محورية
		حدث للتوقف ضمن عقد المدينة
	تغير حيوية المدينة بتوزيع كثافتها	كثافة بنائية متساوية لجميع الاجزاء
		كثافات بنائية عالية عند العقد

الجدول (3) المتغيرات المتعلقة بالتجانس الشكلي للنسيج الحضري الكثيف

المفردات الثانوية	المتغيرات التفصيلية	القيم الممكنة
تعقيد البيئة البصرية بتأثير من الكثافة البنائية	زوايا نظر واضحة	بساطة وسهولة في الادراك
	زوايا نظر متغيرة	تعقيد وصعوبة في الادراك
	بيئة بصرية مزدحمة	تشويش وعدم قدرة على الادراك
تدرج في تعريف المقياس	التدرج من المقياس الكبير للصغير	نمط شكلي متكرر
	التدرج من المقياس الصغير للكبير	انماط شكلية متنوعة
	تعريف لمقاييس محددة	تعريف لمقياس كبير فقط
		تعريف لمقياس صغير فقط
		تعريف لهجين من المقاييس
التنوع	استمرار للاقاع بين التقليد والمعاصر	واجهات متكاملة بهوية محددة
		شكل بنائي موحد، مكعب او اسطوانة
		واجهات هجينة تقليدية ومعاصرة
	استمرار للاقاع بين التقليد والمعاصر	تحول نسب من السطوح الحجرية الى مزججة
		تكرار عناصر متماثلة بين التقليدي والحديث
تحقيق رمزية عالية	اختلاف سياق الذاكرة	وفقاً لسياق المدينة
		وفقاً لسياقها الموقعي
	ذاكرة نصيبية	نصب برمزية عالمية
		نصب برمزية محلية
	انعكاس الرمزية الوظيفية	على مستوى المدينة
		على المستوى الموقعي
تحقيق رمزية عالية	استعارة تاريخية برمزية مستمرة	Boulevard&Avenue
	استعارة معاصرة	ابنية تحقق هوية عالمية
	استعارة تبادلية بين المحلية والعالمية	هوية هجينة معاصرة
انعكاس لروح العصر	انعكاس لقوى التكنولوجيا ورأس المال	تنعكس في نسيج تقليدي
		عقد بكثافات عالية
		نسيج مباني برجية
		ناطحات السحاب المتفرقة

ولغرض إستكمال الجانب التطبيقي للبحث بهدف التحقق من فرضية البحث المتعلقة بطبيعة وتأثيرات العلاقة بين تكامل النسيج الحضري الكثيف بنائياً ومتغيرات الخصائص الشكلية لانماط البيئة الحضرية المختلفة وبسبب العلاقة التبادلية

المتكاملة بين مفردات الاطار النظري الثلاث السابقة، فقد أعتمدت ضمن إستمارة الاستبيان وتحديدًا لمجموعة من المماريين ضمت الاساتذة الاكاديميين والمهندسين المعماريين ذوي الخبرة مع اختلاف فئاتهم العمرية لإختلاف التأثير الحسي في إدراك وتقويم البيئة الحضرية، وتم انتخاب العينات البحثية من فضاءات حضرية لمدينتين كبيرتين هما New York وLondon اعتماداً على التنوع في أنماط التوزيع الهيكلي للمدينتين - بين النسيج العضوي لمدينة لندن والنسيج الشبكي لمدينة نيويورك- وتركزت هذه العينات بين عقدة او محور لكلا المدينتين.

5. العينات البحثية

1.5. العينة البحثية الاولى : New York, Times Square

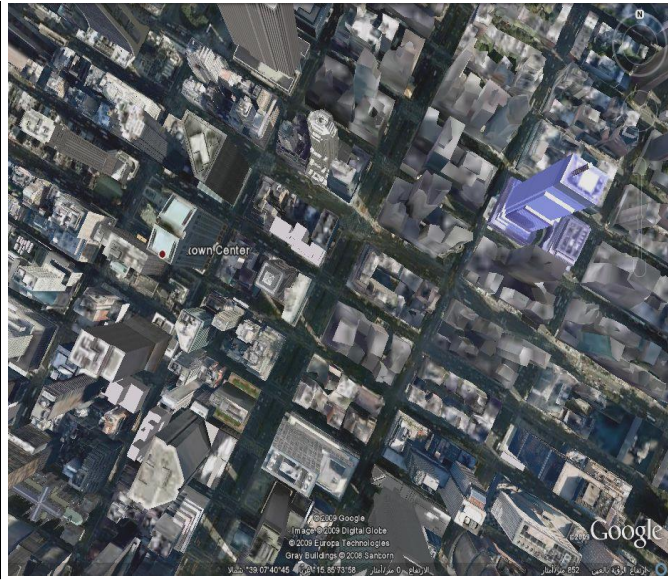
تعد Times Square بؤرة تقاطع رئيسية عند التقاء شارع Broadway و Seventh Avenue وكانت تمثل ضمن تاريخها مع بدايات القرن الماضي " فضاء Agora " من تجمع الفعاليات الثقافية فيها كمسارح وقاعات سينما، وكانت مكاناً لنسبة عالية من الجريمة لعقود بعد الثلاثينات وبسبب هويتها المعرفة كمركز لمئات الاعلانات الرقمية الحركية وربما فوضوية بصورة حيوية واخاذاة فهي تعد واحدة من الصور الايقونية للمدينة العالمية وعلامة دالة في New York.



الشكل (3) صور لعقدة Times Square المزدهمة \ New York

2.5. العينة البحثية الثانية : New York, Park Avenue

يعتبر واحد من شوارع التسوق ذات الماركات العالمية ومركز لتجمع الشركات العالمية ومراكز البورصات كذلك يقع فيه مجموعة من الفنادق الكبرى ويحوي الشارع واحدة من محطات النقل الرئيسية للمدينة Grand Central Terminal. وهو من اعرض الشوارع المخترقة الممتدة بطرز مختلفة للابنية بين التقليدي بواجهاته الحجرية والمعاصر بواجهاته المزججة وناطحات السحاب.



الشكل (4) صور المحور الطولي New York \ Park Avenue

3.5. العينة البحثية الثالثة: London, Piccadilly Circus

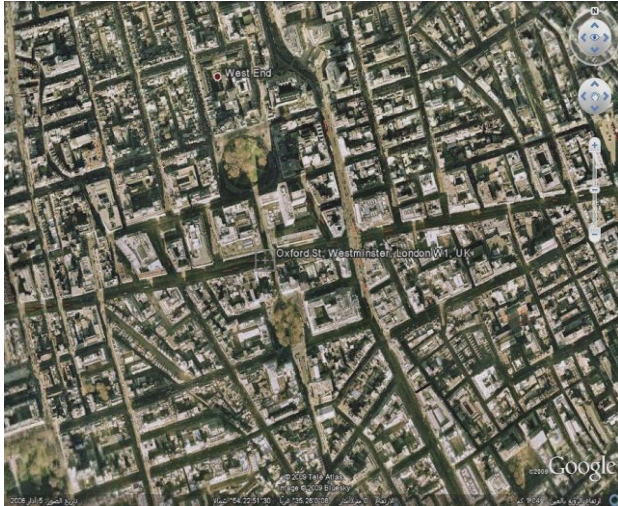
يعد Piccadilly Circus واحد من عقد التقاطع الحركية والفضاءات العامة المهمة في الجانب الغربي لمركز Westminster ، وُجدت هذه العقدة منذ 1819 لربط شوارع التسوق الرئيسية انذاك Regent Street و Piccadilly وتأخذ شكلها الدائري كفضاء حضري من شكل السيرك وهي بؤرة المنطقة التجارية والترفيهية للمركز الغربي بكثافة حركية وسياحية عالية محاطة بواجهات تقليدية لمباني مهمة.



الشكل (5) صور العقدة الحضرية في Piccadilly circus

4.5. العينة البحثية الرابعة: London ,Oxford Street

هو احد شوارع Boulevard الممتدة من غرب الى شرق المدينة حيث يتصل بالمركز المالي فيها عند منطقة Bishop Gate وامتدادات Fenchurch Street ويعد من اهم مراكز المدينة لكونه يربط اجزاء عديدة، يتكون المشهد الحضري من طرز متنوعة بشكل واجهات ابنية منفردة تعتمد مواد وعناصر حديثة وبمعدل ارتفاع مساوي للكثافة البنائية في باقي اجزاء النسيج الحضري لمدينة .



الشكل (6) صور المحور الحركي
Oxford Street / London الممتد

6. نتائج عملية الاستبيان المتعلقة بالخصائص الشكلية للأنماط الهيكلية للبيئة الحضرية

إن النتائج التي أظهرتها عملية الاستبيان جاءت للتحقق من العلاقة بين تكامل النسيج الحضري الكثيف بنائياً ومتغيرات الخصائص الشكلية لأنماط البيئة الحضرية المختلفة ضمن مفردات الاطار النظري المحدد وكما يأتي :

1.6. الارتباطية كبنية تنظيمية

– من الواضح أن الارتباطية تتلازم بعلاقات مباشرة مع طبيعة استعمالات الارض لان القيمة الاقتصادية للارض تتأثر بسهولة الوصول الى الموقع من أجزاء اخرى في المدينة . لذلك يجب أن تعمل منظومة الحركة عند المقياس الكبير في المدينة على انتشار اكبر لحركة السيارة إعتماًداً على نسيج الشوارع المتعامدة الممتدة والمستقيمة وأيضاً تعمل على تقليص الاعتماد على حركة السيارة وزيادة الاستعمالات الجاذبة لحركة المشاة عند المقياس الصغير اعتماداً على البنية المترابطة للنسيج العضوي.

– تتعارض الثبوتية الطويلة الامد لعناصر النسيج الحضري مع ظهور ترابطات جديدة ، وهذا يظهر في عدم وجود تنوع في انماط التوزيع عند النسيج العضوي او الشبكي وانما تظهر مرونة التجميع بين الانماط عند النسيج المختلط ولكن بصورة عشوائية تحدث انقطاعات تبحث عن غنى اكبر لواجهاتها يقلل من التكرار المستمر للعناصر بسبب طول هذه الشوارع الممتدة لكل النسيج.

مما يظهر بأن كلاً من النسيج العضوي والشبكي يعتمدان انماط اولية في هيكلية تجميعها افقياً ويتقبلان انماط شكلية مع زيادة كثافتهما البنائية عمودياً إعتماًداً على تنوع المجال المعلوماتي الذي يضيف للبيئة الحضرية شكلياً .

– لاتظهر عقد ومحاور النسيج العضوي كحافة حضرية بسبب تشابه الكثافة البنائية لكل اجزاء وعناصر النسيج

في النسيج الرابط ، لذلك يجب ان يبدأ التجمع او التزاوج الحضري في اكثر المقاييس صغراً بهدف ربط العناصر التكميلية المتناقضة في وحدة واحدة.

– تبدو المحاور الحركية كواجهة نسيج حضري رغم انها ابنية نقطية بسبب استمرارية المحاور البصرية وعدم تغيير في اتجاهات الحركة عند النسيج الشبكي بينما يظهر ترابط النسيج الحضري كواجهة حضرية متكاملة محددة للبلوك الحضري سواء عند العقدة او المحور للنسيج العضوي مما يظهر امكانية زيادة ترابط النسيج الحضري كواجهة محددة للبلوك الحضري وتوقيع ابنية نقطية بكثافة عالية تزيد من كفاءة استعمالات الارض وزيادة الارتباطية بين الحافة الحضرية والنسيج حولها.

– زيادة الكثافة البنائية عند الفضاءات الساكنة (العقد) لاي نوع من انماط التوزيع يعطي مرونة اكبر في تقبل انماط شكلية وعناصر معمارية جديدة وبالعكس تقل مرونة اضافة انماط وعناصر جديدة لعقد الكثافات البنائية الواطنة بسبب تعاملها مع مقاييس محدودة ووقوعها ضمن محاور النسيج العضوي ذات الارتباطات القصيرة والتغير المستمر لروايات النظر وبسبب الواجهات التقليدية المستمرة التي تخلق التنوع من غنى التفاصيل المعمارية فيها . بينما تظهر المحاور الحركية للنسيج الشبكي مرونة لتقبل انماط شكلية معاصرة رغم انها تحمل الطابع التقليدي لواجهاتها الا انها تحتاج العناصر المعمارية الحديثة لان العضوي وكذلك لاتظهر عقد ومحاور النسيج الشبكي كحافة حضرية قوية ومنفصلة عن باقي نسيجها بسبب ان النسيج الشبكي نسيجاً نقطياً يتوزع بكثافة بنائية متساوية لكل اجزاء النسيج.

2.6. البنية الكثيفة المجزئة كبنية انسانية

– لما كان العقل البشري تجزئياً fractal بطبيعته وناظر من التنظيمات الهندسية، يكون التعامل الافضل مع الواجهات الحضرية على مستوى المقياس الانساني الاصغر micro scale من خلال هندسية تجزئية متدرجة بتناغم خاصة عند العقد ذات الكثافات الواطنة

يجعل من المستحيل تغيير احدها بدون التأثير او تغير الآخر فالتنوع في العناصر والوظائف على المقياس الصغير ضروري لتماسك المقياس الكبير وتكون الحلقة الأضعف في الترابط بين العناصر الأكبر والعناصر الأصغر حين يكون (التناقض تام في المقياس)، او بين العناصر الثانوية الداخلية للنماذج المتباينة او المختلفة وليس شرطاً ان يكون تكرار العناصر المتماثلة قوة ربط وانما التجميع ممكن ان يكون قوة رابطة حتى مع الصفات المتناقضة او يمكن من خلال وجود محفزات وسطية تربط العناصر غير القادرة على التجمع مباشرة.

- ان استعمال المقياس الصغير في دراسة طبيعة المجتمعات ساعدت في تعميق المعرفة في جوانب حيوية النسيج الحضري المتعلقة بالبيئة الاقتصادية- الاجتماعية socio- economic والمعلومات المكانية ثلاثية الابعاد للبيئة الفيزيائية، بينما استعمال المقياس الكبير اظهر اعتماد انماط اولية فضائية فقط في تطبيق المدينة بمستواها الشمولي . فظهر عدم وجود تمازج بين نمطي التوزيع العضوي والشبكي على المقياس الكبير وانما يكون التمازج بين التقليدي والمعاصر على المقياس الصغير مع بقاء نمط التوسع مفتوح بمعالجات تكنولوجية جديدة للواجهات .

وبهذا تمكن البحث من اختبار فرضيته حول تأثير تنوع الانماط الهيكلية والشكلية للبيئة الحضرية في تحقيق التماسك الحضري لاجزاء المدينة المزدهمة والنسيج الرابط حولها من خلال العمل على استكشاف القيم الانسانية في العناصر الشكلية والعلاقات بينها للنسيج الكثيف بنائياً وتفعيلها لزيادة كفاءة المدينة وظيفياً وزيادة حيويتها ضمن سياقها المحلي وتأكيد دورها وهويتها كمدينة عالمية.

7. الاستنتاجات :

ممكن تعريف التماسك الحضري بأنه التكامل لمكونات البيئة الحضرية من خلال المزيج الوظيفي والفيزيائي وتحقيق التكامل الاجتماعي بدلاً عن العزلة للوصول الى الاداء الحضري المتكامل وظيفياً والبنية الفيزيائية المتكاملة شكلياً للوصول الى كل موحد بصرياً وتركيبياً . ويتحقق التماسك الحضري عادة في النسيج العضوي

عند النسيج العضوي بسبب الاحتوائية العالية لفضاء الشارع ، وتتوضح هذه النسب في شرفات الواجهات التقليدية وصفة الحركية في مقاييس العناصر كالأقواس مثلاً عند النسيج العضوي وتفاصيل تجزيئية بتكنولوجية حديثة مثل شاشات العرض كعناصر جذب تحاكي رغبة المتلقي وميله نحو التطور في عقدة النسيج الشبكي.

- من الممكن ان تتناغم الأبنية ذات المقياس الإنساني كالأبنية التقليدية مع ابنية مرتفعة لتحقيق كثافة بنائية عالية كما في معظم مراكز المدن الأوروبية اليوم ولكن بطريقة انسانية ضمن بيئة الشارع حين يكون التعامل مع ابنية بمعدل ارتفاع 7-8 طوابق بدلاً من ابنية برجية بارتفاع 14-16 طابق واكثر لتعطي استغلال افضل للأرض عند المحاور الحركية المستمرة لكل انماط التوزيع ولكن تعمل الكثافات البنائية العالية وحتى ناطحات السحاب على تقوية الدور الوظيفي لعقد التجمع عند النسيج العضوي وتظهر سلبية النسيج الشبكي في عدم وجود عقد متميزة وظيفياً وانما هي تقاطعات لتغيير الحركة ليس إلا مما يظهر حيوية اكبر لفعاليات انسانية عند محاور وعقد النسيج العضوي حتى مع كثافتها البنائية الواطئة ومحدودية وظيفتها وتغير لحيوية اجزاء من المحاور الحركية بالاعتماد على قيم معينة للمجتمع للتجمع في فضاءات خليط لكل الفئات او الانعزال كسكن لمجاميع مرفهة عند المحاور التقليدية للنسيج الشبكي.

3.6. التجانس الشكلي للنسيج الحضري الكثيف

- عند السير خلال شوارع النسيج العضوي يغمر المشاهد شعور بتكرار متماثل للابنية مما يقلل من تعقيدات البيئة الحضرية هناك رغم الغنى والتنوع في العناصر الزخرفية للابنية ولكن تظهر صعوبة في ادراك الخصائص البصرية لاي مشهد الحضري ضمن النسيج الشبكي رغم استمرارية زوايا النظر بسبب ارتفاعات خط السماء مما يصعب معه احتواء كل تفاصيل الابنية الشاهقة ضمن هذا المشهد .

- يرتبط اصغر المقاييس في البيئة المعمارية او الحضرية بصورة حميمية مع اكبر المقاييس فيها مما

حين تحوي البيئة الحضرية تحول العناصر المنسجمة والمتدرجة بنسبها الى مواد بتكنولوجيات حديثة ويبدو تأثير هذا الانسجام في العقد اكثر منه في المحاور الحركية بسبب الاحتوائية العالية التي تجمع هذه العناصر في حدود أضيق .

– تتكامل هوية المدينة حين تحمل اجزائها رمزية ضمن سياقها اولاً من تميز عناصرها المعمارية والحضرية ضمن هوية محلية سواء تقليدية او حديثة معاصرة ، وتعمل الرمزية النصيبية على منح المدينة هوية عالمية بينما تعمل الرمزية الوظيفية على تحقيق هوية المدينة محلياً وعالمياً ضمن إطار الدور الذي تلعبه المدينة في الاقتصاد العالمي الجديد .

النمو المتوازن الكثافة سواء كمحاور حركية وفضاءات او كإبنية تقليدية مرتبطة جيداً بالنسيج الحضري ولكن بالمقابل يظهر أن الابنية المنفردة للنسيج الشبكي المعاصر بعيدة تماماً عن الربط مع نسيج السياق حولها لفشلها في خلق بيئة انسانية فيغيب دورها الحضري ، كما أن التنظيم الشبكي لايربط اجزاء المدينة وانما يعطي شعور مضلل بذلك .

– تتميز البيئة الحضرية الجيدة بالعقد المزدحمة والاستعمالات المختلطة والمتنوعة مع نسيج عالي النوعية من الابنية والاماكن الحضرية التي تحوي تمازج متجانس لصفات فيزيائية متعددة وارتباطية تقلل من استعمال السيارة وتزيد التركيز على حركة المشاة. إلا أن المدن المعاصرة تنتهك قوانين المقياس مما يتسبب في إبتعاد الكثير من المناطق الحضرية عن المقاييس الإنسانية و هذا يساهم في تدهور وإضمحلال مدننا ، حيث إن اعتماد المدن الكبرى العالمية على قواعد نمطية لتوزيع الوحدات الحضرية تبعاً لأكبر مقياس أبعدتها تماماً عن الفعاليات الإنسانية الحيوية والضرورية لحياة اي مدينة في حين إن التتابع الذي يؤدي إلى التماسك الحضري يبدأ من المقياس الصغير micro scale إلى المقياس الكبير macro scale لكن انقلبت هذه القاعدة عند التفكير بنسيج المدن المزدحمة المعاصرة حين يبدأ التتابع من المقياس الكبير إلى الصغير.

– يعتمد كلا النسيجين العضوي والشبكي انماط اولية في هيكالية تجميعها افقياً وتقبل انماط شكلية مع زيادة كثافتها – تعمل الكثافات البنائية العالية عند العقد الحركية على اعطاء مساحات اوسع للتناغم بين التقليدي والمعاصر

المصادر العربية والاجنبية

▪ الحنكاي ، وحدة شكر ، 2004 . " أثر التوجهات الفكرية في البنية الحضرية " ، أطروحة دكتوراه مقدمة الى قسم الهندسة المعمارية / الجامعة التكنولوجية .

- Alexander, Christopher, 1987. " Anew Theory of Urban Design ", Oxford University Press; N.Y., USA.
- Bilson , M , 1995. " Small World and the Groundbreaking Science of Networks" , W.W. Norton & Company press, New York.
- Broadbent, Geoffrey , 1990" Emerging Concept of Urban Space Design ", Van No strand, N.Y., USA.
- Doxiadis , C.A, 1974."Anthropolis ;City for Human Development", Athens publishing center , New York.
- Fishman , Robert, 1987. "Bourgeois Utopia Vision of Suburbia", basic book , New York.
- Frank, L, 2003 . " Community Design: The impact of the built environment on physical activity ", Washington, Island Press.
- Grara, Sigurd , 2002. "Urban Transportation System ", Harvard University press.



- Rossi , Aldo ,1982. " **The Architecture of the City** " , Opposition Books, Cambridge, Mass.
- Johnson , Paul Alan , 1994 . " **Power Structures and the Architect; The Theory of Architecture** " , John Wiley & Sons Inc., New York.
- Lynch, Kevin, 1960. " **The image Of The City** " , The MIT Press.
- Mumford, Lewis, 1961. " **The City in History** " , A Harbinger Book.
- Rogers, Richard,1997. " **Cities for Small Planet** ", Faber – and Faber, Limited, London.
- Unger, Roberto, 1994. " **Theory and Community: Social Implications for Architecture; The Theory of Architecture** " ,John Wiley & Sons Inc., New York.
- Hillier, B & Hanson, J, 1984. ' **The Social Logic of Space** " ; Cambridge University Press, Cambridge .
- Hillier, B., 1996 ." **Space is The Machine**", Cambridge University Press, Cambridge.

- Krier , Leon , 1998." **Choice of Fate**", Cambridge University press
- Salingaros , 2005." **Principles of Urban Structure ;Urban Space and Information field**", Series design – Science – Planning.